

Engineering Light Using Large Area Photonic Crystal Devices

Sheila N. Tandon

B.E., Electrical Engineering
The Cooper Union for the Advancement of Science and Art (1999)

S.M., Electrical Engineering and Computer Science
Massachusetts Institute of Technology (2002)

Submitted to the
Department of Electrical Engineering and Computer Science
in partial fulfillment of the requirements for the degree of

Doctor of Philosophy in Electrical Engineering

at the

MASSACHUSETTS INSTITUTE OF TECHNOLOGY


June 2005

© 2005 Massachusetts Institute of Technology
All rights reserved.

Author.....

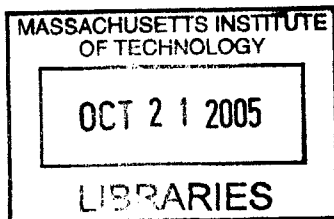
Sheila N. Tandon
Department of Electrical Engineering and Computer Science
May 12, 2005

Certified by.....

 Leslie A. Kolodziejski
Professor of Electrical Engineering and Computer Science
Thesis Supervisor

Accepted by.....

 Arthur C. Smith
Chair, Department Committee of Graduate Students
Department of Electrical Engineering and Computer Science



BARKER

Engineering Light Using Large Area Photonic Crystal Devices

by

Sheila N. Tandon

Submitted to the Department of Electrical Engineering and Computer Science
on May 12, 2005, in partial fulfillment of the
requirement of the degree of
Doctor of Philosophy in Electrical Engineering and Computer Science

Abstract

Photonic crystals are fabricated structures composed of a periodic arrangement of materials with differing indices of refraction. This research has focused on the realization of two distinct photonic crystal structures in which large area has played a key role: 1) large area broadband saturable Bragg reflectors, and 2) large area 2D photonic crystal devices. Saturable Bragg reflectors (SBRs) can be used to self-start ultra-short pulse generation in a variety of solid state and fiber lasers. To form shorter pulses, SBRs with broadband reflectivity and large area (100's of μm) are required. This thesis describes the design and fabrication of large area broadband saturable Bragg reflectors through the monolithic integration of semiconductor saturable absorbers with large area broadband Bragg mirrors. One of the key elements for realizing this device is the development of a wet oxidation process to create buried low-index Al_xO_y layers over large areas. Large area 2D photonic crystals enable new methods for routing and guiding light with applications in compact integrated optical circuits. This research has explored the design and fabrication of two large area (centimeter-scale) 2D photonic crystal devices: a superprism and a supercollimator. A superprism is a photonic crystal device in which the direction of light propagation is extremely sensitive to the wavelength and angle of incidence. A supercollimator is a device in which light is guided by the dispersion properties of a photonic crystal slab without boundaries which define the light's path. Design, fabrication, and testing are discussed for both 2D photonic crystal devices.

Thesis Supervisor: Leslie A. Kolodziejski

Title: Professor of Electrical Engineering and Computer Science

Acknowledgements

This thesis work would not have been possible without the support and encouragement of many individuals who have made my experience at MIT as wonderful as it has been. My fabulous advisor, Professor Leslie Kolodziejski, gave me the opportunity to join her group though I was a nervous young woman, who was daunted by MIT, but excited about optics. With Leslie's warm, supportive guidance, I have learned that a young woman can go far, not only with hard work and scientific proficiency, but by asking many questions, staying organized, and just being herself. Thank-you for helping to shape my life in a way I never thought possible. Gale Petrich, our research scientist, has also been instrumental to my educational development. The open door to his office, has been an open door to countless random questions, brainstorming sessions, and many laughs. Whether it is to read every word of my thesis, run to save me in the lab, or provide an attentive ear, Gale has set an example for generosity that will always make me smile.

I would also like to acknowledge a number of MIT faculty members who have advised and encouraged me throughout my PhD experience. As a collaborative member of the Nanostructures Laboratory since my 1st year in graduate school, Professor Hank Smith has been supportive of my work from the beginning and has always made me feel welcome in his lab both at group meetings and at group parties. Professor Erich Ippen and Franz Kärtner from the Ultrafast Optics Group have also been wonderful advisors, helping me appreciate the context of my work from an optics perspective, encouraging me as my work advanced, and making me feel at home within their groups. I have also been fortunate to work closely with Professor John Joannopoulos from the Materials and Interfaces Group

since the beginning of my graduate studies, and I thank him for the warmth and enthusiasm he has brought to our collaboration.

My collaborations have included a number of MIT researchers, some of whom have graduated, and some who continue their work at MIT. Juliet Gopinath and Hanfei Shen, my closest collaborators in my SBR work, have been an absolute pleasure to work with. Working with them has showed me how great work can stem from great team dynamics. Thank-you for making it so much fun! I also thank Marcus Dahlem and Pete Rakich for showing how hard work and dedication can lead to beautiful optical characterizations. In the Materials and Interfaces Group, I thank Marin Soljacic, Chiyun Luo, and Mihai Ibanescu who have been my theoretical connection to the world of photonic crystals.

A number of individuals have been significant to my education in the laboratory. Jim Daley from the Nanostructures Laboratory has not only been an invaluable technical resource as I have worked to create physical devices, but he has generously helped me any time I've needed him, and has made working in the lab a truly enjoyable experience. Thank-you to Jimmy Carter who has also helped me around the laboratory while bringing me many smiles. I am grateful to a number of former students who really got me started in the laboratory: Alexei Erchak, Mike Walsh, and Tim Savas. Thank-you for holding my hand at the beginning, answering all my questions, and being patient, friendly teachers.

My officemate Ryan Williams deserves a special acknowledgement because he has shared an office with me for over four years. Not only has he been a constant resource for all my materials science questions, but he has been a regular sounding board for all of my issues, materials science or not. Ryan, it's been a ton of fun sharing an office with you! A special thanks also to Christel Zanke, an inspiring research scientist who took a special interest in my development, helped me build confidence to try new techniques in the lab, and continues to cheer me on from across the ocean. And of course, I must thank Melissa Hornstein who took me under her wing from day #1 at MIT, and made sure I wouldn't leave without with a PhD. Melissa's unending generosity has taught me how much fun generosity can be. I can only hope to be as good a friend as she has been.

And last but not least, I thank my family: my mother and father, Nina, Neil and Meera. They have been a huge part of this journey and their love and encouragement have meant the world to me.

Table of Contents

Chapter 1	Introduction	20
1.1	What is a Photonic Crystal?	20
1.2	References.....	21
Chapter 2	Saturable Bragg Reflectors for Ultra-Short Pulse Generation	22
2.1	Motivations	22
2.1.1	Creating ultra-short pulses.....	22
2.1.2	Using a saturable absorber mirror for modelocking	24
2.1.3	Absorber design overview	28
2.1.4	The challenge of broadband mirrors	30
2.1.5	Large scale oxidation for large area SBRs.....	33
2.2	Saturable Bragg Reflector Design Overview	35
2.3	SBR Fabrication Process Overview	37
2.4	Large Scale Oxidation for Large Area Bragg Mirrors	40
2.4.1	The initial challenge of large scale oxidation	40
2.4.2	The AlGaAs/Al _x O _y large area broadband mirror.....	42
2.4.3	Limitations of large area AlGaAs/Al _x O _y mirrors	44
2.4.4	The InGaAlP/Al _x O _y large area broadband mirror	46
2.5	SBRs for Infrared Wavelength Lasers	49
2.5.1	Design motivation.....	49
2.5.2	Absorber Delamination	52
2.5.3	Results: Temperature dependence of absorber delamination	53
2.5.4	Results: Thickness dependence of absorber delamination	55

2.5.5	Observations: Cladding layer dependence of absorber delamination	58
2.5.6	Results: Variation of absorber delamination across wafer	59
2.5.7	Oxidation rate ramping.....	67
2.5.8	Unoxidized structure stability	76
2.6	SBRs for Visible Wavelength Lasers	78
2.6.1	Design motivation.....	78
2.6.2	Observations: Temperature dependence of oxidation	79
2.7	Optical Characterization of Structures	80
2.7.1	Reflectivity measurements	80
2.7.2	Laser system testing	81
2.7.3	Photoluminescence measurements	83
2.8	Conclusions.....	89
2.9	Future Work.....	90
2.10	References.....	91
Chapter 3	Large Area Two-Dimensional Photonic Crystal Devices	95
3.1	Creating Large Area 2D Photonic Crystals.....	95
3.1.1	Introduction.....	95
3.1.2	Interference lithography	96
3.1.3	The trilayer resist process	103
3.1.4	Reactive ion etching.....	106
3.2	The Superprism	113
3.2.1	Motivations.....	113
3.2.2	Design theory and simulations.....	117
3.2.3	Objective.....	123
3.2.4	Superprism fabrication overview	125
3.2.5	Photolithography	126
3.2.6	Interference lithography and photonic crystal alignment.....	129
3.2.7	Large scale oxidation of AIAs for thick buried oxides	131
3.2.8	Device fabrication results.....	140
3.2.9	Testing Requirements and Challenges.....	142
3.2.10	Conclusions	146
3.3	The Super-Collimator	147
3.3.1	Motivations.....	147
3.3.2	Design theory and simulations.....	149
3.3.3	Objective.....	152

3.3.4	Device fabrication	153
3.3.5	Optical characterization	155
3.3.6	Future work	160
3.3.7	Conclusion.....	161
3.4	References.....	162
Chapter 4	List of Contributions	164
4.1	Journal Publications.....	164
4.2	Conference Presentations.....	165
4.3	Seminar Talks	165
Chapter 5	Appendix	166
5.1	Oxidation Log.....	166
5.2	SBR growth log	170
5.3	Table of Relevant Refractive Indices for SBR Designs	171
5.4	Table of Optical Constants for Tri-Layer Processing	172
5.5	References.....	172

Table of Figures

Figure 1-1 From left to right, examples of one, two, and three dimensional photonic crystals. The color differences represent materials with differing index of refraction (adapted from [1]).	21
Figure 3-1 (a) A simplified schematic of the laser system using Kerr Lens Modelocking. (b) A simplified schematic of a pulsed laser system where a saturable absorber is used.	23
Figure 3-2 Schematic illustrating how pulses can self-start in a laser system from initial noise.	26
Figure 3-3 An illustration showing how a 10 femtosecond pulse is formed from a frequency bandwidth of about 40THz. For a center frequency of 1230 nm, this pulse width also implies a wavelength bandwidth of about 200 nm.	26
Figure 3-4 Schematic outlining the challenges of creating a saturable absorber mirror for ultra-short pulse lasers.	27
Figure 3-5 The band gap versus lattice constant diagram for the major III-V alloys. A diagram of the crystal structure is also shown.	28
Figure 3-6 Saturation fluence measurements illustrating the saturable and nonsaturable losses, as well as two photon absorption in a structure with an absorbing InGaAs quantum well and InP cladding layers. The absorber was grown on a 22 pair GaAs/AlAs mirror stack [10].	29
Figure 3-7 Schematic of a Bragg mirror showing alternating layers of high and low refractive index (n).	31
Figure 3-8 Reflectivity measurements contrasting the high reflectivity bandwidth of an all-semiconductor SBR (blue) with an SBR with oxidized mirror layers (red).	33
Figure 3-9 Schematic of a Saturable Bragg Reflector illustrating the cross-section of the layered structure.	35

Figure 3-10 Overview of saturable Bragg reflector fabrication sequence showing major steps.	37
Figure 3-11 Schematic illustrating the lateral oxidation of AlAs layers in a Bragg mirror stack.	39
Figure 3-12 Schematic of oxidation setup showing sample location within furnace, direction of steam flow, temperature monitoring positions, and water supply lines.	39
Figure 3-13 a) Nomarski micrograph showing the plan-view of a GaAs/AlAs dielectric stack deformed due to stresses introduced by oxidation at 435°C for 2 hours. b) Scanning Electron Micrograph (SEM) showing the cross-section of the stack with delaminated layers [40].	41
Figure 3-14 Differential interference contrast images showing the plan-views of two different 7 pair SBR structures after oxidation: (a) GaAs/AlAs structure oxidized at 375°C for 10 hours; (b) Al _{0.7} Ga _{0.3} As/AlAs structure oxidized at 435°C for 2 hours [40].	42
Figure 3-15 (a) Differential interference contrast images showing the plan-view of a 7 pair Al _{0.3} Ga _{0.7} As (92nm)/AlAs (200nm) structure after oxidation at 420°C for 4.25 hr. (b) SEM image showing the SBR cross-section.	43
Figure 3-16 Reflectance measurements of the oxidized and unoxidized Al _{0.3} Ga _{0.7} As/AlAs dielectric stack structures.	43
Figure 3-17 (a) SEM image showing cross-section of the layered structure at the center of the 500 μm mesa. (b) SEM image showing cross-section of the layered structure at the edge of the mesa. (c) Microscope image showing mesa locations for (a) and (b) images.	44
Figure 3-18 (a) Differential interference contrast image of oxidized SBR pointing out two different locations where the reflectivity was measured. (b) FTIR measurements contrasting the reflectivity associated with two different locations on the mesa.	45
Figure 3-19 (a) Differential interference contrast (DIC) image of fully-oxidized SBR. (b) SEM micrograph showing In _{0.15} Ga _{0.15} Al _{0.35} P/Al _x O _y mirror with GaAs absorber and In _{0.15} Ga _{0.15} Al _{0.35} P cladding layers.	46
Figure 3-20 (a) Microspectrophotometer measurement at three different locations of an SBR structure with In _{0.15} Ga _{0.15} Al _{0.35} P/Al _x O _y mirror. (b) DIC image showing the location on the mesa corresponding to each reflectivity trace.	47
Figure 3-21 Differential interference contrast images of partially-oxidized 1mm x 1mm square mesas. Oxidations were carried out for three different durations: (a) 435°C, 5hrs (R1000 sq sample 2, 5/12/04 435°C, 5hr), (b) 435°C, 7hr (R1000 sq sample 3, 5/14/04 435°C, 7hr), (c) 435°C 9hr (R1000 sq sample 4, 6/24/04, 435°C, 9.5hr).	48
Figure 3-22 Microspectrophotometer measurement of the partially oxidized square mesa shown in Figure 3-21(a). The measurement of the oxidized region was from the outer area of the square mesa while the measurement of the unoxidized region was from the center of the square mesa.	49

Figure 3-23 Band gap energy versus lattice constant diagram indicating the band gap associated with each of the layers which compose the SBR for the Cr:Forsterite laser (adapted from [42]). 50

Figure 3-24 (a) Differential interference contrast (DIC) image of oxidized 500 μ m mesa illustrating delamination. (b) SEM image showing absorber delamination from the mirror stack. (c) SEM image showing the patterned absorber delamination. (R958, 3hr, 435C, 3/31/2003) 53

Figure 3-25 Oxidation results illustrating the temperature dependence of absorber delamination. The InGaAs absorber thickness is 80 nm. All mesas have 500 μ m diameters and are from similar areas of the wafer. (a) Oxidation at 435°C, 3 hrs (R958, 3/31/2003), (b) Oxidation at 420°C for 3.5 hr (R958, 12/7/2002), (c) Oxidation at 410°C for 4.5 hours (R958, 12/18/2002). 54

Figure 3-26 Oxidation results illustrating the temperature dependence of absorber delamination. The InGaAs absorber thickness is 10 nm. All mesas have 500 μ m diameters and are from similar areas of the wafer. (a) Oxidation at 435°C, 3 hrs (R957, 3/31/2003), (b) Oxidation at 420°C for 4 hr (R957, 12/6/2002), (c) Oxidation at 410°C for 4.5 hours (R957, 12/18/2002)..... 55

Figure 3-27 Oxidation results illustrating the temperature dependence of absorber delamination. The InGaAs absorber thickness is 40 nm. All mesas have 500 μ m diameters and are from similar areas of the wafer. (a) Oxidation at 435°C, 3 hrs (R946, 10/29/2002), (b) Oxidation at 420°C for 4 hrs (R946, 11/18/2002) [45], (c) Oxidation at 410°C for 4.5 hours (R946, 4/24/2003). 55

Figure 3-28 Oxidation results examining thickness dependence of absorber delamination. (a) 10nm InGaAs absorber, 240nm AIAs (R957, 12/18/2002, 410°C, 4.5 hr), (b) 40nm InGaAs absorber, 200nm AIAs (R946, 4/24/2003, 410°C, 4.5 hr), (c) 80nm InGaAs absorber, 200nm AIAs (R958, 12/18/2002, 410°C, 4.5 hr) 56

Figure 3-29 Oxidation results examining the dependence of absorber delamination on AIAs thickness. (a) 10nm InGaAs absorber, 213nm AIAs (R933, 9/27/2002, 420°C, 3 hr), (b) 10nm InGaAs absorber, 240nm AIAs (R959, 2/14/2003, 410°C, 4.5 hr) 57

Figure 3-30 Oxidation results examining the dependence of absorber delamination on AIAs thickness. (a) 8nm multiple quantum well (MQW) InGaAs absorber, 182nm AIAs (R934, 9/27/2002, 435°C, 3.5 hr), (b) 10nm InGaAs absorber, 240nm AIAs (R957, 3/31/2003, 435°C, 3 hr) 57

Figure 3-31 Oxidation results suggesting cladding layer dependence of absorber delamination. (a) Structure with GaAs cladding (R968, 4/25/2003, 410°C, 5hrs). (a) Another structure with GaAs cladding (R957, 2/14/2003, 410°C, 4.5hr). (c) Structure with InP cladding (R959, 2/14/2003, 410°C, 4.5 hr)..... 58

Figure 3-32 Oxidation results illustrating how delamination effects vary with mesa location on the wafer (R958, 2/14/2003, 410°C, 4.5hr)..... 59

Figure 3-33 Oxidation results for SBR structure with absorber grown at 400C. (a) R970, 4/24/2003, 410C, 4.5hrs (b) R970, 4/25/2003 #2, 410C, 6hrs (c) R970, 4/28/2003, 410C, 5.5hrs (d) R970, 5/23/2003, 410C, 4.7hr. 60

- Figure 3-34 Fourier Transform Infrared Spectroscopy (FTIR) measurements illustrating the trend in the reflectivities of oxidized mesas from the edge of the wafer to the center of the wafer for the sample shown in Figure 1 30 (R958, 2/14/2003, 410°C, 4.5hr). The shaded area is below the FTIR detector's effective range. 61
- Figure 3-35 Oxidation results showing how delamination effects depend on the location of the mesa on the wafer. (a) A mesa from the center of the wafer. (b) A mesa from the edge of the wafer. (R957, 2/14/2003, 410°C, 4.5hr) 62
- Figure 3-36 Fourier Transform Infrared Spectroscopy (FTIR) measurements illustrating the difference in the reflectivities of oxidized mesas from the edge of the wafer and the center of the wafer for the mesas shown in Figure 3-35 (R957, 2/14/2003, 410°C, 4.5hr). The shaded area is below the FTIR detector's effective range. 62
- Figure 3-37 Reflectivity measurements and DIC images of three oxidized mesas of r958 with the $Al_{0.3}Ga_{0.7}As$ and Al_xO_y layer thicknesses implied by theoretical best-fit calculations. Mesa #1 is closest to the edge of the wafer and Mesa #25 is closest to the center of the wafer. Mesa #12 is the mesa closest to the center of the wafer where delamination did not occur. (R958, 2/14/2003, 410°C, 4.5hr)..... 63
- Figure 3-38 Room temperature photoluminescence (PL) measurements on an unoxidized SBR structure (R1000) with a 10nm GaAs quantum well. Results show a variation in PL for regions from the edge of the wafer to the center. Digital photograph of a quarter wafer is shown at the right with measurement locations indicated. 65
- Figure 3-39 Photoluminescence results for unoxidized SBR structure R971 with a single 10nm InGaAs quantum well within InP cladding layers. Raw data was fitted to a 9th order polynomial and normalized. (PL 3/08/2005)..... 66
- Figure 3-40 Photoluminescence results for unoxidized SBR structure R981 with six 10nm InGaAs quantum wells within InP cladding layers. Raw data was fitted to a 9th order polynomial and normalized. (PL 3/08/2005) 66
- Figure 3-41 Photoluminescence results for unoxidized SBR structure R1014 with six 10nm InGaAs quantum wells within InP cladding layers. Raw data was fitted to a 9th order polynomial and normalized. (PL 3/08/2005) 67
- Figure 3-42 Differential interference contrast images showing oxidation results for an SBR structure oxidized (a) for 2 hours at 400°C (b) for 4 hours at 410°C with a temperature ramp before and after oxidation..... 68
- Figure 3-43 SEM image showing cross-section of SBR structure oxidized in Figure 3-42. The structure consists of an absorber with multiple quantum wells of InGaAs within InP cladding layers and a mirror with 7.5 pairs of $Al_{0.3}Ga_{0.7}As$ and Al_xO_y (an extra $Al_{0.3}Ga_{0.7}As$ layer is included at the bottom of the mirror stack as shown)..... 69
- Figure 3-44 Oxidation results illustrating the effect of implementing a temperature ramp before and after oxidation at 410°C for 4.5 hrs. (a) Without temperature ramp (R958, 2/14/2003, 410°C, 4.5hr) (b) With a temperature ramp (R958, 8/14/2003, 410°C, 4.5hr, w/ 50 min ramp)..... 70
- Figure 3-45 Oxidation results illustrating the effect of steam during the ramping process. (a) Unoxidized mesa. (b) Oxidized mesa with no steam present during ramp up (R958

3/10/04) (c) Oxidized mesa with no steam present during ramp down (R958, 3/11/04).	71
Figure 3-46 DIC images of SBR mesas with oxidation initiated by an oxidation ramp. (a) R971 8/21/03 410°C 6hr with ramp. (b) R981 8/14/03 410°C 4.5hr with ramp. (c) R1015 1/26/04 410°C 5hr with ramp. All ramps were from 100 to 410°C for 50 minutes in the presence of steam.	71
Figure 3-47 DIC images of two oxidized mesas of SBR structure R981 oxidized at 435°C for 2 hours after two ramps: 100-400°C, 50min and 400-435°C, 60min (R981 9/4/03 435°C, 2hr, 2 ramps).....	72
Figure 3-48 Average oxidation rate versus temperature. Oxidation rates were averaged over all SBR structures for 500µm mesas that were not completely oxidized. An exponential and a linear best-fit was calculated as shown. Radial dependence and AIAs thickness dependence of the oxidation rate was not considered.....	73
Figure 3-49 Estimate of radial extent of oxidation front for the two oxidation ramps implemented in Figure 3-47 assuming an exponential oxidation rate versus temperature characteristic.	74
Figure 3-50 DIC images showing the results of oxidation of SBR R968 with (a) one ramp (R968 6/7/04 410C 5hr, 50 min. ramp) and (b) two ramps (R968 6/11/04 sample 4, 410C, 4.5hr, 2 ramps).	74
Figure 3-51 DIC images showing the results of oxidation of SBR R1027 with (a) one ramp (R1027 6/7/04 sample 1 410C 5hr w/ 50min ramp) and (b) two ramps (R1027 6/10/04 sample 3 410C 4.5hr w/ 2 ramps).....	75
Figure 3-52 DIC images of unoxidized mesas showing how deterioration occurs after wet etching. (a) A mesa from the center of the wafer from SBR R958. (b) A mesa from the edge of the wafer from SBR R958. (c) A mesa from SBR R968. (d) A mesa from SBR R979.	76
Figure 3-53 SEM images showing oxidation of the AIAs layers at a mesa edge one day after wet etching (R979 unoxidized).	77
Figure 3-54 Band gap energy versus lattice constant diagram indicating the band gap associated with each of the layers which compose the SBR for the Ti:Sapphire laser. .	78
Figure 3-55 DIC images showing oxidation results at (a) 410°C (R1000 sample 13 10/23/03 410°C 4.5hr w/ 50min ramp) and (b) 435°C (R1000 sample 22 3/1/2004 435°C 2.5hr w/ 50 min. ramp) for an SBR structure for the Ti:Sapphire laser.	79
Figure 3-56 Reflectivity measurements of SBR structures fabricated for three different laser systems: Ti:Sapphire, Cr:Forsterite, and Er:Bi ₂ O ₃ fiber laser with theoretical mirror reflectivity > 99% over 294nm, 466nm, and 563nm respectively. All measurements reveal losses due to SBR absorption.....	80
Figure 3-57 Microspectrophotometer measurements of five different oxidized samples of R1000 with sample location shown on a photograph of a ¼ wafer. Reflectivity dip for sample 11's reflectivity curve is an artifact of the measurement due to two different spectrometers used for the lower and upper wavelength ranges.	81

Figure 3-58 SBR-modelocked spectra of (a) Ti:Sapphire (SBR R1000), (b) Cr:Forsterite (SBR R946), (c) Cr:YAG (SBR R921), and (d) Er:Bi₂O₃ (SBR R981) lasers with respective SBR reflectivities. In (a), reflectivities of two SBRs from the same wafer are shown. One measurement (dotted line) was limited in range by the spectrometer used [48]. 82

Figure 3-59 Output power spectra from the Ti:Sapphire laser system for five different samples of SBR structure R1000 with sample location on the wafer as shown. Measurements performed by Dr. Richard Ell in the Ultra-fast Optics Group at MIT. 83

Figure 3-60 Digital photographs of 1/4 wafers of SBR structure R1000 showing a summary of the room temperature photoluminescence measurements on both oxidized and unoxidized samples..... 84

Figure 3-61 PL intensities and reflectivity measurements from two different locations of unoxidized SBR structure R1000. 85

Figure 3-62 Digital photographs of 1/4 wafers representing SBR structure R1020 summarizing photoluminescence measurements on both oxidized and unoxidized samples. 86

Figure 3-63 Calculation of the ground state wavelength for an infinite GaAs quantum well (QW) versus QW width. 87

Figure 3-64 Low temperature photoluminescence measurements on an unoxidized sample of R979 before and after a pure temperature ramp without the presence of steam. Temperature profile: 100-400°C, 50 min; 400-435°C, 60min; 435°C, 2 hr; 435-100°C, 60min. 87

Figure 3-65 Low temperature PL intensity (T=10K) and FTIR measurement for an oxidized and unoxidized sample of SBR structure R979. 88

Figure 3-1 A large area photonic crystal patterned using interference lithography. Image taken using scanning electron microscopy. 96

Figure 3-2 In interference lithography, the standing wave that is formed by the interference of two light beams, exposes a periodic grating on the substrate. The incoming waves are approximated as plane waves when in reality they are spherical. 97

Figure 3-3 Scanning electron micrographs showing the patterning results of two interference lithography exposures in a layer of photoresist. (a) A grating is patterned with one exposure. (b) A second exposure rotated 90° from the first exposure results in a grid. 97

Figure 3-4 Top view of the Lloyd's mirror interferometer system showing light incident upon the mirror and substrate simultaneously. The rotation stage sets the period by changing the orientation of the mirror and substrate with respect to the incident light. (Adapted from [56].) 98

Figure 3-5 The two beam interference lithography system used in the Nanostructures Laboratory (adapted from [56].).....100

Figure 3-6 Examples of grid exposures using the Lloyd's mirror for different exposure times for a laser power of 42mW. Grids are exposed in PFI 88 positive resist on silicon for (a)

2 min (b) 2min 24sec (c) 2 min 48 sec (d) 3 min 12 sec per side (the total exposure time is double). The period is approximately 750 nm for every case..... 101

Figure 3-7 Examples of grid exposures in negative resist using the Lloyd's mirror for different exposure times for a laser power of 42mW. Grids are exposed in OKHA PS4 negative resist on silicon for (a) 1 min (b) 1 min 20 sec (c) 1 min 40 sec (d) 2 min per side (the total exposure time is double). The period is approximately 750 nm for every case. 102

Figure 3-8 An example of a layered structure used for an interference lithography step. Trilayer resist stack consisting of resist, SiO₂, and ARC is shown. The hard mask layer is used to facilitate pattern transfer to substrate. 104

Figure 3-9 Scanning electron micrograph illustrating the trilayer resist stack and hard mask layer after interference lithography exposure and development..... 104

Figure 3-10 Reflectivity profile for layered medium consisting of 200nm OKHA PS4 negative resist, 20nm SiO₂, XHRI-16 ARC, 250nm SiO₂, Si substrate..... 105

Figure 3-11 (a) SEM image of trilayer resist stack after exposure with interference lithography. (b) SEM image of trilayer resist stack with 20 nm SiO₂ layer etched. Etch parameters: CF₄(10mT, 300V, 160W, 1:20). 107

Figure 3-12 SEM images showing (a) etching of the ARC and hard mask layers and (b) magnified image of one of the etched holes. Etch parameters: He/O₂(2:1sccm, 10mT, 250V, 135W, 3:27), CF₄(10mT, 100V, 285W, 1:10)..... 107

Figure 3-13 SEM images showing ~300 nm etching into silicon with a 20 nm SiO₂ hard mask layer. Etch parameters: Cl₂(20sccm, 10mT, 90W, 600V, 2:00 minutes) 108

Figure 3-14 SEM images showing cross-section of trilayer resist stack (a) before RIE and (b) after RIE. Etch parameters: CHF₃(10mT, 100V, 230-245W, 0:56 min), He/O₂(2:1sccm, 10mT, 250V, 105W, 7:20 min), CHF₃(10mT, 100V, 215W, 7:19 min)..... 109

Figure 3-15 SEM images showing sub-micron etching into silicon with Cl₂ reactive ion etching. Etch parameters: Cl₂(10mT, 420V, 50W, 20:00) 110

Figure 3-16 SEM images showing etch results in silicon with two Cl₂ reactive ion etching steps and a HSQ hard mask. Etch parameters: Cl₂(10mT, 60W, 450V 10min), Cl₂(10mT, 60W, 450V 10min)..... 111

Figure 3-17 SEM images showing etch results in silicon with two Cl₂ reactive ion etching steps and an HSQ hard mask. Etch parameters: Cl₂(10mT, 50W, 450V 3min), Cl₂(10mT, 50W, 450V 17min)..... 112

Figure 3-18 SEM images showing HSQ layer after ashing to remove the ARC layer. Notice the discoloration of the silicon substrate underneath the HSQ areas..... 112

Figure 3-19 (a) Illustration of spectral separation in a conventional prism. (b) Illustration of super-dispersion in a superprism (c) Illustration of Angular magnification in a superprism. (adapted from [58]) 114

Figure 3-20 (a) Illustration of a dispersion surface showing an example of a k -vector and the group velocity. (b) Illustration showing how the dispersion surface radius changes with the phase velocity or frequency. 118

Figure 3-21 Three-dimensional dispersion surface calculations for the even mode (TE-like; electric field mostly in the plane of the slab) of a 2D-periodic photonic crystal slab ($r=0.4a$, $t_{Si}=14a/15$). Efficient superprism behavior is enabled by the "flatness" of the dispersion surfaces over large parameter regimes in k -space. Simulations performed by Dr. M. Soljacic. 119

Figure 3-22 Schematic illustrating the mechanism for superprism angular magnification using the dispersion surfaces of silicon and the photonic crystal. (a) The light path through the full superprism structure. (b) Coupling into the photonic crystal from silicon. (c) Coupling out of the photonic crystal into silicon. Note that the dash-dotted lines in (b) and (c) represent lines of constant tangential k [68]. 120

Figure 3-23 Schematic illustrating a superprism structure for use in free space applications. 121

Figure 3-24 Finite-difference time-domain simulation of a simplified 2D model of the structure simulated in Figure 3-21. All cases (a) through (c) are calculated with a normalized frequency of $fa/c = 0.17$, with the electric field in the plane. Propagation of light from silicon ($\epsilon=12$), through the photonic crystal, into air ($\epsilon=1$) is shown. All angles are measured with respect to the normal direction [68]. 122

Figure 3-25 Schematic of superprism device layout (not to scale). The device is a three layered structure with the superprism input and output facets defined by etched facets. 124

Figure 3-26 Superprism fabrication overview for both the GaAs and silicon-based device structures..... 126

Figure 3-27 Mask designs used for patterning superprism device shape. (a) Mask #1 is used to pattern the device shape with alignment marks. (b) Mask #2 is used to protect the open square area where the photonic crystal is patterned during an interference lithography step. 127

Figure 3-28 SEM micrographs showing resist profiles after photolithography and development (without ashing) under three different conditions: (a) No vacuum contact with mask, 20 sec exposure, 4.5 mW/cm². (b) Vacuum contact with mask, 20 sec exposure, 4.5 mW/cm². (c) Vacuum contact with mask, 15 sec exposure, 4.5 mW/cm². 128

Figure 3-29 Schematic illustrating a sample with patterned superprism shape. An alignment grid with a period of 6 μ m, and a line width of 3 μ m, aids in orienting the interference lithography exposure. 129

Figure 3-30 Schematic illustrating technique for orienting the sample in preparation for interference lithography exposures. (a) Unoriented sample. (b) Oriented sample. Proper orientation is achieved when the sample is rotated such that the diffracted beams are projected to the same height from the surface of the table. 130

Figure 3-31 Schematic illustrating the sequence of interference lithography exposures with proper orientation of the sample. After exposure #1, the sample is rotated by 90° for the second exposure.	130
Figure 3-32 Schematic illustrating the cross-section of the structure used to create a thick buried oxide with a plot of the designed aluminum content as a function of structure thickness.....	133
Figure 3-33 Scanning electron micrographs at different locations from the sample edge showing lateral oxidation of AIAs layers with subsequent vertical oxidation of the AlGaAs layers. (Schematic of the structure is shown in Figure 3-32.)	134
Figure 3-34 Auger electron spectroscopy profile verifying complete oxidation of the layered structure. The presence of each element is detected through the peaks in detected intensity at the characteristic Auger electron energies.....	135
Figure 3-35 (a) Differential interference contrast (DIC) image of partially oxidized 500µm mesa. (b) SEM image showing complete oxidation of the layered structure 31µm from the mesa edge. (c) SEM image at a location 122µm from the mesa edge showing the edge of the AIAs oxidation front. (R935, 450°C, 1hr, 10/29/02)	136
Figure 3-36 (a) DIC image of partially oxidized 500µm mesa. (b) SEM image showing complete oxidation of AIAs but unoxidized AlGaAs 128µm from the mesa edge. (c) SEM image at a location 143µm from the mesa edge showing the edge of the AIAs oxidation front. (R935, 460°C, 1hr, 10/30/02)	137
Figure 3-37 (a) DIC image of partially oxidized 500µm mesa. (b) SEM image at the mesa edge showing complete oxidation of AIAs and AlGaAs layers but also partial oxidation of GaAs. (c) SEM image at a location 90µm from the mesa edge showing the edge of the AIAs oxidation front. (R935, 475°C, 1hr, 10/29/02)	138
Figure 3-38 (a) DIC image of the corner of a partially-oxidized 5mm square mesa. (b) SEM image at 40 µm from mesa edge showing complete oxidation of AIAs and AlGaAs layers. A 250 nm HSQ cap layer protects the 450nm GaAs layer but lateral oxidation of GaAs is apparent. (c) SEM image at a location 355µm from the mesa edge showing the edge of the AIAs oxidation front. (R935, 12 hr, 460°C, 4/7/2003).....	139
Figure 3-39 Images of a fabricated superprism structure. (a) Digital photograph showing the full sample. (b) Differential interference contrast image showing the magnified corner area of the photonic crystal. (c) SEM micrograph showing cross-sectional image of a Si monitor sample.	141
Figure 3-40 Microscope image of lensed fiber proposed for creating a wide stripe excitation as the input to the superprism. Image courtesy of Marcus Dahlem.....	143
Figure 3-41 (a) and (b) SEM images showing cross-section of a die-sawed SOI sample. (c) DIC image showing top view of die-saw cut with 40 µm blade and die-saw speed=0. Resist is protecting the top silicon layer in this top-view image.....	144
Figure 3-42 DIC images showing top-view of die-sawed SOI sample with a silicon slab defined by reactive ion etched facets.....	145

Figure 3-43 Three-dimensional dispersion surface calculation for normalized frequencies showing how two k -vectors in air couple into the photonic crystal. The photonic crystal structure is shown at the right. The flatness of the dispersion surfaces allows two k -vectors of different orientation to propagate with the same group velocity, v_g within the photonic crystal. Simulation by Dr. Marin Soljacic.....150

Figure 3-44 Time-domain simulations showing the shift from divergent behavior to super-collimation behavior in a photonic crystal for a shift in frequency. Simulation by Dr. Marin Soljacic.151

Figure 3-45 Super-collimator device design showing top-view and cross-section.152

Figure 3-46 Images of fabricated super-collimator device. Center: SEM image showing large area photonic crystal. Inset left: Digital photograph of the 1 cm x 1cm device. Inset right: SEM image showing detailed cross-section of air holes in silicon on SiO₂. 154

Figure 3-47 Schematic illustrating the three different testing configurations used for studying super-collimation in the photonic crystal slab.156

Figure 3-48 Infrared camera images showing the wavelength dependence of super-collimation at the top surface of the photonic crystal. Measurements by M. Dahlem and P. Rakich.....156

Figure 3-49 (a) Dispersion surfaces for the fabricated photonic crystal. Super-collimation is possible for a normalized frequency of $\omega=0.23$. (b) A detailed view of the of the dispersion surfaces for $\omega=0.22, 0.23, \text{ and } 0.24$. The plot is rotated 45° so that k_x is the k -vector along the propagation direction and k_y is the transverse k -vector. Simulation by M. Ibanescu.157

Figure 3-50 Demonstration of the spatial dependence of super-collimation. The operating wavelength is 1510nm. (a) Infrared camera image of light propagation from the input to the output facets of a 3mm sample. (b)-(d) Near-field scanning optical microscope (NSOM) images taken at four different locations along the length of the 3mm sample. No significant beam divergence is measured. Measurements by M. Dahlem and P. Rakich.158

Figure 3-51 Demonstration of super-collimation as measured at the output facet of a 5mm device with a fiber probe. The inset is a plot of the average x intensity at each y position of the 2D intensity plot with a Gaussian fit of the data. Measurements by M. Dahlem and P. Rakich.159

Figure 3-52 Infrared camera image of input coupling at an 20° angle with respect to the normal to the PC/air interface. The operating wavelength is 1500 nm. The collimated beam still propagates normal to the PC/air interface. Original image by M. Dahlem. .160

Chapter 1

Introduction

1.1 What is a Photonic Crystal?

A photonic crystal is any structure composed of a periodic variation in the index of refraction such that the period is on the order of the wavelength of light. This periodicity can be created in one dimension as alternating layers of material, in two dimensions as holes or rods suspended in a material, or in three dimensions with individual “atoms” of material [Figure 1-1]. The behavior of light as it travels through any such periodic structure is often considered to be analogous to the behavior of electrons as they traverse the periodic lattice of a semiconductor. The periodicity can create allowed and disallowed energy states—energy states for which light in a photonic crystal, or electrons in a semiconductor, can and can not exist. These “band gaps” in allowed energy are what make photonic crystals unique structures for manipulating light. Homogeneous materials can not manipulate light in such novel ways—bending light 90 degrees, reflecting broad spectra with low loss, or dispersing multiple wavelengths in exceptionally divergent directions. In other words, creating a photonic crystal by creating a spatial variation in the index of refraction, allows numerous possibilities for shaping, controlling, and engineering the behavior of light.

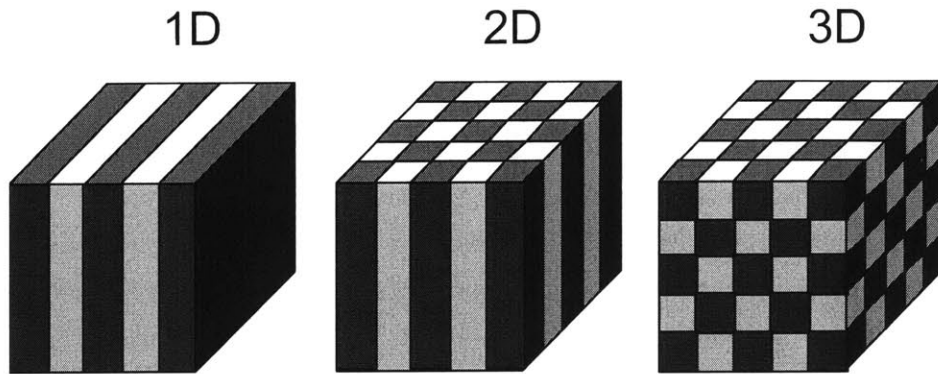


Figure 1-1 From left to right, examples of one, two, and three dimensional photonic crystals. The color differences represent materials with differing index of refraction (adapted from [1]).

The research presented in this thesis focuses on the creation of three different photonic crystal devices. The first device is a saturable Bragg reflector (SBR) which uses a 1D photonic crystal to reflect a very broad spectrum of light for ultra-short pulse generation in a laser system. The second device is a superprism which uses a 2D photonic crystal to steer a beam of light and disperse a spectrum of light over wide angles. The third device is a super-collimator which uses a 2D photonic crystal to guide light without the boundaries of a waveguide. Though all three devices are used for different applications, each device uses a periodic arrangement of high index contrast materials to engineer and control the properties of light in new and innovative ways.

1.2 References

1. Joannopoulos, J., R. Meade, and J. Winn, *Photonic Crystals: Molding the Flow of Light*. 1995: Princeton University Press.

Chapter 2

Saturable Bragg Reflectors for Ultra-Short Pulse Generation

2.1 Motivations

2.1.1 Creating ultra-short pulses

An "ultra-short pulse" is an extremely short burst of light intensity that can be produced by a laser system. "Ultra-short" refers to the duration of this burst which is on the order of femtoseconds, or 10^{-15} seconds. Such a time scale is only a few optical cycles in duration. For example, one optical cycle of 510 nm green light is 1.7 fs in duration. Light travels 3 millimeters in 10,000 fs. One clock cycle of a 2 GHz Intel Pentium IV chip is 500,000 fs.

Short pulses of light generated from a laser can be used for a number of applications. In "optical coherence tomography" short pulses are used to increase resolution for cross-sectional imaging of biological tissue [1]. With an ultra-short pulse, resolution on the order of 10's-of- μm can be achieved. In addition, because low average powers are achieved, *in-vivo* imaging is possible. Femtosecond laser surgery is another medical application enabled by ultra-short pulse lasers. Short pulses allow for higher levels of surgical precision in three dimensions when cutting tissue. Not only is accuracy more precise in the planar dimension, but depth control is also possible due to the fact that tissue removal is accomplished at the

focus of the laser beam. Outside of the focal spot, the intensity of the short pulses is too low for tissue removal. By controlling the depth of the focal point of the laser beam, the depth of tissue interaction is controlled while reducing harm to surrounding tissue [2]. Another application of ultra-short pulse lasers is in the realm of quantum physics involving experiments in "extreme non-linear optics." Because the ultra-short optical pulse creates extremely short bursts of high electromagnetic field, researchers in this field of non-linear optics study the effects of high intensity short pulses on atomic transitions. For example, an ultra-short pulse can ionize an atom via electron tunneling rather than through conventional ionization processes where the ionization energy liberates an electron from the nucleus. Ionization through electron tunneling offers an alternative method for producing x-ray radiation [3, 4]. Ultra-short pulses can also be used in frequency metrology applications such as for the optical atomic clock [5]. If one thinks of a clock as a pendulum that oscillates according to the length of one second, along with a gear that counts the number of oscillations, in the atomic clock, the natural oscillation of electronic transitions in the atom is the "pendulum" and the ultra-short pulse is the "gear." The faster the oscillation, the higher the resolution of the gear. In the conventional cesium atomic clock, cesium's natural resonance of 9.192×10^9 Hz is counted by a microwave signal resulting in an error of 1 second in 30 million years. With the optical atomic clock, a mercury atom with a resonance of 1.064×10^{15} Hz, is counted by the light of an ultra-short pulse laser achieving an error of 1 second in 4 billion years. Applications of the optical atomic clock include higher precision global positioning systems and time-keeping standards [6, 7].

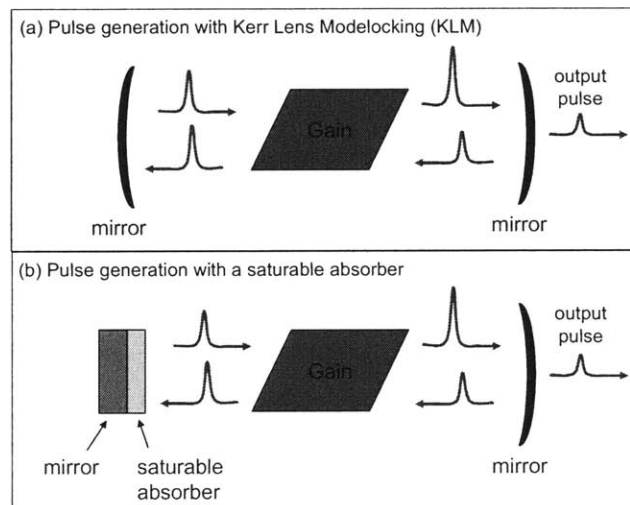


Figure 2-1 (a) A simplified schematic of the laser system using Kerr Lens Modelocking. (b) A simplified schematic of a pulsed laser system where a saturable absorber is used.

Pulses are not automatically produced from a laser system. A laser can emit short pulses if all the longitudinal modes generated by the cavity are locked in phase or "modelocked." Without any mechanism for modelocking the laser, a stream of random phases are emitted and the laser is in "continuous wave" (CW) operation.

Modelocking the laser can be achieved using a variety of methods which may be active or passive in nature. To date, the generation of ultra-short pulses has been dominated by Kerr-lens modelocked (KLM) lasers. Using this passive modelocking method, the laser cavity can be illustrated as shown in Figure 2-1(a). Two opposing mirrors and the gain medium, which is a laser crystal for the solid state lasers referred to in this work, form the laser cavity. The gain medium not only provides amplification through stimulated emission, but also shapes pulses through nonlinear effects. Pulses are produced using the combination of spatial self focusing in the laser crystal due to the nonlinear "Kerr effect," and a spatial aperture which only selects focused pulses. Since the strongest self focusing occurs for highly intense pulses, the aperture will block lower intensity pulses which are not tightly focused. For more details about the mechanism and implementation of KLM in laser systems, please refer to the review paper by Cundiff and Ye [8].

Though Kerr-lens modelocking is the prevailing method for pulse generation, there are a number of challenges to implementing KLM in practice. Because this modelocking scheme requires a pulse of sufficient intensity to initiate the self-focusing process, KLM is not easily self-starting from continuous wave operation. Additionally, the optical components which form the cavity must be physically aligned with high accuracy to maintain KLM [9]. In order to provide a pulse of high enough intensity to initiate self-focusing, noise is introduced into the laser system by physically knocking on one of the mirrors or wiggling its position. However, if alignment of the optical components is important, knocking one of the end mirrors certainly is not desirable. At the same time, because the system is very sensitive to alignment, environmental fluctuations can interfere with pulse generation, switching the system into CW operation without an automatic mechanism for recovery. Another "knock on the mirror" may be required to reinitiate pulsing.

2.1.2 Using a saturable absorber mirror for modelocking

If the mirror on one end of the laser cavity is replaced by the combination of a saturable absorber and a mirror as shown in Figure 2-1(b), a number of the challenges of using Kerr-lens modelocking are addressed. Rather than relying on the laser crystal alone to transition

from CW operation to pulse operation, a saturable absorber is used for its more robust pulse shaping functionality. The distinct advantage of modelocking with a saturable absorber is that the modelocking process can be self-started, meaning that pulses can be initiated from CW operation automatically without external intervention. Self-starting also allows the absorber to stabilize the system from environmental perturbations. In addition, because of the lack of spatial dependence, the saturable absorber is not as sensitive to the alignment parameters in the cavity [9].

As shown in Figure 2-1(b), a saturable absorber and mirror can be used as one end of the laser cavity to initiate modelocking. The mirror is necessary for confining the light within the laser cavity and the absorber is necessary for shaping the pulses. A saturable absorber initiates modelocking by introducing an intensity-dependent loss into the laser cavity. This loss is introduced in such a way that low intensities are completely absorbed while high intensities are only partially absorbed and reflect back into the laser cavity via the attached mirror. The saturable absorber is a semiconductor material that absorbs photons according to its energy bandgap. For illustration, Figure 2-2 presents three different scenarios in which light passes through a semiconductor absorber. Figure 2-2(a) shows the case in which a low intensity pulse passes through the absorber. While passing through the absorber, a low intensity pulse will be fully absorbed as electrons are excited from the valence to the conduction band. Full absorption of the pulse occurs for the case in which the intensity of the pulse is not sufficient enough to excite all available electrons in the valence band to the conduction band. As a result, a low intensity pulse dies out after passing through the absorber. However, for higher intensity pulses, as shown in Figure 2-2(b), the intensity of the pulse is high enough to fully deplete the valence band of electrons so that "saturation" of the absorber occurs. As a result, the remaining pulse energy which was not absorbed is transmitted through the absorber. In a laser system, pulse generation can be initiated from the noise spikes that often exist during continuous wave (CW) operation, as illustrated in Figure 2-2(c). This scenario is considered as a superposition of the cases illustrated in (a) and (b), the absorber will absorb any low intensity spikes but allows high intensity spikes to pass through. Pulses can then form from these high intensity peaks. As a result, the absorber allows pulses to be "self-started" from the initial noise in the laser system. With a mirror attached to the absorber, the pulse will reflect off of the mirror, pass through the absorber again, and then re-enter the laser cavity.

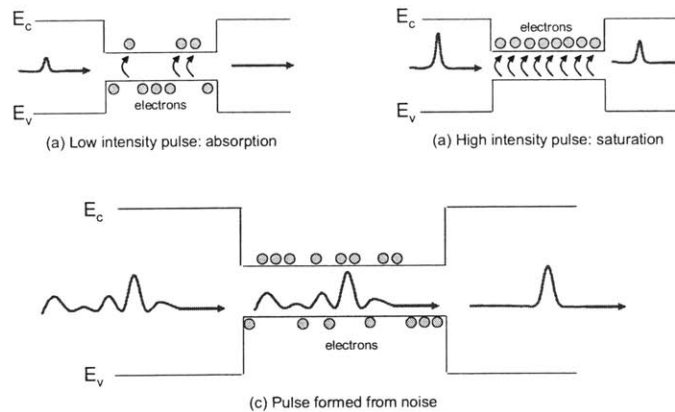


Figure 2-2 Schematic illustrating how pulses can self-start in a laser system from initial noise.

In order for this saturable absorber and mirror to function effectively to initiate modelocking, it must be capable of handling the wide bandwidth associated with ultra-short pulses--the shorter the pulse, the wider the necessary bandwidth. For example, as illustrated in Figure 2-3, the Fourier transform of a 10 femtosecond Gaussian pulse, is a 40 THz Gaussian spectrum in the frequency domain which translates into about 200 nm of wavelength bandwidth at a center frequency of 1230 nm. Therefore in order to create 10 fs pulses from a laser system, modes over a 200 nm wavelength range need to be phase-locked. Creating these pulses from a laser system would require that each component in the laser system is capable of handling this bandwidth—*i.e.* all mirrors sufficiently reflect, and all wave guiding and optical elements sufficiently transmit over this wavelength range. The shortest pulses that can be generated by a laser system are determined by the component with the smallest bandwidth.

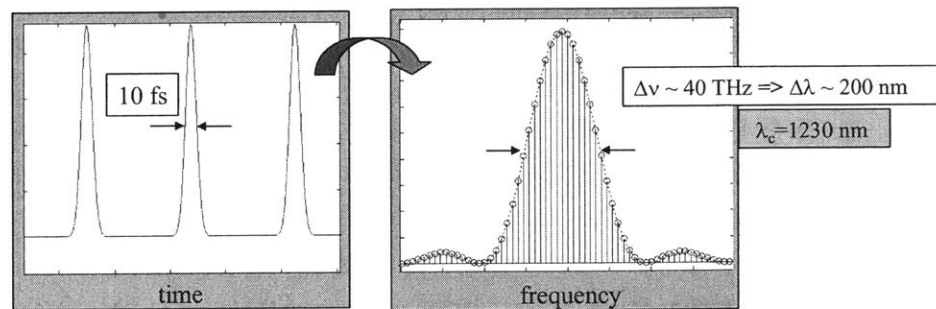


Figure 2-3 An illustration showing how a 10 femtosecond pulse is formed from a frequency bandwidth of about 40THz. For a center frequency of 1230 nm, this pulse width also implies a wavelength bandwidth of about 200 nm.

A number of requirements therefore exist when trying to create a saturable absorber mirror for an ultra-short pulse laser system. These requirements are illustrated in Figure 2-4.

1. The mirror must be capable of reflecting the full bandwidth of the ultra-short pulse as discussed above.
2. The mirror should be low loss so that lasing is not affected. Since lasing occurs when the gain of the laser cavity is equal to the round trip loss, too much loss may make it difficult for that condition to be met, especially since the absorber is already contributing an element of loss into the system.
3. The absorber must be a semiconductor layer that can saturate according to the density of electronic states with the absorption properties tailored to the laser's wavelength.
4. The absorber must have a large area in order to avoid the effects of two-photon absorption (TPA) which can degrade pulse generation (to be discussed in a later section).
5. The absorber must be integrated with mirror.
6. An absorber integrated with a mirror requires a robust interface between the two elements. Weakness of this interface can contribute unnecessary losses into the system which can prevent the system from lasing.
7. The complete structure must be durable enough to withstand the incident intensity of the laser while sinking any heat that may be generated during operation.

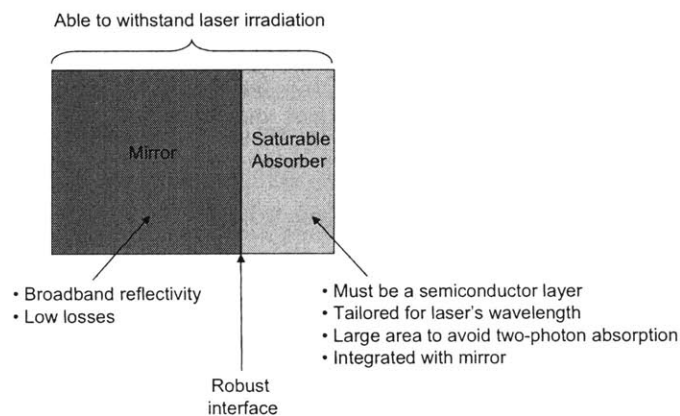


Figure 2-4 Schematic outlining the challenges of creating a saturable absorber mirror for ultra-short pulse lasers.

2.1.3 Absorber design overview

When choosing an appropriate absorber for the laser system, III-V semiconductors offer a convenient solution. A "III-V semiconductor" is a semiconductor composed of combinations of group III elements and group V elements from the periodic table. Through various combinations of group III and group V elements, a whole range of semiconductor materials with varying properties becomes available. Examples include binary III-V's composed of two elements such as GaAs, InP, or AlAs, ternary III-V's composed of three different elements (usually two group III and one group V) such as InGaP or AlGaAs, or even quaternaries with four elements such as InGaAlP. The properties of each material vary with composition and can be tailored for the characteristics desired.

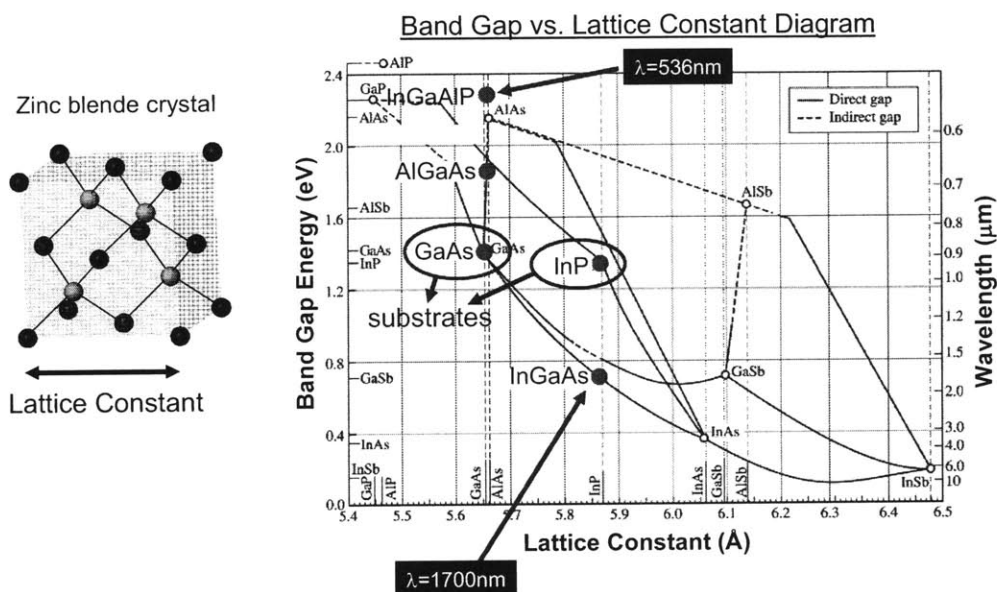


Figure 2-5 The band gap versus lattice constant diagram for the major III-V alloys. A diagram of the crystal structure is also shown.

The absorption wavelength is one of the most important characteristics of a saturable absorber. The band gap versus lattice constant diagram presented in Figure 2-5 is a tool for choosing the appropriate material. This diagram relates the band gap and absorption/emission wavelength to the lattice constant for the major III-V alloys. So for example, depending on its composition, InGaAs can have an emission wavelength of 1700 nm and is a useful material for telecommunication lasers. An alloy of InGaAlP has an emission wavelength of 536 nm and can emit red light. The band gap of the saturable absorber is chosen with respect to the gain spectrum of the laser system. The absorber material composition can be chosen such that the absorber's band gap is at the wavelength

of maximum gain, or it could also be chosen such that the entire gain spectrum has a higher energy than the band gap of the absorber. In general, for the absorbers discussed in this work, the absorber was chosen such that the absorber absorbs a significant part, but not all, of the laser's wavelength spectrum.

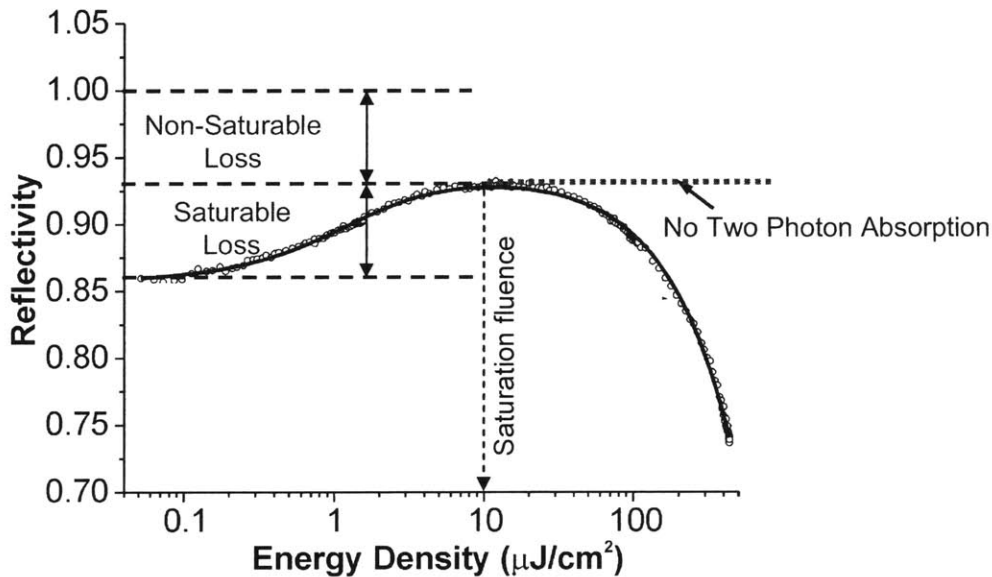


Figure 2-6 Saturation fluence measurements illustrating the saturable and nonsaturable losses, as well as two photon absorption in a structure with an absorbing InGaAs quantum well and InP cladding layers. The absorber was grown on a 22 pair GaAs/AlAs mirror stack [10].

Absorber losses are also key parameters when choosing an absorber material. There are generally two types of losses that the absorber can produce: 1) a saturable loss and 2) non-saturable loss. The saturable loss of the absorber is the loss introduced by the absorbing action of the absorber. It is this loss mechanism that initiates modelocking in the laser system as discussed previously. Figure 2-6 illustrates how the saturable loss relates the reflectivity of a saturable absorber mirror to the incident energy density. For low energy densities, the absorber has the capacity to absorb a large amount of incident light since the absorber is not saturated—*i.e.* the electronic energy states in the valence band are not fully depleted. Thus for low energy densities, the reflectivity from the saturable absorber mirror is low. As the energy density increases, the absorber begins to saturate as the valence band energy states are depleted. As a result, with a lower proportion of absorbed photons, the total reflectivity of the saturable absorber mirror increases. The energy density at which full saturation occurs is known as the “saturation fluence.” The saturable loss of the absorber equals the difference between the unsaturated and fully saturated reflectivities.

The saturation loss is also referred to as the "modulation depth" of the absorber. On the other hand, the non-saturable loss is independent of laser power and absorber action and is measured when the absorber is fully saturated.

The saturable losses, or modulation depth, of the absorber can be tailored to the desired characteristics of the laser system. Fiber lasers often require absorbers with a larger modulation depth (3%-20%) than solid state lasers (0.3%-2%) for self-starting modelocking [11]. The saturable losses are determined by the thickness of the absorbing layer and the non-saturable losses are determined by the quality of the absorber material. The saturation fluence can be influenced by the placement of the absorber with respect to the standing wave of the electric field that forms in the laser cavity. If the absorber is placed at a peak in the standing wave pattern, the saturation fluence can be minimized.

One consideration when choosing the absorber material is its lattice matching to commonly available substrate materials such as GaAs or InP. Though all of the arsenic and phosphorous III-V alloys have the zinc blende crystal structure, which is shown in Figure 2-5, the lattice constant varies. If the lattice constant of an epilayer differs from the lattice constant of the substrate, strain can be introduced into the structure. In certain situations, the characteristics of a laser system will imply that the appropriate absorber material can not be lattice-matched to a common substrate material and therefore must be strained. This strain can introduce defects into the material which can contribute to higher non-saturable losses. However, sometimes this strain may be desired because strain can influence recovery times of the absorber. With higher defect densities, an absorber which has been saturated can recover quickly because of the larger number of mid-gap energy states which increase recombination rates. At the same time, strain may also contribute to mechanical instability within the structure--an undesirable effect. Faster recovery times can also be achieved through defects introduced by low temperature growth or by ion bombardment after growth. However, in general, there is a trade-off between fast recovery times and non-saturable losses.

2.1.4 The challenge of broadband mirrors

Broadband mirrors can be created in a number of different ways. Metals, such as gold and silver, inherently have a high reflectivity over a broad wavelength range. If metal mirrors are used with saturable absorbers for modelocking, the metal mirror must be in contact with the epitaxially-grown saturable absorber. Fluck, *et al.* integrated a AlGaAs/GaAs/AlAs

absorber structure with a broadband silver mirror [9]. The device was fabricated using a number of postgrowth processing steps including metallization, bonding to a Si wafer with epoxy, selective wet etching, and lapping of the GaAs substrate. One of the disadvantages of the device was the introduction of losses of approximately 2% due to the absorption of silver. The processing steps and anti-reflection coating introduced further losses. Zhang, *et al.* showed that they could decrease the total losses of a gold mirror based semiconductor saturable absorber by inserting high index contrast $\text{SiO}_2/\text{TiO}_2$ layers between the gold and the semiconductor absorber layers [12, 13]. Though this structure demonstrated an improvement in terms of loss, the structure's fabrication still required significant postgrowth processing steps.

Another option for the creation of broadband mirrors is the use of Bragg stack mirrors. Bragg stack mirrors are 1D photonic crystals which are composed of alternating layers with high and low indices of refraction as shown in Figure 2-7. The Bragg stack's mirror reflectivity bandwidth corresponds to the photonic band gap of the 1D photonic crystal. As the index contrast between the layers increases, the photonic band gap widens, hence the high reflectivity bandwidth of the mirror increases.

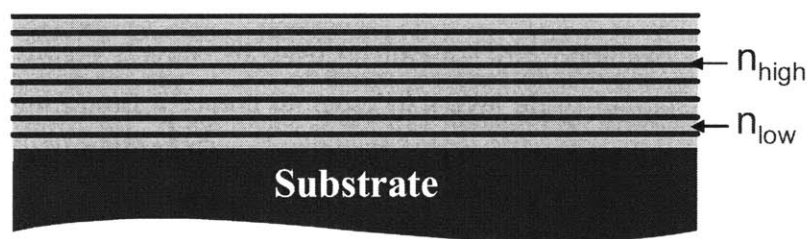


Figure 2-7 Schematic of a Bragg mirror showing alternating layers of high and low refractive index (n).

Designing a Bragg mirror suitable for use in an ultra-fast laser requires choosing the appropriate materials for the high and low index layers such that the requirements of broadband, low loss, and a robust interface with a saturable absorber are all satisfied. Two types of material combination can be considered for Bragg mirrors:

1. All-semiconductor Bragg mirrors
2. Semiconductor/oxide Bragg mirrors

As implied by the name, an all-semiconductor Bragg mirror would be designed such that both the high and low index materials are semiconductor layers. An example would be a

GaAs/AlAs mirror. Because semiconductor materials do not absorb light for photon energies below the band gap, mirrors with low loss can be designed. An additional advantage of using these materials for a Bragg mirror is that through epitaxial growth, semiconductor absorbers can be monolithically-integrated with semiconductor mirrors. Indeed GaAs/AlAs mirrors ($n \sim 3.4/2.9$) [14, 15] and AlGaAs/AlAs mirrors [16-18] have been used with semiconductor absorbers for modelocking a number of different laser systems. However, the low index contrast (maximum $\Delta n \sim 0.5$) results in a narrow-bandwidth mirror which limits the pulse widths that are generated.

By incorporating oxide layers into the mirror stack, creating semiconductor/oxide Bragg mirrors, higher index contrasts can be achieved. For example, a mirror composed of Si/SiO₂ layers ($\Delta n \sim 2.1$) would result in a much broader high reflectivity bandwidth than in the all-semiconductor case. Other dielectric combinations such as SiO₂/TiO₂ ($\Delta n \sim 1.1$), or SiO₂/Ta₂O₅ ($\Delta n \sim 0.7$) would also enable broader bandwidths than those achieved in the all-semiconductor case [19]. However, the disadvantage of using these material combinations is that monolithic integration with III-V semiconductor absorber layers is challenging or post-processing steps would be necessary.

As an alternative, a wet oxidation process can be used to convert epitaxially-grown AlAs layers into low-index aluminum oxide layers in order to create a Bragg mirror with a high index contrast between the layers. Using this technique, a GaAs/AlAs ($n \sim 3.4/2.9$) layered structure can be converted into a broadband GaAs/Al_xO_y ($n \sim 3.4/1.6$) Bragg mirror. The advantages of this approach are threefold: 1) monolithic integration with semiconductor absorbers is possible, and the resulting mirror is 2) low loss and 3) broadband.

When a semiconductor absorber is integrated with a Bragg mirror, the device is called a "saturable Bragg reflector" (SBR). Figure 2-8 illustrates the difference in the measured reflectivity profiles associated with the Bragg mirrors of two different SBR structures centered at a wavelength of 1550 nm: a 22 pair GaAs/AlAs mirror, and a 7 pair GaAs/Al_xO_y mirror. Each structure also has an absorber consisting of a single or multiple InGaAs quantum wells integrated with the Bragg mirror. All of the mirror layers have a thickness of $\lambda/(4n)$, where n is the index of refraction for each layer. As illustrated in the figure, the high index contrast GaAs/Al_xO_y SBR clearly has a much wider bandwidth than the lower index contrast, all-semiconductor GaAs/AlAs SBR.

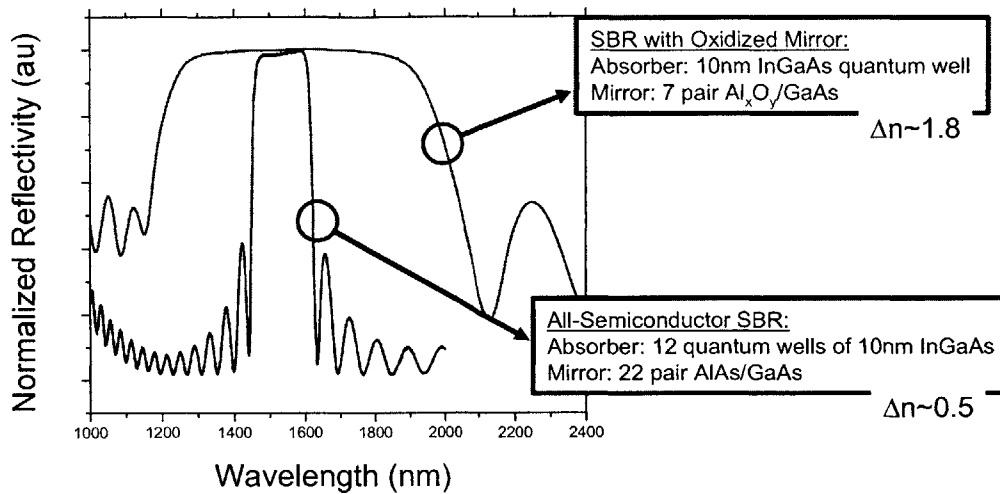


Figure 2-8 Reflectivity measurements contrasting the high reflectivity bandwidth of an all-semiconductor SBR (blue) with an SBR with oxidized mirror layers (red).

2.1.5 Large scale oxidation for large area SBRs

Though the advantage of designing a SBR structure with low index oxide layers for broadband reflectivity is clear, fabricating the structure to meet all of the necessary requirements is a challenge. One of the important challenges is in creating oxide layers with a large enough area to avoid the effects of two-photon absorption.

Two photon absorption (TPA) occurs in the saturable absorber when the laser's incident energy density becomes so high that two photons are absorbed for every electron excited. When TPA occurs within an absorber, high intensity pulses no longer pass through the absorber but are absorbed. An illustration of TPA can be observed by again referring to Figure 2-6 which presents a measurement of the reflectivity from an SBR versus energy density. At high energy densities, the absorber conduction band becomes saturated with electrons so that further increases in energy density begin to result in the absorption of two photons per electron transition. The result is a decrease in the reflectivity of the SBR as shown for energy densities beyond $10 \mu\text{J}/\text{cm}^2$. If TPA occurs in a laser system, the pulse width can be limited and may result in pulse breakup with pulses not necessarily spaced at equal intervals [10, 20].

To decrease the effect of TPA, the absorber should be used at lower energy densities. Without changing the total laser power, a decrease in energy density can be implemented by increasing the spot size incident on the absorber. A larger spot size requires a larger

area absorber. A large area absorber also needs to be integrated with a large area Bragg mirror. If this Bragg mirror is to be created with Al_xO_y , a large scale oxidation process is required to convert AIAs to Al_xO_y .

The wet oxidation of AIAs and AlGaAs layers of varying aluminum content, has already been used in a wide range of applications requiring aluminum oxide. However, for this wide range of applications, the length scale of the oxidation process has been limited to 10's of microns. Oxidized Al-containing materials have been used as the index-guiding layer in edge-emitting lasers [21], as current confinement layers in vertical cavity surface emitting lasers [22-25], as low-dielectric-constant layers in distributed Bragg mirror stacks [20, 26-28], and as low index of refraction materials suitable for optical confinement when integrated with high index materials [29, 30]. Electronic use of oxidized Al-containing material was investigated as a gate dielectric for GaAs-based transistor [31-33] structures similar to the well-studied Si/SiO₂ counterpart. Furthermore, the high degree of etch selectivity, which is created by combining the oxide with III-V materials, presents other opportunities to use the oxide as a sacrificial layer in micro-electro-mechanical structures (MEMS) and nano-electro-mechanical structures (NEMS) [34, 35]. Recently, the use of the low index, oxidized Al-containing material has been employed in photonic band gap crystal structures that require high dielectric contrast in their design [26, 36]. A wet oxidation process has also been investigated for the creation of high-dielectric-contrast distributed Bragg mirror stacks by a number of groups [26-28, 37].

An oxidized SBR structure with large area oxides was described by Ripin, *et al.* in which a GaAs/ Al_xO_y Bragg mirror created with a width of 300 μm [20]. This broadband SBR structure was then used to create 36 fs pulses from a Cr:YAG laser. However, Ripin, *et al.* claim that the 36 fs pulsewidth produced by their laser system seemed to be limited by the effects of two photon absorption. Ripin, *et al.* observed that in their laser system, a width greater than 300 μm is necessary.

As a result, in this thesis research, an approach is investigated for creating large scale aluminum oxide layers on the length scales of 100's of microns in order to avoid the effects of two-photon absorption.

2.2 Saturable Bragg Reflector Design Overview

The objective of this research is to design and fabricate broadband Saturable Bragg Reflectors (SBRs) which are used to self-start and modelock a number of laser systems including the Cr:Forsterite, Cr:YAG, Ti:Sapphire, and Er:Bi₂O₃ fiber lasers. Each SBR is uniquely designed for the center wavelength and loss tolerances of each laser. The goal has been to fabricate the SBR structure such that the SBR will not limit the pulse width emitted by the laser. A successfully designed and fabricated SBR must therefore satisfy the following criteria:

- The mirror's bandwidth sufficiently reflects the laser's gain bandwidth.
- The mirror loss is low.
- The absorber is monolithically-integrated with the mirror.
- The absorber's material composition and loss is appropriate for the laser system.
- The device has a large area to avoid the effects of two photon absorption.
- The device is stable, durable, and easily fabricated.

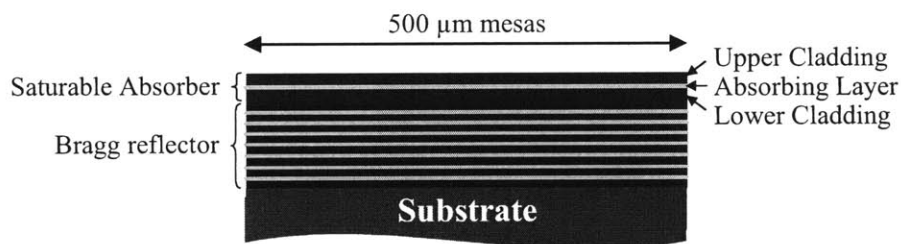


Figure 2-9 Schematic of a Saturable Bragg Reflector illustrating the cross-section of the layered structure.

Saturable Bragg reflectors are layered structures consisting of a saturable absorber monolithically-integrated with a Bragg mirror as shown in Figure 2-9. The saturable absorber is composed of an absorbing layer between two cladding layers, and the Bragg stack mirror consists of alternating high and low index of refraction layers. For the mirror of these SBRs, the high index material is either Al_{0.3}Ga_{0.7}As or In_{0.15}Ga_{0.15}Al_{0.35}P while the low index layer is Al_xO_y. The absorbing layer can be created using absorbing structures such as quantum dots, quantum wells, or thick semiconductor layers--the choice depends on the amount of loss and modulation depth that is desired for the laser system. The material

composition and thickness of this layer will determine the wavelength at which photon absorption will occur. $\text{In}_x\text{Ga}_{1-x}\text{As}$ absorbing layers of varying composition have been used in the SBRs described here. Increasing the indium content will shift photon absorption to longer wavelengths, while increasing the gallium content will shift the absorption to shorter wavelengths. As the indium content increases, the lattice mismatch between InGaAs and GaAs introduces strain into the layered structure. Because the SBR is an absorbing rather than an emitting device, higher misfit dislocation densities and higher non-radiative recombination rates due to lattice mismatch can be tolerated in the absorber, and are even desirable for faster recovery times. The material composition of the cladding layers which surround the absorber is designed to distribute strain throughout the absorber thus influencing SBR recovery times. For example, the strain of an $\text{In}_{0.53}\text{Ga}_{0.47}\text{As}$ absorber grown on GaAs can be distributed away from the absorber interface by using InP cladding layers. Using GaAs cladding layers instead concentrates strain at the absorber/lower cladding layer interface.

Most of the studied SBRs are circular mesas with a 500 μm diameter. However, SBRs of larger areas have also been explored. SBR layer thicknesses depend on the center wavelength (λ) of the laser system. In general, layers in the mirror stack are $\lambda/(4n)$ thick (n is the index of refraction within the respective material), while the total saturable absorber, which includes the absorber and two cladding layers, is $\lambda/(2n)$ thick. The absorber layer thickness is chosen based on the desired absorption. The placement of the absorber within the cladding layers is designed by considering the standing waves that develop in the SBR. Shifting the position of the absorber within the standing wave pattern not only affects the SBR's saturation fluence, but also alters the wavelength dependence of the saturable absorption. Thus, the absorber position determines the wavelength range over which the laser is SBR modelocked.

Additional coatings on the top surface of the SBR may enhance the SBR's performance by decreasing the saturation fluence. For example, an anti-reflective layer deposited on the top surface an SBR structure can improve coupling into the SBR while lowering the saturation fluence. Quarter-wave layers of Al_2O_3 and HfO_2 were used as an anti-reflective layer for a few SBR structures as discussed in [11]. Additional mirror layers (such $\text{SiO}_2/\text{TiO}_2$ layers) can be deposited onto the SBR to create a resonant structure. A resonant SBR structure can enhance the electric field within the absorber thereby decreasing the saturation fluence. However, resonant coatings were not incorporated into the SBRs discussed in this work.

2.3 SBR Fabrication Process Overview

As illustrated in Figure 2-10, the following steps are necessary for the successful fabrication of broadband SBRs:

1. Growth of the heterostructure using molecular beam epitaxy (MBE).
2. Patterning of the mesa structure using photolithography and wet etching to define the mesa structure.
3. Steam oxidation to convert the AlAs layers to low index Al_xO_y layers.

In "Step 1" of Figure 2-10, SBR layers are grown using gas source molecular beam epitaxy (MBE) on GaAs (100) substrates using a Riber 32P MBE system. The first layers grown on the substrate are the Bragg mirror layers which are grown as $\text{Al}_{0.3}\text{Ga}_{0.7}\text{As}/\text{AlAs}$ or $\text{In}_{0.15}\text{Ga}_{0.15}\text{Al}_{0.35}\text{P}/\text{AlAs}$ layers. The absorber and cladding layers are then grown on top of the mirror layers. The growth temperature of the GaAs and $\text{Al}_x\text{Ga}_{1-x}\text{As}$ layers was approximately 600°C. The growth rate of the $\text{Al}_{0.3}\text{Ga}_{0.7}\text{As}$ layers is dependent on the desired Al content. Since the MBE system contains only one Ga and Al cell, for the AlAs/ $\text{Al}_{0.3}\text{Ga}_{0.7}\text{As}$ dielectric stacks, the growth rates were 0.4 $\mu\text{m}/\text{hr}$ and 1.3 $\mu\text{m}/\text{hr}$ respectively. The growth temperature of the absorber and cladding layers was the subject of experimentation and will be discussed in Section 2.5.6.

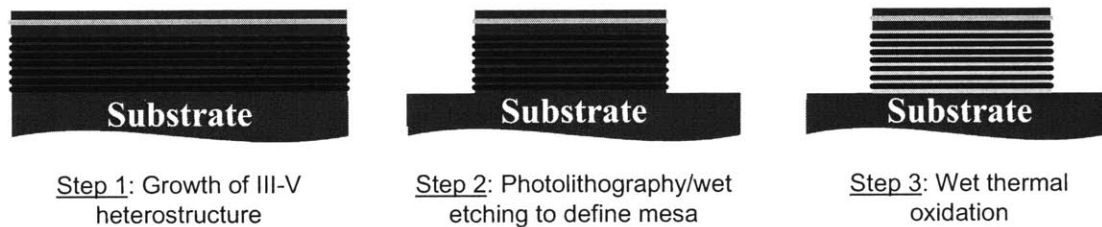


Figure 2-10 Overview of saturable Bragg reflector fabrication sequence showing major steps.

In "Step 2" of Figure 2-10, SBR mesas are defined using photolithography and wet etchants in order to expose the cross-section of the SBR structure for lateral oxidation in "Step 3." Before spinning the photoresist, samples were baked on a hotplate at 100°C in order to remove any residual water on the sample's surface to promote resist adhesion. Shipley 1813 photoresist was spun at 3 krpm for one minute yielding a resist thickness of about 1.6 μm . Samples were then baked in a 90°C furnace for 30 minutes. Mesas with 500 μm diameter were patterned in the resist using a quartz photomask and the Tamarak ultraviolet

lamp in MIT's Nanostructures Laboratory. Typical exposure times were about 15 seconds at an intensity of 4.5 mW/cm^2 . Samples were then developed using Shipley 352 developer for 1 min followed by a rinse with de-ionized water. Wet chemical etching was then used to etch the mesa pattern into the semiconductor heterostructure. A (1:8:40) $\text{H}_2\text{SO}_4:\text{H}_2\text{O}_2:\text{H}_2\text{O}$ etch is used for arsenic-based SBRs. With this etchant, GaAs/InGaAs/ $\text{Al}_{0.3}\text{Ga}_{0.7}\text{As}$ SBR structures can be conveniently etched in one etching step. Typical etch rates were about $2.3 \text{ }\mu\text{m/min}$. In addition, because the solution is quite dilute, the photoresist layer is not compromised. A (1:1:2) $\text{HCl}:\text{H}_2\text{NO}_3:\text{H}_2\text{O}$ solution is used to etch SBR heterostructures with layers that did not contain arsenic. Since this acid mixture etches all III-V materials, it is the preferred mixture for etching multiple InGaAs quantum well structures with InP cladding, or mirror stacks with AlAs/ $\text{In}_{0.15}\text{Ga}_{0.15}\text{Al}_{0.35}\text{P}$ layers. Etching using (1:1:2) $\text{HCl}:\text{H}_2\text{NO}_3:\text{H}_2\text{O}$ was performed using an unheated ultrasonic bath to increase the etch rate. Since the etch rates are compositionally-dependent, etch rates for each material were not measured with accuracy. The etch rate for GaAs was observed to be about $1 \text{ }\mu\text{m/min}$ while faster average etch rates of $1.5 \text{ }\mu\text{m/min}$ were observed for SBR structures with layers of GaAs, InGaAs, $\text{Al}_{0.3}\text{Ga}_{0.7}\text{As}$, and AlAs. Higher etch rates were also observed using higher ratios of acid to water. However, increasing the acid concentration can also result in significant photoresist etching which degrades the etch process. After the mesas are etched, the photoresist is removed with a solvent called NMP (N-Methylpyrrolidone) which is heated to 130°C . After 10 minutes of immersion within heated NMP, the photoresist is fully removed. Shorter immersion times may be possible as well. Removing photoresist with acetone was not sufficient for samples that had been etched using $\text{HCl}:\text{H}_2\text{NO}_3:\text{H}_2\text{O}$, but was sufficient for cleaning samples that had been etched using the weak $\text{H}_2\text{SO}_4:\text{H}_2\text{O}_2:\text{H}_2\text{O}$ mixture. Perhaps exposure to strong acidic solutions alters the chemical composition of photoresist making it difficult to remove in acetone.

After chemical etching, in "Step 3" in Figure 2-10, the exposed AlAs layers are converted to Al_xO_y layers through a lateral oxidation process. The oxidation process proceeds as illustrated in Figure 2-11. When exposed to water vapor at an elevated temperature, AlAs begins to oxidize and is converted to Al_xO_y . Because the wet chemical etching process in "Step 2" only exposed the sides of the layered structure, the oxidation reaction begins at the edges of the structure where AlAs is exposed and can therefore react with H_2O . As water vapor diffuses into the structure and reacts with AlAs, the oxidation reaction moves laterally from the edges of the structure to the center of the structure, converting AlAs to aluminum oxide. The oxidation process is complete when all of the AlAs has been converted

to Al_xO_y . AIAs was chosen as the oxidizing layer because it experiences the fastest oxidation rates of all of the AlGaAs alloys thus allowing for larger-scale oxidations.

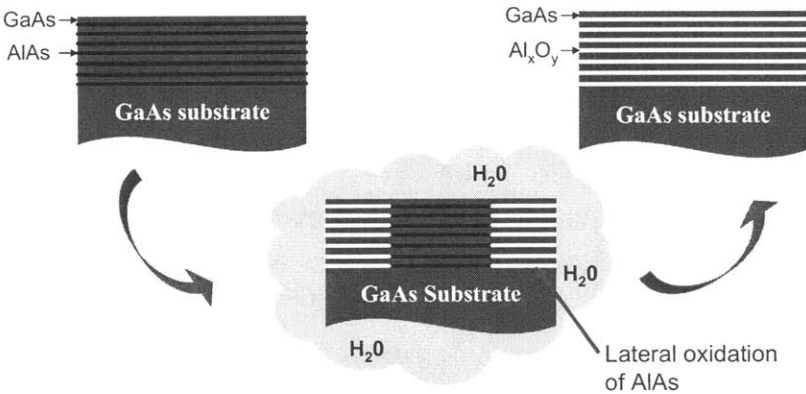


Figure 2-11 Schematic illustrating the lateral oxidation of AIAs layers in a Bragg mirror stack.

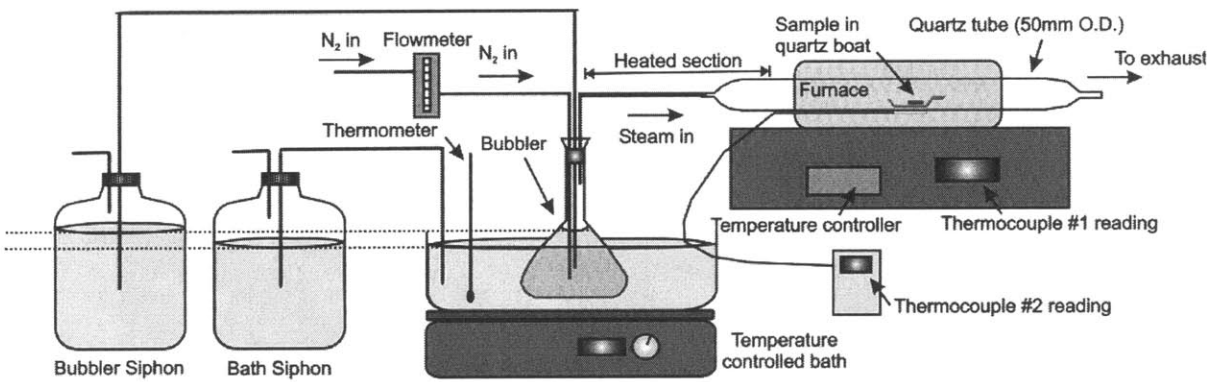


Figure 2-12 Schematic of oxidation setup showing sample location within furnace, direction of steam flow, temperature monitoring positions, and water supply lines.

The apparatus used to perform the oxidation process is shown in Figure 2-12. The SBR sample sits in a quartz boat located within a quartz tube that runs lengthwise through a furnace. The boat is used to move the sample into and out of the tube. During oxidation, nitrogen gas bubbles into a flask containing 90°C de-ionized (DI) water so that steam is pushed out of the flask and through the quartz furnace tube. The flow rate of the nitrogen gas is maintained at 2,205 sccm in order to maintain a steady flow rate of steam over the sample. Heating tape is used on the exposed sections of the quartz tube to prevent condensation of the steam upon entering and exiting the furnace. Condensation at the input end of the quartz tube will decrease the flow of steam into the furnace, thus affecting oxidation rates. Any condensed water at the exhaust of the quartz tube can flow back into the furnace section of the tube, cool the furnace temperature and create a thermal

shock during oxidation. Because typical oxidations last for multiple hours, siphons slowly feed water into the bubbler flask and heating bath in order to maintain water levels sufficient for oxidation. Typical oxidation temperatures range from 400-435°C and are read by thermocouples inside the furnace.

Once the device has been fabricated, a number of tools are used for characterization:

1. Plan-view inspection using differential interference contrast (DIC) microscopy.
2. High-resolution x-ray diffraction rocking curves to determine pre-oxidation layer thicknesses.
3. Cross-sectional inspection using Scanning Electron Microscopy (SEM) of monitor samples.
4. Reflectance characterization using Fourier Transform Infrared Spectroscopy (FTIR) or a microspectrophotometer.
5. Recovery time measurements using pump-probe analysis.
6. Photoluminescence to characterize the material composition of the absorber layer.
7. Overall performance characterization via testing in the laser system.

The interpretation of information gathered from each of these characterization methods will be discussed in detail in subsequent sections.

2.4 Large Scale Oxidation for Large Area Bragg Mirrors

2.4.1 The initial challenge of large scale oxidation

A number of dielectric stack structures have been studied with the goal of creating large area SBRs with broadband high-index-contrast mirrors. In the simplest design, a structure with alternating layers of GaAs and AlAs was grown, and 500 μm circular mesas were defined and oxidized in an attempt to form GaAs/Al_xO_y dielectric mirror stacks. Upon oxidation, however, this type of structure can suffer from severe deformation. For example, Figure 2-13(a) shows the deformation of one mesa after an oxidation at 435°C for 2 hours.

The cross-section, that is shown in Figure 2-13(b), illustrates that the distortion is due to delamination between the GaAs (106 nm thick) and AIAs (240 nm thick) layers. This delamination is most likely due two factors which are working in conjunction with each other: 1) the difference in volume between AIAs and Al_xO_y , and 2) weak bonding between the GaAs and Al_xO_y layers. As Choquette, *et al.* point out, the volume per Al atom in AIAs is $(3.57\text{\AA})^3$ while in $\gamma\text{-Al}_2\text{O}_3$ it is $(2.85\text{\AA})^3$, corresponding to a 20% linear contraction of AIAs layers upon oxidation [38]. Experimentally however, the linear contraction seems to be approximately 10-12%. If the bonding at the interface between the oxidized AIAs and the surrounding layers is not strong enough, this amount of volume contraction can contribute to delamination of the structure. The delamination illustrated in Figure 2-13 therefore suggests that the bonding strength at a GaAs/ Al_xO_y interface is insufficient to withstand the volume contraction of the AIAs layers. MacDougal, *et al.* claim that the weakness of the interface is due to gallium-oxygen bonds which form at the oxide boundary and are much weaker than aluminum-oxygen bonds [39]. With lateral oxidation of AIAs, it is possible that thin layers of GaAs are then oxidized in the vertical direction to weaken the GaAs/ Al_xO_y interface.

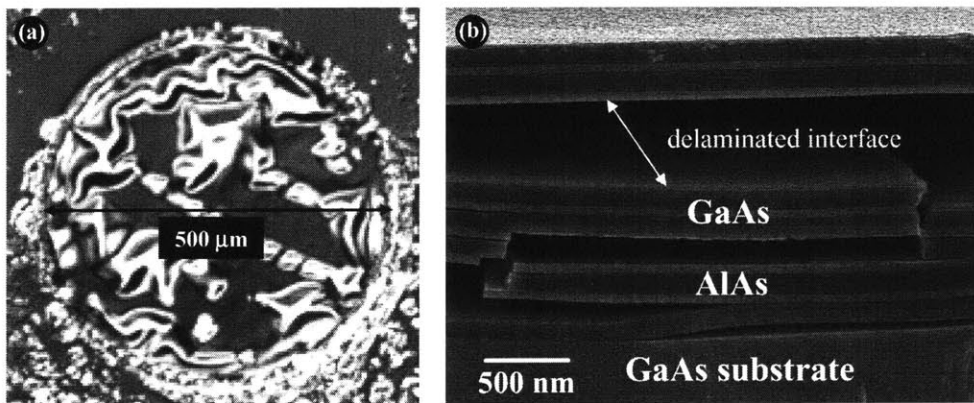


Figure 2-13 a) Nomarski micrograph showing the plan-view of a GaAs/AIAs dielectric stack deformed due to stresses introduced by oxidation at 435°C for 2 hours. b) Scanning Electron Micrograph (SEM) showing the cross-section of the stack with delaminated layers [40].

With the same GaAs/AIAs layered structure, oxidizing at lower temperatures lessens the delamination effects but with the trade-off of increased oxidation times. Figure 2-14(a) shows that by lowering the oxidation temperature to 375°C, a 10 hour oxidation only partially oxidized the mesa (140 μm from the edge) but eliminated the delamination effects. At temperatures above 375°C, faster oxidation rates are achieved but with increasing delamination effects suggesting that the delamination effect is thermally activated.

2.4.2 The AlGaAs/Al_xO_y large area broadband mirror

Instead of varying oxidation temperature to stabilize the layered structure, variations in material composition were considered as an alternative. To strengthen the bonding between the high index and oxide layers, aluminum was added to the high index GaAs layer of the dielectric stack structure. In a first attempt, Al_{0.7}Ga_{0.3}As was initially considered for the high index layer. Figure 2-14(b) shows a 500μm diameter mesa with an Al_{0.7}Ga_{0.3}As (130nm)/AlAs (240nm) stacked structure that was completely oxidized in 2 hours at 435°C with significantly reduced deformation of the mirror structure. SEM images suggested, however, that oxidation of the Al_{0.7}Ga_{0.3}As layers was significant--especially towards the edges of the mesa where complete oxidation of all the AlAs and Al_{0.7}Ga_{0.3}As layers had occurred.

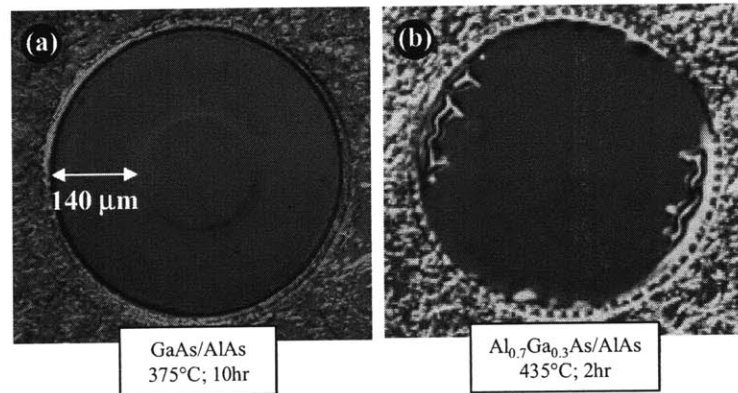


Figure 2-14 Differential interference contrast images showing the plan-views of two different 7 pair SBR structures after oxidation: (a) GaAs/AlAs structure oxidized at 375°C for 10 hours; (b) Al_{0.7}Ga_{0.3}As/AlAs structure oxidized at 435°C for 2 hours [40].

In order to slow the oxidation rate of the Al_xGa_{1-x}As layer, the aluminum content was decreased to 30%. Figure 2-15(a) shows that by oxidizing AlAs at 420°C for 4.25 hours, complete oxidation of the mesa was achieved with no delamination of the Al_{0.3}Ga_{0.7}As (92nm)/AlAs (200nm) layered structure. SEM images shown in Figure 2-15(b) also suggested no significant oxidation of the Al_{0.3}Ga_{0.7}As layer at the center of the mesa. Figure 2-15(b) also illustrates the polycrystalline/single crystal nature of the SBR layered structure. The crystalline layers appear smooth due to their distinct crystal planes while the polycrystalline Al_xO_y layers appear rough due to the lack of distinct crystal planes

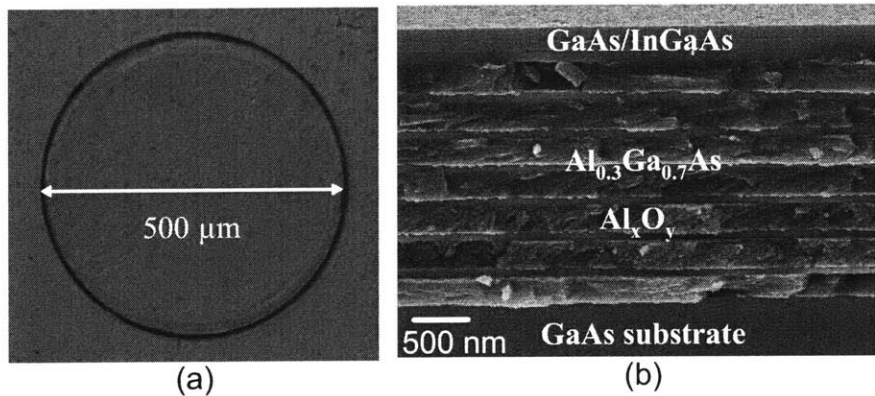


Figure 2-15 (a) Differential interference contrast images showing the plan-view of a 7 pair $\text{Al}_{0.3}\text{Ga}_{0.7}\text{As}$ (92nm)/AIAs (200nm) structure after oxidation at 420°C for 4.25 hr. (b) SEM image showing the SBR cross-section.

Reflectivity measurements taken using Fourier-transform infrared (FTIR) spectroscopy and a microspectrophotometer were used to characterize the performance of the dielectric stack as a mirror. The reflectance measurements shown in Figure 2-16 contrast the reflectivities of the oxidized and unoxidized $\text{Al}_{0.3}\text{Ga}_{0.7}\text{As}$ (92nm)/AIAs (200nm) structures. The high dielectric contrast between layers in the oxidized structure creates a mirror with high reflectivity over a broad wavelength range. This measurement verifies that after the oxidation process, high index contrast stacks were created. Therefore, low Al-content AlGaAs layers can be used as the high index layer of a dielectric stack to help stabilize the structure during large area oxidations.

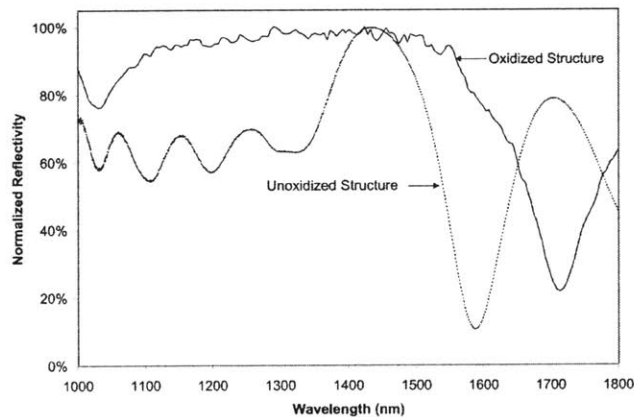


Figure 2-16 Reflectance measurements of the oxidized and unoxidized $\text{Al}_{0.3}\text{Ga}_{0.7}\text{As}$ /AIAs dielectric stack structures.

2.4.3 Limitations of large area AlGaAs/Al_xO_y mirrors

Though the reflectance measurement shown in Figure 2-16 indicates that oxidation of the high index layers was not appreciable at the center of the mesas; at the edges of the mesas, oxidation of the high index layer can be much more noticeable. An exaggerated case is shown in Figure 2-17 where the sample was oxidized for a longer time than necessary for full oxidation.

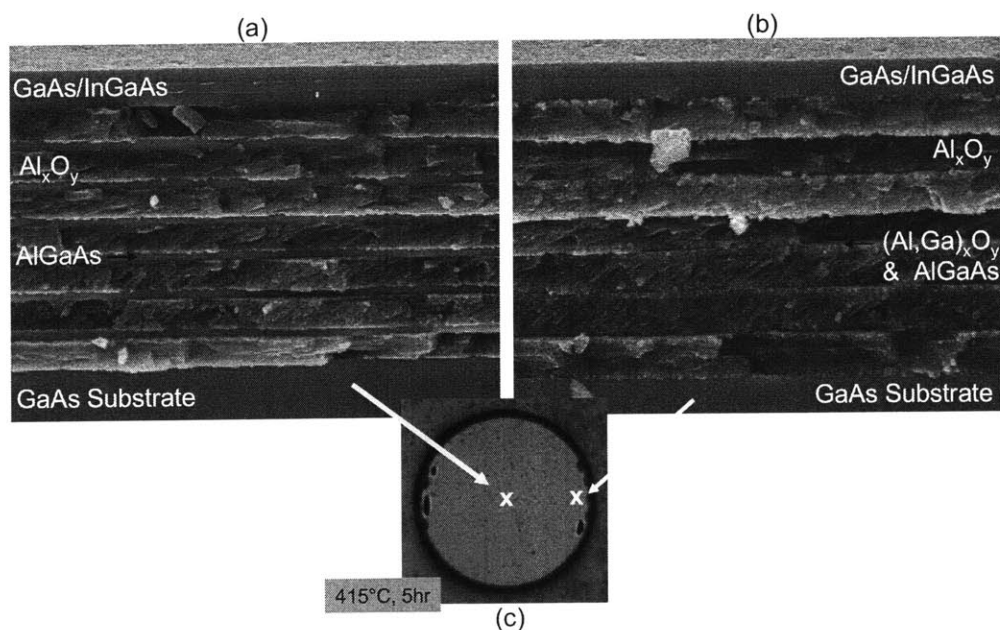


Figure 2-17 (a) SEM image showing cross-section of the layered structure at the center of the 500 μm mesa. (b) SEM image showing cross-section of the layered structure at the edge of the mesa. (c) Microscope image showing mesa locations for (a) and (b) images.

The SEM micrograph, shown in Figure 2-17(a), shows an image of an SBR cross-section at the center of the mesa while Figure 2-17(b) shows the cross-section of the layered structure after oxidation at 415°C for 5 hours. At a temperature of 410°C complete oxidation of the structure would require about 5 hours. Therefore, at a temperature of 415°C, it is expected that full oxidation of the structure would be complete in less than 5 hours. This figure represents a situation in which the structure was over-oxidized. At the center of the mesa, shown in Figure 2-17(a), the crystalline Al_{0.3}Ga_{0.7}As and polycrystalline Al_xO_y layers are visibly distinct. The cross-section of the high index Al_{0.3}Ga_{0.7}As layers appears smooth while the aluminum oxide layers appears rough in comparison due to the lack of distinct cleavage planes. In Figure 2-17(b), however, the crystalline and polycrystalline layers are less distinct due to the oxidation of the Al_{0.3}Ga_{0.7}As layers. After 5 hours of oxidation, Al_{0.3}Ga_{0.7}As will oxidize laterally therefore reducing the index contrast of the dielectric stack.

Vertical oxidation of $\text{Al}_{0.3}\text{Ga}_{0.7}\text{As}$ layers also occurs as reactants diffuse from oxidized AIAs layers into the neighboring $\text{Al}_{0.3}\text{Ga}_{0.7}\text{As}$ layers. The effect of this vertical oxidation is a thinning of the high index $\text{Al}_{0.3}\text{Ga}_{0.7}\text{As}$ and a thickening of the oxide layers.

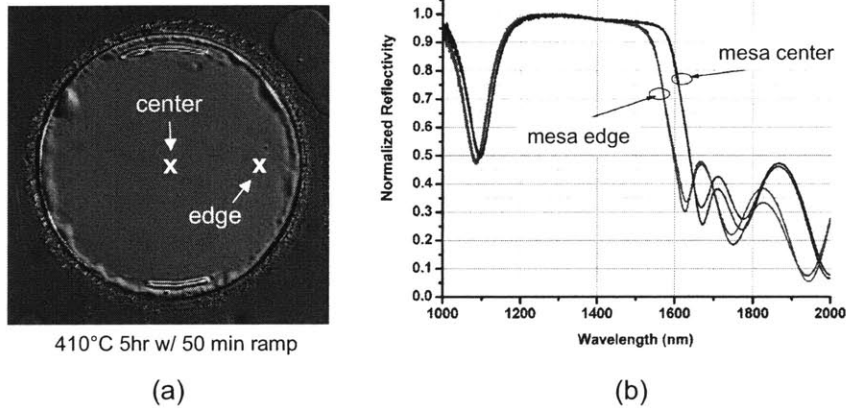


Figure 2-18 (a) Differential interference contrast image of oxidized SBR pointing out two different locations where the reflectivity was measured. (b) FTIR measurements contrasting the reflectivity associated with two different locations on the mesa.

Evidence of the changes in layer thickness due to oxidation is evident from reflectivity measurements taken at different parts of the oxidized mesa. Figure 2-18 shows how the reflectivity can vary from the edge of the mesa to the center of the mesa due to oxidation of the $\text{Al}_{0.3}\text{Ga}_{0.7}\text{As}$ layers. At the center of the mesa, where vertical oxidation of the $\text{Al}_{0.3}\text{Ga}_{0.7}\text{As}$ layers is less significant, the reflectivity bandwidth of the mirror is wider than the reflectivity bandwidth at the edge of the mesa where oxidation of the $\text{Al}_{0.3}\text{Ga}_{0.7}\text{As}$ layers has progressed further. This variation can occur because oxidation of the AIAs layers at the edge of the mesa is complete hours before AIAs can oxidize at the center of the mesa. Thus, the vertical oxidation of the $\text{Al}_{0.3}\text{Ga}_{0.7}\text{As}$ layers is more likely to occur at the edges of the mesa. As a result, the thicknesses of the $\text{Al}_{0.3}\text{Ga}_{0.7}\text{As}$ and Al_xO_y layers at the center of the mesa are closer to the $\lambda/4$ thickness required by the SBR design implying a broader bandwidth of reflectivity. At the edge of the mesa where the high index $\text{Al}_{0.3}\text{Ga}_{0.7}\text{As}$ is thinner than $\lambda/4$ and the total oxide thickness is thicker than $\lambda/4$ due to the effect of vertical oxidation, the reflectivity bandwidth narrows as shown in Figure 2-18(b).

Though $\text{Al}_{0.3}\text{Ga}_{0.7}\text{As}/\text{Al}_x\text{O}_y$ layered stacks enable stable broadband Bragg mirrors for sizes on the scale of 100's of microns, the oxidation of $\text{Al}_{0.3}\text{Ga}_{0.7}\text{As}$ imposes a limitation on larger scale oxidations. The vertical oxidation of $\text{Al}_{0.3}\text{Ga}_{0.7}\text{As}$ shown in the above SEM images and reflectivity measurements, shows how the effective size of the mirror can be reduced because of the lower index contrast and narrower reflectivity of the mesa edges. For the

applications discussed, this limitation did not preclude successful use of the $\text{Al}_{0.3}\text{Ga}_{0.7}\text{As}/\text{Al}_x\text{O}_y$ SBR structures in a number of laser systems. However, for applications in which a larger area would be necessary, an alternative should be considered where oxidation of the high index layer is not significant for longer duration oxidations. Reducing the aluminum content of the $\text{Al}_{0.3}\text{Ga}_{0.7}\text{As}$ layer is one option. However, reducing the aluminum content too significantly may jeopardize the bonding strength between the AlGaAs layer and the neighboring oxide layer as in the case of the $\text{GaAs}/\text{Al}_x\text{O}_y$ structure as shown in Figure 2-13.

2.4.4 The $\text{InGaAlP}/\text{Al}_x\text{O}_y$ large area broadband mirror

As an alternative to $\text{Al}_{0.3}\text{Ga}_{0.7}\text{As}$, $\text{In}_{0.15}\text{Ga}_{0.15}\text{Al}_{0.35}\text{P}$ was explored as the high index layer for SBR structures designed for the Ti:Sapphire laser which has a wavelength of 800 nm. Because $\text{Al}_{0.3}\text{Ga}_{0.7}\text{As}$ begins absorbing at a wavelength of approximately 690 nm, it is not an appropriate high-index layer for a broadband mirror structure designed to operate at 800 nm.

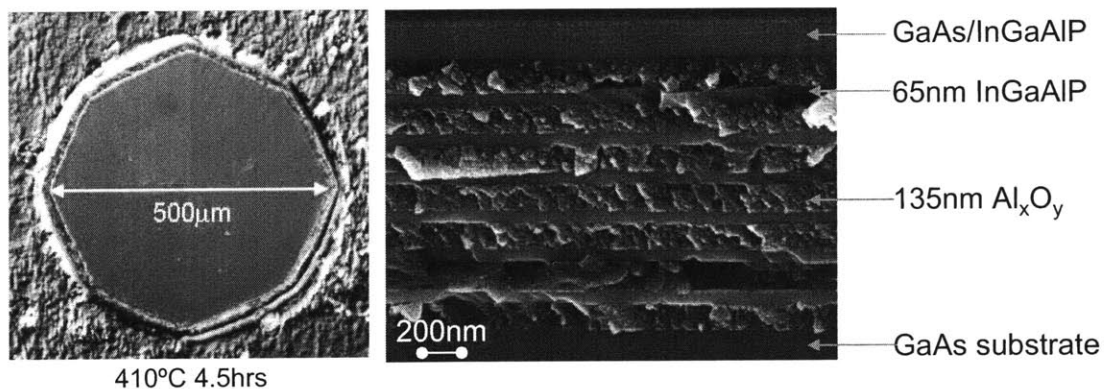


Figure 2-19 (a) Differential interference contrast (DIC) image of fully-oxidized SBR. (b) SEM micrograph showing $\text{In}_{0.15}\text{Ga}_{0.15}\text{Al}_{0.35}\text{P}/\text{Al}_x\text{O}_y$ mirror with GaAs absorber and $\text{In}_{0.15}\text{Ga}_{0.15}\text{Al}_{0.35}\text{P}$ cladding layers.

Figure 2-19(a) and (b) show a SBR design for a Ti:Sapphire laser (800 nm). The 500 μm mesas [Figure 2-19(a)] are not circular due to the $\text{HCl}:\text{H}_2\text{NO}_3:\text{H}_2\text{O}$ wet etch. A 10 nm GaAs absorber with 60 nm $\text{In}_{0.15}\text{Ga}_{0.15}\text{Al}_{0.35}\text{P}$ cladding layers was integrated with a 7-pair $\text{In}_{0.15}\text{Ga}_{0.15}\text{Al}_{0.35}\text{P}/\text{Al}_x\text{O}_y$ (60nm/ \sim 135nm) mirror. $\text{In}_{0.15}\text{Ga}_{0.15}\text{Al}_{0.35}\text{P}$, with an absorption wavelength of 536 nm, and refractive index of \sim 3.1, is lattice-matched to GaAs and has a lower absorption wavelength than AlGaAs alloys. With an $\text{In}_{0.15}\text{Ga}_{0.15}\text{Al}_{0.35}\text{P}$ -based layered structure, the SBR design is nominally unstrained. AlAs layers are completely oxidized at 410°C in 4.5 hours with no observable delamination. As seen in both broadband SBR

designs, the oxidized AlAs layer is polycrystalline whereas the high-index semiconductor layer remains single crystal.

Reflectivity measurements also indicate that by using $\text{In}_{0.15}\text{Ga}_{0.15}\text{Al}_{0.35}\text{P}$ as the high index layer in the mirror, the problems associated with slow oxidation rates can be avoided. Figure 2-20 presents reflectivity measurements taken at three locations across the 500 μm mesa. This measurement shows that the mirror's bandwidth experiences no noticeable change from the center of the mesa to the edge of the mesa. This measurement also seems to suggest that the $\text{In}_{0.15}\text{Ga}_{0.15}\text{Al}_{0.35}\text{P}$ layer does not oxidize or change composition in an elevated temperature steam environment.

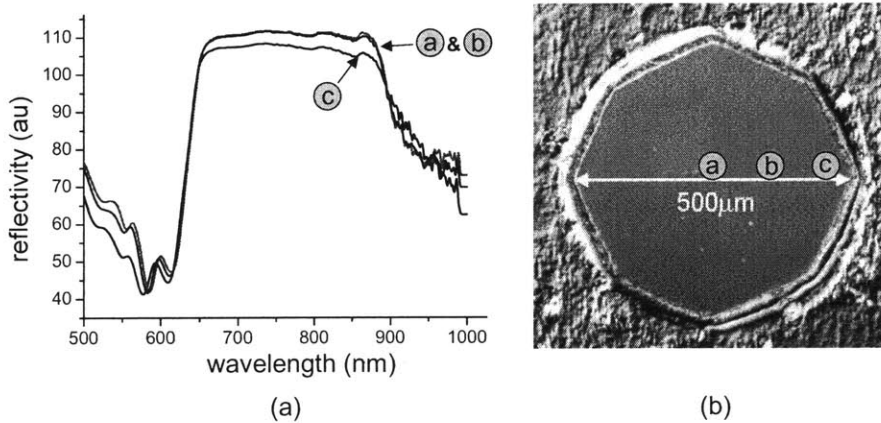


Figure 2-20 (a) Microspectrophotometer measurement at three different locations of an SBR structure with $\text{In}_{0.15}\text{Ga}_{0.15}\text{Al}_{0.35}\text{P}/\text{Al}_x\text{O}_y$ mirror. (b) DIC image showing the location on the mesa corresponding to each reflectivity trace.

With strong bonding to aluminum oxide, $\text{In}_{0.15}\text{Ga}_{0.15}\text{Al}_{0.35}\text{P}$ can be used as the high index layer in large area broadband $\text{In}_{0.15}\text{Ga}_{0.15}\text{Al}_{0.35}\text{P}/\text{Al}_x\text{O}_y$ mirrors. In addition because $\text{In}_{0.15}\text{Ga}_{0.15}\text{Al}_{0.35}\text{P}$ experiences no noticeable oxidation during the large-scale oxidation process, $\text{In}_{0.15}\text{Ga}_{0.15}\text{Al}_{0.35}\text{P}/\text{Al}_x\text{O}_y$ mirrors are more uniformly reflective than their $\text{Al}_{0.3}\text{Ga}_{0.7}\text{As}/\text{Al}_x\text{O}_y$ counterpart.

$\text{In}_{0.15}\text{Ga}_{0.15}\text{Al}_{0.35}\text{P}/\text{Al}_x\text{O}_y$ mirrors were also explored for larger areas than the 500 μm diameter mesas already mentioned. Figure 2-21 shows the results of three different oxidation experiments where the goal was to oxidize a full 1mm x 1mm square mesa.

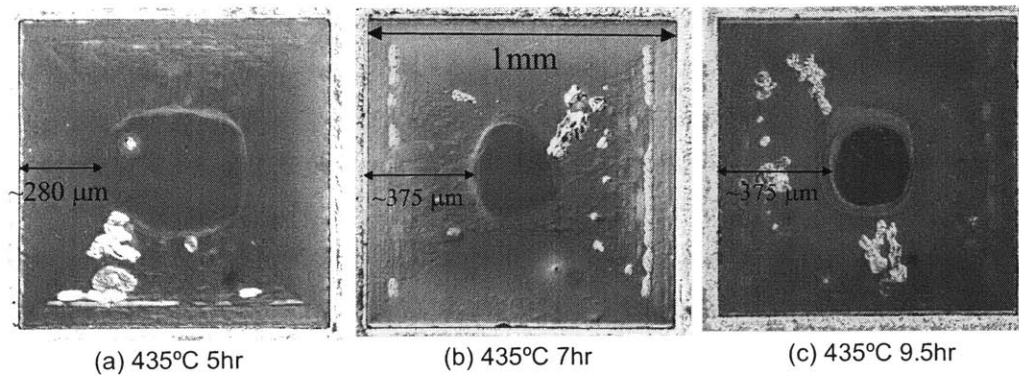


Figure 2-21 Differential interference contrast images of partially-oxidized 1mm x 1mm square mesas. Oxidations were carried out for three different durations: (a) 435°C, 5hrs (R1000 sq sample 2, 5/12/04 435°C, 5hr), (b) 435°C, 7hr (R1000 sq sample 3, 5/14/04 435°C, 7hr), (c) 435°C 9hr (R1000 sq sample 4, 6/24/04, 435°C, 9.5hr).

These oxidation results demonstrate how the geometry of the mesa can affect oxidation rates dramatically. After a 2.5 hour oxidation at 435°C, a 500 μm diameter circular mesa is completely oxidized, implying that the oxidation front traveled a 250 μm radius (a radial oxidation rate of 100 $\mu\text{m/hr}$). However, for the 1mm square mesa, after a 5 hour oxidation at 435°C, the oxidation front only traveled 280 μm from the square's edge. Thus, the oxidation front progresses more slowly through a square mesa than through a circular mesa. If the oxidation rate for mesa (a) in Figure 2-21 is calculated to be 56 $\mu\text{m/hr}$. (280 $\mu\text{m}/5\text{hr}$.), then for mesa (b), the oxidation rate is 54 $\mu\text{m/hr}$ (375 $\mu\text{m}/7\text{hr}$.), and for mesa (c), the oxidation rate is 40 $\mu\text{m/hr}$. (375 $\mu\text{m}/9.5\text{hr}$.). The difference in the oxidation rates between the square and circular geometries may be due to pure geometrical effects or possibly a dependence of the oxidation rates on crystal orientation. Choquette, *et al.* observed a slightly faster oxidation rate along the $\langle 100 \rangle$ crystal axes than along the $\langle 110 \rangle$ axes for the oxidation of AlAs layers [41]. Choquette, *et al.* claims that this difference in the oxidation rate is consistent with the lower surface reactivity of the $\{110\}$ planes. It is noteworthy that after 9.5 hr., the oxidation front did not advance appreciably. Full explanation of this observation will be left as a topic for future work. However, several mechanisms may be suggested to explain the slowing oxidation rate. Firstly, a slight decrease in the oxidation temperature may have decreased the oxidation rate for mesa (c) relative to the other cases. Though this is possible, it is unlikely considering the repeatability in oxidation temperature observed between other oxidation runs. Secondly, it may be possible that the aluminum oxide forms a barrier to the lateral diffusion of oxygen into the SBR structure, thus slowing oxidation.

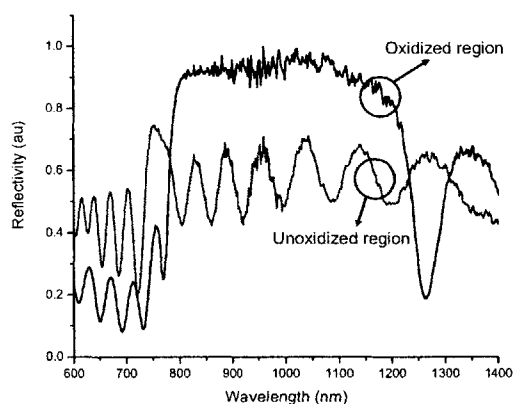


Figure 2-22 Microspectrophotometer measurement of the partially oxidized square mesa shown in Figure 2-21(a). The measurement of the oxidized region was from the outer area of the square mesa while the measurement of the unoxidized region was from the center of the square mesa.

Though the exact explanation for the incomplete oxidation of the 1 mm squares is unknown at this time, it seems that oxidation at larger scales to create $\text{In}_{0.15}\text{Ga}_{0.15}\text{Al}_{0.35}\text{P}/\text{Al}_x\text{O}_y$ mirrors is possible. Reflectivity measurements with a microspectrophotometer verified that broadband mirrors were created as shown in Figure 2-22 with the center of the square mesa remaining unoxidized. In future work, changing the geometry of the mesa to a 1mm diameter circle would most likely lead to increased oxidation rates.

2.5 SBRs for Infrared Wavelength Lasers

2.5.1 Design motivation

A number of SBR structures were investigated for a number of different laser systems. For the infrared wavelengths, SBR structures were designed for the Cr:YAG and Cr:Forsterite laser systems at wavelengths of 1.55 μm and 1.3 μm respectively. High modulation depth SBRs were also investigated for an erbium-doped fiber laser with a wavelength of 1.55 μm and an experiment on supercontinuum generation. The layers which compose the SBR structure were selected based on the wavelength of the laser system while keeping in mind other considerations such as tolerable losses or recovery times.

For all SBR designs for infrared laser systems, the mirror structure consisted of a 7.5 pair $\text{Al}_{0.3}\text{Ga}_{0.7}\text{As}/\text{Al}_x\text{O}_y$ mirror with an $\text{In}_{0.53}\text{Ga}_{0.47}\text{As}$ absorber. The structures fabricated for each laser system varied in a number of ways:

- 1) the thickness of the mirror layers
- 2) the thickness of the absorber layer
- 3) the structure of the absorber layer
- 4) the material composition of the cladding layers

The thickness of the mirror layers is determined by the center wavelength of the laser system such that each layer has a thickness of $\lambda/(4n)$ in their respective material. The thickness of the absorber layer will be chosen based on the desired saturable loss, or modulation depth, of the absorber. As discussed earlier, fiber lasers generally require higher modulation depths than solid-state lasers. As a result, a thicker absorber is often implemented. The structure of the absorbing layer can consist of a number of absorbing structures such as quantum dots, quantum wells, or bulk semiconductor layers depending on the amount of saturable loss desired in the laser system. The absorbing layer consists of either a single quantum well, multiple quantum wells, or a semi-bulk layer. The absorbing layer is then surrounded by wider band gap cladding layers which confine carriers within the absorbing layer. The cladding layers must be chosen such that they are transparent to the incident laser radiation. In addition, the choice of the cladding layers can also influence the strain distribution within the structure.

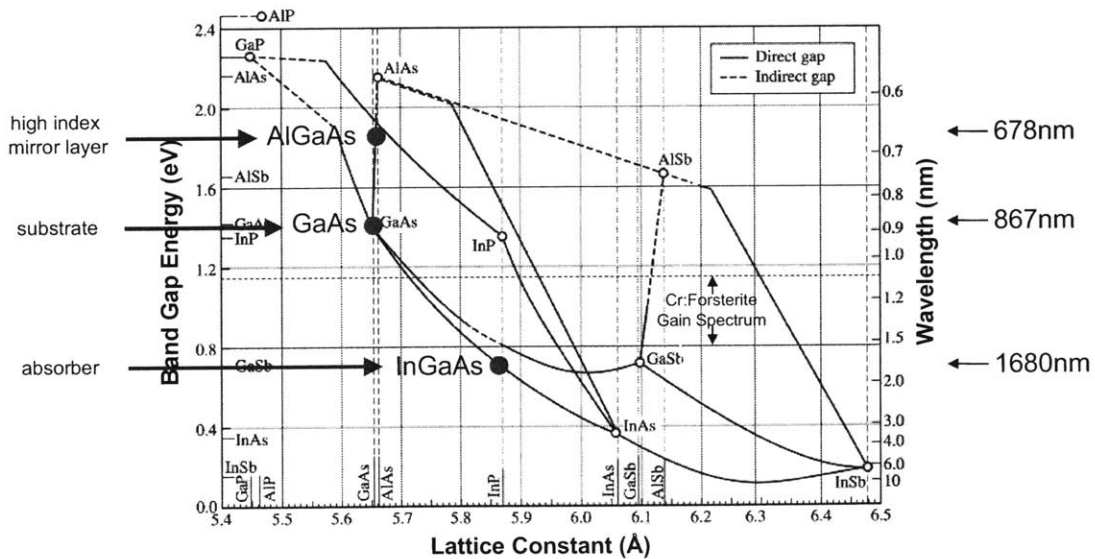


Figure 2-23 Band gap energy versus lattice constant diagram indicating the band gap associated with each of the layers which compose the SBR for the Cr:Forsterite laser (adapted from [42]).

As illustrated in Figure 2-23, $\text{In}_{0.53}\text{Ga}_{0.47}\text{As}$ is approximately 5% lattice-mismatched to GaAs. Using InGaAs as the absorbing layer in the SBR therefore introduces large amounts of strain into the structure. Because the thickness (10s of nm) of the InGaAs layer for all of the SBRs designed, is much thicker than the critical thickness (10s of Å), strain results in the generation of misfit dislocations at the interface between the two mismatched materials during growth. The choice of the cladding layers which surround the InGaAs absorber therefore determines the interface where the misfit dislocation density is highest. For the SBR structures for infrared laser systems, saturable absorbers of two different types were fabricated (see Figure 2-9 for an illustration of the structure). Both were grown on 7 pairs of $\text{Al}_{0.3}\text{Ga}_{0.7}\text{As}$ and AlAs on a GaAs substrate:

- 1) an $\text{In}_{0.53}\text{Ga}_{0.47}\text{As}$ absorber with InP cladding layers
- 2) an $\text{In}_{0.53}\text{Ga}_{0.47}\text{As}$ absorber with GaAs cladding layers

Both structures introduce strain into the structure via lattice mismatch. However, by choosing one structure over the other, misfit dislocations are generated at different interfaces. In the first structure, the $\text{In}_{0.53}\text{Ga}_{0.47}\text{As}$ layer is closely lattice-matched to the InP cladding layers so that the initial lattice mismatch, and therefore misfit dislocation formation, is at the InP/ $\text{Al}_{0.3}\text{Ga}_{0.7}\text{As}$ interface (the interface between the lower cladding and first mirror layer). In the second structure, the $\text{In}_{0.53}\text{Ga}_{0.47}\text{As}$ layer is highly mismatched to the GaAs cladding layers so that in this case, the initial lattice mismatch, and dislocation formation, is at the InGaAs/GaAs interface. Though the generation of misfit dislocations often results in threading dislocations which climb perpendicularly to the interface, as the thickness of the strained layer increases, the density of the threading dislocations decreases [43, 44]. Therefore, despite the fact that the InGaAs absorbing layer in the first structure may have threading dislocations which propagate through the InP cladding layers, overall, the InGaAs layer in the first structure is speculated to have fewer dislocations than in the second structure. The result is that the number of mid-band-gap recombination sites will be lower for the first structure. Mid-gap recombination sites may be desired for faster absorber recovery times, though higher dislocation densities increase the total nonsaturable loss of the SBR. Choosing the type of cladding layers therefore also involves consideration of the tolerable losses of the laser system.

2.5.2 Absorber Delamination

The need for strained layers within the SBRs designed for infrared laser systems creates another challenge for monolithically-integrating absorbers with broadband oxidized Bragg mirrors: delamination due to a strained absorber. Though the as-grown strained heterostructure does not suffer from any type of structural deformation, the oxidation process used to convert the AIAs layers to aluminum oxide often results in delamination between layers in the structure. A typical example of the delamination observed after oxidation is illustrated in Figure 2-24. The top view of the 500 μm mesa in Figure 2-24(a) shows stripes of deformation across the sample. SEM imaging in Figure 2-24(b) and (c) indicate that this deformation is attributed to separation of the saturable absorber from the mirror layers. In fact, not only is the absorber delaminating, but all of the crystalline layers above the first oxide layer in the mirror stack are delaminating along with strained absorber. These layers consist of: 52nm GaAs, 80 nm $\text{In}_{0.53}\text{Ga}_{0.47}\text{As}$, 52 nm GaAs, and 100 nm $\text{Al}_{0.3}\text{Ga}_{0.7}\text{As}$ (see growth log in the appendix for details on the layered structure growth). This result suggests that delamination occurs at the interface of weakest bonding ($\text{Al}_{0.3}\text{Ga}_{0.7}\text{As}$ -oxide interface) rather than at an interface where dislocations may reside (InGaAs -GaAs interface). It is also interesting to note that from the SEM image in Figure 2-24(b), at the location where buckling of the absorber/cladding layers occurs, there is also oxidation of the attached $\text{Al}_{0.3}\text{Ga}_{0.7}\text{As}$ layer. Oxidation of the second $\text{Al}_{0.3}\text{Ga}_{0.7}\text{As}$ layer is also apparent as the $\text{Al}_{0.3}\text{Ga}_{0.7}\text{As}$ and polycrystalline Al_xO_y layers are less visibly distinct. In the lowest layers of the structure, the crystalline $\text{Al}_{0.3}\text{Ga}_{0.7}\text{As}$ and polycrystalline Al_xO_y layers are more visibly distinct suggesting that oxidation of the $\text{Al}_{0.3}\text{Ga}_{0.7}\text{As}$ has not occurred. The noticeable oxidation of these $\text{Al}_{0.3}\text{Ga}_{0.7}\text{As}$ layers towards the top of the structure suggests that once delamination of the absorber layers occurred, steam had the opportunity to now diffuse into the structure at the buckled areas to oxidize $\text{Al}_{0.3}\text{Ga}_{0.7}\text{As}$ layers in the vertical direction.

Another interesting feature of the delamination presented in Figure 2-24, is the pattern in which buckling of the absorber layers occurs. Figure 2-24(a) shows how the delamination has created "stripes" which have propagated across the structure in straight lines. The cross-section of two such lines is illustrated in Figure 2-24(c). This type of delamination initially seems surprising considering the fact that the oxidation process proceeds with a cylindrical geometry from the outside of the mesa inward. However, this pattern of delamination occurred frequently for many different SBR structures. In all cases, the lines of delamination always lay perpendicular to the major flat of the GaAs wafer upon which the

structure was grown. For all of the wafers used in this work, the major flat is terminated on the $(1\bar{1}0)$ plane.

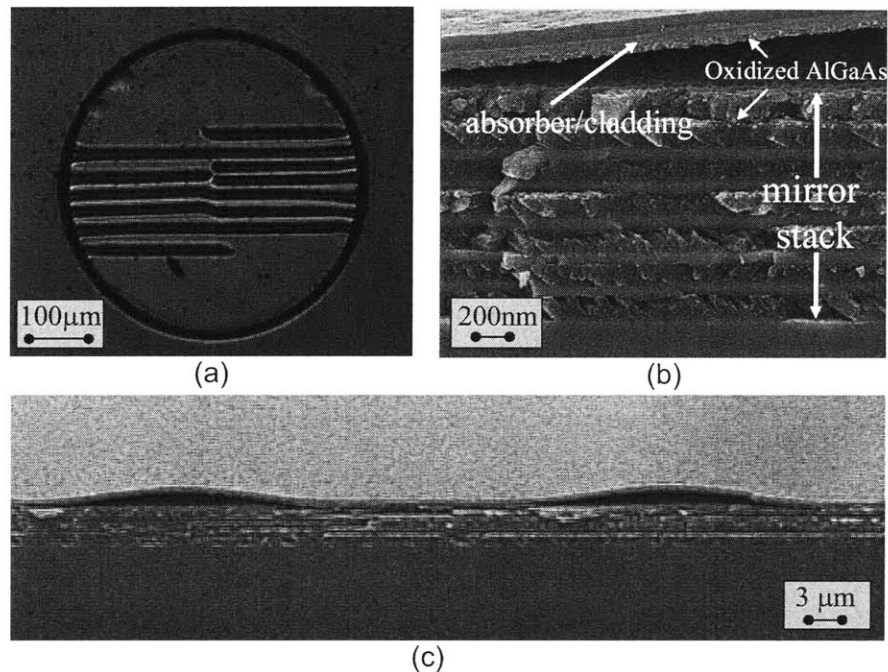


Figure 2-24 (a) Differential interference contrast (DIC) image of oxidized 500µm mesa illustrating delamination. (b) SEM image showing absorber delamination from the mirror stack. (c) SEM image showing the patterned absorber delamination. (R958, 3hr, 435C, 3/31/2003)

The initial challenges associated with delamination in the mirror layers discussed in Section 2.4.2 were overcome by considering the variables surrounding the oxidation process, in combination with their interaction with the materials that compose the structure. This same approach has been investigated for incorporating strained absorbers into the SBR structure. However, the difficulty in addressing the absorber delamination problem has been that there are many variables which can influence the stability of the structure. Some of those variables have been identified in the sections to follow. Oxidation and characterization results have been compared across a number of variables in order to better understand the oxidation process and its interaction with the materials in the layered stack.

2.5.3 Results: Temperature dependence of absorber delamination

The first variable which directly influences absorber delamination is the temperature of the oxidation reaction. Figure 2-25, Figure 2-26, and Figure 2-27 show oxidation results associated with three different SBR structures with InGaAs absorber thicknesses varying

between 10nm and 80nm, GaAs cladding layers, and $\text{Al}_{0.3}\text{Ga}_{0.7}\text{As}/\text{Al}_x\text{O}_y$ mirrors. The appendix contains the specific growth information related to each structure. For each structure, oxidation results are presented for temperatures between 410°C and 435°C. For mesas of growth R958 presented in Figure 2-25, delamination occurred at each temperature with the most severe delamination occurring at the higher temperature of 435°C. With an exponential relationship between the oxidation rate of AlAs and the oxidation temperature, it is not unreasonable that delamination effects would be highly sensitive to a temperature change of 15°C. In order to successfully oxidize this SBR without delamination, decreasing the oxidation temperature would be a viable solution. However, decreasing the oxidation temperature results in a longer oxidation time to completely oxidize the 500 μm mesas. Oxidations of similar structures at 400°C required oxidation times of approximately 8 hours—not an unreasonable amount of time for the oxidation set-up. However, with longer oxidation times, oxidations of the $\text{Al}_{0.3}\text{Ga}_{0.7}\text{As}$ layers and even GaAs layers can be noticeable. Varying other parameters of the oxidation process to stabilize the structure would be more favorable.

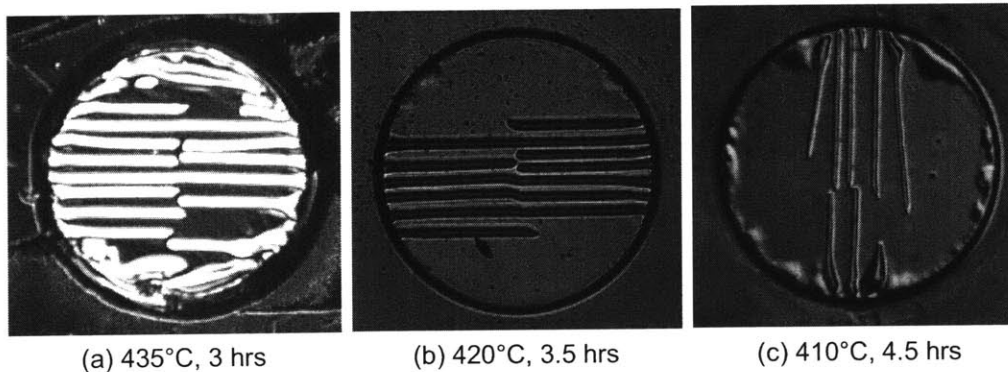


Figure 2-25 Oxidation results illustrating the temperature dependence of absorber delamination. The InGaAs absorber thickness is 80 nm. All mesas have 500 μm diameters and are from similar areas of the wafer. (a) Oxidation at 435°C, 3 hrs (R958, 3/31/2003), (b) Oxidation at 420°C for 3.5 hr (R958, 12/7/2002), (c) Oxidation at 410°C for 4.5 hours (R958, 12/18/2002).

With a thinner 10nm InGaAs absorbing layer, Figure 2-26 shows how the delamination effects again vary with temperature--the most severe delamination occurring at the highest temperatures. However, in this case, the pattern of the delamination does not consist of stripes across the center of the mesas but wider stripes which form at $\sim 60^\circ$ angles as shown in Figure 2-26.

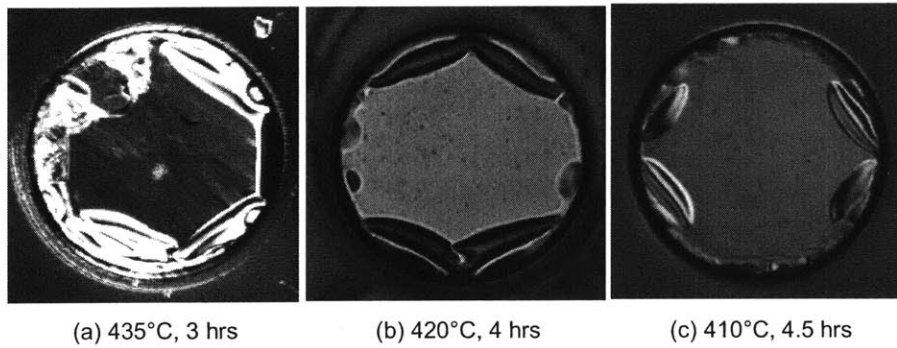


Figure 2-26 Oxidation results illustrating the temperature dependence of absorber delamination. The InGaAs absorber thickness is 10 nm. All mesas have 500 μm diameters and are from similar areas of the wafer. (a) Oxidation at 435°C, 3 hrs (R957, 3/31/2003), (b) Oxidation at 420°C for 4 hr (R957, 12/6/2002), (c) Oxidation at 410°C for 4.5 hours (R957, 12/18/2002).

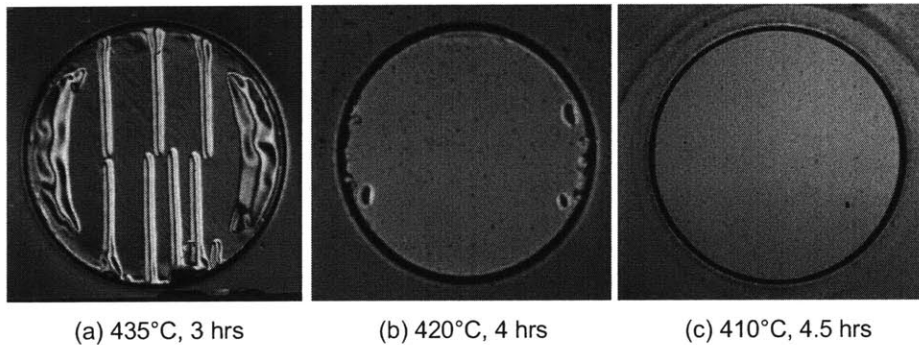


Figure 2-27 Oxidation results illustrating the temperature dependence of absorber delamination. The InGaAs absorber thickness is 40 nm. All mesas have 500 μm diameters and are from similar areas of the wafer. (a) Oxidation at 435°C, 3 hrs (R946, 10/29/2002), (b) Oxidation at 420°C for 4 hrs (R946, 11/18/2002) [45], (c) Oxidation at 410°C for 4.5 hours (R946, 4/24/2003).

The delamination effects observed for the 80nm and 10nm InGaAs absorbers seem to indicate that while increasing the temperature of the oxidation reaction increases the delamination problems, decreasing the absorber thickness decreases the delamination problems. Figure 2-27 presents the oxidation results associated with a structure consisting of a 40 nm InGaAs absorber. Again, the most severe delamination occurs at an oxidation temperature of 435°C. However, at 420°C and 410°C no observable delamination has occurred. Perhaps the increase in strain introduced by the increased InGaAs thickness is not the only contributor to absorber delamination.

2.5.4 Results: Thickness dependence of absorber delamination

By comparing oxidation results for structures with varying thicknesses both in the absorbing layer thickness and in the AIAs thickness, other trends become apparent. Figure 2-28

compares oxidation results for the three structures presented in Section 2.5.3 for an oxidation temperature of 410°C. While it seems reasonable for delamination effects to increase with increased InGaAs thickness, it seems unusual that the structure with 40 nm of InGaAs should have no apparent delamination while the 10 nm InGaAs structure has delamination occurring at the edges of the mesas. However, closer investigation reveals that there is another difference between the two structures--the pre-oxidation AIAs thickness. R957 shown in Figure 2-28(a) has an AIAs thicknesses of 240 nm while R946 and R958 shown in Figure 2-28(b) and (c) have 200nm thick AIAs layers.

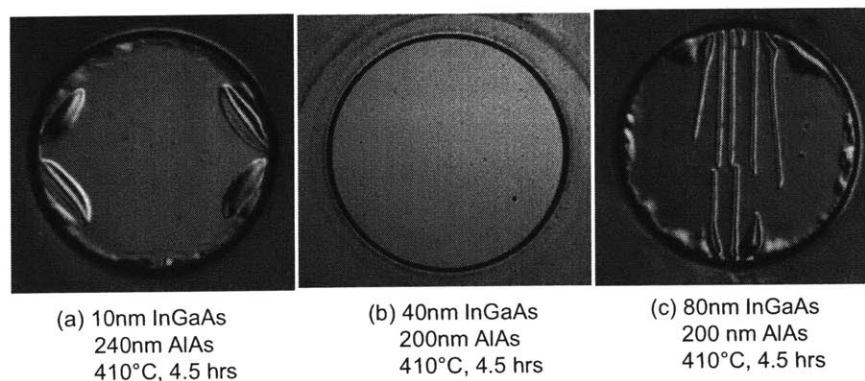


Figure 2-28 Oxidation results examining thickness dependence of absorber delamination. (a) 10nm InGaAs absorber, 240nm AIAs (R957, 12/18/2002, 410°C, 4.5 hr), (b) 40nm InGaAs absorber, 200nm AIAs (R946, 4/24/2003, 410°C, 4.5 hr), (c) 80nm InGaAs absorber, 200nm AIAs (R958, 12/18/2002, 410°C, 4.5 hr)

As discussed previously, AIAs experiences a volume contraction of approximately 10% upon conversion to polycrystalline Al_xO_y . With seven layers of AIAs in each SBR structure, slight differences in the AIAs layer thickness may result in noticeable differences in the stability of the structure when all seven layers contract simultaneously. Considering the various structures presented in Figure 2-28, during oxidation, the thickness of each AIAs layer in R957 will contract $\sim 24\text{nm}$ from 240nm to an Al_xO_y thickness of $\sim 216\text{nm}$. The total contraction of the SBR layered structure will therefore be multiplied by 7 for a total contraction of 168nm. In R946 and R958 where the AIAs thickness is 200nm, the contraction of each AIAs layer is 20nm for a total contraction of 140nm (20nm x 7 AIAs layers). In R958, both the strain of the InGaAs layer and the stress introduced by volume contraction contribute to delamination of the absorber. In R946, though the volume contraction is the same as R958, the strain from the InGaAs absorber may not be sufficient to result in delamination. However, for R957, where the InGaAs thickness is thinner than R946 but where the AIAs layer is thicker, the interaction between the strain and contraction is enough to result in delamination effects.

These results suggest that there is a relationship between absorber strain and AIAs volume contraction during oxidation. With thinner absorbers, delamination can occur if the volume contraction is too high. With thicker absorbers, delamination can occur due to strain. With the appropriate balance between absorber strain and volume contraction, however, a stable structure can be created with oxidation.

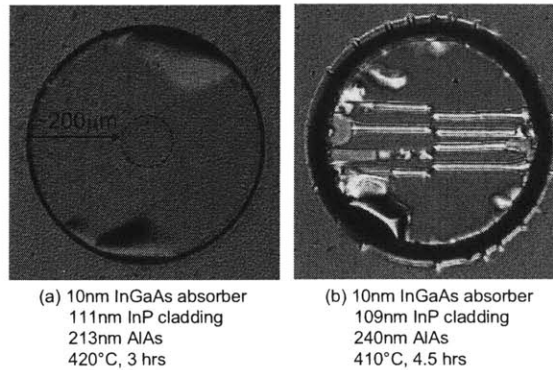


Figure 2-29 Oxidation results examining the dependence of absorber delamination on AIAs thickness. (a) 10nm InGaAs absorber, 213nm AIAs (R933, 9/27/2002, 420°C, 3 hr), (b) 10nm InGaAs absorber, 240nm AIAs (R959, 2/14/2003, 410°C, 4.5 hr)

Further evidence for the need to balance absorber strain and AIAs contraction is exhibited by the results shown in Figure 2-29. Both structures have the same absorber thicknesses and have InP cladding layers. However, the AIAs layer thicknesses differ by 27nm, implying a 19nm difference ($27 \text{ nm} \times 10\% \text{ contraction} \times 7 \text{ layers}$) in the total contraction between the structures. With thinner AIAs layers, as shown in Figure 2-29(a), delamination was much less severe than for the structure shown in Figure 2-29(b) even for a higher oxidation temperature.

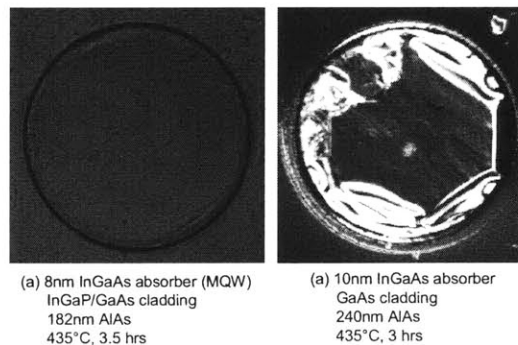


Figure 2-30 Oxidation results examining the dependence of absorber delamination on AIAs thickness. (a) 8nm multiple quantum well (MQW) InGaAs absorber, 182nm AIAs (R934, 9/27/2002, 435°C, 3.5 hr), (b) 10nm InGaAs absorber, 240nm AIAs (R957, 3/31/2003, 435°C, 3 hr)

A similar trend is suggested by the results presented in Figure 2-30. The two structures have slightly different absorber thicknesses and larger differences in the AIAs thickness. The first structure presented in Figure 2-30(a) has two 4 nm InGaAs quantum wells within GaAs cladding layers and a lattice-matched InGaP cap layer. For an oxidation at 435°C, the structure exhibits no apparent delamination. On the other hand, with a slightly thicker InGaAs absorber but AIAs layers which are each 58 nm thicker, the delamination effects for the structure shown in Figure 2-30(b) are quite significant in comparison. With a 58 nm difference in the AIAs thickness, the difference in the total contraction is about 41 nm (58 nm x 10% contraction x 7 layers). Therefore with a much larger contraction of the layered structure, delamination can occur despite a thinner strained absorber.

2.5.5 Observations: Cladding layer dependence of absorber delamination

Oxidation results also suggest that the choice of cladding layers can affect the stability of the structure upon oxidation. Figure 2-31 shows the results for three structures, the first two [Figure 2-31(a) and (b)] were grown with the same material composition and thicknesses. However, in (a), the absorber and cladding layers were grown at a lower substrate temperature than (b). Figure 2-31(c) shows the oxidation results for a structure with the same absorber thickness and AIAs thickness but with InP cladding layers. The worst of the delamination effects seem to be for the structure with the InP cladding layers--suggesting that this cladding layer choice adds more strain into the SBR structure.

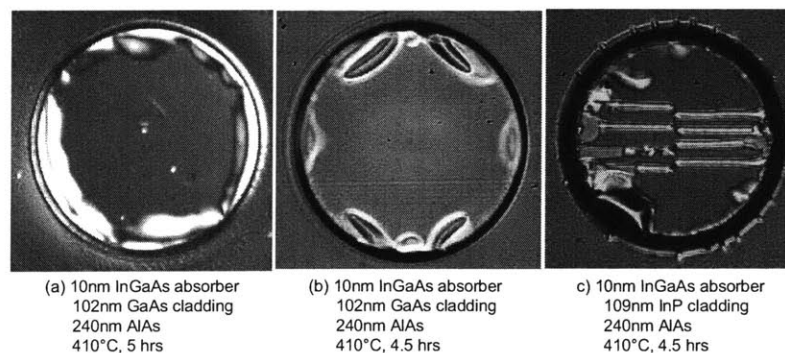


Figure 2-31 Oxidation results suggesting cladding layer dependence of absorber delamination. (a) Structure with GaAs cladding (R968, 4/25/2003, 410°C, 5hrs). (b) Another structure with GaAs cladding (R957, 2/14/2003, 410°C, 4.5hr). (c) Structure with InP cladding (R959, 2/14/2003, 410°C, 4.5 hr).

By choosing either InP or GaAs layers to clad the InGaAs absorbing layer, the strain distribution within the layered structure differs. The total strain would be less in the structure with GaAs cladding layers because the thickness of the mismatched layer (*i.e.*

InGaAs) is thinner and the cladding layers above and below the absorber will strain the InGaAs layer towards the GaAs lattice constant. With InP cladding layers, the full strain of the lattice mismatch is confined to the cladding layer/mirror layer interface, and the thickness of the strained layer is greater. Therefore the strain in the InP clad structure is greater than the GaAs clad structure which influences the delamination problems.

2.5.6 Results: Variation of absorber delamination across wafer

Another observation noted during the course of multiple oxidation experiments was the variation in delamination effects across the wafer. As illustrated in Figure 2-32, mesas located at the center of the wafer experienced greater delamination problems than mesas located towards the edge, or perimeter, of the wafer.

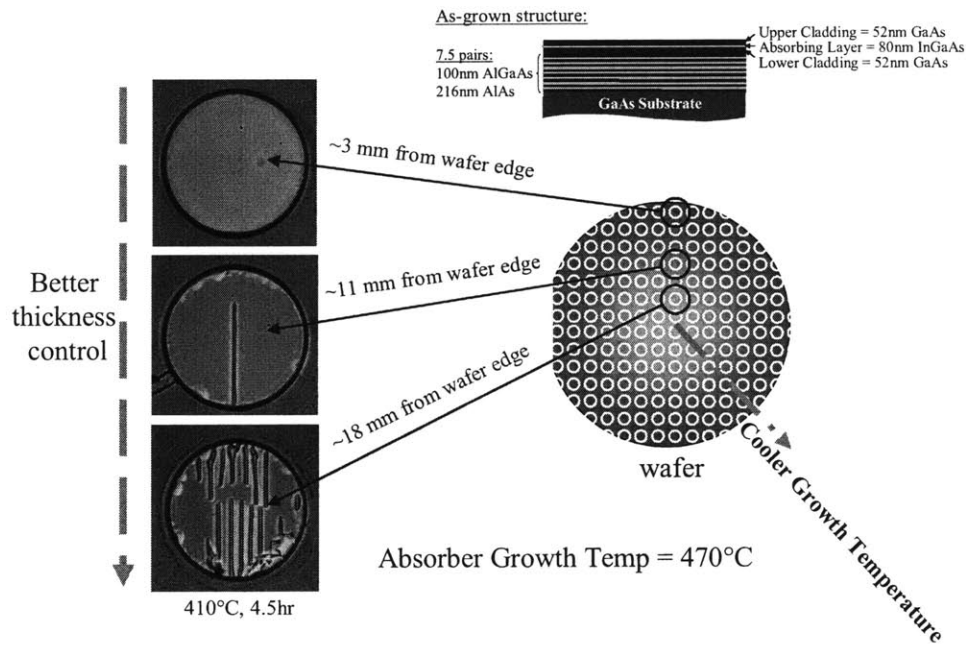


Figure 2-32 Oxidation results illustrating how delamination effects vary with mesa location on the wafer (R958, 2/14/2003, 410°C, 4.5hr).

The variation in delamination effects with mesa location may be due to a number of different variables. The first variable may be absorber growth temperature. During the molecular beam epitaxy growth process, substrate heating is not uniform due to the design of the sample holder, with the cooler temperatures at the edge of the wafer. Growing the SBR structure at lower growth temperatures may influence the structure in many ways. In general, the temperature of MBE growth can influence the incorporation of impurity

elements into the structure, the formation of energy levels within the band gap due to impurities, or the formation of lattice defects. Growth temperature can also influence the roughness of surfaces or interfaces [43]. If defect densities or surface morphology have an influence on delamination, then growth temperature variations may affect the occurrence of delamination over the wafer surface. At the same time, a second variable affecting the delamination process may be the variations in layer thicknesses over the wafer area. If the AIAs thickness varies over the wafer surface, the amount of volume contraction and therefore delamination can vary. In addition, if the InGaAs absorber thickness varies over the wafer area, the amount of strain changes which also affects the delamination process.

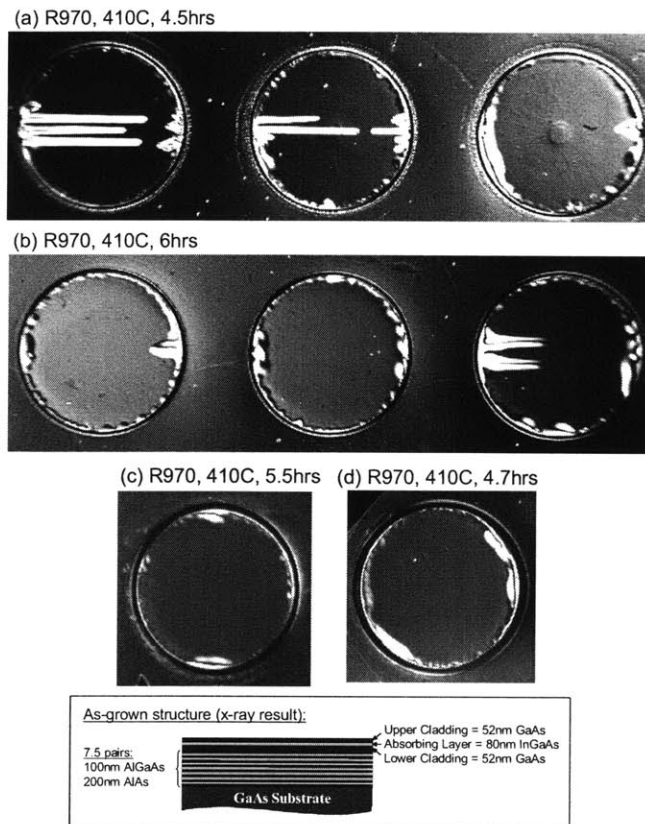


Figure 2-33 Oxidation results for SBR structure with absorber grown at 400C. (a) R970, 4/24/2003, 410C, 4.5hrs (b) R970, 4/25/2003 #2, 410C, 6hrs (c) R970, 4/28/2003, 410C, 5.5hrs (d) R970, 5/23/2003, 410C, 4.7hr.

To explore the possible dependence of the delamination process on the growth temperature, structures with the same material composition were grown, but with the absorber layers grown at a lower temperature. A structure with the same composition as R958 (Figure 2-32) was grown with absorber layers grown at 400°C instead of 470°C. Mesas were patterned, etched, and oxidized. Mesa images from several oxidations of this structure

(structure R970) are shown in Figure 2-33. All of the mesas are from the center regions of the wafer. The images show that although the delamination effects are still present, they seem to be less severe than those observed for oxidations of R958. However, while the SBR designs for R958 and R970 were the same, high-resolution x-ray diffraction (400) rocking curves for the unoxidized structures indicated that the AIAs thicknesses were actually different: 200 nm AIAs for R970, and 206 AIAs for R958 at the center of each wafer. The $\text{Al}_{0.3}\text{Ga}_{0.7}\text{As}$ thicknesses were identical for both structures. With a 6 nm difference in AIAs thickness, the total volume contraction difference for the structure is 4.2nm (6 nm x 7 pairs x 10%). This difference seems quite small relative to some of the AIAs thickness differences noted in Section 2.5.4. However, the small AIAs difference may explain why the delamination results were less severe but still present for oxidations of R970.

Therefore, the results presented in Figure 2-33 do not conclusively show that growth temperature variations over the wafer area contribute to delamination effects. The slight decrease in delamination observed for structure R970, relative to R958 which was grown at a higher temperature, may be more directly related to the thinner measured AIAs thickness than growth temperature differences.

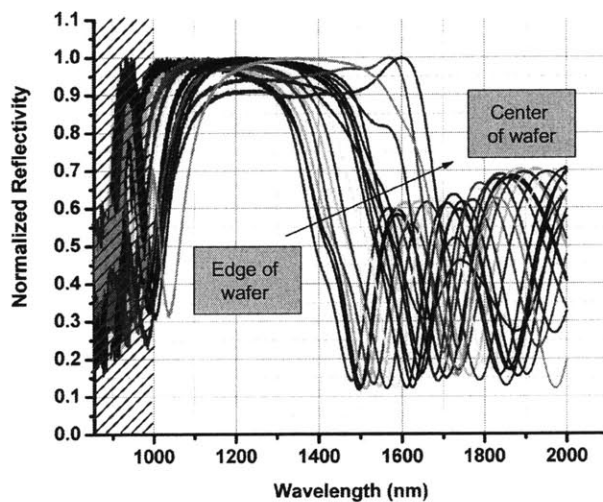


Figure 2-34 Fourier Transform Infrared Spectroscopy (FTIR) measurements illustrating the trend in the reflectivities of oxidized mesas from the edge of the wafer to the center of the wafer for the sample shown in Figure 1 30 (R958, 2/14/2003, 410°C, 4.5hr). The shaded area is below the FTIR detector's effective range.

Reflectivity measurements of mesas from the structure (R958) illustrated in Figure 2-32 are shown in Figure 2-34. Figure 2-34 is a plot of the reflectivity versus wavelength for 18 mesas progressing from the edge of the wafer to the center of the wafer. The plot reveals that mesas at the edge of the wafer are highly reflective for shorter wavelengths than

mesas at the center of the wafer--implying that the mirror layers are thinner at the edge of the wafer than at the center.

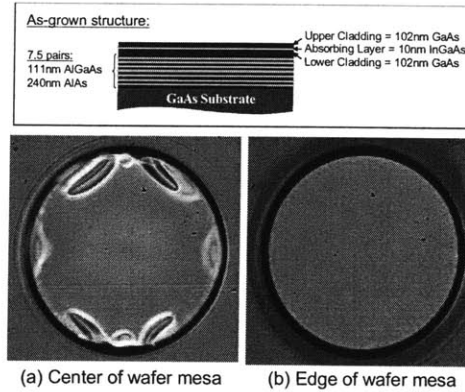


Figure 2-35 Oxidation results showing how delamination effects depend on the location of the mesa on the wafer. (a) A mesa from the center of the wafer. (b) A mesa from the edge of the wafer. (R957, 2/14/2003, 410°C, 4.5hr)

Other structures exhibited similar delamination and reflectivity trends. Figure 2-35 shows how mesas from growth R957 (see Appendix) experienced varying delamination effects for the same oxidation conditions. Again, delamination was more severe for mesas at the center of the wafer [Figure 2-35 (a)] than for mesas at the edge of the wafer [Figure 2-35 (b)]. Reflectivity measurements for oxidized mesas of R957 also indicated that mesas at the center of the wafer are reflective for longer wavelengths than mesas at the edge as shown in Figure 2-36 implying that the mirror layers are thinner towards the edge of the wafer. The downward slope in the reflectivity measurement for the "edge sample" in Figure 2-36 is an artifact of the FTIR tool.

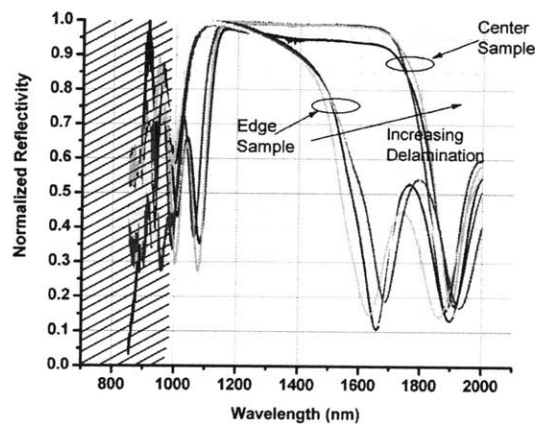


Figure 2-36 Fourier Transform Infrared Spectroscopy (FTIR) measurements illustrating the difference in the reflectivities of oxidized mesas from the edge of the wafer and the center of the wafer for the mesas shown in Figure 2-35 (R957, 2/14/2003, 410°C, 4.5hr). The shaded area is below the FTIR detector's effective range.

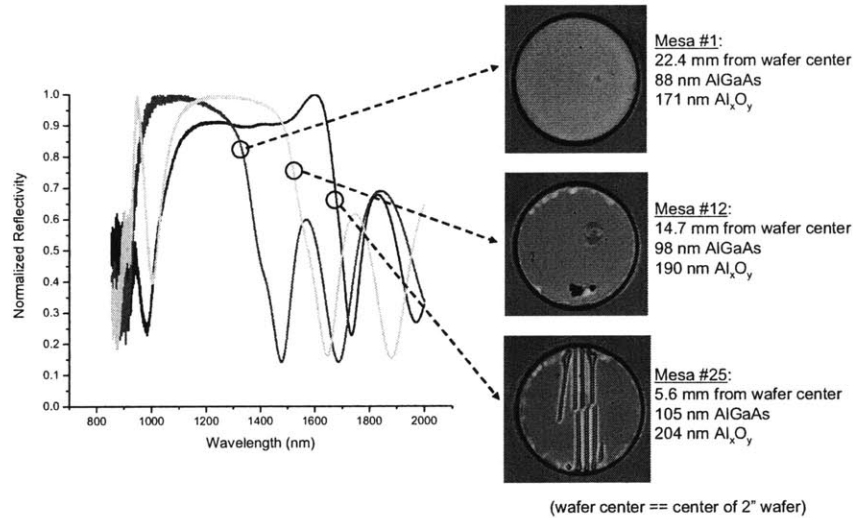


Figure 2-37 Reflectivity measurements and DIC images of three oxidized mesas of r958 with the $\text{Al}_{0.3}\text{Ga}_{0.7}\text{As}$ and Al_xO_y layer thicknesses implied by theoretical best-fit calculations. Mesa #1 is closest to the edge of the wafer and Mesa #25 is closest to the center of the wafer. Mesa #12 is the mesa closest to the center of the wafer where delamination did not occur. (R958, 2/14/2003, 410°C, 4.5hr)

The thickness variation over the wafer area can be estimated by comparing measured reflectivity curves to theoretical predictions. Figure 2-37 presents the measured reflectivities, differential interference contrast (DIC) images, and implied layer thicknesses associated with three different mesas from the oxidized structure presented in Figure 2-32 and Figure 2-34. Mesa #1 is the mesa located closest to the edge of the wafer and is 22.4 mm from the center of the 2" wafer upon which R958 was grown. As apparent from the DIC image, mesa #1 experienced no delamination. By fitting the measured FTIR reflectivity to a theoretical calculation of the FTIR reflectivity for SBR structure R958, the thicknesses of the $\text{Al}_{0.3}\text{Ga}_{0.7}\text{As}$ and Al_xO_y layers were 88nm and 171nm respectively [46]. Mesa #12 is located 14.7mm from the center of the wafer and was the mesa closest to the wafer's center where delamination did not occur. The theoretical best-fit calculation implied that the $\text{Al}_{0.3}\text{Ga}_{0.7}\text{As}$ and Al_xO_y layer thicknesses were 98nm and 198nm respectively—thicker than the layers of Mesa #1. Mesa #25 was the mesa on this sample which was closest to the center of the wafer. In order to theoretically fit the measured reflectivity, the structure needed to be modified to take into account the air gap introduced by the delamination, as well as the top two layers of $\text{Al}_{0.3}\text{Ga}_{0.7}\text{As}$ which had oxidized in the vertical direction due to steam entering the delaminated areas. The air gap and oxidized $\text{Al}_{0.3}\text{Ga}_{0.7}\text{As}$ layers for this mesa are visible in the SEM images presented in Figure 2-24. The structure with the best theoretical fit for delaminated Mesa #25 was as follows:

Design

GaAs/In_{0.53}Ga_{0.47}As/GaAs (52nm/80nm/52nm)
100nm Al_{0.3}Ga_{0.7}As
7 pairs: Al_xO_y/Al_{0.3}Ga_{0.7}As (194nm/100nm)
GaAs substrate

Theoretical Best Fit

GaAs/In_{0.53}Ga_{0.47}As/GaAs (55nm/84nm/55nm)
21nm Al_{0.3}Ga_{0.7}As
84nm (Al,Ga)_xO_y
600nm Air
204nm Al_xO_y
105nm (Al,Ga)_xO_y
5 pairs: Al_xO_y/ Al_{0.3}Ga_{0.7}As (204nm/105nm)
GaAs substrate

An interesting observation is the impact of delamination on the reflectivity. Through simulation experiments, it seems that the air gap increases the reflectivity bandwidth of the SBR probably due to the larger index contrast. However, the main result of this simulation is that the layers of Mesa #25 are thicker than the design, and thicker than the layers for mesas #1 and #12 by 16% and 7%, respectively. Therefore, for SBR structure R958, the threshold of delamination is at an oxide thickness of 198nm corresponding to Mesa #12. An oxide thickness of 198nm implies a pre-oxidation AIAs thickness of 220nm (198nm/90%) and therefore a total contraction of 154nm (220nm*10%*7pairs). If the contraction is larger than 154nm, delamination occurs, but if the contraction is less than 154nm, the structure remains stable during oxidation.

As a result, with thinner AIAs layers, delamination problems seem to be reduced. If thinner AIAs layers are accompanied by thinner strained absorber layers, delamination problems could be reduced more substantially than with thinner AIAs layers alone. Therefore the question arises as to whether the absorber strain also varies over the wafer area. The strain from an InGaAs absorber can change with thickness or with composition. Photoluminescence (PL) measurements may help isolate one of these variables. Room temperature PL measurements on nominally unstrained SBR structures with GaAs absorbers grown in the same MBE system, can be used to study thickness variations independent of compositional change. PL measurements taken at different locations of an unoxidized SBR structure (R1000) with a GaAs quantum well of 10 nm nominal thickness, are presented in Figure 2-38. The six curves were taken at six locations across a quarter of a 2-inch wafer as shown. The measurements indicate that the luminescence shifts to longer wavelengths as the measurement location moves from the edge of the wafer (peak = 848nm) to the center of the wafer (peak = 863nm). A shift from 863nm to 848nm corresponds to a 1.7% shift in wavelength.

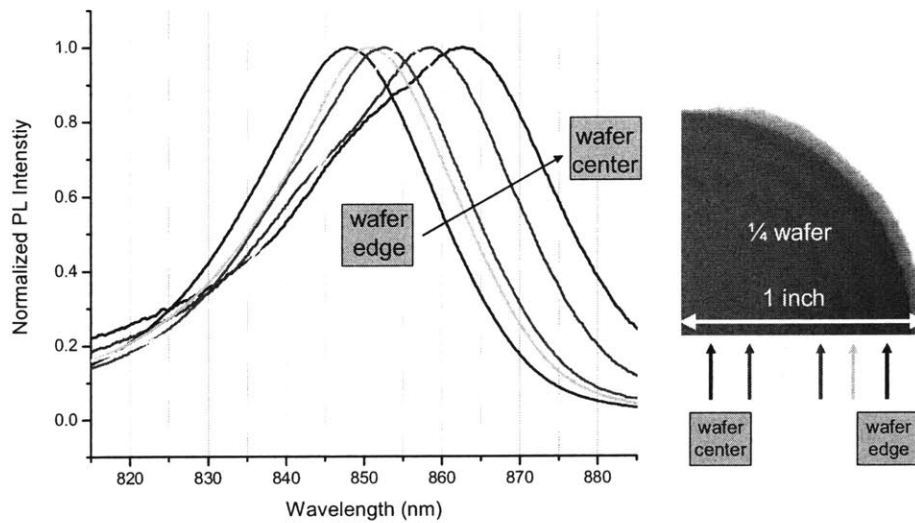


Figure 2-38 Room temperature photoluminescence (PL) measurements on an unoxidized SBR structure (R1000) with a 10nm GaAs quantum well. Results show a variation in PL for regions from the edge of the wafer to the center. Digital photograph of a quarter wafer is shown at the right with measurement locations indicated.

For a GaAs quantum well, a shift in the photoluminescence peak implies a change in the quantum well thickness--with thinner quantum wells located towards the edge of the wafer. The fundamental energy level for an infinite GaAs quantum well was calculated in order to approximate the thickness change. For a nominal thickness of 10nm, the first energy level in the infinite well is 832nm. This number seems reasonable as the energies for an infinite quantum well are higher than those of a finite quantum well. In order to blue-shift the first energy level by 1.7%, or by 14nm to a wavelength of 818nm, the thickness of the quantum well should decrease from 10nm to 8.5nm (a 25% decrease).

Though room temperature photoluminescence measurements were performed on structures with InGaAs absorbers and InP cladding layers, because of the high defect densities due to lattice mismatch, the signal-to-noise ratios were low and the PL spectra were broad, making it difficult to recognize true PL peaks. PL data could not be obtained for SBR structures with InGaAs absorbers and GaAs cladding layers because of the larger number defects in the quantum well than for the structures with InP cladding layers.

Using polynomial fit (9th order was chosen) to smooth the raw photoluminescence data, peaks of the fitted data revealed general PL trends from the edge to the center of the wafer. Figure 2-39, Figure 2-40 and Figure 2-41 present the PL data after fitting and normalization for three different unoxidized structures. All three structures consist of a single (R971, Figure 2-39) or multiple (R981, Figure 2-40 and R1014, Figure 2-41) 10 nm InGaAs

quantum wells. Nominally, the InGaAs composition is $\text{In}_{0.53}\text{Ga}_{0.47}\text{As}$ which is the standard InGaAs composition for lattice matching to InP. In all three cases, a representative measurement from the edge and the center of the wafer are shown, and in all three cases, the PL peak at the center of the wafer occurs at a longer wavelength than the PL peak at the edge of the wafer. PL peaks for measurement locations between the center and the edge of the wafer were at wavelengths between the peak wavelengths plotted. While the PL peaks for R971 agree with those for R1014, the PL peaks for R981 are shifted to longer wavelengths perhaps due to a difference in InGaAs composition.

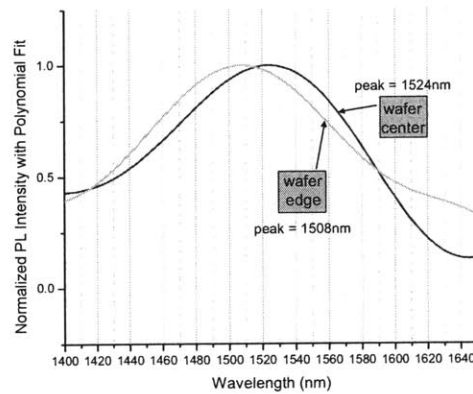


Figure 2-39 Photoluminescence results for unoxidized SBR structure R971 with a single 10nm InGaAs quantum well within InP cladding layers. Raw data was fitted to a 9th order polynomial and normalized. (PL 3/08/2005)

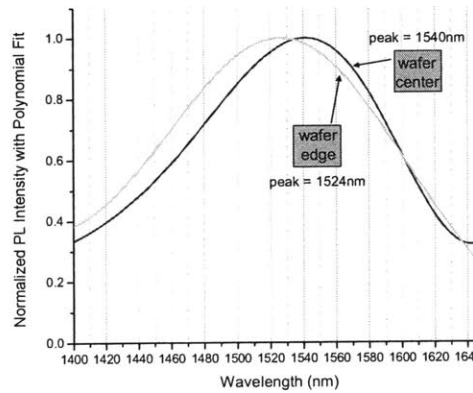


Figure 2-40 Photoluminescence results for unoxidized SBR structure R981 with six 10nm InGaAs quantum wells within InP cladding layers. Raw data was fitted to a 9th order polynomial and normalized. (PL 3/08/2005)

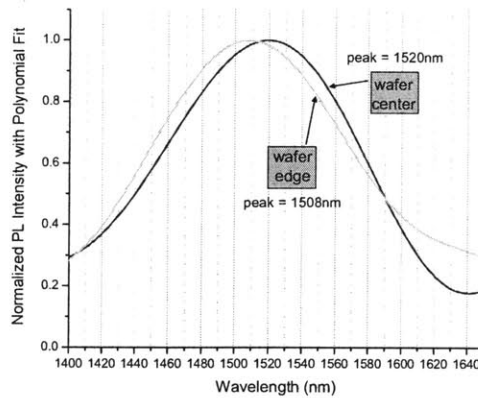


Figure 2-41 Photoluminescence results for unoxidized SBR structure R1014 with six 10nm InGaAs quantum wells within InP cladding layers. Raw data was fitted to a 9th order polynomial and normalized. (PL 3/08/2005)

For each of the structures presented, the wavelength shift is approximately 1% from the edge to the center of the wafer. Calculating the fundamental energy level in a 10nm infinite quantum well of $\text{In}_{0.53}\text{Ga}_{0.47}\text{As}$, yields a peak wavelength of 1457nm. In order to shift this peak by 1% to 1442nm, the InGaAs thickness must decrease from 10nm to 9.6nm. However, assuming that the total layer thickness decreases by 25% to 8.5nm, as in the GaAs case discussed above, to achieve the same 1% wavelength shift, the InGaAs composition must change from $\text{In}_{0.53}\text{Ga}_{0.47}\text{As}$ to $\text{In}_{0.56}\text{Ga}_{0.44}\text{As}$ which would increase the lattice mismatch in the structure. The location of the indium and gallium cells relative to the wafer during MBE growth can affect the flux distributions at the substrate surface. Though the total flux decreases from the center to the edge of the wafer, the gallium/indium ratios may change slightly such that the InGaAs composition can become more indium rich towards the edge of the wafer. The effect of the increase in lattice mismatch due to higher indium concentration may be offset by the lower absorber thickness so that the overall strain does not change significantly. Whether there is a pure thickness variation over the wafer surface, or a thickness variation combined with a compositional change, thinner InGaAs absorber layers occur in parallel with thinner AlAs layers so that delamination effects are lessened for mesas towards the edge of the wafer. Future work would be necessary to isolate the effect of each of these variables even further.

2.5.7 Oxidation rate ramping

The observations discussed above seem to indicate that delamination effects can be reduced by decreasing the strain due to lattice mismatch and decreasing structure contraction during the oxidation of AlAs layers. However, if an SBR structure is designed for a particular laser

system, then the AIAs thickness and the InGaAs absorber thicknesses are functions of the design and are not true variables. Though thinner layers help the stability of the oxidation process, if the AIAs layers become too thin, the reflectivity bandwidth of the SBR may shift away from the desired range. Decreasing the absorber growth temperature did not significantly alleviate delamination problems. Decreasing the oxidation temperature has already been demonstrated for stabilizing the structure during oxidation. However, a decrease in the oxidation temperature slows the oxidation rate significantly.

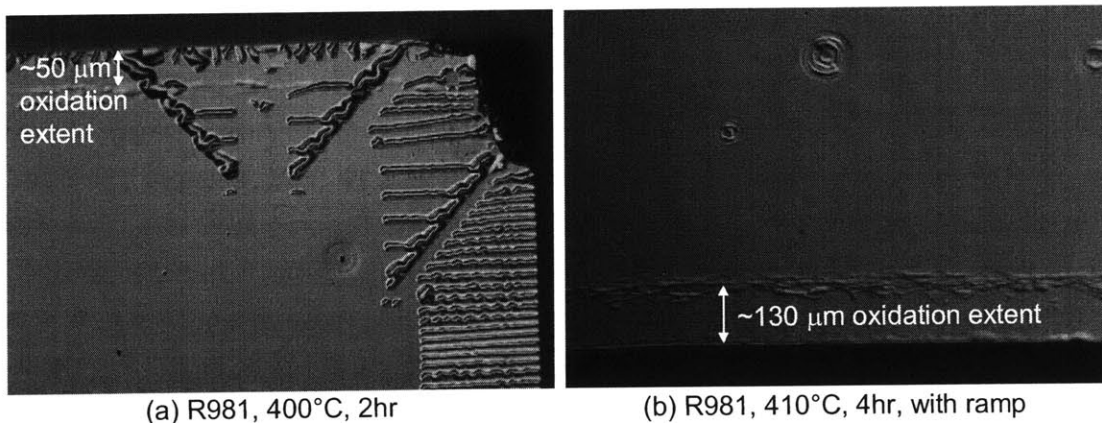


Figure 2-42 Differential interference contrast images showing oxidation results for an SBR structure oxidized (a) for 2 hours at 400°C (b) for 4 hours at 410°C with a temperature ramp before and after oxidation.

The oxidation experiment presented in Figure 2-42(a) shows how decreased absorber growth temperature and decreased oxidation temperature still resulted in delamination. The absorbing layers of SBR structure R981 with multiple quantum wells of InGaAs within InP cladding layers were grown at a growth temperature of 400°C in an attempt to stabilize the structure during oxidation. However, after an oxidation at 410°C for 1 hour (not shown), and at 400°C for 2 hours [Figure 2-42(a)], stripes of delamination were still observed across the sample. Oxidation was performed from the edge of a cleaved sample. With a lower growth temperature, and a lower oxidation temperature, the structure could not be oxidized without delamination.

Further investigations into the oxidation process suggest that the manner in which the oxidation process is initiated has more influence over the stability of the structure during oxidation than all of the variables already discussed. By implementing a temperature ramp before and after the oxidation process, many of the delamination effects were eliminated. Oxidation of the same SBR structure was performed at 410°C for 4 hours but with a temperature ramp before and after the 4 hour period. The ramp consisted of a linear ramp

in temperature beginning at 100°C and ending at 410°C over a duration of 50 minutes. The linear ramp was programmed into the furnace temperature controller. The same ramp was programmed for the opposite direction at the end of the oxidation process. The result of oxidation with this time-temperature profile is shown in Figure 2-42(b). No stripes of delamination were observed. An SEM showing the cross-section of this stabilized SBR is shown in Figure 2-43.

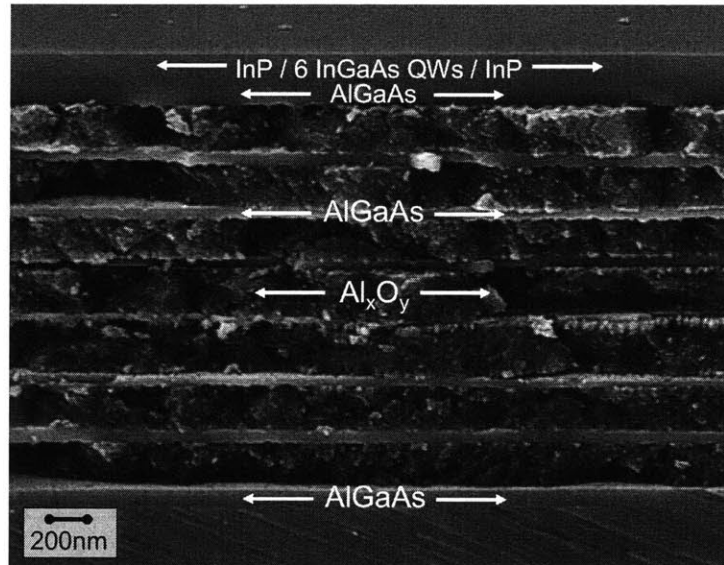


Figure 2-43 SEM image showing cross-section of SBR structure oxidized in Figure 2-42. The structure consists of an absorber with multiple quantum wells of InGaAs within InP cladding layers and a mirror with 7.5 pairs of $\text{Al}_{0.3}\text{Ga}_{0.7}\text{As}$ and Al_xO_y (an extra $\text{Al}_{0.3}\text{Ga}_{0.7}\text{As}$ layer is included at the bottom of the mirror stack as shown).

This same time-temperature profile was implemented for SBR structures which had been considered previously. For example, mesas of R958 located at the center of the wafer oxidized at 410°C for 4.5 hours exhibited stripes of delamination across the mesa area as shown in Figure 2-44(a). In this case, the time-temperature profile corresponded to an abrupt temperature change before and after the oxidation process as the sample is inserted directly into, and removed from the 410°C furnace. By implementing a more gradual change in the oxidation temperature before and after the oxidation process by ramping the temperature between 100°C and 410°C over 50 minutes, the oxidation of mesas from the same area of the wafer no longer exhibited delamination as shown in Figure 2-44(b). Perhaps the abrupt change in the oxidation temperature was thermally shocking the sample and contributing to delamination.

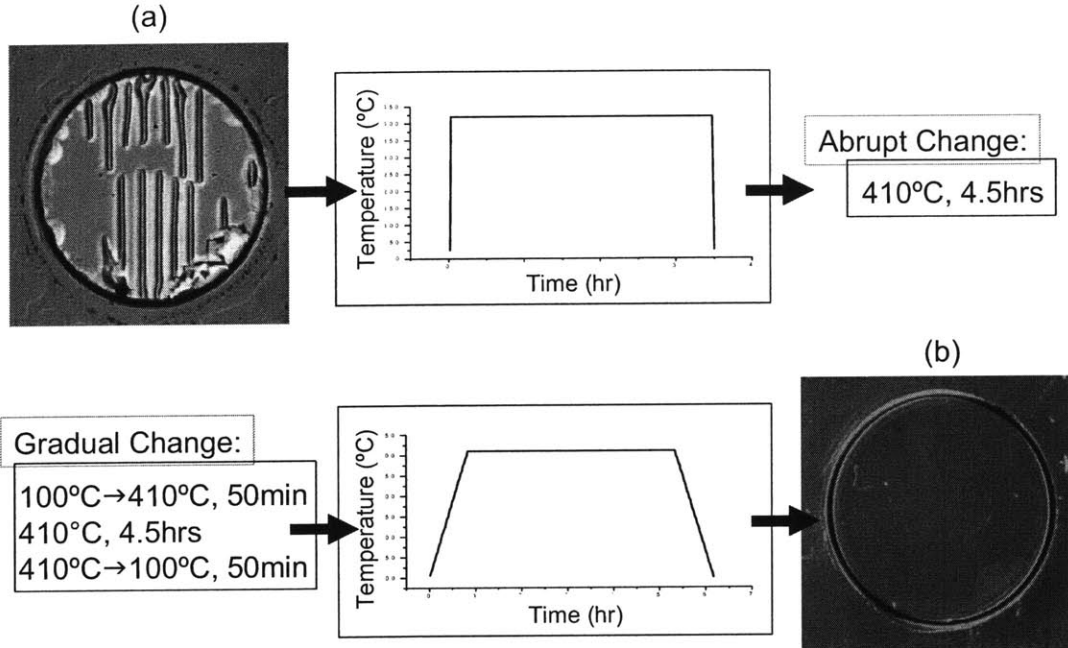


Figure 2-44 Oxidation results illustrating the effect of implementing a temperature ramp before and after oxidation at 410°C for 4.5 hrs. (a) Without temperature ramp (R958, 2/14/2003, 410°C, 4.5hr) (b) With a temperature ramp (R958, 8/14/2003, 410°C, 4.5hr, w/ 50 min ramp)

Closer investigations revealed that the presence of steam during the ramping process influenced the occurrence of delamination. As illustrated in Figure 2-45, two oxidations were performed on mesas of the same SBR structure from similar areas of the wafer. Both oxidations were performed with the same time-temperature profile: 100°C to 410°C over 50 minutes, 410°C for 4.8 hours, 410°C to 100°C over 50 minutes. The first oxidation was implemented with no steam present during the ramp up, but steam present during the 4.8 hour oxidation and during the ramp down. The second oxidation was implemented with steam present during the ramp up and during the 4.8 hour oxidation, but not during the ramp down. Figure 2-45 shows how with no steam present during the ramp up, severe delamination problems occurred. However, when steam was present during the ramp up, the delamination problems were not observed. These results indicate that steam must be present during the initial ramp up to reduce delamination, but is not critical during the ramp down. Thus, a pure temperature shock does not initiate delamination in the absorber. Instead, an *oxidation* shock can initiate delamination. With steam present during the initial ramp up, the oxidation process is slowly initiated with the oxidation rate increasing gradually over the duration of the ramp. With no steam present, the oxidation process abruptly begins with the rate determined by the furnace temperature at which steam was introduced. If this oxidation rate is too fast, delamination occurs.

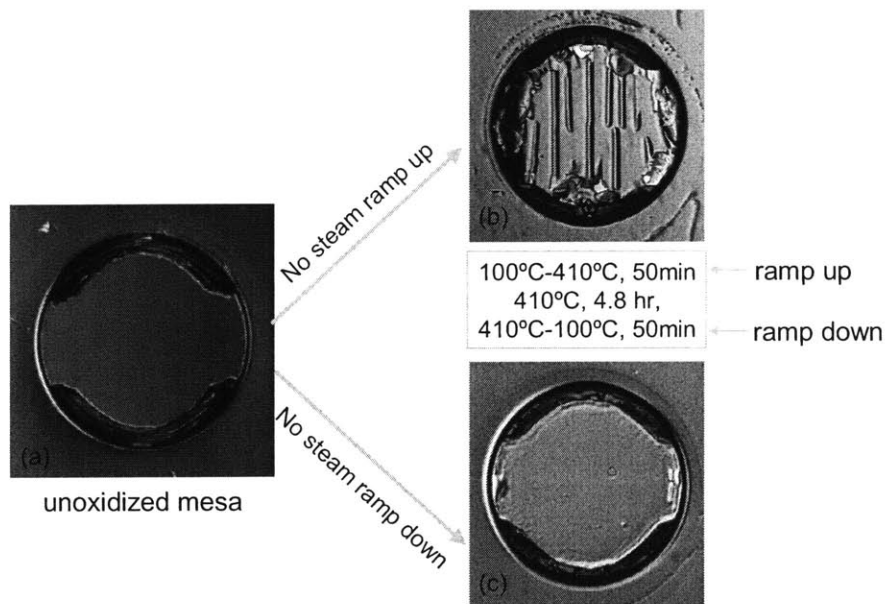


Figure 2-45 Oxidation results illustrating the effect of steam during the ramping process. (a) Unoxidized mesa. (b) Oxidized mesa with no steam present during ramp up (R958 3/10/04) (c) Oxidized mesa with no steam present during ramp down (R958, 3/11/04).

The success of the oxidation ramp at reducing delamination effects was observed for SBR structures with varying absorber thickness, AIAs thickness, and cladding layer composition as shown by the examples presented in Figure 2-46. For all of these structures, delamination effects were observed when oxidations were performed without ramping of the oxidation temperature and hence oxidation rate.

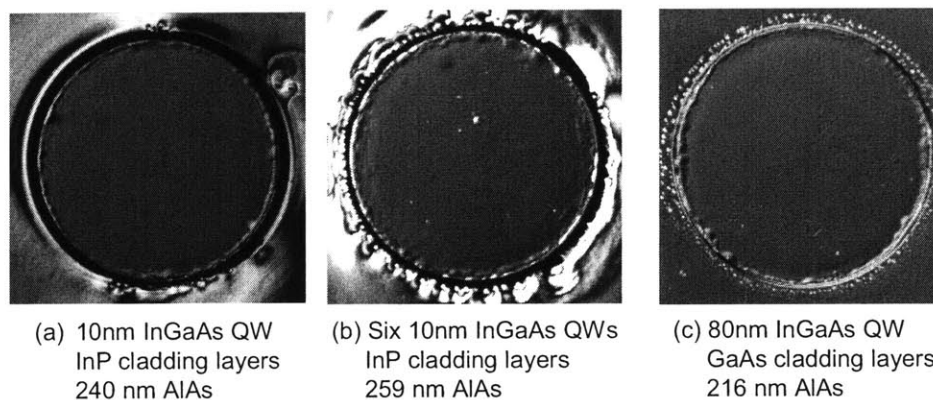


Figure 2-46 DIC images of SBR mesas with oxidation initiated by an oxidation ramp. (a) R971 8/21/03 410°C 6hr with ramp. (b) R981 8/14/03 410°C 4.5hr with ramp. (c) R1015 1/26/04 410°C 5hr with ramp. All ramps were from 100 to 410°C for 50 minutes in the presence of steam.

Indeed, the dependence of delamination effects on oxidation was already noted in Section 2.5.3 where oxidations performed at higher temperatures resulted in greater delamination

effects. By lowering the temperature of the oxidation, even with an abrupt temperature profile, delamination effects could be reduced or eliminated. However, by lowering the overall temperature, the oxidation rates were exponentially reduced making the time necessary for large area oxidations more impractical. The success of the oxidation ramp at reducing delamination shows that oxidations may be performed at higher temperatures as long as the initial oxidation rate is slow.

What is the highest temperature at which the SBR can be oxidized using an oxidation ramp? To explore this question, oxidation of center-wafer mesas from SBR structure R981 was performed at a temperature of 435°C instead of the usual temperature of 410°C. In an attempt to decrease the probability of delamination, two oxidation ramps were sequentially implemented to initiate oxidation: 100 to 400°C in 50 minutes, followed by 400 to 435°C in 60 minutes. The goal of the second oxidation ramp was to increase the oxidation rate even more gradually than in the previous cases so that the structure may remain stable during the more rapid oxidation at 435°C. The result of this oxidation is illustrated in Figure 2-47.

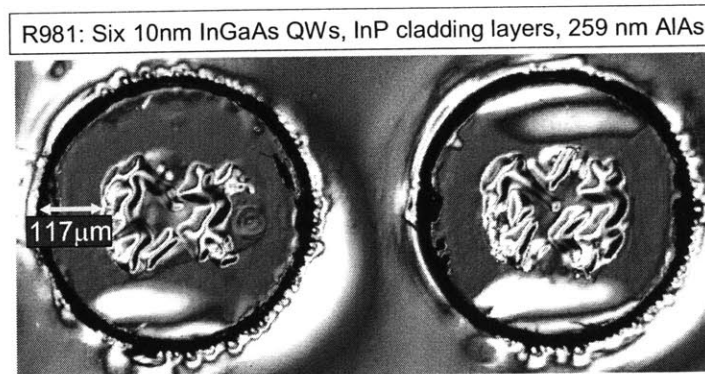


Figure 2-47 DIC images of two oxidized mesas of SBR structure R981 oxidized at 435°C for 2 hours after two ramps: 100-400°C, 50min and 400-435°C, 60min (R981 9/4/03 435°C, 2hr, 2 ramps).

As evident from Figure 2-47, despite the slower oxidation ramp, oxidation of R981 mesas was degraded by delamination effects. Similar delamination was also observed for mesas at the edge of the wafer which were oxidized under the same conditions. The area of the delamination seems to be confined to the center areas of the mesa rather than the full mesa area suggesting that delamination occurred some time after the oxidation process had begun. During the 50 minute ramp between 100 and 400°C, it is unlikely that significant oxidation would have occurred. However, during the 60 minute ramp between 400 and 435°C, faster oxidation rates would lead to appreciable oxidation. To test the reasonableness of this assumption, oxidation rates versus temperature for other SBR

structures are plotted in Figure 2-48. The oxidation rates plotted here are for all 500 μm mesas which were not fully oxidized, including all SBR designs and all oxidation extents. In future work, a more systematic study of the oxidation process would investigate how the oxidation rate varies with the radial extent of oxidation in a circular mesa, AIAs thickness, and mesa geometry. The oxidation rates were fitted to both linear and exponential curves yielding the formulas presented in Figure 2-48. Though the linear curve yields a better fit according to its R^2 value, the exponential fit is more physically plausible. Please note that oxidation rates for a length scale of 100's of μm have not been reported in the literature to date.

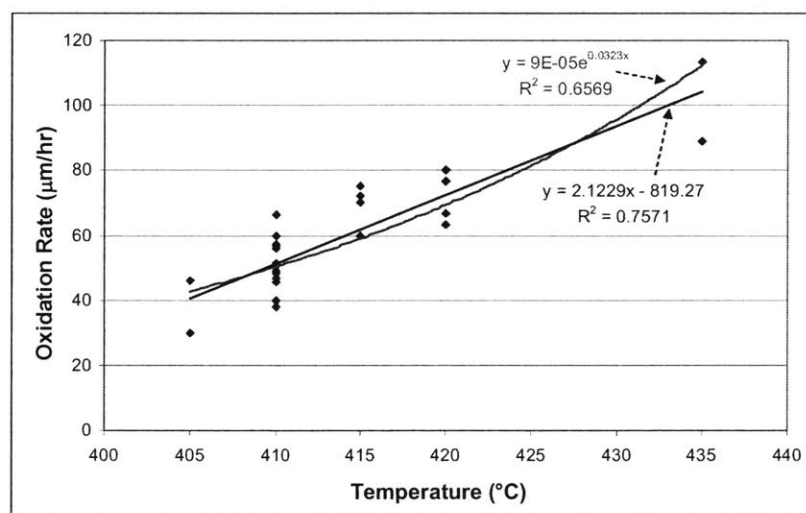


Figure 2-48 Average oxidation rate versus temperature. Oxidation rates were averaged over all SBR structures for 500 μm mesas that were not completely oxidized. An exponential and a linear best-fit was calculated as shown. Radial dependence and AIAs thickness dependence of the oxidation rate was not considered.

According to the calculated oxidation extent presented in Figure 2-49, after the sequence of two ramps, the extent of oxidation should be approximately 50 μm from the edge of the mesa. The oxidation result presented in Figure 2-47 shows that the delamination effects begin at approximately 117 μm from the edge of the mesa which is greater than the estimated oxidation distance after the ramp sequence. Though the estimated distance predicted in Figure 2-49 is subject to a number of variables that were not considered, it seems that the delamination effects observed in this case occur after oxidation has been initiated and after the sample reaches a temperature of 435°C.

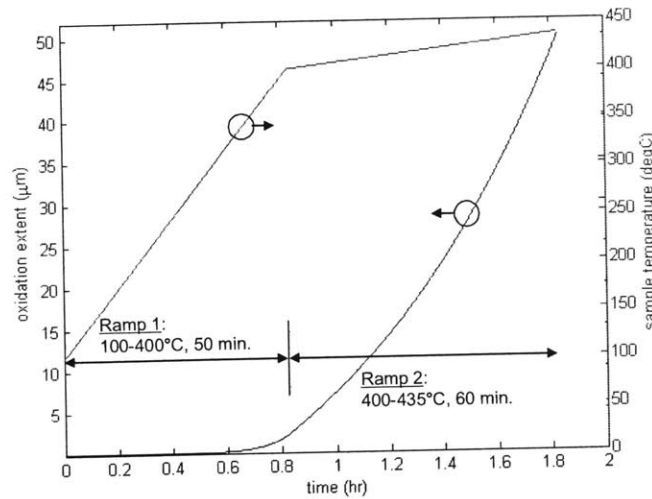


Figure 2-49 Estimate of radial extent of oxidation front for the two oxidation ramps implemented in Figure 2-47 assuming an exponential oxidation rate versus temperature characteristic.

Further experiments were not performed to assess whether similar delamination results would be observed for other SBR structures oxidized with the identical oxidation profile. However, the fact that the slow oxidation ramp did not eliminate delamination for higher oxidation temperatures provides further evidence that overall delamination effects are temperature dependent--not only during the initial temperature ramp, but for the full duration of the oxidation.

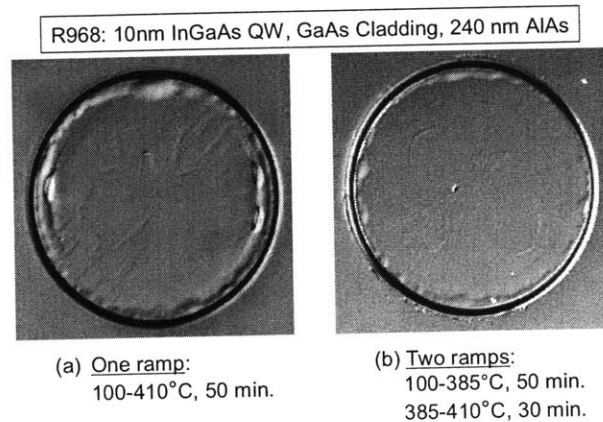


Figure 2-50 DIC images showing the results of oxidation of SBR R968 with (a) one ramp (R968 6/7/04 410C 5hr, 50 min. ramp) and (b) two ramps (R968 6/11/04 sample 4, 410C, 4.5hr, 2 ramps).

Additional investigations were conducted to explore the effect of the ramping speed on delamination effects. With the implementation of a 50 minute temperature ramp, slight delamination was still observed at the edges of the mesas on certain samples [Figure

2-50(a)]. To address this delamination, the effects of a slower temperature ramp were explored.

As observed in Figure 2-50, the delamination at the edges of mesa (a) were eliminated in mesa (b) by adding a second temperature ramp which slowed the initiation of the oxidation process even further. The effects of adding this extra oxidation ramp are even more dramatic when the SBR strain is much greater. For example, when an SBR structure with a 100nm InGaAs absorber was oxidized using the same oxidation profiles, the delamination effects were quite different.

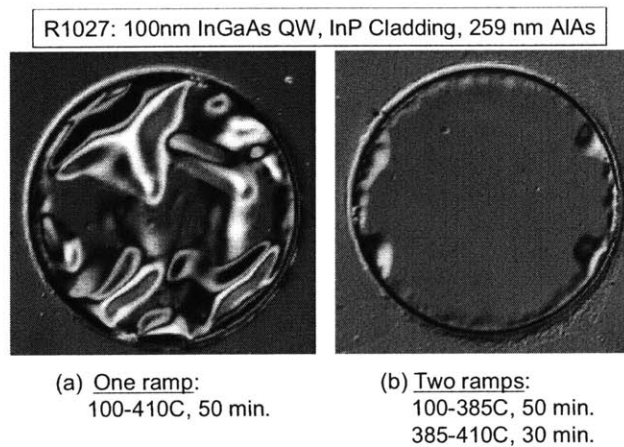


Figure 2-51 DIC images showing the results of oxidation of SBR R1027 with (a) one ramp (R1027 6/7/04 sample 1 410C 5hr w/ 50min ramp) and (b) two ramps (R1027 6/10/04 sample 3 410C 4.5hr w/ 2 ramps).

With a single temperature ramp from 100 to 410°C, followed by a 5 hour oxidation, Figure 2-51(a) shows how severe delamination of R1027 occurred. However, slowing the temperature ramp by inserting a second more gradual ramp, the delamination effects were dramatically reduced though some edge delamination is still observed. Please note that for these experiments, the control variable is the ramping temperature at which oxidation occurs. The actual oxidation rate is unknown but is inferred by Figure 2-48.

Further future investigations are necessary to determine the exact relationships between delamination effects and the oxidation rate profile. These initial results show how slowing the oxidation rate by employing a temperature ramp at the beginning of the oxidation process allows SBR mesas to be oxidized at higher temperatures without delamination. However, the highest temperature at which oxidation can occur still seems to be limited by other delamination effects which seem to be independent of the initial oxidation temperature ramp.

Because the oxidation process is extremely sensitive to changes in temperature, great care must be taken to ensure that the furnace temperature controller does not allow a temperature overshoot as the linear ramp is executed. Future work would involve interfacing the temperature controller to a computer so that the temperature/time profile can be closely monitored. For the oxidations presented, such monitoring was not implemented. With such a monitoring system, delamination effects and oxidation rates can be studied with greater accuracy.

2.5.8 Unoxidized structure stability

Another experimental observation regarding strained SBR structures that has not been mentioned is their instability in the unoxidized state. Figure 2-52 shows four different unoxidized mesas which had been wet etched at least 6 months previously. In all four cases, deterioration of the mesa structure is observed at the mesa edges. The pattern of this deterioration seems to be symmetric, and in the most dramatic case, shown in Figure 2-52(c), the deterioration progresses at definite angles despite the circular geometry of the mesa. Another interesting observation is the difference in the extents of the deterioration effect for mesas at the center of the wafer versus the mesas at the edge of the wafer as shown in Figure 2-52(a) and (b). For mesas at the center of the wafer, the deterioration has progressed further than for mesas at the edge.

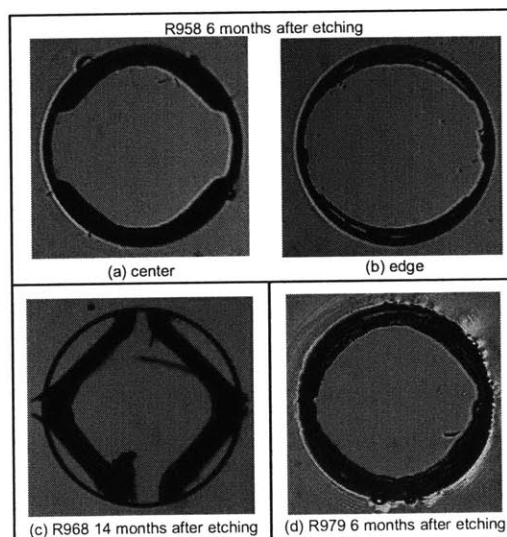


Figure 2-52 DIC images of unoxidized mesas showing how deterioration occurs after wet etching. (a) A mesa from the center of the wafer from SBR R958. (b) A mesa from the edge of the wafer from SBR R958. (c) A mesa from SBR R968. (d) A mesa from SBR R979.

Examining the edge of the mesa one day after wet etching reveals that oxidation of the AlAs layers of the SBR structure begins immediately at room temperature. SEM images shown in Figure 2-53, show how one day after wet etching, exposed AlAs layers have oxidized due to exposure to air. However, the observed oxidation is accompanied by breakage of the surrounding $\text{Al}_{0.3}\text{Ga}_{0.7}\text{As}$ and absorber layers. SEM images of mesas similar to those shown in Figure 2-52 revealed that the deterioration observed at the edges of the mesa after months of air exposure is a more dramatic version of the slight deterioration observed in Figure 2-53. At the edges of the mesa, the layered structure collapses due to atmospheric oxidation of the AlAs.

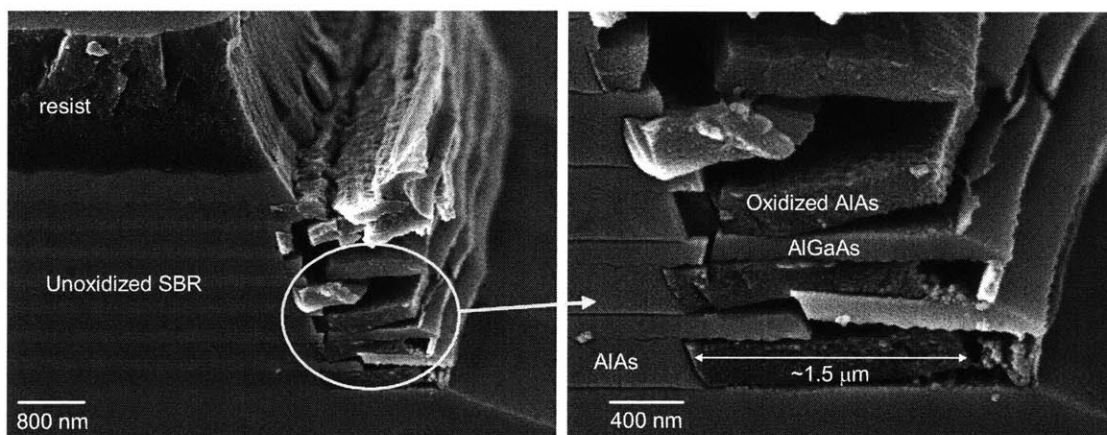


Figure 2-53 SEM images showing oxidation of the AlAs layers at a mesa edge one day after wet etching (R979 unoxidized).

Dallesasse, *et al.* also observed this atmospheric deterioration, or “hydrolyzation” of AlAs, and found that by oxidizing the AlAs layers at elevated temperatures, the quality of the oxidized material had greatly improved [47]. Thus, this same deterioration is not observed for samples that had been oxidized using the steam process described in Section 2.3. Perhaps the strain in the structure also accelerates the deterioration because the edges of the mesas may crack more easily in the presence of a strained absorber.

Even in the presence of deterioration of the unoxidized mesa in atmosphere, stable oxidation of the mesa can be accomplished at elevated temperatures. One example was presented in Figure 2-45 where oxidation of the mesa was completed despite the hydrolyzation at the edges of the mesa as observed in the unoxidized structure. However, to prevent deterioration of the mesa, elevated temperature oxidation should be performed soon after wet chemical etching of the structure.

2.6 SBRs for Visible Wavelength Lasers

2.6.1 Design motivation

SBR designs were also investigated for the Ti:Sapphire laser system with a center wavelength of 800 nm. As illustrated in Figure 2-54, the gain bandwidth of the Ti:Sapphire laser spans from the infrared at approximately 1100 nm to the visible at approximately 600 nm. Because $\text{Al}_{0.3}\text{Ga}_{0.7}\text{As}$ begins absorbing at an approximate wavelength of 680 nm, it is not appropriate as the high index layer in the SBR's broadband mirror stack. $\text{In}_{0.15}\text{Ga}_{0.15}\text{Al}_{0.35}\text{P}$, with a bandgap at 536 nm and a refractive index of ~ 3.1 , is lattice-matched to GaAs and has a lower absorption wavelength than AlGaAs alloys. As a result, the $\text{In}_{0.15}\text{Ga}_{0.15}\text{Al}_{0.35}\text{P}/\text{Al}_x\text{O}_y$ broadband mirror discussed in Section 2.4.4 is appropriate for the Ti:Sapphire laser system. As in all SBR structures, the mirror layers are designed with a thickness of $\lambda/(4n)$ in each material. The absorber layer in the designed SBRs was chosen as GaAs which has an absorption wavelength at approximately 870 nm. The cladding layers were chosen as $\text{In}_{0.15}\text{Ga}_{0.15}\text{Al}_{0.35}\text{P}$. With an $\text{In}_{0.15}\text{Ga}_{0.15}\text{Al}_{0.35}\text{P}/\text{GaAs}$ -based layered structure, this SBR design is nominally unstrained.

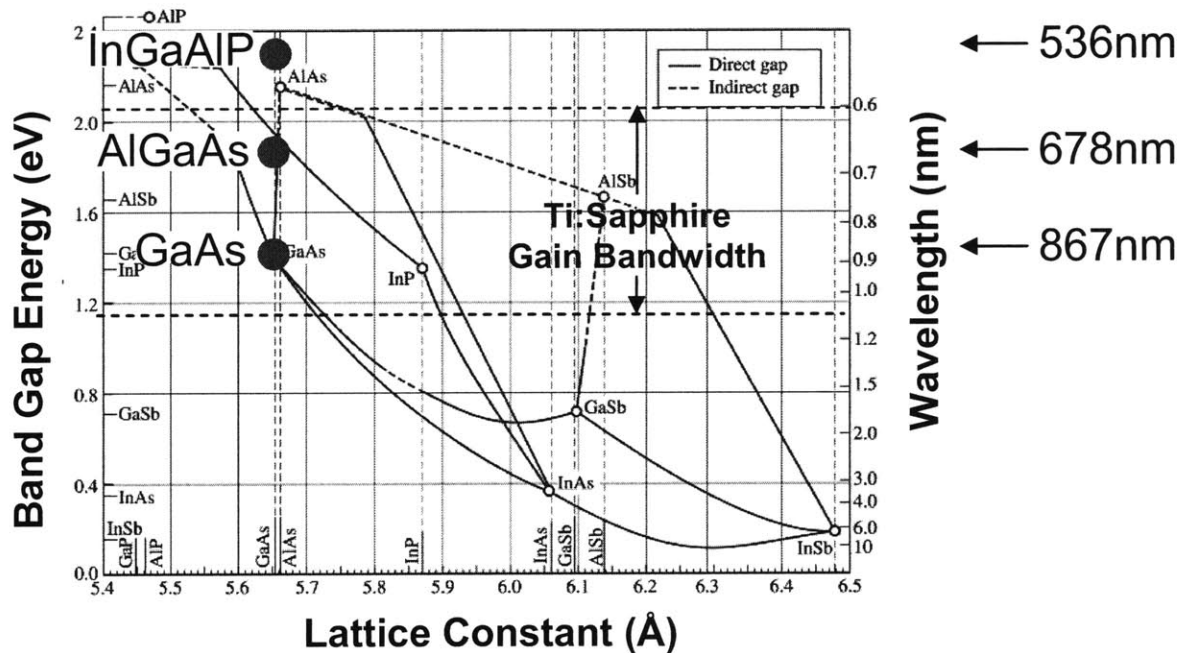


Figure 2-54 Band gap energy versus lattice constant diagram indicating the band gap associated with each of the layers which compose the SBR for the Ti:Sapphire laser.

2.6.2 Observations: Temperature dependence of oxidation

With a nominally unstrained SBR structure, delamination problems were not observed upon oxidation. As a result, this SBR structure could be oxidized at higher temperatures without delamination. The oxidation ramp discussed in Section 2.5.7 was implemented for all of the oxidations of the SBRs for the Ti:Sapphire laser.

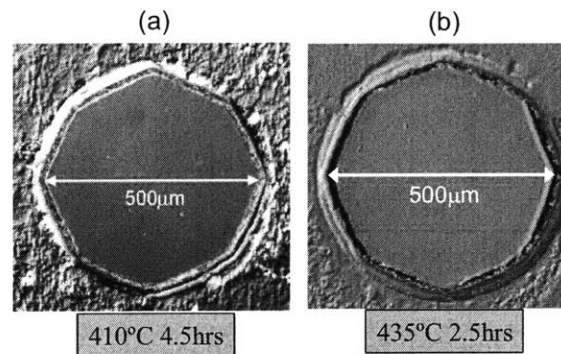


Figure 2-55 DIC images showing oxidation results at (a) 410°C (R1000 sample 13 10/23/03 410°C 4.5hr w/ 50min ramp) and (b) 435°C (R1000 sample 22 3/1/2004 435°C 2.5hr w/ 50 min. ramp) for an SBR structure for the Ti:Sapphire laser.

Figure 2-55 shows the results of two oxidations performed at two different temperatures. The images show how at both 410°C and 435°C, the SBR structure could be completely oxidized without any noticeable delamination. By increasing the temperature to 435°C, the necessary oxidation time decreased by two hours, demonstrating the sensitivity of the oxidation rate to temperature. An SEM image of the SBR cross-section was presented in Figure 2-19(b).

Oxidations of strained SBR structures for the infrared laser systems could not be successfully accomplished at a temperature of 435°C even in the presence of a slower oxidation ramp. Therefore these nominally unstrained InGaAlP-containing SBR structures seem to be more robust during oxidation. In addition to the lower strain, these SBR structures for the Ti:Sapphire laser have thinner AIAs layers due to the shorter wavelength of the design. SBR designs for lasers at 1550nm required AIAs layers with a thickness of 259 nm. SBR designs for lasers at 1300nm required AIAs layers with a thickness of 216 nm. On the other hand, in the above SBR design for the Ti:Sapphire laser at 800nm, the required AIAs thickness was only 150nm. Thus, the volume contraction experienced for the shorter wavelength SBR design would be significantly less. As demonstrated in Section 2.5, the combined effect of lower strain and lower volume contraction results in a more stable structure upon oxidation.

2.7 Optical Characterization of Structures

2.7.1 Reflectivity measurements

With a properly engineered layered structure and a controlled large scale oxidation, SBR designs have been fabricated with broadband reflectivities spanning from 750 to 1850 nm. Figure 2-56 presents reflectivity measurements of the SBRs for three different laser systems: Ti:Sapphire (800 nm), Cr:Forsterite (1300 nm), and Er:Bi₂O₃ (1550 nm). Theoretical mirror reflectivities are greater than 99% over bandwidths of 294 nm, 466 nm, and 563 nm respectively. The Ti:Sapphire SBR reflectivity was measured with a microspectrophotometer while reflectivities for the Cr:Forsterite and Er:Bi₂O₃ SBRs were measured with a Fourier Transform Infrared (FTIR) spectrometer. All measurements reveal absorption losses originating from the SBR's absorber layer. Absorption loss results in a decrease in the reflectivity of the SBR for decreasing wavelength.

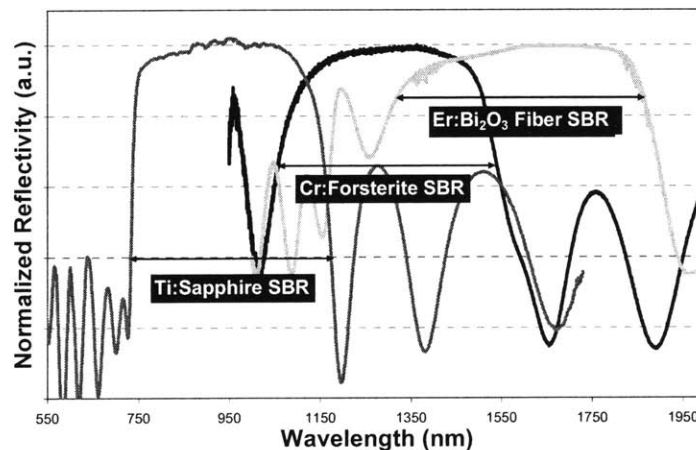


Figure 2-56 Reflectivity measurements of SBR structures fabricated for three different laser systems: Ti:Sapphire, Cr:Forsterite, and Er:Bi₂O₃ fiber laser with theoretical mirror reflectivity > 99% over 294nm, 466nm, and 563nm respectively. All measurements reveal losses due to SBR absorption.

Reflectivity measurements have previously been presented for a number of fabricated SBR structures. As demonstrated in Section 2.5.6, the reflectivity bandwidth changes depending on the sample's location on the wafer. As another example of this effect, reflectivity measurements of a number of oxidized SBR samples from structure R1000 are shown in Figure 2-57. Figure 2-57 shows how the reflectivity shifts to shorter wavelengths as the sample location moves from the center to the edge of the wafer.

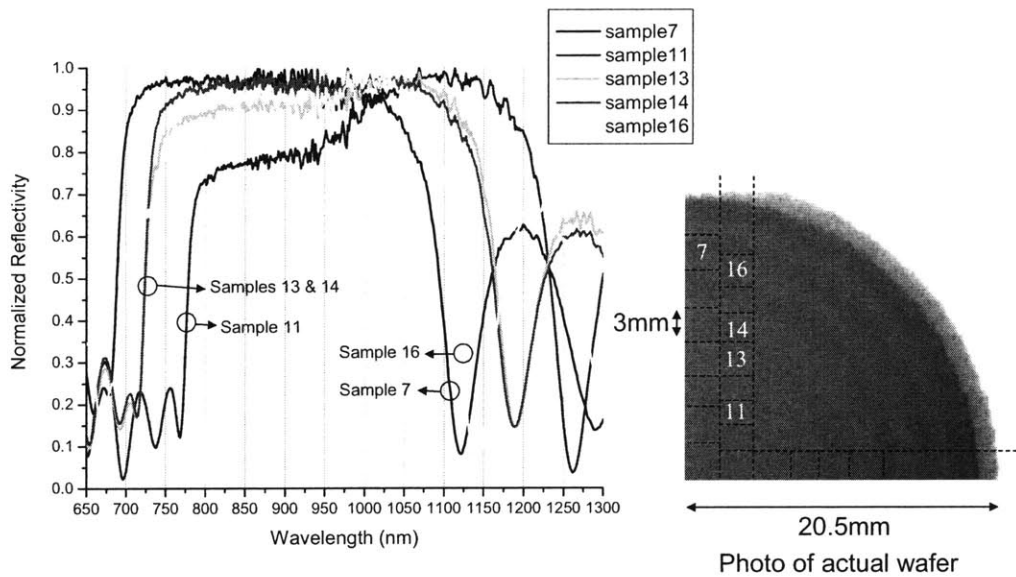


Figure 2-57 Microspectrophotometer measurements of five different oxidized samples of R1000 with sample location shown on a photograph of a 1/4 wafer. Reflectivity dip for sample 11's reflectivity curve is an artifact of the measurement due to two different spectrometers used for the lower and upper wavelength ranges.

2.7.2 Laser system testing

Many of the samples discussed in Sections 2.5 and 2.6 were used in a number of different laser systems. The results of particular tests with each sample have been discussed in [11] and will not be discussed here. Instead, a summary of the results will be presented with some general comments.

Figure 2-58 presents the results associated with using four different SBR designs in four different laser systems. The plots in Figure 2-58 show the SBR-modelocked power spectra of the (a) Ti:Sapphire ($\lambda=800\text{nm}$), (b) Cr:Forsterite ($\lambda=1300\text{nm}$), (c) Cr:YAG ($\lambda=1550\text{nm}$), and (d) Er:Bi₂O₃ fiber ($\lambda=1550\text{nm}$) lasers with their respective SBR reflectivities. In Figure 2-58(a), reflectivities of two representative SBRs from the same wafer are shown. Thickness variation across the wafer resulted in center wavelength differences between SBRs. Femtosecond pulses were produced by using the broadband SBRs in each of the laser systems. Two types of measurements were performed to measure the pulse widths emitted from the different laser systems. The Fourier limit (a measurement of the pulse width independent of its phase) implies pulse widths of 15-30 fs for the Ti:Sapphire, and 20 fs for the Cr:Forsterite laser. Autocorrelation measurements (a pulse width measurement which accounts for the phase) reveal pulse widths of 32 fs and 155 fs for the Cr:YAG and Er:Bi₂O₃ lasers respectively. Both types of measurements were not performed for all laser

systems. All of the SBRs tested produced self-started modelocking which could be sustained for several days without observable absorber degradation, illustrating the SBR's durability and high damage threshold.

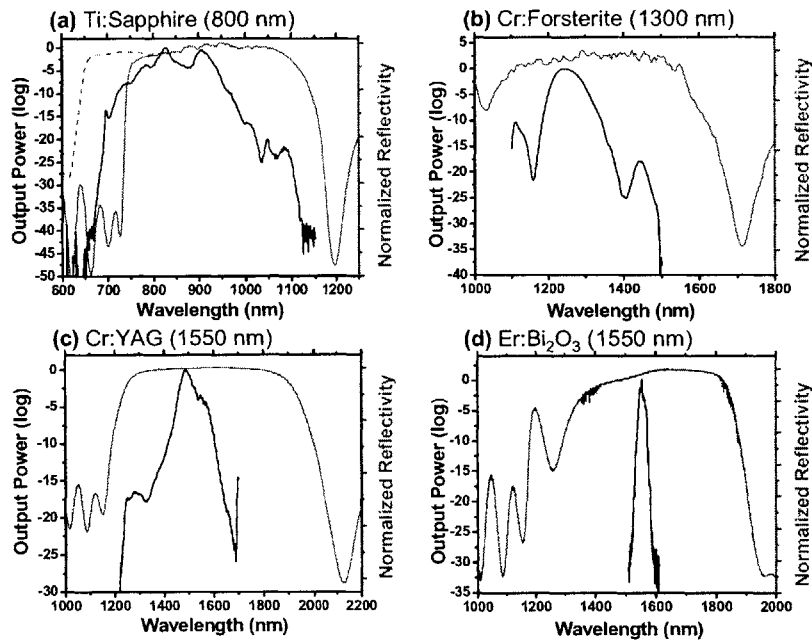


Figure 2-58 SBR-modelocked spectra of (a) Ti:Sapphire (SBR R1000), (b) Cr:Forsterite (SBR R946), (c) Cr:YAG (SBR R921), and (d) Er:Bi₂O₃ (SBR R981) lasers with respective SBR reflectivities. In (a), reflectivities of two SBRs from the same wafer are shown. One measurement (dotted line) was limited in range by the spectrometer used [48].

With the non-uniformity between SBR samples, it is important that the reflectivity of the SBR overlaps well with the gain spectrum of the laser system. For example, the five different samples whose reflectivity curves were shown in Figure 2-57, were tested in the Ti:Sapphire laser system to produce the power spectra shown in Figure 2-59. The broadest spectrum [also shown in Figure 2-58(a)], was produced by sample #7. Sample #16 produced a similar result. The spectra produced using the other three samples were not as broad due to the limited SBR reflectivity at the shorter wavelengths. For example, sample #11 is highly reflective starting at $\sim 800\text{nm}$. However, because the gain-bandwidth of the Ti:Sapphire laser system extends below 800nm , this wavelength range is not reflected by the SBR and therefore does not contribute to the power output. The pulses generated using this sample are therefore longer in duration than the pulses generated using samples #7 or #16.

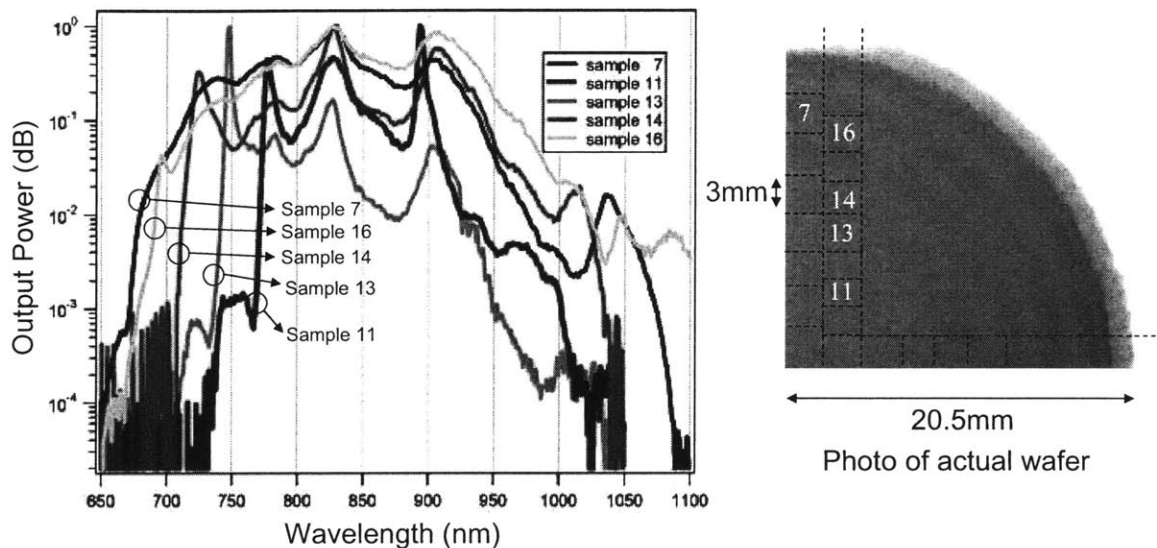


Figure 2-59 Output power spectra from the Ti:Sapphire laser system for five different samples of SBR structure R1000 with sample location on the wafer as shown. Measurements performed by Dr. Richard Ell in the Ultra-fast Optics Group at MIT.

If no delamination is present in a SBR sample, the sample can be used for long periods of time without degradation as mentioned. However, samples with areas of delamination are not appropriate for use in a laser system and are often destroyed if used. For example, the oxidized sample of R958 illustrated in Figure 2-32, was tested in the Cr:Forsterite laser system. Mesas with delaminated areas were destroyed almost instantly when irradiated with the laser spot. This destruction was most likely due to heating of the air pockets formed by the delaminated semiconductor material. When the air pockets heat up, the air expands, forcing the buckled semiconductor layers to burst.

Other measurements of SBR characteristics have been performed by members of the Ultra-Fast Optics group at MIT [48] and are described in more detail in [11]. SBRs designed for the Cr:YAG laser (1550 nm) have a saturation fluence of $\sim 10 \mu\text{J}/\text{cm}^2$, nonsaturable loss of $< 0.8\%$, and modulation depth of 0.3%. SBRs for the Er:Bi₂O₃ laser have a saturation fluence of $\sim 10 \mu\text{J}/\text{cm}^2$ and modulation depth of 3%. Ti:Sapphire SBRs have a nonsaturable loss of $< 2\%$. Pump-probe measurements were performed to measure the recovery times associated with SBRs designed for 1550 nm as discussed by Gopinath in [11].

2.7.3 Photoluminescence measurements

Room temperature photoluminescence (PL) measurements were performed to measure the band gap or quantum well energies associated with SBR absorbers. The results of several

of these measurements were already discussed in Section 2.5.6 where unoxidized SBR structures were analyzed. The photoluminescence spectra from unstrained GaAs absorbers and strained InGaAs absorbers were measured to extract information about absorber thickness variations over the area of the wafer. For unstrained GaAs absorbers, measurements showed that the PL wavelength shifted to shorter wavelengths towards the edge of the wafer implying thinner absorbers. For strained InGaAs absorbers, though the PL data suffered from a low signal-to-noise ratio, a similar trend was observed.

PL measurements were also used to study the effect of oxidation on the absorber characteristics. For strained SBRs, room temperature PL signals for oxidized mesas were too weak to extract information on absorber characteristics. Some results are presented from low temperature PL measurements of strained SBRs. For nominally unstrained SBRs, PL measurements were performed for both unoxidized and oxidized structures.

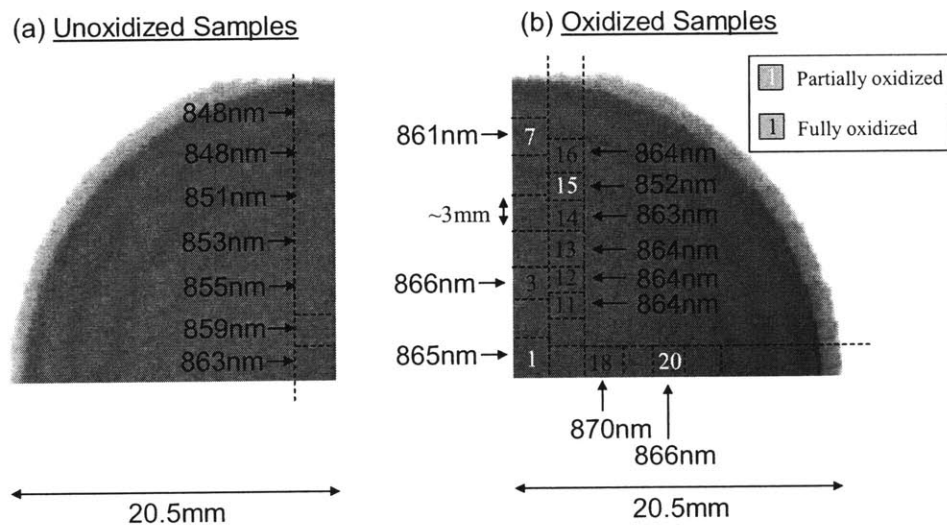


Figure 2-60 Digital photographs of 1/4 wafers of SBR structure R1000 showing a summary of the room temperature photoluminescence measurements on both oxidized and unoxidized samples.

Figure 2-60 summarizes the PL measurements performed on unoxidized samples of SBR structure R1000. PL results showing the PL peak versus wavelength for the unoxidized samples of R1000 were presented in Figure 2-38. These measurements on the unoxidized structure seem to indicate that the absorber thickness is decreasing as the measurement location moves to the edge of the wafer. One question is whether the reflectivity of the unoxidized SBR structure affects the position of the PL peak? Figure 2-61 plots the PL peaks and reflectivities associated with two different locations of the unoxidized SBR structure R1000. The PL peak for location (a) overlaps with a null in the reflectivity of the

structure and would therefore decrease the total PL intensity measured. The slight asymmetry of the PL peak at location (a) may be due to modulation by the reflectivity characteristic. The peaks in the reflectivity may increase the off-peak PL intensities giving the PL curve its asymmetry on the short wavelength side. At location (b), the PL peak overlaps with a peak in the reflectivity which only enhances the total peak PL intensity. Though it seems that reflectivity of the unoxidized structure may modulate the total PL intensity, it does not seem that this modulation is enough to move the wavelength at which the PL peak occurs.

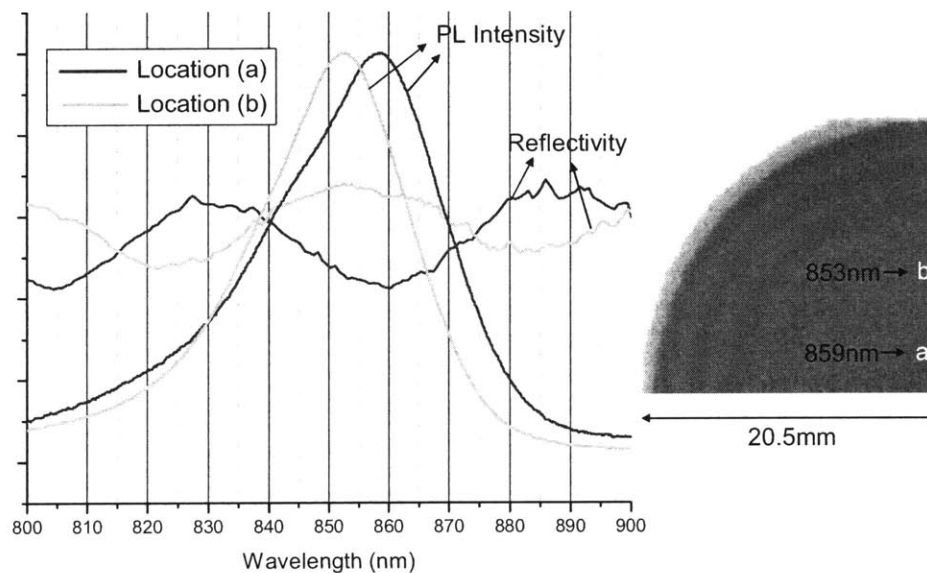


Figure 2-61 PL intensities and reflectivity measurements from two different locations of unoxidized SBR structure R1000.

For the oxidized structure, modulation of the PL intensity by the SBR’s reflectivity is not a concern because the PL peak is well within the high reflectivity bandwidth of the oxidized mirror. However, as evident from Figure 2-60, upon oxidation, the peak of the PL intensity experiences a shift for similar locations on the wafer. While the PL peak in the unoxidized structure shows a definite trend towards shorter wavelengths as the measurement location moves to the edge of the wafer, such a trend does not exist for measurements of the oxidized structure. For the oxidized structure, the PL intensity is close to uniform over the wafer area.

A similar set of room temperature PL measurements were performed on unoxidized and oxidized samples of SBR structure R1020. The main difference between SBR structures R1000 and R1020 is the quantum well thickness which is nominally 10nm and 20nm

respectively for each of the structures. The results of PL measurements on R1020 are presented in Figure 2-62. For the unoxidized structure, a definite trend in the PL is not observed as it was for the case of R1000. At the same time, for the oxidized structure, the uniformity in the PL peak that was present for R1000 is no longer present for R1020.

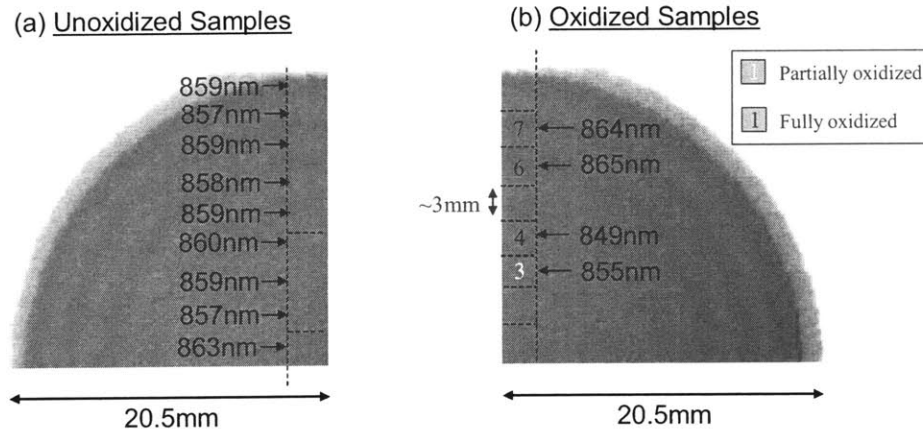


Figure 2-62 Digital photographs of 1/4 wafers representing SBR structure R1020 summarizing photoluminescence measurements on both oxidized and unoxidized samples.

The changes in PL peak wavelength observed for the 10nm quantum well structure and the thicker 20 nm quantum well structure may be explained by Figure 2-63 which shows a plot of the wavelength of the quantum well ground state versus the GaAs QW thickness. As evident from the plot, as the thickness of the QW increases, the wavelength associated with the ground state energy, increases. However, for thin quantum wells, the shift in wavelength is much more sensitive to QW thickness than for thicker quantum wells. As the quantum well becomes thicker, the QW acts more like a bulk semiconductor so that the fundamental energy approaches the band gap of the material. Thus for unoxidized samples of R1000, a shift in the thickness of the QW from the center to the edge of the wafer would imply a greater PL shift than for R1020. Indeed no appreciable shift is observed for R1020 though x-ray measurements indicate that layers become thinner towards the edge of the wafer by approximately 12%. Figure 2-63 shows that between 20 and 25 nm, the PL shift is less than 5nm which is within the error margin of the PL measurement. A 20nm finite quantum well may be approximated by a thicker infinite quantum well. Therefore, the quantum well for R1020 may more closely resemble the 25nm infinite quantum well.

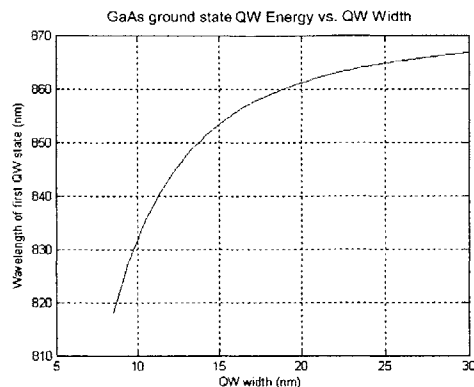


Figure 2-63 Calculation of the ground state wavelength for an infinite GaAs quantum well (QW) versus QW width.

PL shifts between the unoxidized and oxidized structures may be due to a number of factors. Liverini, *et al.* was able to shift the PL associated with a InGaAsN quantum well absorber by subjecting the sample to rapid thermal annealing after MBE growth [49]. With rapid thermal annealing, many of the material defects in the quantum well can be removed while improving the crystallinity of the quantum well through bond structure alterations [50]. It is possible that through oxidation, the bonding structure of the quantum well changes such that a shift in the PL is observed.

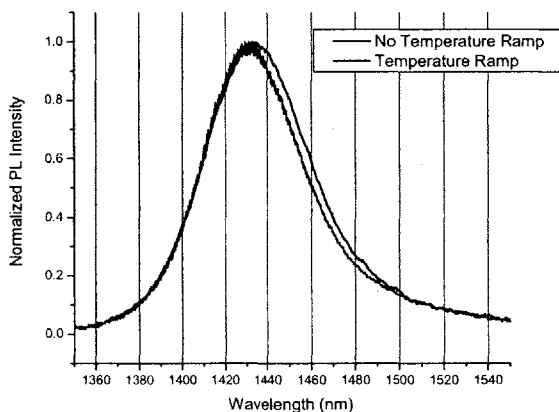


Figure 2-64 Low temperature photoluminescence measurements on an unoxidized sample of R979 before and after a pure temperature ramp without the presence of steam. Temperature profile: 100-400°C, 50 min; 400-435°C, 60min; 435°C, 2 hr; 435-100°C, 60min.

Temperature cycling during the SBR oxidation process may also affect diffusion of elements into or out of the quantum well. However, PL measurements on a sample of unoxidized SBR R979 taken at low temperature (10K) before and after implementation of a temperature cycle indicates that the PL did not shift due to temperature cycling alone. As shown in

Figure 2-64, the sample was subjected to a temperature cycle in the presence of nitrogen flow but no steam. The temperature profile was the same profile that would have been used to oxidize the sample if steam were present: 100-400°C, 50 min; 400-435°C, 60min; 435°C, 2 hr; 435-100°C, 60min. Figure 2-64 shows that the sample's quantum well did not experience a PL shift after this temperature cycling.

When this same sample was oxidized for 5 hours at 410°C, the photoluminescence (T=10K) was measured again as shown in Figure 2-65. However after oxidation, the PL peak shifted by 50 nm--from 1430nm before oxidation, to 1480nm after oxidation. This result seems to indicate that it is the oxidation process that is contributing to the shift in PL.

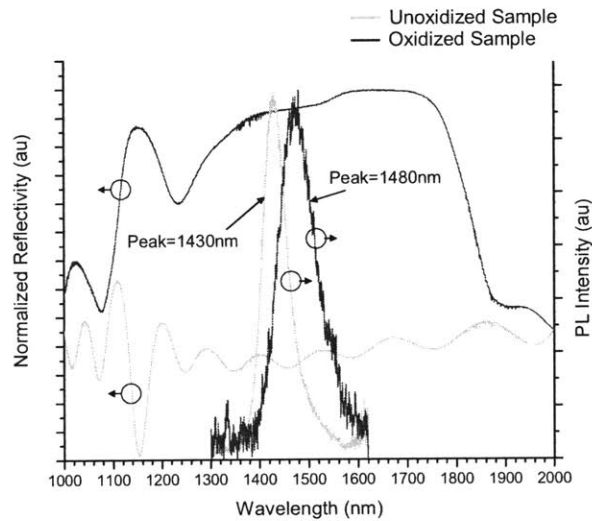


Figure 2-65 Low temperature PL intensity (T=10K) and FTIR measurement for an oxidized and unoxidized sample of SBR structure R979.

A number of groups have observed structural changes in a semiconductor material due to oxidation of a neighboring AlAs layer. Mathis, *et al.* observed strain relaxation of an InGaAs layer due to oxidation of an adjoining AlAs layer. Mathis, *et al.* proposes that during the oxidation process, misfit dislocations are removed from the interface between AlAs and the strained InGaAs layer [51]. With the misfit dislocations removed, threading dislocations can move through the film during oxidation allowing the InGaAs film to relax. The relaxation of InGaAs through lateral oxidation of a buried AlAs layer was also reported by Chang, *et al.* [52] and Seo, *et al.* [53]. Mathis, *et al.* also proposes that the stress produced by volume contraction of the oxidizing AlAs layer may help relax the InGaAs layer. Landesman, *et al.* studied the impact of AlAs oxidation on a neighboring GaAs layer [54]. Oxidation of both AlAs and Al_{0.98}Ga_{0.02}As layers, resulted in induced strain at the GaAs interface. Landesman, *et al.* concluded that this strain is most likely due to the transformed nature of the GaAs-

oxide interface rather than volume contraction, since the resultant strain was similar for both AIAs and AlGaAs (which has a lower volume contraction).

The observed shift in PL may be related to the observations made by these groups. For the oxidized SBRs, the quantum well does not interface the oxidizing layer, while for the groups mentioned above, the interfaces studied were usually the oxide-semiconductor interface. However, even with the quantum well distanced from the oxide interface by a cladding layer, it is possible that structural changes introduced by the oxide would affect the properties of other layers in the structure.

Future work will be necessary to determine the origin of the oxidation induced PL shifts observed in this work. Though it seems that the PL shift is due to the oxidation process, it is not possible to conclude whether the shift is due to a strain relaxation of the quantum well induced by dislocation movement, or structural changes at the oxide-cladding layer interface which may introduce a strain at the quantum well interface. Of course, these dynamics would differ for the cases of the strained and unstrained SBR structures. Auger electron spectroscopy could be used to study any compositional change in the quantum well due to diffusion or intermixing. Defect density measurements can be used to study any defect changes with oxidation.

2.8 Conclusions

In this work, a strategy has been presented for the design and fabrication of large area broadband saturable Bragg reflectors using oxidized AIAs. The need for the large area and broadband characteristics of the device have been discussed and the challenges of meeting this need have been presented. The greatest challenge associated with creating broadband SBRs on the length scale of 100's-of-microns has been delamination associated with the mirror layers and also with the delamination of strained absorber layers. By altering the material composition of the high index layers in the Bragg mirror stack, the delamination problems associated with the mirror stack were alleviated. By introducing an oxidation ramp to slowly initiate the oxidation process, the delamination problems associated with the strained absorber were alleviated for a wide variety of SBR designs from 750nm to 1850nm.

As was demonstrated in this work, the stability of the SBR structure upon lateral oxidation of AIAs layers depends on the interplay between a number of variables. The most important

variables are the thickness of the AIAs layer, the amount of strain within the structure, and the temperature of the oxidation process. Examination of the many oxidation results showed that the volume contraction experienced by AIAs highly influences the stability of the structure. At the same time, if there is strain in the structure due to lattice mismatch, another destabilizing factor is added to the scenario. The interaction between the AIAs volume contraction and the strain can be controlled during the oxidation process by the temperature profile which is used. With steam flowing over the sample, if the temperature is gradually increased before oxidation at elevated temperatures, delamination can be greatly minimized. If the temperature ramp is not gradual enough, delamination can occur. At the same time, the temperature of the oxidation process can be used to control delamination. Even with a temperature ramp, if the oxidation is performed at temperatures which are too high, delamination can occur. With lower strain and lower volume contraction, the sample is less sensitive to the oxidation and ramping temperatures.

Optical characterization of the structures indicate that the SBR designs function well in their respective laser systems to produce femtosecond-scale pulses. With non-uniformity between samples, certain samples function more optimally than others. With no delamination, the SBR is very robust under laser irradiation. Characterization with photoluminescence indicated that absorber characteristics are transformed by the oxidation process. Though the origin of this transformation is unclear, it seems that the strain of the AIAs conversion process may introduce a structural change to the absorber. Such an idea does not seem unreasonable since the same oxidation process can produce structural damage exhibited by delamination of the absorber layers.

2.9 Future Work

Creating broadband SBRs for femtosecond laser systems through the oxidation of AIAs layers, has been full of interesting materials science challenges leaving plenty of room for future work. A number of these ideas have been described already but for convenience will be summarized here:

1. Understanding the limitations to creating SBRs with millimeter-scale areas. (Section 2.4.4)

2. Studying the compositional change of InGaAs quantum wells from the center to the edge of the wafer in order to assess its influence on delamination effects. (Section 2.5.6)
3. Studying the geometry dependence of the AIAs oxidation rate. How does the oxidation rate change with geometry? How does the oxidation rate change with radial extent of the oxidation front on circular mesas? (Section 2.5.7)
4. Further investigation of the effect of ramping speed on structure stability. (Section 2.5.7)
5. Implementing a temperature monitoring system so that the sample's temperature profile can be recorded. (Section 2.5.7)
6. Understanding the origin of the photoluminescence differences observed between unoxidized and oxidized structures. (Section 2.7.3)

2.10 References

- [1] I. Hartl, X. D. Li, C. Chudoba, R. K. Hganta, T. H. Ko, J. G. Fujimoto, J. K. Ranka, and R. S. Windeler, "Ultrahigh-resolution optical coherence tomography using continuum generation in an air-silica microstructure optical fiber," *Optics Letters*, vol. 26, pp. 608-10, 2001.
- [2] T. Juhasz, R. Kurtz, C. Horvath, C. Suarez, F. Raksi, and G. Spooner, "The femtosecond blade: Applications in corneal surgery," *Optics and Photonics News*, vol. 13, pp. 24-29, 2002.
- [3] T. Sekikawa, A. Kosuge, T. Kanai, and S. Watanabe, "Nonlinear optics in the extreme ultraviolet," *Nature*, vol. 432, pp. 605-608, 2004.
- [4] M. Lenzner, M. Schnurer, C. Spielmann, and F. Krausz, "Extreme nonlinear optics with few-cycle laser pulses," *IEICE Transactions on Electronics*, vol. E81-C, pp. 112-122, 1998.
- [5] J. Roach, "New Clock Will Lead to More Accurate Measure of Time," in *National Geographic News*, 2001.
- [6] S. A. Diddams, D. J. Jones, J. Ye, S. T. Cundiff, J. L. Hall, J. K. Ranka, R. S. Windeler, R. Holzwarth, T. Udem, and T. W. Hansch, "Direct Link between Microwave and Optical Frequencies with a 300 THz Femtosecond Laser Comb," *Physical Review Letters*, vol. 84, pp. 5102-5105, 2000.
- [7] S. A. Diddams, T. Udem, K. R. Vogel, C. W. Oates, E. A. Curtis, R. S. Windeler, A. Bartels, J. C. Bergquist, and L. Hollberg, "A compact femtosecond-laser-based optical clockwork," presented at Laser Frequency Stabilization, Satandards, Measurement, and Applications, Jan 24-26 2001, San Jose, CA, 2001.
- [8] S. T. Cundiff and J. Ye, "Colloquium: Femtosecond optical frequency combs," *Reviews of Modern Physics*, vol. 75, pp. 325-342, 2003.

- [9] R. Fluck, I. D. Jung, G. Zhang, F. X. Kartner, and U. Keller, "Broadband saturable absorber for 10-fs pulse generation," *Optics Letters*, vol. 21, pp. 743-5, 1996.
- [10] E. R. Thoen, E. M. Koontz, D. J. Jones, F. X. Kartner, E. P. Ippen, L. A. Kolodziejski, and D. Barbier, "Suppression of instabilities and pulsewidth limitation by two-photon absorption in mode-locked lasers," presented at Technical Digest. Summaries of papers presented at the Conference on Lasers and Electro-Optics. Postconference Edition. CLEO '99. Conference on Lasers and Electro-Optics, 23-28 May 1999, Baltimore, MD, USA, 1999.
- [11] J. T. Gopinath, "Studies of Third-Order Nonlinearities in Materials and Devices for Ultrafast Lasers." Cambridge, MA: PhD Thesis in Electrical Engineering and Computer Science, MIT, 2005.
- [12] Z. Zhang, T. Nakagawa, K. Torizuka, T. Sugaya, and K. Kobayashi, "Self-starting mode-locked Cr⁴⁺:YAG laser with a low-loss broadband semiconductor saturable-absorber mirror," *Optics Letters*, vol. 24, pp. 1768-1770, 1999.
- [13] Z. Zhang, T. Nakagawa, K. Torizuka, T. Sugaya, and K. Kobayashi, "Gold-reflector-based semiconductor saturable absorber mirror for femtosecond mode-locked Cr⁴⁺:YAG lasers," *Applied Physics B (Lasers and Optics)*, vol. B70, pp. 59-62, 2000.
- [14] U. Keller, D. A. B. Miller, G. D. Boyd, T. H. Chiu, J. F. Ferguson, and M. T. Asom, "Solid-state low-loss intracavity saturable absorber for Nd:YLF lasers: an antiresonant semiconductor Fabry-Perot saturable absorber," *Optics Letters*, vol. 17, pp. 505-7, 1992.
- [15] Y. Chang, R. Maciejko, R. Leonelli, and A. S. Thorpe, "Self-starting passively mode-locked tunable Cr⁴⁺: yttrium-aluminum-garnet laser with a single prism for dispersion compensation," *Applied Physics Letters*, vol. 73, pp. 2098-100, 1998.
- [16] S. Tsuda, W. H. Knox, E. A. de Souza, W. Y. Jan, and J. E. Cunningham, "Low-loss intracavity AlAs/AlGaAs saturable Bragg reflector for femtosecond mode locking in solid-state lasers," *Optics Letters*, vol. 20, pp. 1406-8, 1995.
- [17] J.-M. Shieh, T. C. Huang, K. F. Huang, C.-L. Wang, and C.-L. Pan, "Broadly tunable self-starting passively mode-locked Ti:sapphire laser with triple-strained quantum-well saturable Bragg reflector," *Optics Communications*, vol. 156, pp. 53-7, 1998.
- [18] S. J. White, J.-M. Hopkins, W. H. Knox, and A. Miller, "Dual-wavelength, self-starting saturable Bragg reflector mode-locked Ti:sapphire laser," *IEEE Journal of Quantum Electronics*, vol. 38, pp. 246-51, 2002.
- [19] R. Kretz, "Physical Constants of Minerals," in *CRC Handbook of Chemistry and Physics*, R. C. Weast, Ed., 58 ed: CRC Press, 1978, pp. B214-B219.
- [20] D. J. Ripin, J. T. Gopinath, H. M. Shen, A. A. Erchak, G. S. Petrich, L. A. Kolodziejski, F. X. Kartner, and E. P. Ippen, "Oxidized GaAs/AlAs mirror with a quantum-well saturable absorber for ultrashort-pulse Cr⁴⁺:YAG laser," *Optics Communications*, vol. 214, pp. 285-9, 2002.
- [21] J. M. Dallesasse and N. Holonyak, Jr., "Native-oxide stripe-geometry Al(x)Ga(1-x)As-GaAs quantum well heterostructure lasers," *Applied Physics Letters*, vol. 58, pp. 394-6, 1991.
- [22] F. A. Kish, S. J. Caracci, N. Holonyak, J. M. Dallesasse, Jr., K. C. Hsieh, M. J. Ries, S. C. Smith, and R. D. Burnham, "Planar native-oxide index-guided Al(x)Ga(1-x)As-GaAs quantum well heterostructure lasers," *Applied Physics Letters*, vol. 59, pp. 1755-7, 30.
- [23] S. A. Maranowski, A. R. Sugg, E. I. Chen, and N. Holonyak, Jr., "Native oxide top- and bottom-confined narrow stripe p-n Al(y)Ga(1-y)As-GaAs-In(x)Ga(1-x)As quantum well heterostructure laser," *Applied Physics Letters*, vol. 63, pp. 1660-2, 20.
- [24] K. D. Choquette, R. P. Schneider, Jr., K. L. Lear, and K. M. Geib, "Low threshold voltage vertical-cavity lasers fabricated by selective oxidation," *Electronics Letters*, vol. 30, pp. 2043-4, 1994.

- [25] G. M. Yang, M. H. MacDougal, and P. D. Dapkus, "Ultralow threshold current vertical-cavity surface-emitting lasers obtained with selective oxidation," *Electronics Letters*, vol. 31, pp. 886-8, 1995.
- [26] A. A. Erchak, D. J. Ripin, S. Fan, P. Rakich, J. D. Joannopoulos, E. P. Ippen, G. S. Petrich, and L. A. Kolodziejski, "Enhanced coupling to vertical radiation using a two-dimensional photonic crystal in a semiconductor light-emitting diode," *Applied Physics Letters*, vol. 78, pp. 563-5, 2001.
- [27] M. H. MacDougal, H. Zhao, P. D. Dapkus, M. Ziari, and W. H. Steier, "Wide-bandwidth distributed Bragg reflectors using oxide/GaAs multilayers," *Electronics Letters*, vol. 30, pp. 1147-9, 1994.
- [28] M. H. MacDougal, P. D. Dapkus, V. Pudikov, H. Zhao, and G. M. Yang, "Ultralow threshold current vertical-cavity surface-emitting lasers with AlAs oxide-GaAs distributed Bragg reflectors," *IEEE Photonics Technology Letters*, vol. 7, pp. 229-31, 1995.
- [29] S. J. Caracci, M. R. Krames, N. Holonyak, Jr., C. M. Herzinger, A. C. Crook, T. A. DeTemple, and P.-A. Besse, "Native-oxide-defined low-loss AlGaAs-GaAs planar waveguide bends," *Applied Physics Letters*, vol. 63, pp. 2265-7, 1993.
- [30] D. J. Ripin, K.-Y. Lim, G. S. Petrich, P. R. Villeneuve, S. Fan, E. R. Thoen, J. D. Joannopoulos, E. P. Ippen, and L. A. Kolodziejski, "One-dimensional photonic bandgap microcavities for strong optical confinement in GaAs and GaAs/Al(x)O(y) semiconductor waveguides," *Journal of Lightwave Technology*, vol. 17, pp. 2152-60, 1999.
- [31] W. T. Tsang, M. Olmstead, and R. P. H. Chang, "Multidielectrics for GaAs MIS devices using composition-graded Al/sub x/Ga/sub 1-x/As and oxidized AlAs," *Applied Physics Letters*, vol. 34, pp. 408-10, 1979.
- [32] E. I. Chen, N. Holonyak, Jr., and S. A. Maranowski, "Al(x)Ga(1-x)As-GaAs metal-oxide semiconductor field effect transistors formed by lateral water vapor oxidation of AlAs," *Applied Physics Letters*, vol. 66, pp. 2688-90, 1995.
- [33] P. A. Grudowski, R. V. Chelakara, and R. D. Dupuis, "An InAlAs/InGaAs metal-oxide-semiconductor field effect transistor using the native oxide of InAlAs as a gate insulation layer," *Applied Physics Letters*, vol. 69, pp. 388-90, 1996.
- [34] K.-Y. Lim, D. J. Ripin, G. S. Petrich, P. R. Villeneuve, S. Fan, J. D. Joannopoulos, E. P. Ippen, and L. A. Kolodziejski, "Role of the thermal oxide in GaAs-based photonic bandgap waveguide microcavities," *Advanced Materials*, vol. 11, pp. 501-505, 1999.
- [35] M. L. Povinelli, R. E. Bryant, S. Assefa, S. G. Johnson, S. Fan, A. A. Erchak, G. S. Petrich, E. Lidorikis, J. D. Joannopoulos, L. A. Kolodziejski, and E. P. Ippen, "Design of a nanoelectromechanical high-index-contrast guided-wave optical switch for single-mode operation at 1.55 μm ," *IEEE Photonics Technology Letters*, vol. 15, pp. 1207-9, 2003.
- [36] E. Chow, S. Y. Lin, J. R. Wendt, S. G. Johnson, and J. D. Joannopoulos, "Quantitative analysis of bending efficiency in photonic-crystal waveguide bends at $\lambda = 1.55 \mu\text{m}$ wavelengths," *Optics Letters*, vol. 26, pp. 286-8, 2001.
- [37] P. W. Evans, J. J. Wierer, and N. Holonyak, Jr., "Al(x)Ga(1-x)As native-oxide-based distributed Bragg reflectors for vertical cavity surface emitting lasers," *Journal of Applied Physics*, vol. 84, pp. 5436-40, 1998.
- [38] K. D. Choquette, K. M. Geib, C. I. H. Ashby, R. D. Twisten, O. Blum, H. Q. Hou, D. M. Follstaedt, B. E. Hammons, D. Mathes, and R. Hull, "Advances in selective wet oxidation of AlGaAs alloys," *Ieee Journal of Selected Topics in Quantum Electronics*, vol. 3, pp. 916-926, 1997.
- [39] M. H. MacDougal and P. D. Dapkus, "Wavelength shift of selectively oxidized Al(x)O(y)AlGaAs-GaAs distributed Bragg reflectors," *IEEE Photonics Technology Letters*, vol. 9, pp. 884-6, 1997.

- [40] S. N. Tandon, J. T. Gopinath, A. A. Erchak, G. S. Petrich, L. A. Kolodziejski, and E. P. Ippen, "Large-area oxidation of AlAs layers for dielectric stacks and thick buried oxides," *Journal of Electronic Materials*, vol. 33, pp. 774-9, 2004.
- [41] K. D. Choquette, K. M. Geib, H. C. Chui, B. E. Hammons, H. Q. Hou, T. J. Drummond, and R. Hull, "Selective oxidation of buried AlGaAs versus AlAs layers," *Applied Physics Letters*, vol. 69, pp. 1385-7, 1996.
- [42] E. F. Schubert, *Light-Emitting Diodes*. Cambridge, U.K.: Cambridge University Press, 2003.
- [43] R. F. C. Farrow, "Molecular Beam Epitaxy: Applications to Key Materials." Park Ridge, NJ: Noyes Publications, 1995.
- [44] A. E. Romanov, W. Pompe, G. E. Beltz, and J. S. Speck, "An approach to threading dislocation "reaction kinetics"," *Applied Physics Letters*, vol. 69, pp. 3342-3344, 1996.
- [45] T. R. Schibli, J. Kim, O. Kuzucu, J. T. Gopinath, S. N. Tandon, G. S. Petrich, L. A. Kolodziejski, J. G. Fujimoto, E. P. Ippen, and F. X. Kaertner, "Attosecond active synchronization of passively mode-locked lasers by balanced cross correlation," *Optics Letters*, vol. 28, pp. 947-9, 2003.
- [46] *The simulation was performed in collaboration with Hanfei Shen in the Ultra-fast Optics Group at MIT.*
- [47] J. M. Dallesasse, N. Holonyak, A. R. Sugg, T. A. Richard, and N. Elzein, "Hydrolyzation Oxidation of Al(x)Ga(1-x)As-AlAs-GaAs Quantum-Well Heterostructures and Superlattices," *Applied Physics Letters*, vol. 57, pp. 2844-2846, 1990.
- [48] S. N. Tandon, J. T. Gopinath, H. M. Shen, G. S. Petrich, L. A. Kolodziejski, F. X. Kartner, and E. P. Ippen, "Large-area broadband saturable Bragg reflectors by use of oxidized AlAs," *Optics Letters*, vol. 29, pp. 2551-2553, 2004.
- [49] V. Liverini, S. Schon, R. Grange, M. Haiml, S. C. Zeller, and U. Keller, "Low-loss GaInNAs saturable absorber mode locking a 1.3- μ m solid-state laser," *Applied Physics Letters*, vol. 84, pp. 4002-4004, 2004.
- [50] M. Kondow and T. Kitatani, "Molecular beam epitaxy of GaNAs and GaInNAs," *Semiconductor Science and Technology*, vol. 17, pp. 746-754, 2002.
- [51] S. K. Mathis, P. Chavarkar, A. M. Andrews, U. K. Mishra, and J. S. Speck, "Strain relaxation of InGaAs by lateral oxidation of AlAs," *Journal of Vacuum Science & Technology B*, vol. 18, pp. 2066-2071, 2000.
- [52] K. L. Chang, J. H. Epple, G. W. Pickrell, H. C. Lin, K. Y. Cheng, and K. C. Hsieh, "Strain relaxation and defect reduction in In(x)Ga(1-x)As/GaAs by lateral oxidation of an underlying AlGaAs layer," *Journal of Applied Physics*, vol. 88, pp. 6922-6924, 2000.
- [53] J. H. Seo and K. S. Seo, "Strain relaxation of InGaAs/GaAs superlattices by wet oxidation of underlying AlAs layer," *Applied Physics Letters*, vol. 72, pp. 1466-1468, 1998.
- [54] J. P. Landesman, A. Fiore, J. Nagle, V. Berger, E. Rosencher, and P. Puech, "Local stress measurements in laterally oxidized GaAs/AlxGa1-xAs heterostructures by micro-Raman spectroscopy," *Applied Physics Letters*, vol. 71, pp. 2520-2522, 1997.

Chapter 3

Large Area Two-Dimensional Photonic Crystal Devices

3.1 Creating Large Area 2D Photonic Crystals

3.1.1 Introduction

As discussed previously, photonic crystals are periodic structures where the periodicity of the refractive index occurs in one or more dimensions. In this thesis research, the realization of two novel devices were explored where a large area two-dimensional photonic crystal enabled dramatic effects on light. The devices are:

- 1) a "Superprism," and
- 2) a "Super-Collimator."

Both devices necessitate that the photonic crystal, which consists of nanometer scale features, be created over centimeter-scale areas. In addition, both devices require light to couple into and out of the device so that the unique behavior of the photonic crystal can be observed and measured. Therefore, before the specifics of each device are discussed, the strategy for realizing the photonic crystals for each device will be described.

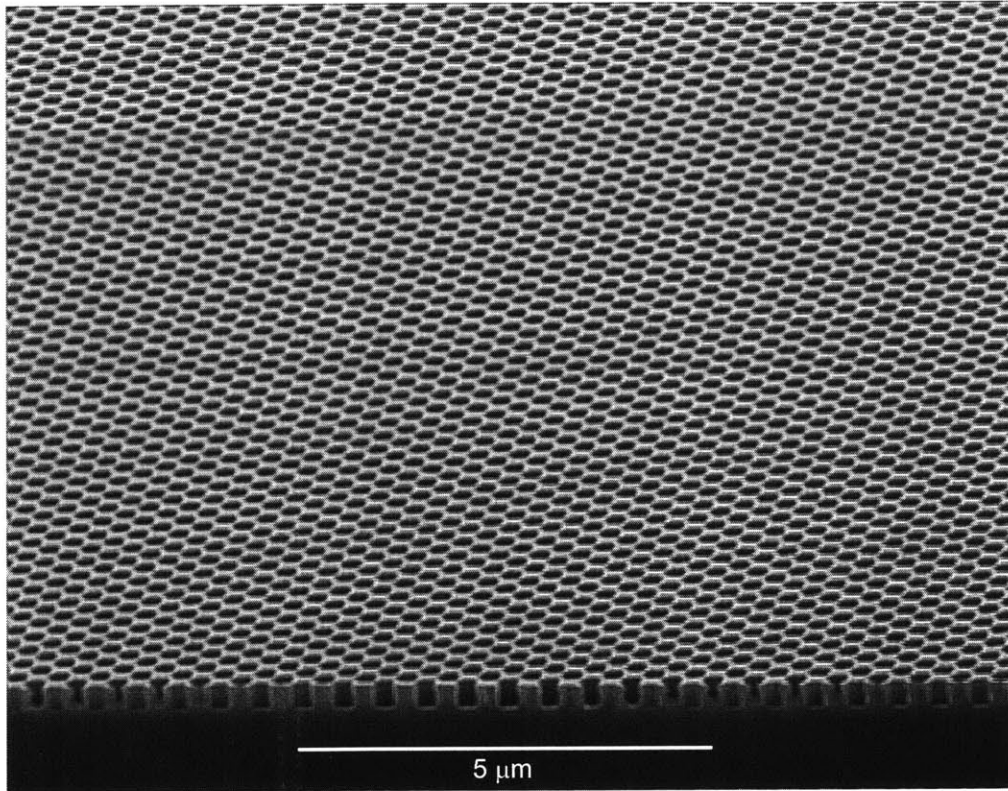


Figure 3-1 A large area photonic crystal patterned using interference lithography. Image taken using scanning electron microscopy.

3.1.2 Interference lithography

The origin of the word "lithography" comes from two greek words: "litho" (stone) and "graphy" (writing). Therefore *lithography* literally means *to write in stone*. For most devices made from semiconductor materials, the "stone" is the semiconductor, and before the device can be made, the shape of the device must be *written* on the semiconductor surface. Hence, a *lithography* step is crucial for creating any planar semiconductor device.

A lithography technique known as "interference lithography" is used to define large area photonic crystals discussed in this thesis. Interference lithography (IL) allows the patterning of periodic structures over the centimeter-scaled areas necessary for the superprism and super-collimator. Interference lithography is a more appropriate lithography technique than conventional photolithography or electron beam lithography for large area photonic crystals because the pattern is periodic, covering a large centimeter-scaled area, and with minimum feature sizes less than $1\mu\text{m}$. The periodic pattern is formed by the constructive and destructive interference of light waves which form a standing wave

at the substrate surface. This standing wave exposes a grating pattern on the substrate as illustrated in Figure 3-2.

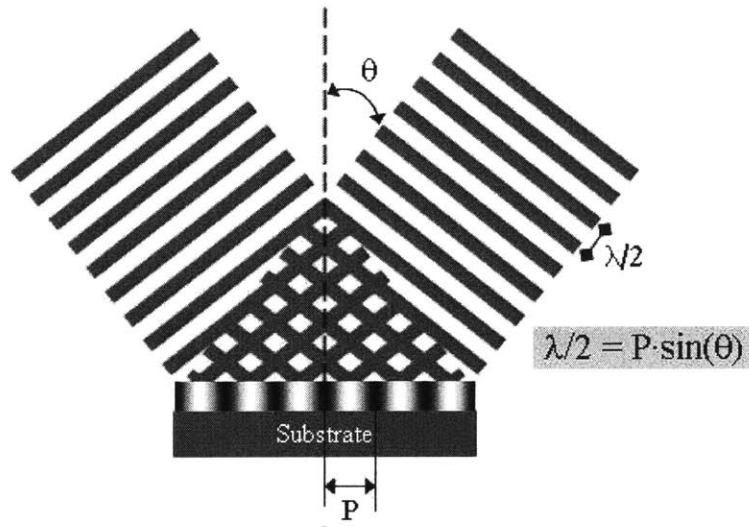


Figure 3-2 In interference lithography, the standing wave that is formed by the interference of two light beams, exposes a periodic grating on the substrate. The incoming waves are approximated as plane waves when in reality they are spherical.

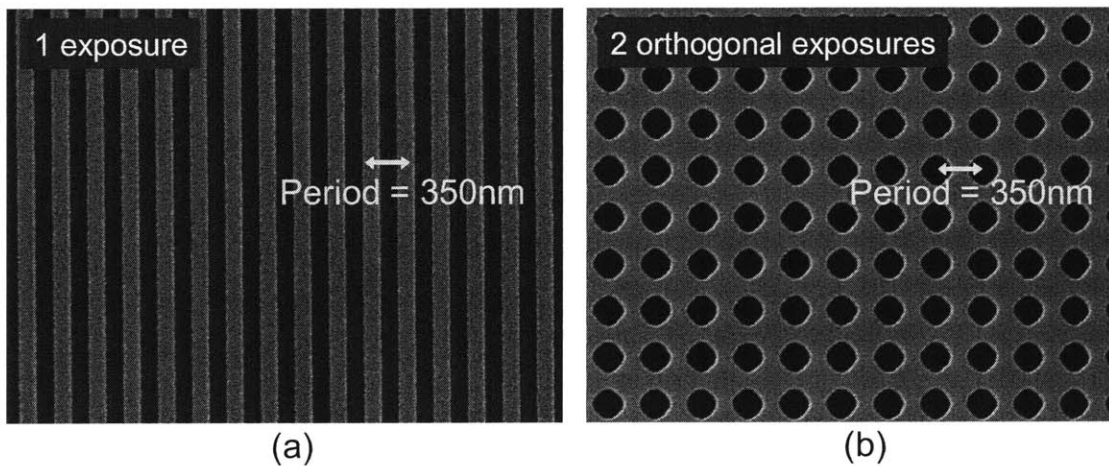


Figure 3-3 Scanning electron micrographs showing the patterning results of two interference lithography exposures in a layer of photoresist. (a) A grating is patterned with one exposure. (b) A second exposure rotated 90° from the first exposure results in a grid.

The period of the grating (P), which is the spacing between the exposed lines, depends on the source wavelength (λ) and the half-angle between the two interfering beams (θ) according to:

$$P = \lambda / 2 \sin(\theta) \quad \text{Eq (1)}$$

With one interference lithography exposure, a grating of lines is formed as shown in Figure 3-3(a). To fabricate two-dimensional grids, two grating exposures are necessary. A two-dimensional square grid is accomplished with two orthogonal exposures where the substrate is rotated by 90 degrees between exposures to produce a pattern as shown in Figure 3-3(b). The period of both the grating and grid are 350 nm. With two rotated interference lithography exposures, large area photonic crystal grids can be patterned.

Two IL systems in the Nanostructures Laboratory at MIT were used for patterning the photonic crystals used in this thesis:

- 1) the Lloyd's mirror interferometer, and
- 2) the two-beam interferometer.

The Lloyd's mirror interferometer uses a broad beam of light and a mirror to create an interference pattern on the substrate as shown in Figure 3-4. The mirror sits perpendicular to the substrate surface, and the periodic pattern is formed by the interference between light directly incident on the substrate, and light reflected off the mirror which then exposes the substrate. The period of the grating is given by $P=(\lambda/2)\sin(\theta)$ where θ is determined by the orientation of the mirror and substrate with respect to the incoming light as shown in the inset to Figure 3-4.

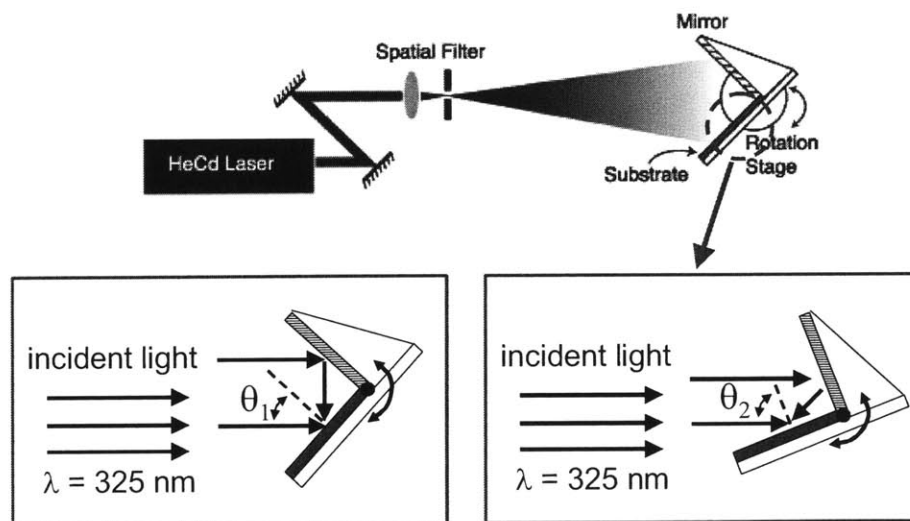


Figure 3-4 Top view of the Lloyd's mirror interferometer system showing light incident upon the mirror and substrate simultaneously. The rotation stage sets the period by changing the orientation of the mirror and substrate with respect to the incident light. (Adapted from [56].)

The present Lloyd's mirror system, illustrated in Figure 3-4, uses a 325 nm HeCd laser as its exposure source. The mirror, which is positioned at right angles to the substrate, is attached to the substrate chuck via vacuum suction. A rotation stage sets the period of the grating by rotating this mirror/substrate combination with respect to the fixed direction of incident light. A spatial filter is implemented to remove high frequency noise from the beam's profile in order to create a clean Gaussian beam profile which exposes the substrate. A pinhole allows the beam diameter to expand so that the beam exposes a large area when the beam reaches the mirror/substrate.

There are several advantages to the Lloyd's mirror system. Firstly, the Lloyd's mirror is fairly immune to external mechanical vibrations. Vibrations affecting the relative path length of the two interfering beams are the only vibrations that affect the pattern exposed on the substrate. Because the separation of the two interfering beams does not occur until light reflects off the mirror, and with the mirror rigidly connected to the substrate, such vibrations are minimal. The result is that the relative path lengths of the two beams remains very stable over the duration of the exposure. A second advantage of the Lloyd's mirror system is the ease with which the period of the grating can be adjusted. Changing the period only requires the rotation of the mirror/substrate stage; no additional alignment steps are necessary. Because the Lloyd's mirror interferes two halves of the beam diameter at the substrate surface, the exposure area is limited to one half of the beam's surface area—a disadvantage of the system.

Another interference lithography configuration is the two-beam interferometer (Figure 3-5). The $\lambda=325$ nm beam emitted from a HeCd laser source is divided by a dielectric beamsplitter into two beams with approximately the same power. These two beams are then directed toward the substrate via two mirrors. Each beam passes through its own spatial filter and pinhole to remove high frequency noise and expand the beam diameter. An interference pattern is formed as the two beams interact at the substrate surface.

A feedback system is used to correct for relative path length differences between the two beams which may occur due to perturbations in the system. A beamsplitter that is located above the substrate chuck, samples and recombines the two incoming beams in a Mach-Zehnder interferometer configuration. Interference fringes, formed by the recombined beams, pass through each side of the beamsplitter cube onto two photodiodes. Any change in the path length of either beam will cause the photodiode current to change. A differential amplifier that is connected to the two photodiodes then drives a piezoelectric motor which

adjusts the position of the first beamsplitter stage. By changing the position of the beamsplitter, the relative path length of the two beams is adjusted to stabilize the system. With a feedback system that stabilizes the phase difference between the two beams, the interference pattern, which exposes the substrate surface is also stabilized.

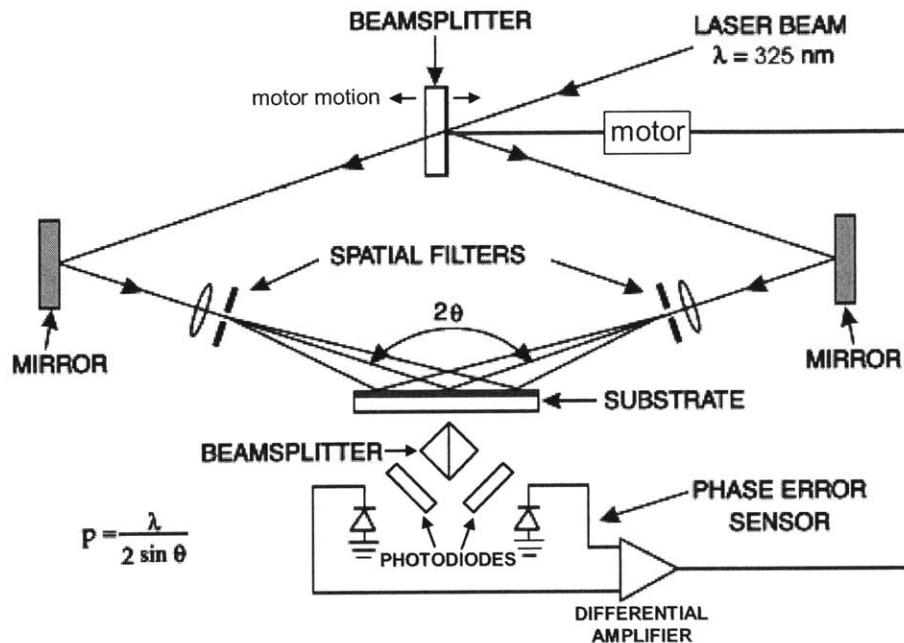


Figure 3-5 The two beam interference lithography system used in the Nanostructures Laboratory (adapted from [56].)

The period of the grating exposed using the two-beam IL tool is determined by the angle with which the beams are directed towards the substrate. For example, to achieve a periodicity of 750 nm, the half-angle between the two beams must be 12.5°. The mirrors and spatial filters should therefore be placed so that the light exposes the sample at this angle. In order to change the resulting grating period, the spatial filters must be moved and the steering mirrors must be adjusted to the appropriate angle. This adjustment process requires a realignment of the beam path through all of the optical elements--which is not trivial and can take several hours.

From the perspective of stabilization and period adjustment, the Lloyd's mirror interferometer is an easier tool to use. There is no need for additional feedback mechanisms to stabilize the fringe pattern nor is any readjustment process necessary for changing the period. However, there are some distinct advantages of the two-beam interferometer. The greatest advantage of the two-beam interferometer over the Lloyd's mirror is that the two-beam system fixes the period of interest allowing a higher degree of

repeatability between exposures. With the Lloyd's mirror system, the stage is reset between each exposure so that the sample can be mounted or rotated. This disadvantage is an artifact of the system and the system can be redesigned such that the stage does not move between exposures. Another distinct advantage of the two-beam set-up is the ability to pattern larger areas. The two-beam system allows the full beam diameter to expose the surface therefore allowing for a greater exposure area. To achieve equivalent exposure areas with the Lloyd's mirror, the beam divergence must be increased significantly, requiring a larger mirror. Another distinct advantage of the two-beam IL system is the ability to precisely rotate the sample either to orient the sample with respect to previously patterned structures on the substrate, or to rotate the sample between exposures. Rotation of the sample in the two-beam system is accomplished with a substrate chuck attached to a rotation stage which is rotated by 90 degrees between exposures to form the photonic crystal grid. The resolution of the substrate rotation stage in the two beam IL system is less than one degree whereas on the Lloyd's mirror interferometer, no such stage exists and therefore the substrate would have to be manually rotated. A stage can be designed to allow for substrate rotation, so at the present, this disadvantage is an artifact of the system.

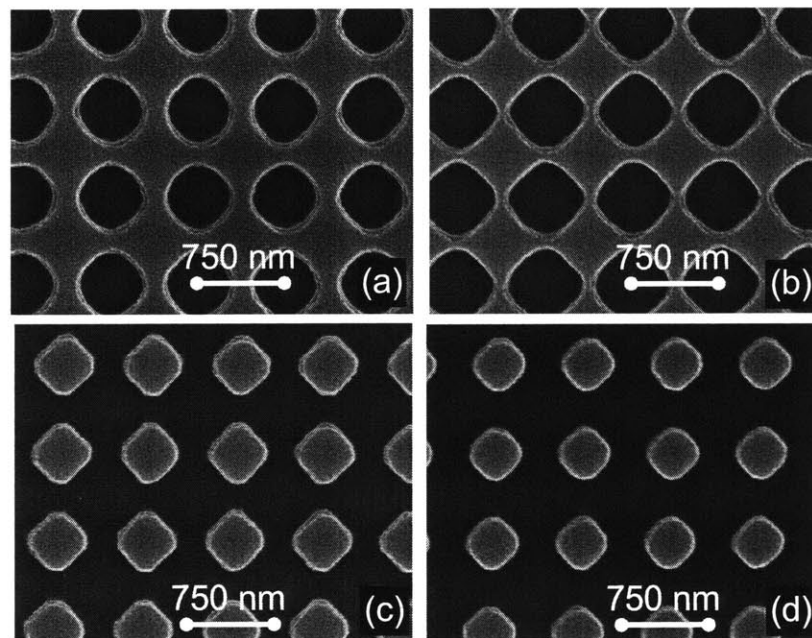


Figure 3-6 Examples of grid exposures using the Lloyd's mirror for different exposure times for a laser power of 42mW. Grids are exposed in PFI 88 positive resist on silicon for (a) 2 min (b) 2min 24sec (c) 2 min 48 sec (d) 3 min 12 sec per side (the total exposure time is double). The period is approximately 750 nm for every case.

Examples of a number of grid exposures using the Lloyd's mirror are shown in Figure 3-6 and Figure 3-7. By varying the exposure time, the hole size can be varied. In general, these exposure times are a function of the intensity of the laser beam at the substrate surface and the sensitivity and type of the resist. When using a positive resist as in Figure 3-6, a small exposure time results in a smaller hole size. With longer exposure times, the holes become large enough to interfere with neighboring holes resulting in *post* structures rather than *holes*. When using a negative resist as in Figure 3-7, the opposite effect is observed. A longer exposure time results in a smaller hole size and short exposure times result in post structures.

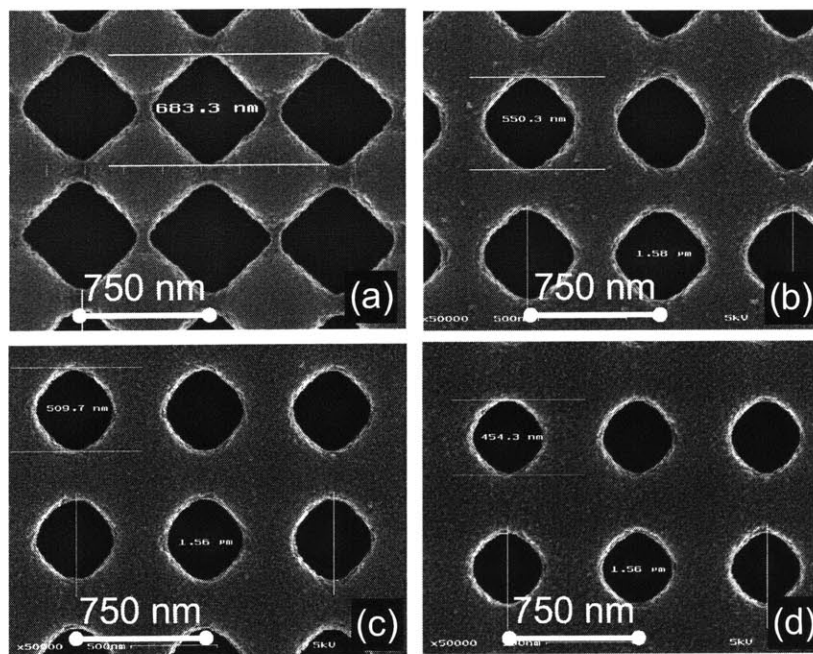


Figure 3-7 Examples of grid exposures in negative resist using the Lloyd's mirror for different exposure times for a laser power of 42mW. Grids are exposed in OKHA PS4 negative resist on silicon for (a) 1 min (b) 1 min 20 sec (c) 1 min 40 sec (d) 2 min per side (the total exposure time is double). The period is approximately 750 nm for every case.

Because the Lloyd's mirror interferometer is an easier tool to use than the two-beam setup, certain improvements can be made for future work in order to remove some of its current disadvantages. Implementing a rotation stage on the substrate chuck would allow multiple exposures to be made on the same substrate without manually handling the sample between exposures. Integrating a rotation stage would require the mirror to be separated from the substrate chuck to facilitate rotation.

The performance of both IL systems would be improved by integrating photodiodes into the substrate chuck in order to measure the laser power distribution at the substrate. Being able to measure the power distribution would have two benefits:

- 1) Knowing the power distribution at several spots on the substrate chuck would allow the user to more effectively focus the laser beam to produce a more uniform spot for exposure. Currently, this focusing process is implemented by qualitatively examining the spot size and shape on a fluorescent card placed in front of the substrate. Using photodiodes to measure the laser intensity would make this process more quantitatively based.
- 2) Measuring the power distribution at the substrate chuck would also allow the exposure dose to be controlled more accurately. Currently, the power is measured at one place near the substrate and the exposure time is calculated based on this measurement. However, because the laser power can vary over time, this measurement needs to be repeated often. With photodiodes integrated within the substrate chuck, the measurement would be easier to implement so that necessary doses can be calculated more easily. A computer-controlled shutter at the laser output could control and adjust the exposure time based on the measured power.

3.1.3 The trilayer resist process

The exposure of a periodic pattern in resist using interference lithography can be degraded by reflections from layers underneath the resist. Light reflected off layers under the resist can interfere with the incident light forming a standing wave pattern in the vertical direction which exposes the resist profile. As a result, after development, the sidewalls of the resist pattern may not be perfectly straight which can degrade pattern transfer in subsequent etching steps.

To mitigate this effect, a trilayer resist process can be implemented. As shown in Figure 3-8, the trilayer resist stack consists of a resist layer, an SiO₂ interlayer, and an anti-reflective layer (ARC). The ARC layer allows reflections to be minimized through a combination of the ARC's absorption properties, and its index properties relative to the other layers of the stack. With an ARC layer below the resist layer, the reflected power from the layers below the resist can be minimized. Since the resist layer is not durable enough as a mask layer for etching the pattern into the ARC layer, and the ARC and resist etch in the same reactive ion etching chemistry, an SiO₂ interlayer is often used in between.

Using a thicker resist layer is not desirable due to the increased exposure times required. The SiO₂ interlayer facilitates pattern transfer from the resist layer to the ARC layer after the interference lithography exposure. The thicknesses of the resist, interlayer, and hard mask layers are chosen such that each layer can be used effectively as mask layers for subsequent etching of the lower layers. Once these thicknesses are chosen, the thickness of the ARC is calculated such that the total reflected power, as illustrated in Figure 3-8, is minimized. A scanning electron micrograph of the trilayer resist stack with a hard mask layer after an interference lithography exposure and development is shown in Figure 3-9. The spacing between holes, or the period, is 750 nm.

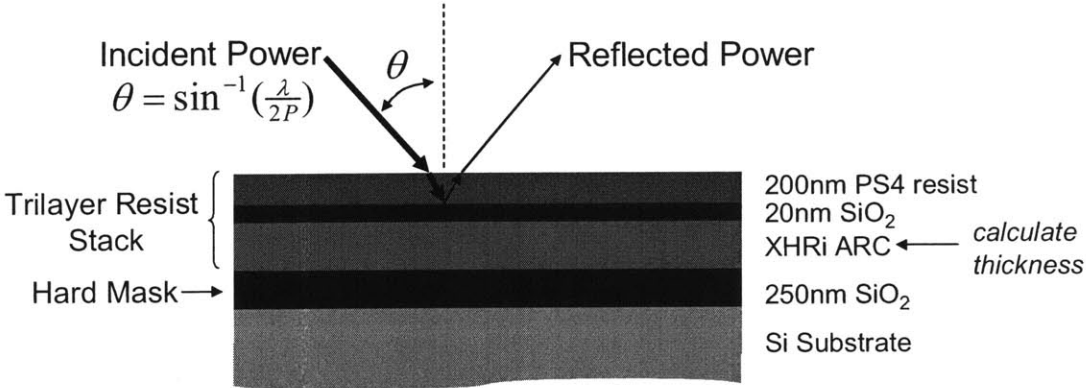


Figure 3-8 An example of a layered structure used for an interference lithography step. Trilayer resist stack consisting of resist, SiO₂, and ARC is shown. The hard mask layer is used to facilitate pattern transfer to substrate.

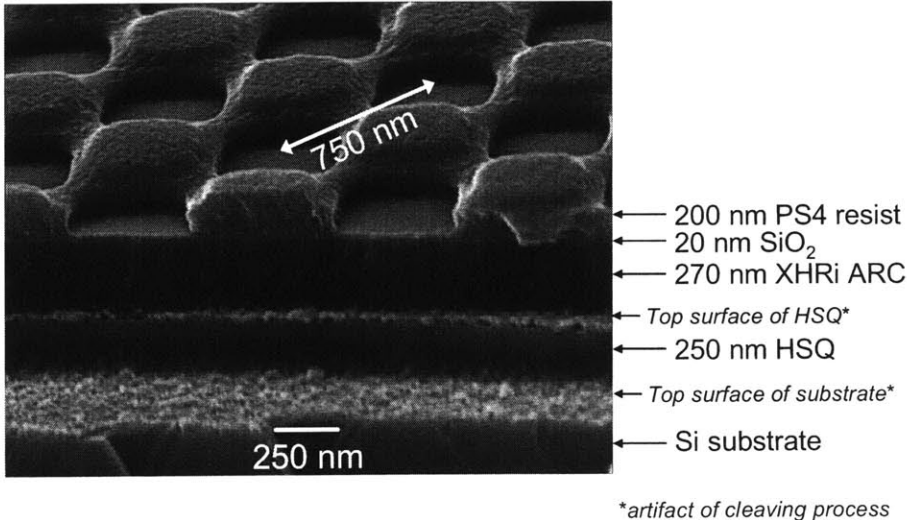


Figure 3-9 Scanning electron micrograph illustrating the trilayer resist stack and hard mask layer after interference lithography exposure and development.

Reflection at the resist/ARC boundary is dependent on the indices of refraction, and thicknesses of all the layers beneath the resist, as well as the angle of incidence and the wavelength of the incident light. The ARC thickness required to minimize the reflected power is calculated based on all of these properties. A software simulation similar to the one used in [56] was used to determine this thickness. The program calculates the reflectivity at any boundary of any arbitrary layered medium. The program then generates reflectivity curves for different variables of interest. The indices of refraction for each layer at the interference lithography exposure wavelength need to be known. A table of the relevant indices used in this work can be found in the Appendix.

The plot shown in Figure 3-10 shows how the reflected power varies with ARC thickness for the layered medium shown in Figure 3-8 and Figure 3-9, assuming a grating period of 750 nm (12.5° incident angle with respect to the substrate normal), and an exposure wavelength of 325 nm. Though the absolute minimum reflectivity occurs at an ARC thickness of 170 nm, the thickness was chosen to be 270 nm to allow for an ARC layer sufficiently thick to permit reactive ion etching of the 250 nm hard mask layer underneath. The ARC thickness necessary to minimize the reflected power does not vary between the Lloyd's mirror interferometer and the two-beam interferometer because the exposure beam's incident angle is the same for both systems.

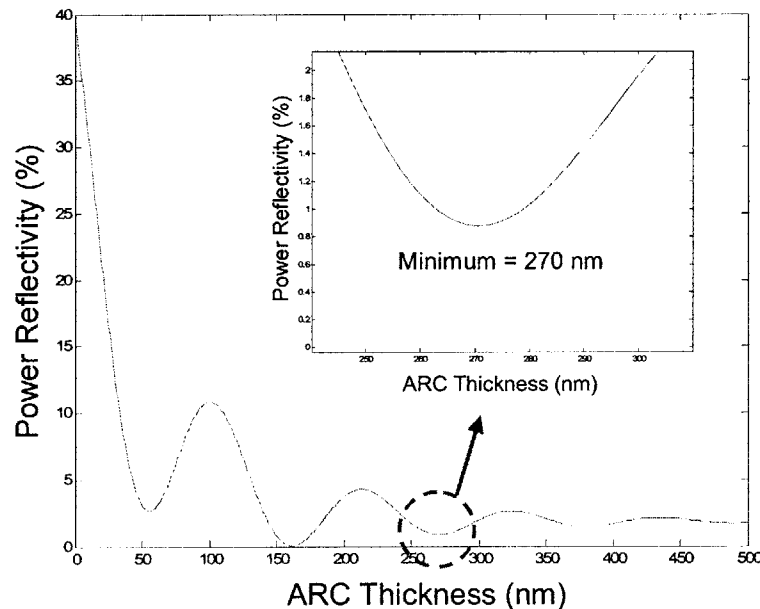


Figure 3-10 Reflectivity profile for layered medium consisting of 200nm OKHA PS4 negative resist, 20nm SiO₂, XHRi-16 ARC, 250nm SiO₂, Si substrate.

For most of the exposures discussed in this thesis, an ARC named XHRi manufactured by Brewer Science, Inc. was used in the trilayer resist stack. (XHRi-16 refers to the thickness grade used). The ARC layer is usually a polymer that is spun onto the wafer and then baked at 170°C on a hotplate for 1 minute before the SiO₂ interlayer is evaporated. The resist layer was usually OKHA PS4, a chemically amplified negative resist manufactured by Okha America, Inc. For a 200nm resist thickness, the resist was spun at 3 krpm for 1 minute followed by a 1 minute hotplate bake at 90°C. After exposure but before development, the resist is baked again on a hotplate at 110°C for 1 minute before development in CD-26 (manufactured by Rhome & Haas) or OPD-262 (manufactured by Arch Chemicals) for 1 minute.

3.1.4 Reactive ion etching

Reactive ion etching is used to transfer patterns exposed during the lithography steps through the intermediary trilayer and hard mask layers into the device layers. Reactive ion etching is a dry etching technique whereby ions accelerate towards the substrate to *physically* remove material while also reacting with the surface material to *chemically* remove material. This etching method allows for highly anisotropic etching with straight sidewalls.

Once the pattern has been exposed in resist with interference lithography, a number of different reactive ion etching steps are necessary to transfer the pattern into the device layers. After the IL exposure, the pattern must be transferred from the resist layer through the SiO₂ interlayer, ARC layer, the SiO₂ hard mask layer, and finally into the device layer. Since each material requires its own particular etch chemistry, different gases are used to etch each layer. SiO₂ is etched using fluorine-containing gases such as CHF₃ or CF₄, the ARC layer is etched using O₂, and the silicon device layer is etched using Cl₂. Each etching step must be performed in such a way that the mask layer is not etched simultaneously.

An image of a pattern in resist before reactive ion etching is shown in Figure 3-11(a). The SiO₂ interlayer was then etched as shown in Figure 3-11(b). The 20 nm SiO₂ layer was etched using CF₄ at 10 mT, 300V, 160W for 1 minute, 20 seconds. CHF₃ is also a suitable gas for this step because it does not chemically etch polymers such as resist and ARC. However, CHF₃ does physically sputter etch the surface.

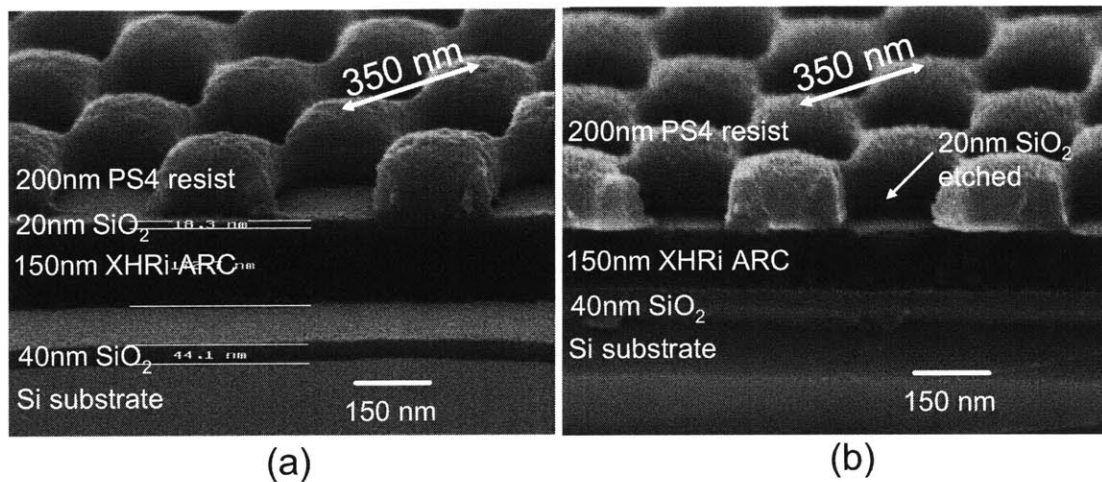


Figure 3-11 (a) SEM image of trilayer resist stack after exposure with interference lithography. (b) SEM image of trilayer resist stack with 20 nm SiO₂ layer etched. Etch parameters: CF₄(10mT, 300V, 160W, 1:20).

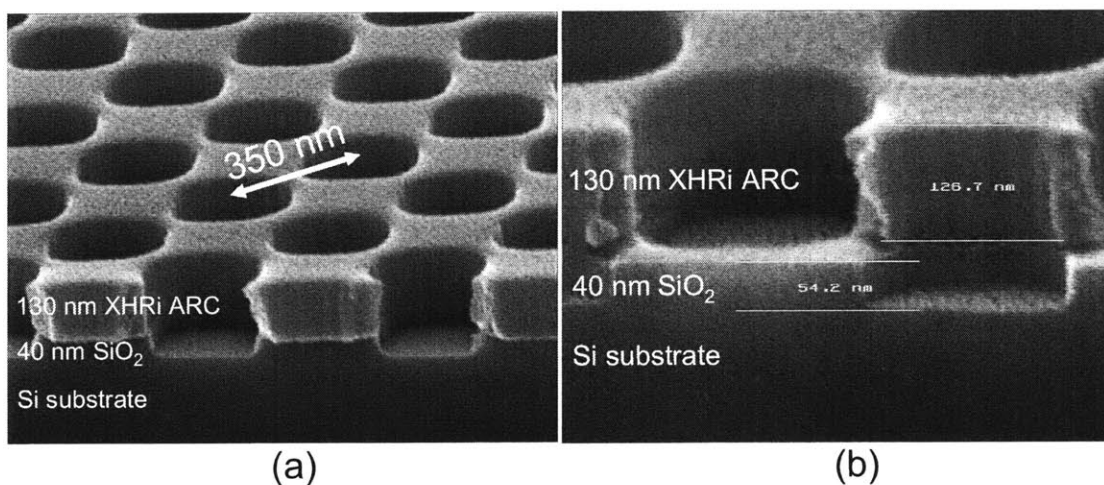


Figure 3-12 SEM images showing (a) etching of the ARC and hard mask layers and (b) magnified image of one of the etched holes. Etch parameters: He/O₂(2:1sccm, 10mT, 250V, 135W, 3:27), CF₄(10mT, 100V, 285W, 1:10).

The ARC layer was then etched using a 2:1 mix of He and O₂ at a pressure of 10 mT, 250 V bias, 135 W power, for 3 minutes, 27 seconds. Adding helium to the ARC etching step reduces the partial pressure of oxygen in order to slow the etch rate for a more controllable etch. Helium does not etch ARC. The SiO₂ hard mask was etched using CF₄ as shown in Figure 3-12. Please note that while the SiO₂ hard mask layer is etched, the SiO₂ interlayer is removed as evident in Figure 3-12. Because CF₄ etches polymers such as ARC, the ARC layer is etched simultaneously with the SiO₂ layer. With simultaneous etching of the ARC during a CF₄ etch, the RIE chamber is cleaner than it would be during a CHF₃ etch where physical sputtering leaves polymer deposits on the chamber walls. Thus etching with CF₄ is

preferred. The etch rate of ARC in CF_4 is approximately 3 times as fast as the etch rate of SiO_2 . Therefore, since the ARC is more than three times as thick as the SiO_2 and is capped by the SiO_2 interlayer at the beginning of the etch, it will be able to endure full etching of the SiO_2 layer.

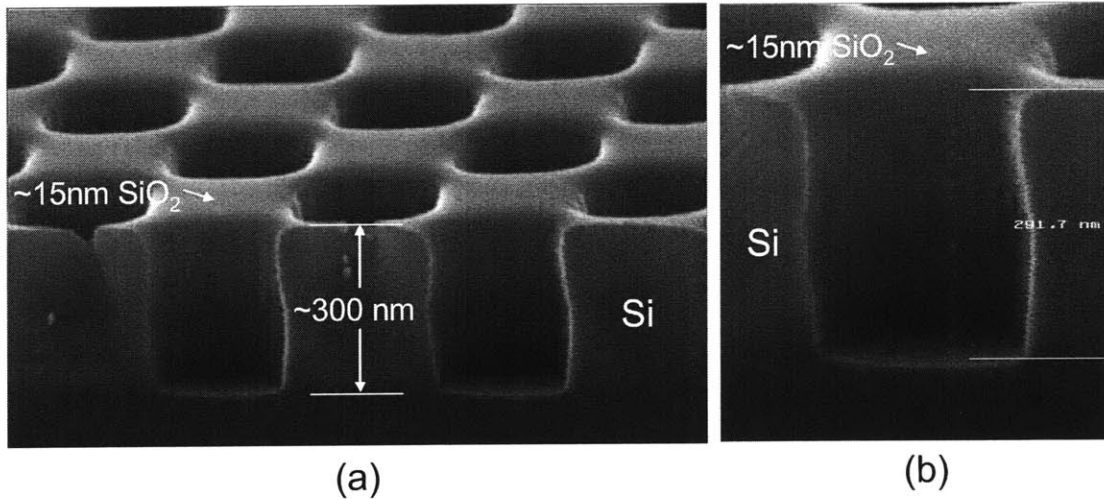


Figure 3-13 SEM images showing ~300 nm etching into silicon with a 20 nm SiO_2 hard mask layer. Etch parameters: Cl_2 (20sccm, 10mT, 90W, 600V, 2:00 minutes)

The SiO_2 hard mask layer can then be used to etch into the silicon device layers which were etched with chlorine gas. The ARC layer was not removed before this etching step. If the ARC layer was removed using an ashing step, etching of the silicon layer was not possible using chlorine. A chemical stripper known as EKC 265 manufactured by EKC Technology Ltd. can also be used to chemically remove the ARC layer, but this process was not implemented here. As shown in Figure 3-13, after 2 minutes of etching in chlorine, holes were etched ~300nm deep into the silicon layer. The remaining SiO_2 hard mask layer has been sputtered and is therefore thinner than its original 40 nm thickness. As evident from Figure 3-13, the sidewalls of the hole profile are not perfectly straight. This hole profile has been seen a number of times during the etching of silicon and may be due to the angular distribution of ions as they accelerate into the holes to etch the material. If ions travel into the holes with a small velocity component parallel to the substrate surface, etching can occur in the horizontal direction contributing to rounded side-walls.

The reactive ion etching process described for the trilayer resist stack and the silicon device layer was also explored for devices requiring deeper holes in silicon. For the process described above, 300nm holes in silicon were fabricated. However, as discussed below, fabricating deeper holes with a depth of ~750 nm was also accomplished.

Etching deeper holes in silicon requires a thicker hard mask layer that can withstand the longer etch times. In this case, a hard mask layer consisting of 250 nm of HSQ was used. HSQ (hydrogen silsesquioxane) is a spin-on dielectric, or a “flowable oxide,” produced and sold by Dow Corning, Inc. When spun onto a substrate and baked to remove solvents, HSQ consists of molecules of SiOH. However, when exposed with an electron beam, or baked at high temperatures, many H-O bonds in this structure are converted to O₂ bonds so that the material more closely resembles SiO₂ and etches in the same RIE and wet etch chemistries. HSQ is often used in the Nanostructures Lab at MIT because it can be exposed and patterned as a negative resist using electron beam lithography. In this thesis, however, HSQ was explored as a convenient, thick (250nm) hard mask layer for etching devices in silicon.

After spinning FOX 14 HSQ (FOX 14, manufactured by Dow Corning, refers to the thickness grade of HSQ) onto wafers at 3 krpm for 1 minute to achieve a layer thickness of ~250 nm, the wafers were baked on hotplates at 150°C for 2 minutes and then at 220°C for 2 minutes. In order to incorporate more oxygen into the HSQ, the samples were He/O₂ ashed for 20 minutes. Without this ashing step, subsequent spinning of ARC was difficult because of poor adhesion to HSQ. Ashing seemed to help promote adhesion of the ARC layer. Using an adhesion primer such as HMDS (Hexamethyldisilazane), seemed to chemically alter the HSQ layer and was therefore not used. Once the ARC layer was successfully spun on, a 20 nm SiO₂ interlayer was evaporated and the resist layer was spun in a similar manner as described previously for preparing the trilayer resist stack.

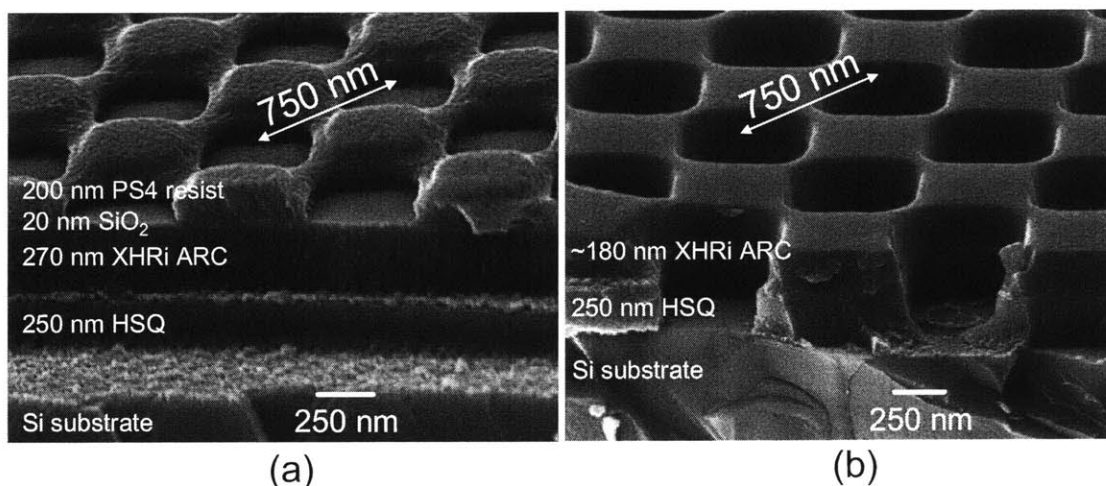


Figure 3-14 SEM images showing cross-section of trilayer resist stack (a) before RIE and (b) after RIE. Etch parameters: CHF₃(10mT, 100V, 230-245W, 0:56 min), He/O₂(2:1sccm, 10mT, 250V, 105W, 7:20 min), CHF₃(10mT, 100V, 215W, 7:19 min)

SEM images of the trilayer resist stack and etched HSQ hard mask layer are shown in Figure 3-14. Etching of the thicker hard mask layer was performed using CHF_3 rather than CF_4 because CHF_3 sputters, but does not chemically etch the ARC layer. For etching of a 250 nm hard mask layer, the simultaneous etching of the ARC layer may compromise the pattern transfer process if the ARC becomes too thin.

With successful etching of the HSQ hard mask layer using CHF_3 RIE, the remaining ARC is removed, and the silicon device layers can then be etched. He/O_2 ashing for 30 minutes successfully removed the remaining ~ 150 nm of ARC. Figure 3-15 shows SEM images after the hole pattern in HSQ was etched into silicon using chlorine reactive ion etching. An etch depth of approximately 780 nm was accomplished in 20 minutes implying an etch rate of ~ 40 nm/minute. As evident from Figure 3-15(a), the HSQ hard mask layer withstands silicon etching with $\sim 10\%$ sputtered away over the duration of the etch (implied etch selectivity $>30:1$). This result suggests that deeper etches may be accomplished with this same hard mask layer.

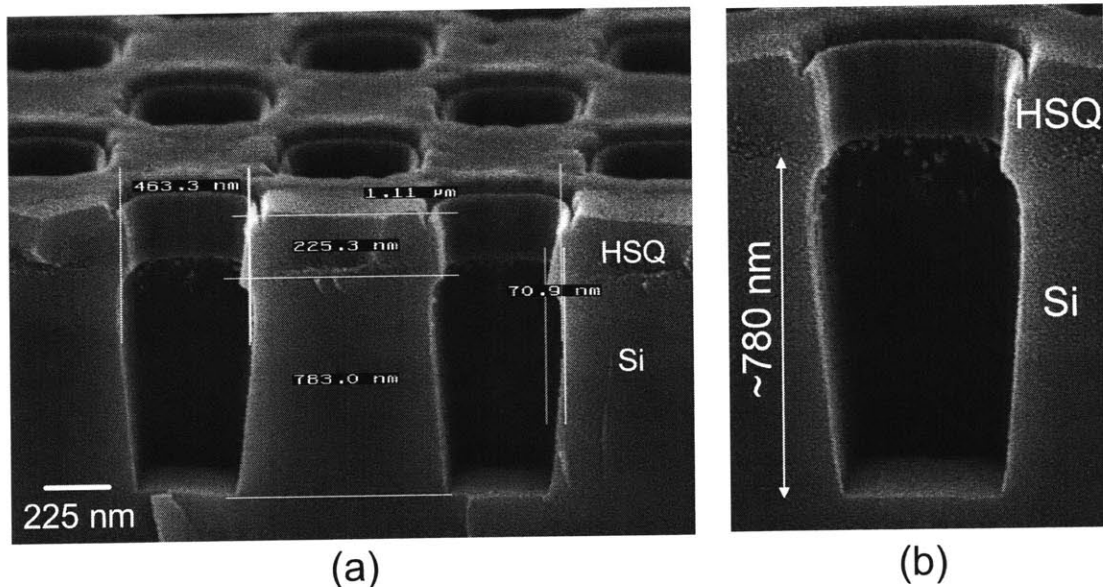


Figure 3-15 SEM images showing sub-micron etching into silicon with Cl_2 reactive ion etching. Etch parameters: $\text{Cl}_2(10\text{mT}, 420\text{V}, 50\text{W}, 20:00)$

Though these etch results seem to indicate that HSQ can be used as a good hard mask layer for etching silicon, one problem was encountered that seemed to compromise its performance. In order to improve the side wall profile of reactive-ion-etched silicon using chlorine, it has been suggested that the total etch time be divided into a number of steps. In between each etching step, the RIE chamber should be vented so that the sample is

exposed to atmosphere, and then pumped down again for another etching step. The idea behind the multiple etching steps, as suggested by Hastings [57], is that exposing the sample to atmosphere passivates the etched sidewalls such that they are more resilient to subsequent etching steps. The result is that deeper etching with straight sidewalls can be accomplished with little etching in the horizontal direction. Implementing this technique is particularly relevant for greater etch depths.

However, with an HSQ hard mask, using this etch technique was a challenge. As a first attempt, the 20 minute etch presented above in Figure 3-15 was divided into two 10 minute etches. Between the two 10 minute etches, the RIE chamber was vented, opened to atmosphere for ~5 minutes, and then pumped down again. An SEM showing the cross-section of the etched holes is shown in Figure 3-16. Though the 20-minute etch discussed above resulted in an etch depth of ~780 nm, two 10-minute etches resulted in an etch depth of ~350nm which is less than half.

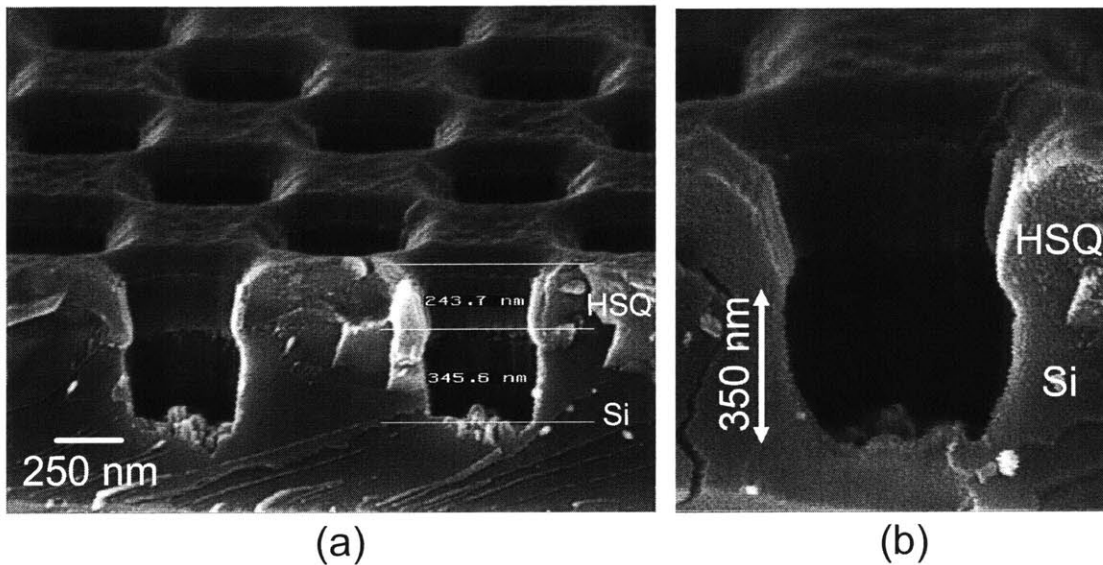


Figure 3-16 SEM images showing etch results in silicon with two Cl_2 reactive ion etching steps and a HSQ hard mask. Etch parameters: Cl_2 (10mT, 60W, 450V 10min), Cl_2 (10mT, 60W, 450V 10min)

A second attempt was made where the etch duration was split into two etches, only for this attempt, the etches were for 3 minutes and then 17 minutes. The result of this etch sequence is shown in Figure 3-17. With this etch sequence, an etch depth of only ~120nm was attained.

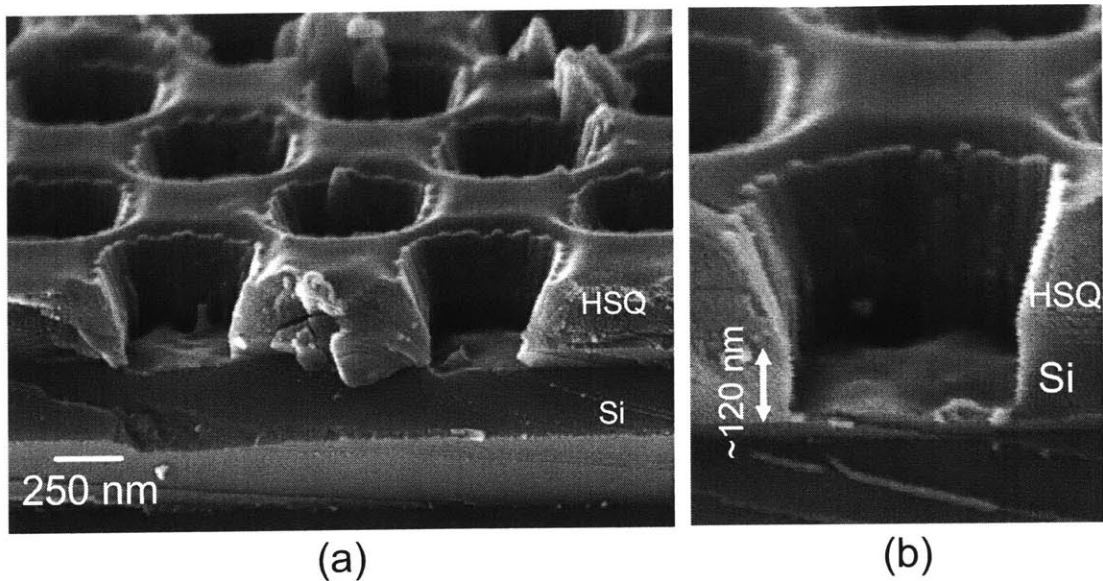


Figure 3-17 SEM images showing etch results in silicon with two Cl_2 reactive ion etching steps and an HSQ hard mask. Etch parameters: Cl_2 (10mT, 50W, 450V 3min), Cl_2 (10mT, 50W, 450V 17min)

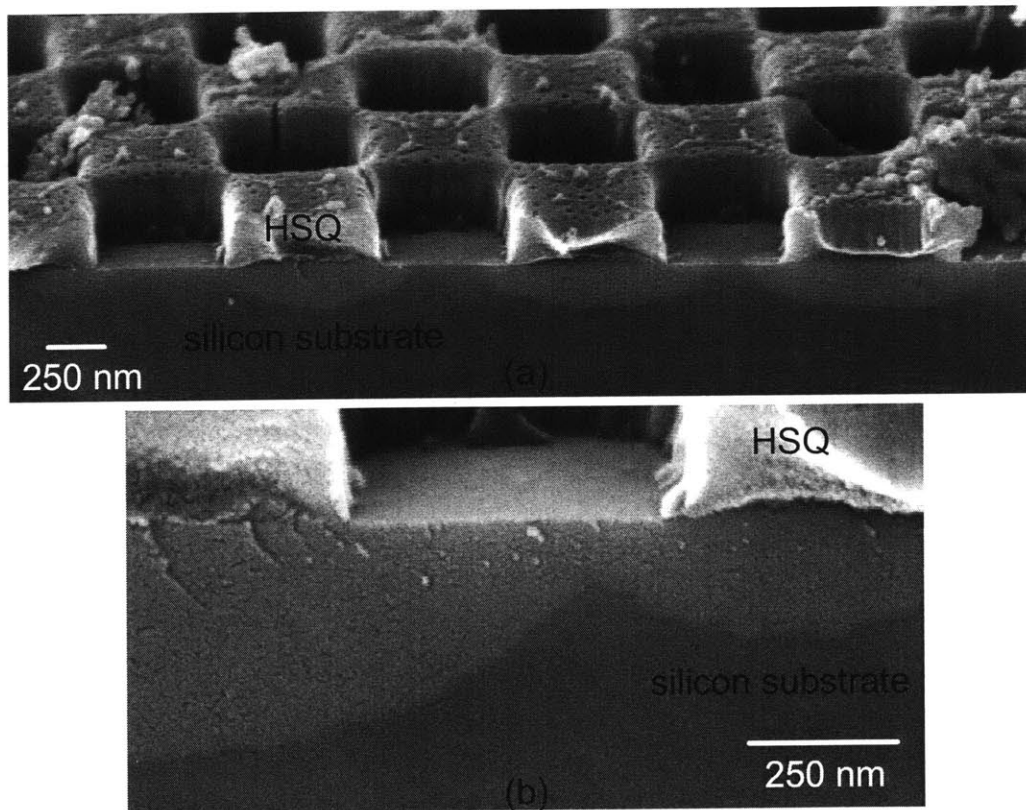


Figure 3-18 SEM images showing HSQ layer after ashing to remove the ARC layer. Notice the discoloration of the silicon substrate underneath the HSQ areas.

The result of this etch sequence seems to indicate that after the first etch step, the substrate is not etched during the second etch. Perhaps, the material composition at the bottom of the holes has been altered such that it no longer etches in chlorine. Further investigation of this phenomenon was not pursued though another observation was made which may be related. SEM images (see Figure 3-18) of the HSQ hard mask layer after removal of the ARC layer with ashing but before reactive ion etching of the silicon, show discoloration of the substrate material underneath areas of HSQ. Under the hole regions, the discoloration is less present or not present at all. In fact, it seems that the discoloration grows from HSQ regions and expands isotropically into hole regions. Perhaps the ashing step, promotes diffusion of ions into the silicon substrate which alters the silicon's chemical composition. Referring back to Figure 3-15(b), the discoloration seems to have been driven deeper into the substrate over the duration of the 20 minute etch. The high temperatures achieved during reactive ion etching may be responsible for the observed diffusion process.

Further investigation of these observations was not performed. The conclusion is that deep etching into silicon with an HSQ hard mask can be accomplished as long as one etching step is used. Straight sidewalls are not achieved and a "bowing" of the sidewall is observed which changes the effective hole size. However, because the hole size often results in a shift in the optimal wavelength of operation in many photonic crystal devices, the effects of such "bowing" can be compensated for during the device testing process with a tunable laser source.

3.2 The Superprism

3.2.1 Motivations

The "superprism effect" is one example of the unique behavior of light in photonic crystals. A photonic crystal allows the creation of a "superprism" which behaves similarly to a conventional prism only with greatly enhanced sensitivities with respect to the wavelength and direction of incident light, termed: 1) super-dispersion and 2) angular magnification, respectively. Just as a conventional prism separates multiple wavelength components of incident light to form a "rainbow," a superprism will separate the wavelengths over much wider angles due to "super dispersion." Alternatively, for a light beam consisting of a single wavelength, a small tilt in the incident angle will result in a much larger change in the propagation direction of the outgoing beam. Thus, a superprism can be used to magnify the

angular range of a single wavelength of light in order to steer a beam over wider angles; this second property is termed “angular magnification.” Being able to realize the enhanced effects of a superprism would be very useful for a number of applications ranging from new devices for wavelength-division-multiplexed (WDM) systems to a new class of optical elements for beam manipulation within integrated optical circuits. Spectral separation and beam steering functions are more compactly controlled using a single superprism device rather than a larger system composed of prisms, lenses, and mirrors.

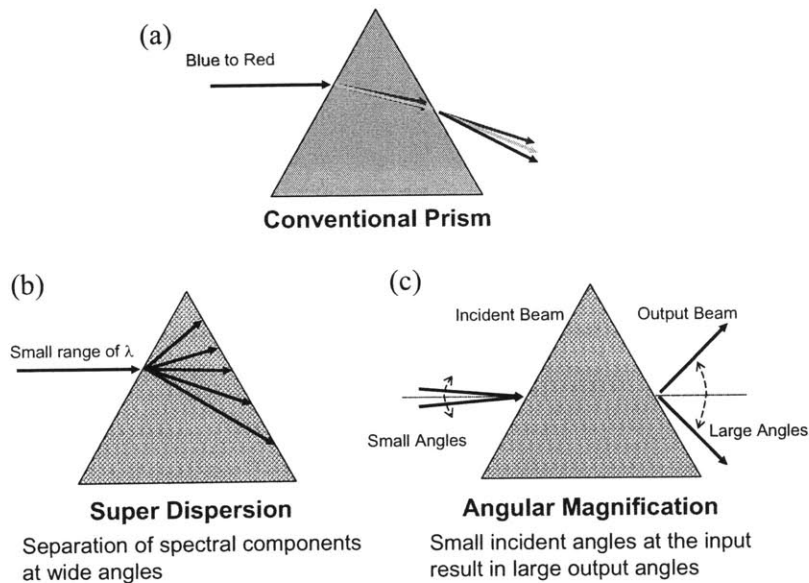


Figure 3-19 (a) Illustration of spectral separation in a conventional prism. (b) Illustration of super-dispersion in a superprism (c) Illustration of Angular magnification in a superprism. (adapted from [58])

A material can influence the propagation of light by affecting its group velocity and/or phase velocity characteristics. The group velocity is a vector which indicates the direction of energy propagation ($\mathbf{v}_g = \nabla_{\mathbf{k}}\omega$), while the phase velocity is a scalar whose value ($v_p = \omega/|\mathbf{k}|$) is the “speed of light,” or the speed of the electromagnetic phase front within a material. The vector k ($|\mathbf{k}| = 2\pi/\lambda$) indicates the direction the phase fronts propagate. In uniform isotropic materials, the group velocity and the k -vector point in the same direction and are dependent on orientation and frequency. For example, inside a conventional glass prism, a spectrum of colors diverges due to the frequency dependence of the phase and group velocities. By creating a periodic variation in the index of refraction of a material to form a “photonic crystal,” the group velocity and phase velocity characteristics of light can be engineered to have a much stronger dependence on frequency and/or orientation. As a result, photonic crystals (PCs) are at the heart of the superprism effect. In addition,

because the group velocity and k -vector in a PC can point in very different directions, the conditions in which the group velocity is highly sensitive to orientation and wavelength can differ from the conditions in which phase velocity is sensitive to orientation and wavelength.

A number of groups have previously designed and fabricated superprism devices using different photonic crystal designs [58-62]. The common theme between these groups is that they have utilized the sensitivity of the group velocity, to accomplish either angular magnification or super dispersion. The photonic crystals utilized by these groups were designed to exhibit large changes in the group velocity for small changes in wavelength or orientation. Kosaka, *et al.* used a three-dimensional (3D) photonic crystal to demonstrate both super dispersion and angular magnification based on the directional and spectral sensitivity of the group velocity within the PC [58, 63]. Large changes in the beam direction within the photonic crystal were demonstrated for small changes in both angle and wavelength. For a wavelength shift of $0.01\mu\text{m}$, Kosaka, *et al.* demonstrated a 50° shift in the direction of propagation within the photonic crystal. In a conventional silicon prism, they calculated this shift to be less than one degree. They also demonstrated that changing the incident angle from $\pm 7^\circ$ at the input resulted in a swing of $\pm 70^\circ$ within the photonic crystal. Though these two-dimensional results seem promising as a demonstration of superprism phenomena in photonic crystals, the three-dimensional structure is complicated to fabricate. However, this experiment does not preserve the angular characteristics of the beam once it exits the photonic crystal. The superprism effect may reverse itself, or the beam may "refract back" at the output of the device. Alternatively, to circumvent the fabrication complexities associated with the 3D superprism, Nelson, *et al.* demonstrated that strong wavelength dispersion effects can be achieved using a simpler one-dimensional photonic crystal composed of multiple GaAs/AlGaAs layers [60]. For this device, wavelength separation due to dispersion in the angle of propagation within the crystal, translates into a lateral shift in the position of each wavelength upon exiting the crystal. While the fabrication is indeed simpler, this device shifts the location of the output beam rather than affecting its angle of propagation. In addition, the multiple bounces necessary to introduce significant beam shifting with a thin layered structure introduce heavy losses into the system. Wu, *et al.* also used group velocity effects to demonstrate that a 2D photonic crystal of air holes in GaAs can be used to observe superprism effects using a planar configuration [61]. Wu, *et al.* relied on the group velocity sensitivity to change the direction of the beam as the incident wavelength changes. In Wu's design, the photonic crystal hole array occupies a semi-circular area. A wide input waveguide couples light into the flat facet of the semi-circle while output light is collected via a number of waveguides positioned at

various angles along the curved facet. Wu observed that by changing the wavelength at the input, the output power would shift from one waveguide to another demonstrating the super-dispersive property of the photonic crystal. Though Wu could successfully demonstrate wavelength dispersion using the photonic crystal, a number of other issues are left unresolved. For example, the curved output facet of the photonic crystal introduces scattering centers due to the break in the periodicity of the photonic crystal. Using a wide, multimode input waveguide, while preventing diffraction into the photonic crystal, will excite multiple photonic crystal modes that will propagate in different directions. Because the input excitation from the waveguide does not have a plane wave profile, it will also excite multiple modes in the photonic crystal. Therefore a number of factors in this design can allow multiple modes to propagate through the photonic crystal--an unwanted effect if only one output beam is desired. In addition, Wu's design has weak confinement in the vertical direction as a GaAs slab ($n \sim 3.4$) was used as the guiding layer, with SiO_2 (~ 1.5) as the upper cladding layer, and $\text{Al}_{0.9}\text{Ga}_{0.1}\text{As}$ ($n \sim 2.9$) as the bottom cladding layer. However, Wu's device does demonstrate that 2D photonic crystals can be fabricated with simple fabrication processes and can be used to observe superprism effects at a device output. With a silicon-on-insulator (SOI) layered structure, Lupu, *et al.* also demonstrated that group velocity effects within a 2D photonic crystal slab allow small changes in the incident beam's wavelength to significantly alter a beam's direction [62].

Each of the aforementioned reports have shown that photonic crystals can be used to greatly alter the propagation angle of light while traveling within the photonic crystal. A small change in the direction of light at the input to the photonic crystal can result in a larger change in direction while traveling within the PC. To maintain the angular effect when light exits the photonic crystal or a region containing the photonic crystal, group velocity sensitivity is not sufficient. While the sensitivity of the group velocity *within a photonic crystal* can allow significant bending of light within the PC for small input variations, the phase velocity determines the angle of propagation when light exits the PC and enters a uniform material. In uniform materials, the propagation angle is calculated using Snell's Law, whereas in photonic crystals, the propagation angle depends on the band structure. In general, the propagation angle after *any* interface is determined by a boundary condition which requires the tangential component of the k -vector to remain constant. Since the phase velocity is related to the k -vector through $v_p = \omega/|\mathbf{k}|$, while the group velocity is related through a derivative, the phase velocity directly determines the behavior of light at the boundary. For a small change in k -vector orientation at the input, if the photonic crystal introduces large differences in the group velocity with no difference in

the phase velocity, the small angular change at the input only results in a translation of the beam's output location with no change in its angular properties. In other words, the beam "refracts back" to its original angle of incidence at the output of the photonic crystal.

In this thesis research, a superprism structure is designed using a large area two-dimensionally periodic photonic crystal slab such that angular magnification can be observed in an output slab of uniform material. For a given input and output of the structure, a small angular swing in the input angle results in a large angular swing of the output angle. The superprism effect explored in this work relies on angular sensitivity of the phase velocity rather than sensitivity of the group velocity. By affecting the angular dependence of the phase velocity, the enhanced effects introduced by the photonic crystal are preserved as the beam propagates out of the photonic crystal into uniform material. An additional advantage of the phase velocity approach is that the photonic crystal can be terminated along lines of symmetry, thereby avoiding scattering effects normally associated with photonic crystal structures of other terminations. To demonstrate the feasibility of the phase velocity-dependent superprism approach, the relevant equi-frequency curves are calculated with a 3D eigen-frequency solver [64]. Finite-difference time-domain (FDTD) simulations [65] of a 2D model are also performed. The 2D calculations indicate that a wide excitation beam approximating a plane wave, is necessary for clearly observing the angular magnification property of the superprism. As a result, the superprism structure containing a large area photonic crystal is required to allow the wide beam to propagate through the photonic crystal. A technique for fabricating the large area 2D slab structure has also been explored using interference lithography to pattern nanometer-sized features over centimeter-scale areas. The requirements for testing the structure will also be discussed.

3.2.2 Design theory and simulations

The superprism structure described herein was designed to use a photonic crystal to observe angular magnification as light enters a uniform medium. Therefore, the photonic crystal slab was designed such that large changes in the phase velocity (and k -vector) are created for small changes in the angle of incidence as suggested by Luo, *et al.* [66] and Baba, *et al.* [67]. A convenient way to analyze the directional dependence of the k -vector within the photonic crystal is by calculating and plotting its dispersion surface. The dispersion surface, also known as an equi-frequency surface, maps out the allowed k -vectors for all orientations within a structure for a constant frequency. As illustrated in Figure 3-20, in a uniform isotropic material the dispersion surface is a circle, so that the

phase and group velocities are independent of orientation. The radius of the circle is the magnitude of the k -vector, which scales with the phase velocity, and the group velocity points away from the circle in the direction normal to the surface. However, in photonic crystals, due to the periodicity in the refractive index, neither the phase velocity nor group velocity are constant and both depend on direction. Hence, the dispersion surface is no longer circular.

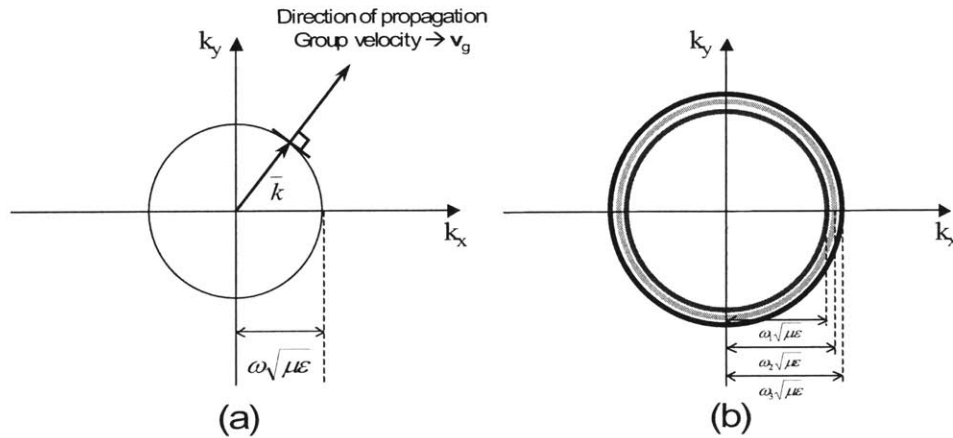


Figure 3-20 (a) Illustration of a dispersion surface showing an example of a k -vector and the group velocity. (b) Illustration showing how the dispersion surface radius changes with the phase velocity or frequency.

A dispersion surface with low curvature regions is ideal for causing the superprism effect where large changes in the phase velocity occur for small changes in direction. In contrast, dispersion surfaces with regions of high curvature are ideal for creating a large group velocity change for a small shift in orientation. Figure 3-21 presents the calculated dispersion surfaces associated with a number of frequencies for the structure shown. The structure consists of a photonic crystal slab with a square lattice of air holes in the top silicon layer of a silicon-on-insulator wafer. The dispersion surfaces are presented as a function of normalized frequency and scale linearly with wavelength. The photonic crystal has a lattice constant a , a hole radius $r=0.4a$, a silicon layer thickness $t_{\text{Si}}=14a/15$, and an underlying SiO_2 layer thickness $t_{\text{ox}}=4a$. The "flattest" dispersion surface occurs at a normalized frequency of $fa/c=0.22$ suggesting that superprism operation will occur at this frequency. The lattice constant is then chosen to be $a=0.22\lambda_{\text{air}}$ based on the desired operating wavelength. With a square lattice of holes, the dispersion surfaces have a square symmetry that allows for "flatness" to be achieved for a larger range of k . Using a hexagonal lattice would create hexagonally-symmetric dispersion surfaces which are "flat" for a smaller range of k -vector orientations.

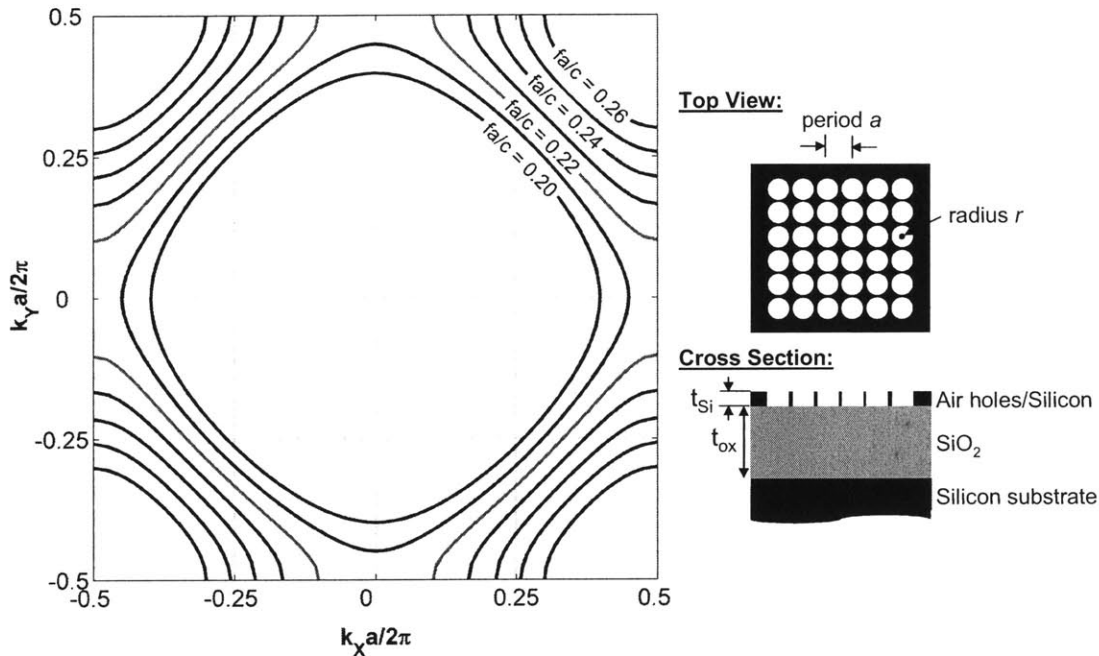


Figure 3-21 Three-dimensional dispersion surface calculations for the even mode (TE-like; electric field mostly in the plane of the slab) of a 2D-periodic photonic crystal slab ($r=0.4a$, $t_{Si}=14a/15$). Efficient superprism behavior is enabled by the "flatness" of the dispersion surfaces over large parameter regimes in k -space. Simulations performed by Dr. M. Soljacic.

The superprism phenomenon expected from the relevant dispersion surface ($fa/c=0.22$) in Figure 3-21, is illustrated in Figure 3-22. A schematic of the light path through the entire photonic crystal with input and output interfaces is shown in Figure 3-22(a). Note that for the phase velocity-dependent superprism effect, the output PC/Si interface is rotated 90° with respect to the input Si/PC interface [see Figure 3-22(a)]. Figure 3-22(b) illustrates the refraction of light using the dispersion surfaces at the Si/PC interface, and Figure 3-22(c) illustrates refraction at the PC/Si interface. The grey and black arrows in Figure 3-22(b) represent k -vectors for two different input beams which differ by only a small angle ($\Delta\theta_{IN}=0.79^\circ$). As light propagates from silicon into the photonic crystal, the k -vectors move from the circular uniform dispersion surface of silicon to the square-shaped photonic crystal dispersion surface. At the Si/PC interface, the tangential component of the incident k -vector must be conserved as the input beam propagates into the photonic crystal (illustrated by the dash-dotted construction line which is a line of constant tangential k). The intersection of the construction line with the photonic crystal dispersion curve determines the k -vector within the photonic crystal. The small angular difference between the two input wavevectors translates into a large change in the normal component of the wavevector inside the

photonic crystal due to the flatness of the dispersion surface (tangential k is conserved). The two beams then travel toward the output interface of the photonic crystal with the energy propagating in the direction of the group velocity ($\mathbf{v}_g = \nabla_{\mathbf{k}} \omega$) as shown in Figure 3-22(b).

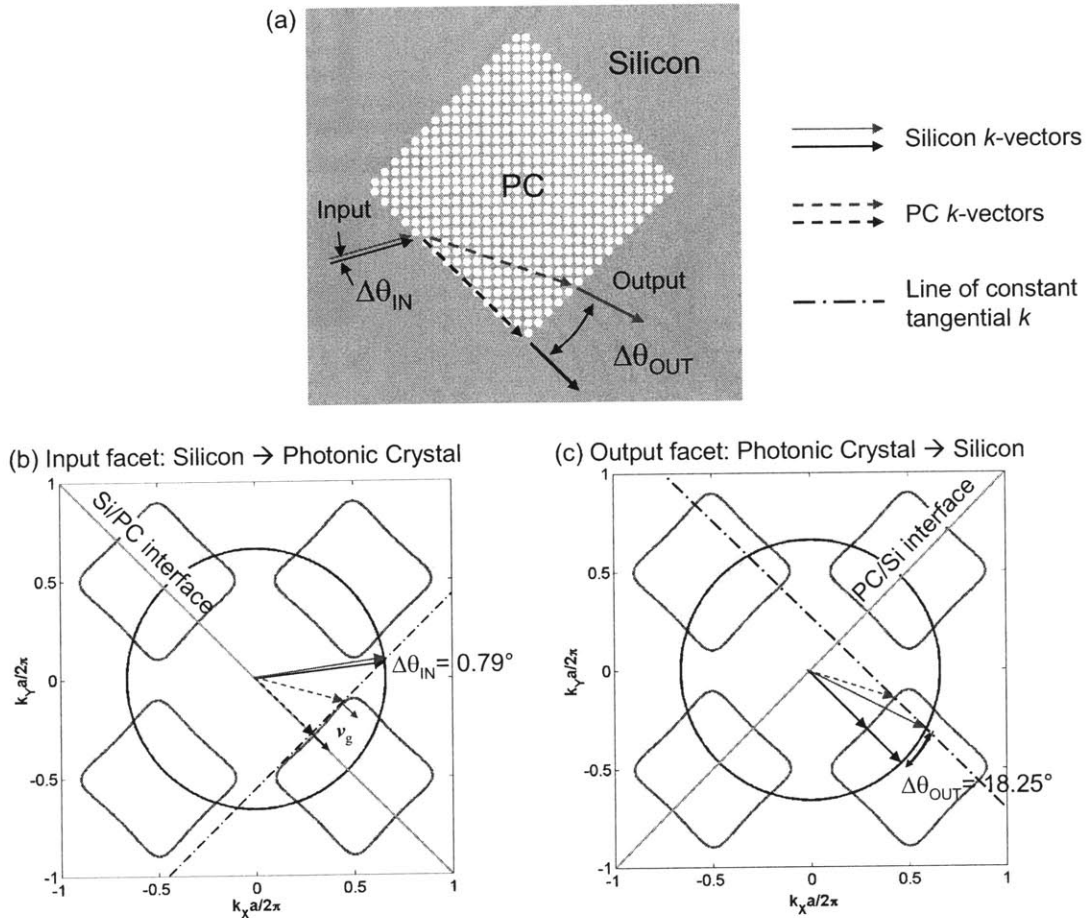


Figure 3-22 Schematic illustrating the mechanism for superprism angular magnification using the dispersion surfaces of silicon and the photonic crystal. (a) The light path through the full superprism structure. (b) Coupling into the photonic crystal from silicon. (c) Coupling out of the photonic crystal into silicon. Note that the dash-dotted lines in (b) and (c) represent lines of constant tangential k [68].

In the designed structure, the output interface is rotated by 90° with respect to the input interface [Figure 3-22(a)] so that the large difference in the normal component of the k -vector introduced at the input, results in a large difference in the tangential k -vector at the output. With the tangential k -vector conserved as the beam propagates out of the photonic crystal, the two beams now travel in different directions within the uniform silicon slab [Figure 3-22(c)]. The result is a large angular change at the output of the photonic crystal

for a very small angular difference at the input of the photonic crystal. For example, with $fa/c=0.22$, changing the input angle from $\theta_{IN}=38.71^\circ$ to $\theta_{IN}=37.92^\circ$ ($\Delta\theta=0.79^\circ$) will result in the output angle shifting from $\theta_{OUT}=0^\circ$ to $\theta_{OUT}=18.25^\circ$, implying an angular magnification factor $\Delta\theta_{OUT}/\Delta\theta_{IN}\approx 23$. All angles are defined with respect to the normal at the boundary.

Because the process implemented for fabricating the superprism structure can result in holes with a square shape, dispersion surface calculations were repeated for a structure with square-shaped holes of equal area to the circular holes discussed above (*i.e.* squares of width $d=0.71a$). At a 5% higher frequency, the calculated dispersion surfaces for square holes resemble the dispersion surfaces for circular holes. More specifically, for the circular hole structure, the dispersion surface at the normalized frequency of $fa/c=0.22$ closely resembles the dispersion surface at $fa/c=0.22*1.05$ for the structure with square-shaped holes. Operating a superprism with square-shaped holes at a frequency of $fa/c=0.22$, would imply that the angular magnification is $\Delta\theta_{OUT}/\Delta\theta_{IN}\approx 15.5$ ($\theta_{IN}=36.90^\circ$ to $\theta_{IN}=36.10^\circ$, $\theta_{OUT}=0^\circ$ to $\theta_{OUT}=12.43^\circ$). Changing the frequency of operation to $fa/c=0.22*1.05$ would improve the magnification factor to $\Delta\theta_{OUT}/\Delta\theta_{IN}\approx 23$ --which is equivalent to the performance of the structure with circular holes.

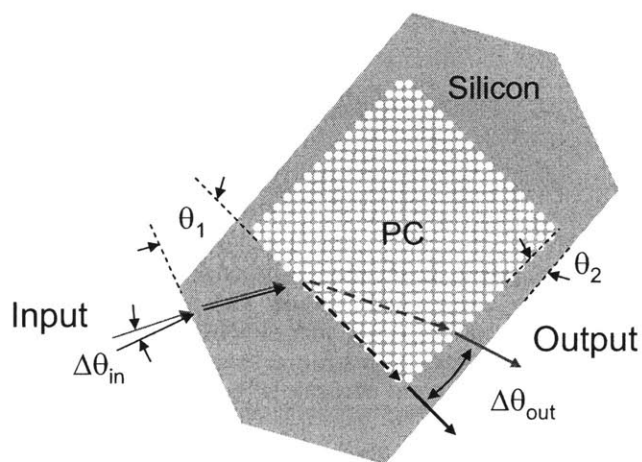


Figure 3-23 Schematic illustrating a superprism structure for use in free space applications.

The phase velocity effect can also be explored for realizing the superprism effect outside of the dielectric slab in air. As illustrated in Figure 3-23, input and output facets can be defined as air-silicon boundaries positioned at specific angles (θ_1 , θ_2) with respect to the photonic crystal edge. The orientation of these facets with respect to the photonic crystal edge can be designed such that light entering the input facet at near normal incidence, then exits the output facet at larger angles centered about the normal direction. The silicon regions thus

act as conventional prisms to facilitate coupling to the photonic crystal from air at the appropriate angle for superprism action.

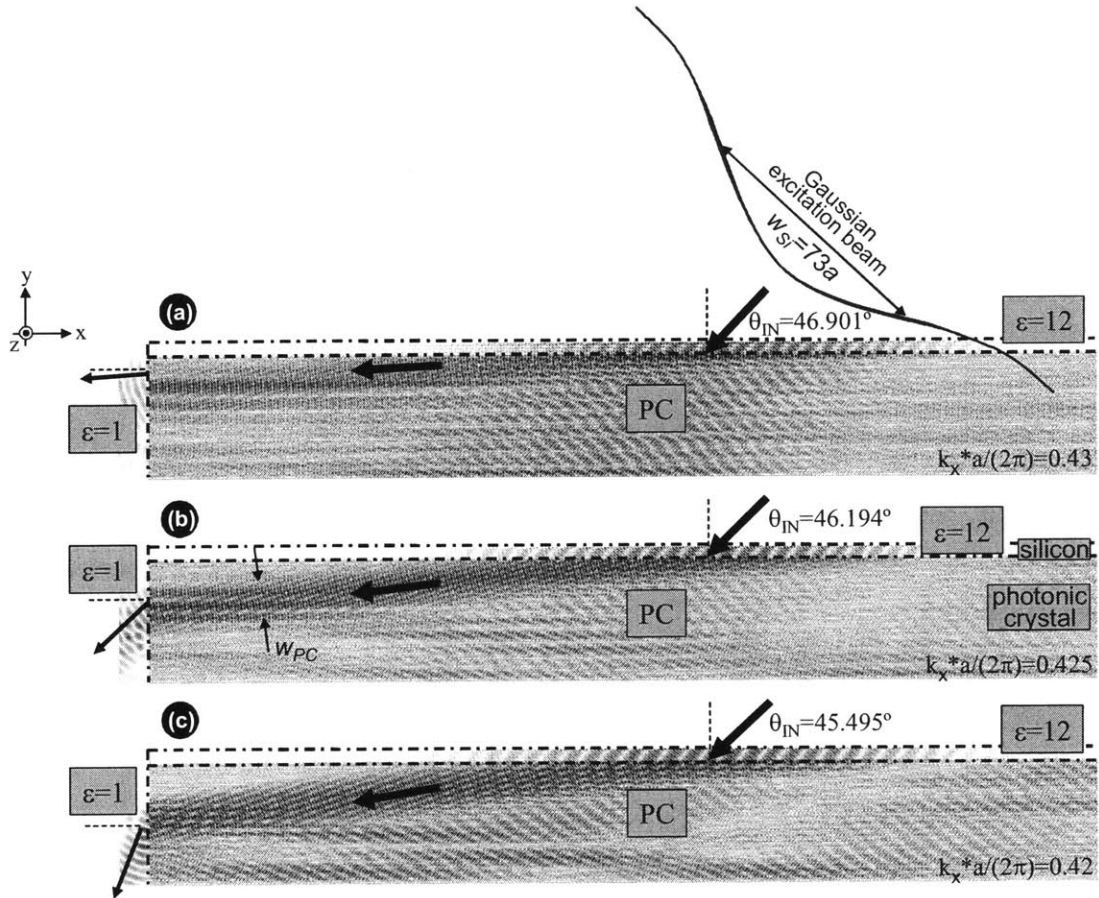


Figure 3-24 Finite-difference time-domain simulation of a simplified 2D model of the structure simulated in Figure 3-21. All cases (a) through (c) are calculated with a normalized frequency of $fa/c = 0.17$, with the electric field in the plane. Propagation of light from silicon ($\epsilon=12$), through the photonic crystal, into air ($\epsilon=1$) is shown. All angles are measured with respect to the normal direction [68].

To demonstrate the feasibility of the phase velocity-dependent superprism effect, finite-difference time-domain simulations were performed on a simplified, more numerically tractable two-dimensional model. The simplified system has a square lattice photonic crystal of lattice constant a , circular air holes with radius $r=0.35a$, and dielectric constant $\epsilon=12$ (silicon), but is purely 2D, assuming infinite structure thickness. The dispersion curves of the 2D system are similar to those of the 3D case that was presented in Figure 3-21 but with small quantitative differences which result in an optimal operating frequency of $fa/c=0.17$. At this frequency, changing the input angle for the structure described in Figure

3-22 from $\theta_{IN}=46.41^\circ$ to $\theta_{IN}=44.56^\circ$ will result in the output angle swinging from $\theta_{OUT}=0^\circ$ to $\theta_{OUT}=24.92^\circ$ for an angular magnification of $\Delta\theta_{OUT}/\Delta\theta_{IN}=13.47$.

In the simulation that is shown in Figure 3-24, a single frequency ($fa/c=0.17$) Gaussian beam [$I \propto \exp(-2r^2/w_{Si}^2)$, where $w_{Si}=73.12a$] is launched within the high index silicon region ($\epsilon=12$), propagates into and within the photonic crystal, and then exits into air ($\epsilon=1$). Figure 3-24(a) through (c) show the time evolution of the z component of the magnetic field distribution for three slightly different angles, θ_{IN} ($46.2^\circ \pm 0.7^\circ$). All of the simulations were performed with a numerical spatial resolution of 20 points/ a with a simulation area of $450a \times 50a$. The arrows within the figures serve as guides to the eye demonstrating how the direction of the beam shifts for a slight change in the input angle. Also, notice that the width of the magnetic field distribution in the photonic crystal is narrow ($w_{PC} \sim 15a$) and fairly constant for small input variations. A wide range of wavevectors are excited in the slab as the beam enters the PC. By applying the Fourier transform, a wide range of k -vectors implies a narrow beam width in space. In each of these cases, [Figure 3-24 (a), (b), and (c)], the total transmitted output power was approximately one quarter of the input power. The remaining power was lost in two forms: 1) insertion loss due to reflection at the photonic crystal's input facet, and 2) power internally reflected within the photonic crystal at the output facet. In all of the simulation cases, internal reflection from the output facet then experiences subsequent reflections within the photonic crystal.

Since the output beam in air, shown in Figure 3-24, is excited with a narrow beam within the photonic crystal ($w_{PC} \sim 15a$), the output beam is divergent, implying that it is composed of a range of k -vectors. With a divergent output beam, observation of the superprism effect becomes difficult to resolve. To broaden the propagating light within the PC and lessen its divergence, a wide excitation beam with a minimal range of input k -vectors is necessary. In other words, because a superprism is inherently sensitive to differences in k , the excitation beam should approximate a plane wave (*i.e.* a single k -vector) if the superprism effect is to be clearly resolved. A 2D simulation with a very broad excitation is computationally intensive. Nevertheless, the simulated behavior of light demonstrated in Figure 3-24 indicates that when a broad excitation beam is used, a large area PC is required.

3.2.3 Objective

The goal of this thesis research is to design and fabricate a superprism device using a two-dimensional photonic crystal such that the superprism effects are observed at the output

using only one excited mode of the photonic crystal. The device will allow for a small angular sweep at the input to translate into a large angular sweep at the output (*i.e.* angular magnification). In addition, an input beam with a small spread in frequencies will result in a large angular separation of these frequencies at the output (super-dispersion).

The device fabrication is explored in two different materials systems, GaAs and Si, and at two different wavelengths, 1.55 μm and 3.1 μm , as shown in Figure 3-25. In the GaAs material system, the high index material and substrate is GaAs, while the low index material is aluminum oxide. In the silicon material system, the high index material and substrate is silicon, while the low index material is silicon dioxide. Since GaAs and silicon have similar indices of refraction, the feature sizes of the device do not change with material.

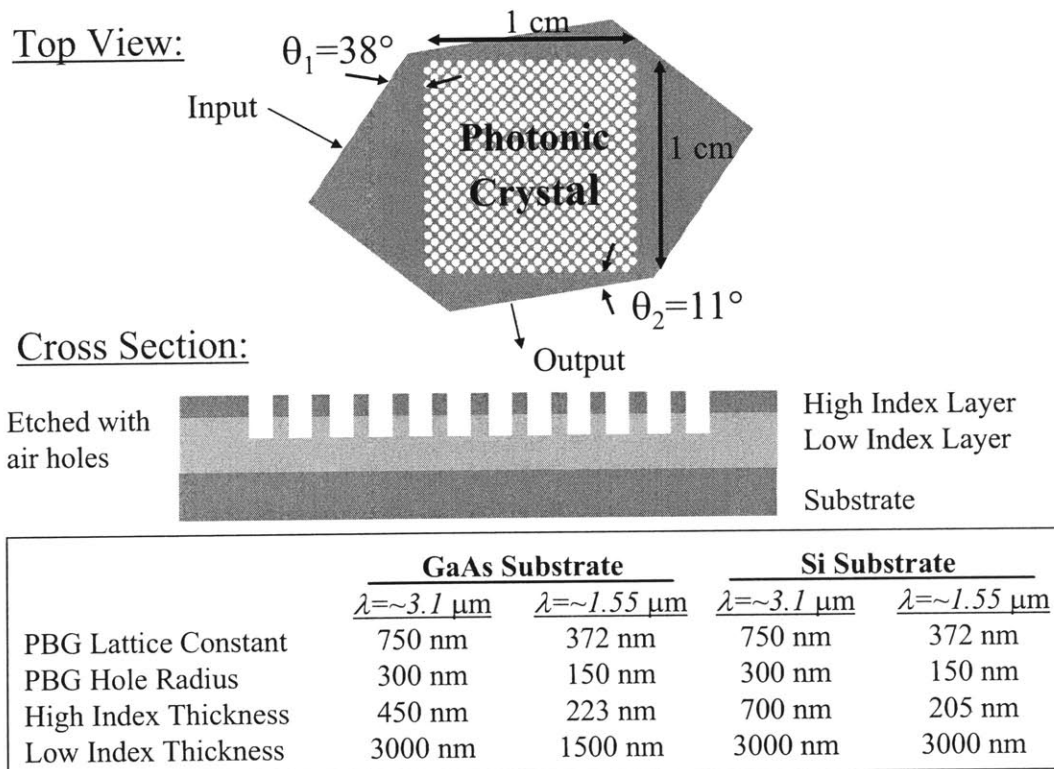


Figure 3-25 Schematic of superprism device layout (not to scale). The device is a three layered structure with the superprism input and output facets defined by etched facets.

The superprism is composed of a two-dimensional photonic crystal with a square lattice of air holes in high index material (see Figure 3-25). The photonic crystal resides on a low index layer which is bound to a substrate. The feature sizes of the photonic crystal depend on the wavelength of operation. The desired wavelengths of 1.55 μm and 3.1 μm imply lattice constants of 372 nm and 750 nm, and hole radii of 150 nm and 300 nm, respectively.

The input and output facets will be the air-high index interfaces positioned at angles with respect to the photonic crystal. The total thickness of the device (excluding substrate) will be approximately 3.5 μm , while the top surface will have an area of about 2x2 cm.

The orientation of the input and output facets with respect to the photonic crystal edge is designed such that light entering the input facet near normal incidence, exits the output facet at larger angles centered around its normal direction. The ideal performance is designed such that an input angular sweep of approximately $\pm 2^\circ$ will be amplified to about $\pm 30^\circ$ at the output for a wavelength of 3.1 μm .

3.2.4 Superprism fabrication overview

The following steps are necessary for the successful fabrication of the superprism and are illustrated in Figure 3-26:

1. The layered structure is obtained. For the GaAs-based device, the GaAs/AlGaAs layered structure is grown using gas source molecular beam epitaxy. For the silicon-based device, silicon on insulator (SOI) wafers are purchased from an outside vendor.
2. Two hard mask layers are deposited: 250 nm HSQ (spin-on glass), and 50 nm of chrome.
3. Photolithography and a wet etch is used to define the superprism shape in the chrome layer.
4. The samples are prepared with a trilayer resist stack [200 nm resist, 20 nm SiO_2 , 300 nm anti-reflection coating (ARC)]. Interference Lithography is used to pattern the photonic crystal holes using an alignment grid to align the hole pattern to the superprism shape.
5. Reactive ion etching is used to transfer the hole pattern into the HSQ hard mask layer.
6. Photolithography is used to mask the square photonic crystal area.
7. Reactive ion etching is used to remove the holes patterned outside the device shape. The photoresist and metal layers are removed.
8. Reactive ion etching is used to etch the layered structure. Cl_2 is used to etch the Si layers and BCl_3 is used for the GaAs/AlGaAs layers. The HSQ hard mask is removed.

9. For the GaAs superprism, an oxidation process is used to convert the buried AlGaAs layer to aluminum oxide.

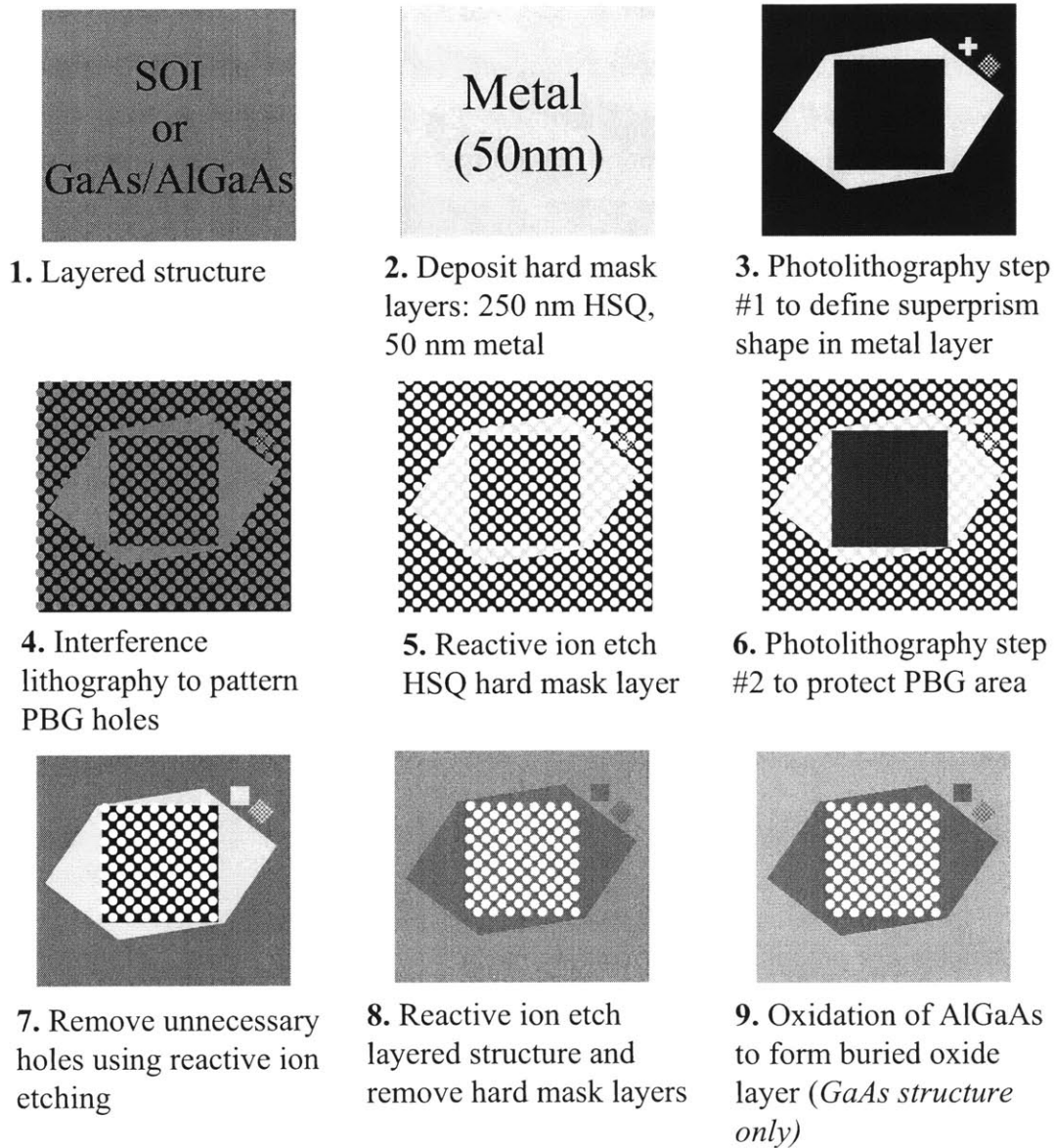


Figure 3-26 Superprism fabrication overview for both the GaAs and silicon-based device structures.

3.2.5 Photolithography

As discussed above, two photolithography steps are used to pattern the superprism device area. Both photolithography steps were performed using the Tamarak ultraviolet lamp in the Nanostructures Laboratory at MIT. Mask layouts were designed in a 2D CAD software

program called QuickCAD and the masks were fabricated by Advance Reproductions, North Andover, MA. The mask designs for both lithography steps are shown in Figure 3-27. Mask #1 shown in Figure 3-27(a) is used to pattern the superprism device shape in a resist layer. The mask features include an alignment grating which consists of crossed lines with a period of 6 μm . The lines of the alignment grating are rotated 45° with respect to the open square area. This alignment grating is used during the interference lithography step to orient the photonic crystal with respect to the device shape patterned with mask #1. Alignment marks on mask #1 allow for alignment of mask #2 [Figure 3-27(b)] to the pattern from mask #1. After the mask #1 pattern is transferred into the metal layer via wet etching, holes are patterned using interference lithography. Mask #2 is used to protect the square area in the middle of the device, so that the holes patterned outside the device area during the interference lithography step, are removed via reactive ion etching (RIE).

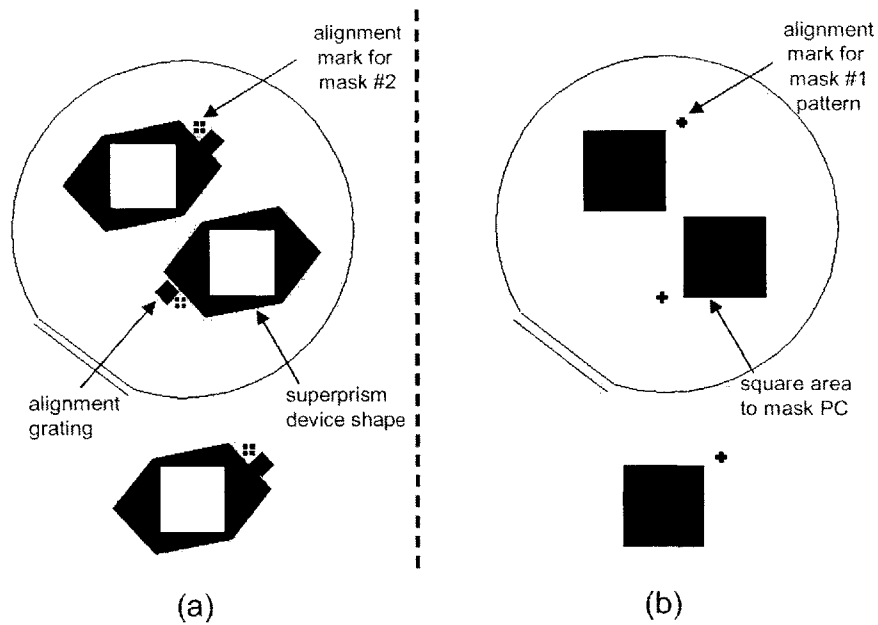


Figure 3-27 Mask designs used for patterning superprism device shape. (a) Mask #1 is used to pattern the device shape with alignment marks. (b) Mask #2 is used to protect the open square area where the photonic crystal is patterned during an interference lithography step.

Before each photolithography step, Shipley 1813 photoresist was spun at 3 krpm for one minute yielding a resist thickness of about 1.6 μm (as measured by a Dektak profilometer). The photoresist was filtered using an acrodisc filter, rated for 0.2 μm sized particles, attached to syringe while dispensing the resist onto the sample. Samples were then baked in a 90°C furnace for 30 minutes. The mask was then brought into vacuum contact with the sample and exposed with the Tamarak UV lamp. Samples were then developed using

Shipley 352 developer for 1 minute followed by a rinse with DI water. Without vacuum contact, the sidewall profile of the resist may not be perfectly straight as shown in Figure 3-28(a). Typical exposure times for straight sidewalls were about 15 seconds at an intensity of 4.5 mW/cm^2 as shown in Figure 3-28(c). Longer exposure times result in a resist profile with a more sloped sidewall as shown in Figure 3-28(b). Sloped sidewalls in the resist profile can result in sloped sidewalls when the pattern is transferred into the lower layers during subsequent etching steps. A 20 second He/O_2 ashing step is then used to clear any residual resist that may remain after development. The exposed pattern is transferred into the chrome layer by immersing the sample in CR7 chrome etchant for approximately 4 minutes. Overetching the sample during this step can potentially degrade transfer of small features from the resist into the metal layer due to the anisotropic nature of the wet etch. After etching of the chrome layer, photoresist is removed using hot NMP at 135°C for ~ 10 minutes. Acetone or another resist stripper can also be used to remove the resist.

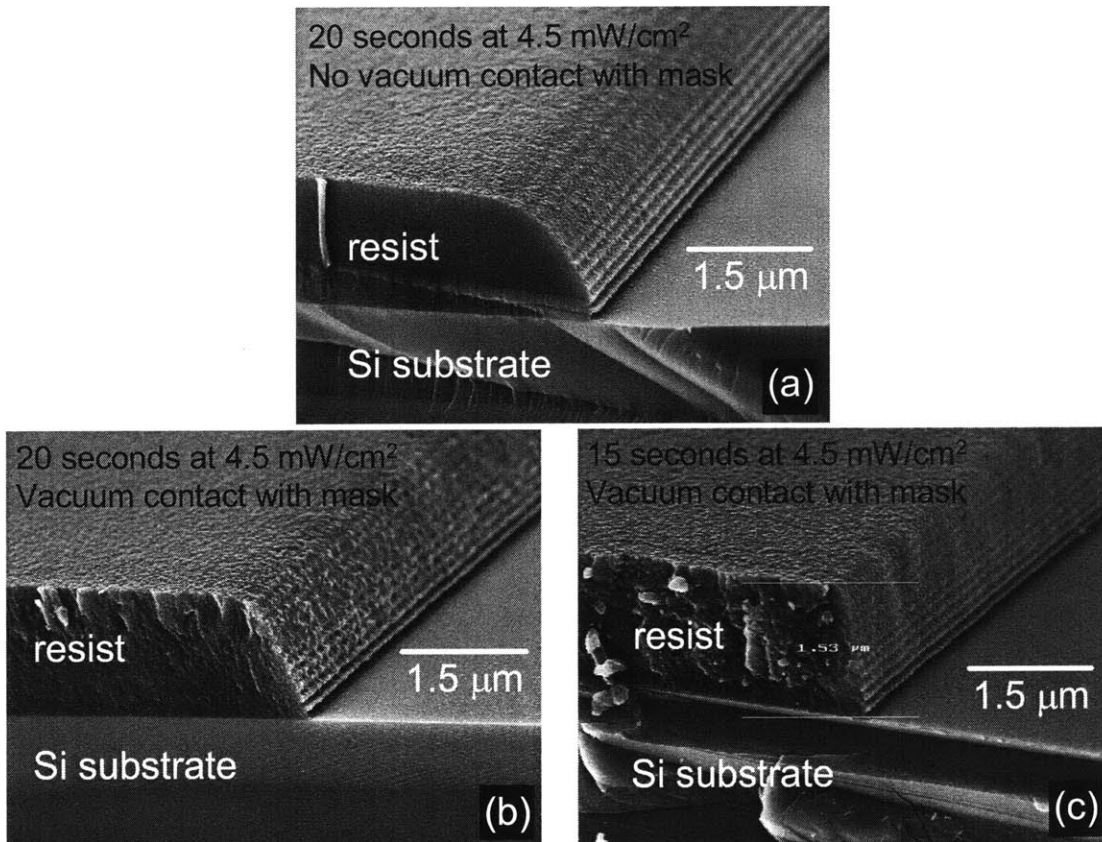


Figure 3-28 SEM micrographs showing resist profiles after photolithography and development (without ashing) under three different conditions: (a) No vacuum contact with mask, 20 sec exposure, 4.5 mW/cm^2 . (b) Vacuum contact with mask, 20 sec exposure, 4.5 mW/cm^2 . (c) Vacuum contact with mask, 15 sec exposure, 4.5 mW/cm^2 .

3.2.6 Interference lithography and photonic crystal alignment

As discussed in Section 3.1, interference lithography is used to pattern the photonic crystal holes that are necessary for the large area photonic crystal devices. Samples were prepared with a trilayer resist stack on top of the superprism device shape that was etched into the chrome layer. For the superprism structure, the two-beam interference lithography system was used because it has a substrate rotation stage in order to align the sample to the interference pattern. In order to orient the sample, an alignment grid consisting of crossed lines spaced by $6\ \mu\text{m}$ was integrated into the photolithography mask design and was transferred into a chrome layer prior to the interference lithography step. Figure 3-29 illustrates the superprism shape patterned onto a sample with the $6\ \mu\text{m}$ alignment grid.

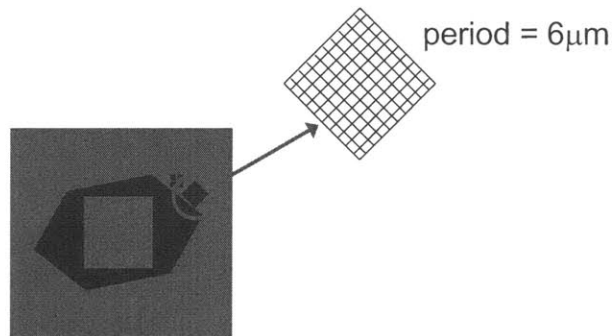


Figure 3-29 Schematic illustrating a sample with patterned superprism shape. An alignment grid with a period of $6\ \mu\text{m}$, and a line width of $3\ \mu\text{m}$, aids in orienting the interference lithography exposure.

In the two-beam IL setup, the orientation of the exposed grating is determined by the relative heights of the two beams. The grating lines form perpendicular to the plane defined by the two beams. When both beams are aligned such that they travel at the same height relative to the optical table, the grating lines are exposed perpendicularly to the table. The orientation of the $6\ \mu\text{m}$ grid matches the orientation that is desired for exposure of the photonic crystal. A HeNe laser ($\lambda=633\text{nm}$) which is mounted on the same optical table, can be used to orient the sample without exposing the sample's resist layer. The HeNe and HeCd laser beams are aligned such that both beams travel parallel to the table at the same height. As illustrated in Figure 3-30, the HeNe beam diffracts off the alignment grid so that the diffracted orders are projected from the sample. Perfect alignment is achieved when the direction of diffraction for the HeNe beam matches the orientation of the two HeCd beams used for exposure. For the superprism design, the alignment grid is rotated by 45° from the $1\ \text{cm} \times 1\ \text{cm}$ square area within the device so that the exposed photonic crystal is also rotated by 45° relative to the square opening. With the alignment grid patterned onto

the sample, the sample is placed onto the substrate chuck in the interference lithography setup. With the sample rotated by 45° as shown in Figure 3-30(b), the diffracted beams are projected either perpendicularly or horizontally to the optical table upon which the IL system is mounted. The sample is rotated until the horizontally-diffracted beams project to equal heights from the optical table surface. Greater alignment accuracy is achieved by equalizing the heights of the higher order diffracted beams. However, because the higher order beams have lower intensity, detecting them can be a challenge. Please note that the period chosen for the alignment grating is not critical and is chosen such that diffracted beams can be observed at suitable angles for the particular IL setup with the HeNe laser.

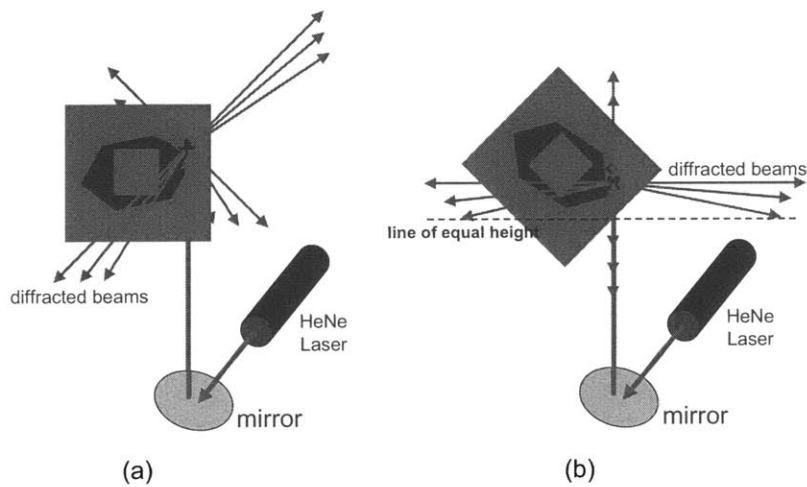


Figure 3-30 Schematic illustrating technique for orienting the sample in preparation for interference lithography exposures. (a) Unoriented sample. (b) Oriented sample. Proper orientation is achieved when the sample is rotated such that the diffracted beams are projected to the same height from the surface of the table.

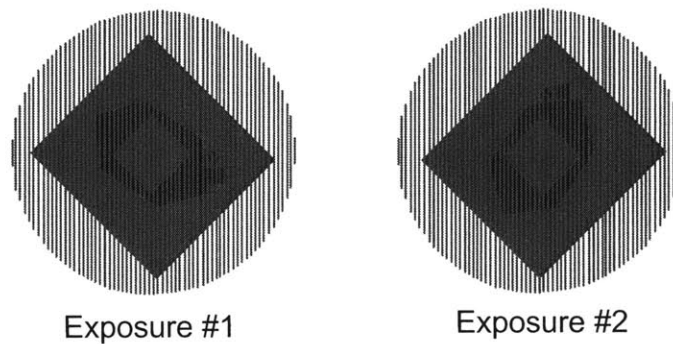


Figure 3-31 Schematic illustrating the sequence of interference lithography exposures with proper orientation of the sample. After exposure #1, the sample is rotated by 90° for the second exposure.

Once the sample is oriented, the first interference lithography exposure is performed as illustrated in Figure 3-31 with grating lines exposed along the vertical direction. After this

exposure step, the sample is rotated by 90°, oriented again with the HeNe laser and exposed for a second time with the grating lines as shown. The result is an exposure of a square grid of holes rotated by 45° with respect to the square area of the superprism.

In order to achieve the appropriate hole size necessary for the superprism device (radius = 0.4*period), the laser power at the substrate position was measured and multiple exposures were made with different exposure times. Because the interference lithography process results in holes having a square shape for large hole sizes, the hole size was adjusted in order to maintain the same air/silicon ratio. This implied a square with a width (d) of 0.71*period. For 237nW of laser power at the substrate position, an exposure time of 42 seconds/exposure was required to achieve this hole size in OKHA PS4 resist as discussed in Section 3.1.2.

3.2.7 Large scale oxidation of AIAs for thick buried oxides

Fabrication of the superprism device in the GaAs materials system was also explored with a structure as outlined in Figure 3-25. In order to ensure proper optical isolation of the GaAs guiding layer from the substrate, the GaAs guiding layer needs to rest on a sufficiently thick buried oxide. This oxide can be created through the conversion of aluminum containing layers, such as AIAs or AlGaAs, to aluminum oxide (Al_xO_y).

The necessary buried thickness varies with wavelength. For the $\lambda=3.1 \mu\text{m}$ superprism devices, a buried oxide of 3 μm is required. For the $\lambda=1.55 \mu\text{m}$ devices, a buried oxide of 1.5 μm is required. Oxidizing AlGaAs to create a 1.5 μm buried oxide for photonic crystal waveguides was utilized by Assefa [69]. For the devices investigated by Assefa, the oxidation lengths were on the order of nanometers so that the slower oxidation rates of high aluminum content AlGaAs were tolerable. For the superprism device, oxidation lengths directly beneath the photonic crystal area are on the nanometer scale. However, for the large area slabs at the input and output facets, millimeter lateral oxidation lengths are required. As a result, oxidation of AIAs, which has the highest oxidation rate of the AlGaAs alloys, must be employed.

In the majority of the work that has been reported to date, the oxidation of aluminum-based materials has been limited to relatively small areas (\sim several-to-tens of μm^2), or to relatively thin ($\lambda/4$) layers. Oxidation areas may have been limited due to the fact that the process of creating oxidized layers at larger dimensions can easily be degraded by the effects of structure delamination. In the previous chapter on large area broadband

saturable Bragg reflectors, a strategy was developed to oxidize AIAs over the length scale of 100's of μm . Similar techniques are utilized here for the superprism device, only with the additional requirement of a thick buried oxide. Thus, the goal here is to create a large area semiconductor-on-insulator structure, with a very thick, low index oxide which is buried beneath a thinner GaAs device layer. Such a GaAs/oxide structure is analogous to widely used Si/SiO₂ silicon-on-insulator (SOI) structures.

Al-containing layers were oxidized in a tube furnace in which nitrogen gas transports water vapor from a heated bath to the sample located in the center of a furnace tube as described in the previous chapter. As an initial experiment, an oxidation was performed on a GaAs-based structure consisting of a 450 nm thick GaAs layer on a 3000 nm thick AIAs layer. Surrounding the AIAs layer were two 50 nm Al_{0.50}Ga_{0.50}As layers. The goal was to completely oxidize the 3000 nm thick AIAs layer thereby creating a thick buried oxide and to use the 50 nm intermediary Al_{0.50}Ga_{0.50}As layers to reduce the strain between the Al_xO_y and the GaAs epilayer and underlying substrate. Three oxidation runs were performed on cleaved samples of the above structure at temperatures of 470°C, 430°C, and 400°C for 1 hour. All three runs resulted in severe deformation of the structure. This deformation was likely caused by the lattice contraction of the very thick AIAs layer which strained the AlGaAs intermediary layers and the top GaAs layer. With a 3000 nm thick AIAs layer, a linear contraction of approximately 10% would result in a 300 nm contraction which approaches the layer thickness of the 450nm thick GaAs layer.

This experiment illustrates that even by lowering the oxidation temperature, oxidizing a thick buried layer of AIAs will not result in a stable structure. Varying the aluminum composition of the heterostructure was considered as an alternative. Oxidations performed on the SBR structures described previously illustrated that GaAs/AIAs structures are not suitable for large scale oxidations, and that the use of AlGaAs instead of GaAs stabilized these structures. Low Al-content AlGaAs stabilized the SBR structure without significant oxidation of the AlGaAs layers. With high Al-content AlGaAs, the SBR structure can be stabilized with significant oxidation of the AlGaAs layers [41].

Using these results, the GaAs/Al_{0.50}Ga_{0.50}As/AIAs semiconductor-on-insulator structure described above, was modified in order to reduce the volume contraction of the oxidizing layer while maintaining reasonable oxidation times. The approach uses alternating layers of AIAs and high Al-content AlGaAs to create a thick aluminum layer that can be completely oxidized. By using the layered structure, the high oxidation rates of AIAs layers can be

combined with the lower volume contraction of AlGaAs layers [40] to create thick buried oxides over a large area. A schematic of the structure is shown in Figure 3-32. The structure consists of a 450 nm GaAs layer on top of 9 1/2 pairs of AlAs/Al_{0.7}Ga_{0.3}As grown on a GaAs substrate. To stabilize the structure even further, the interfaces between each AlAs and Al_{0.7}Ga_{0.3}As layer were continuously graded during the molecular beam epitaxy (MBE) growth to reduce interfacial stresses during oxidation.

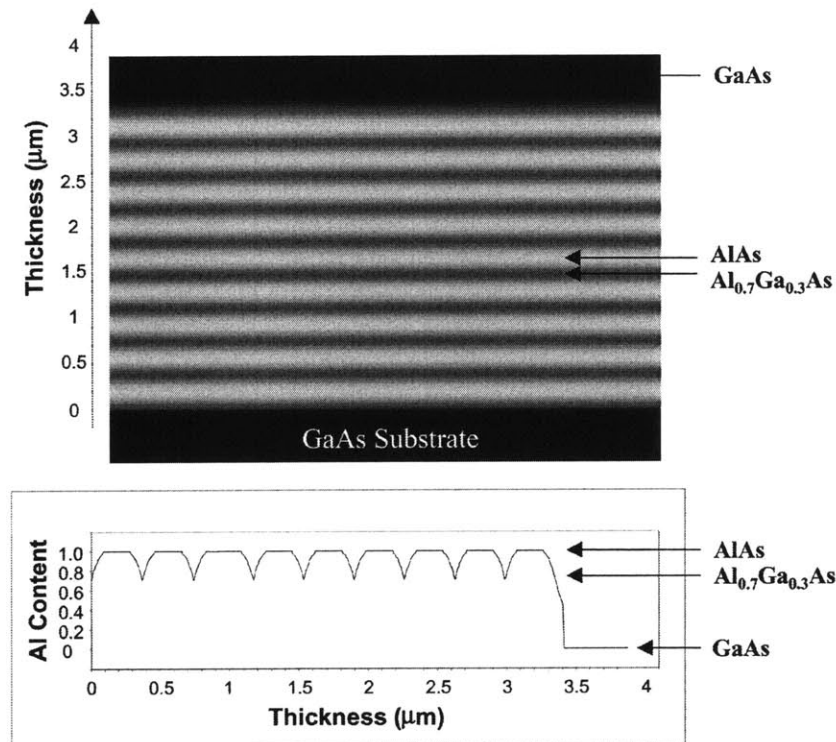


Figure 3-32 Schematic illustrating the cross-section of the structure used to create a thick buried oxide with a plot of the designed aluminum content as a function of structure thickness.

Figure 3-33(a)-(d) present the results of a lateral oxidation from the cleaved edge of the aforementioned sample that was illustrated in Figure 3-32. Steam oxidation was performed at an oxidation temperature of 420°C for 11 hours. A sequence of SEM images that were obtained along the path of the oxidation front, shows how the thick layered structure becomes fully oxidized. After 11 hours, the oxidation front advanced ~500 μm from the sample edge. Figure 3-33(a) shows a cross-sectional profile at the oxide terminus. The oxide terminus for two of the oxidized AlAs layers is clearly visible due to the contrast between AlAs and Al_xO_y. The AlGaAs layers, between the oxidized AlAs layers, remain unoxidized. Figure 3-33(b) shows a cross-sectional image further away from the oxide

terminus, approximately 400 μm from the sample edge. Three oxidized AIAs layers are shown between the AlGaAs layers that are now partially oxidized in the vertical direction. The oxidized AlGaAs appears brighter and with more contrast than the oxidized AIAs. Figure 3-33(c), which is an image approximately 300 μm from the sample edge, shows that the vertical oxidation of the AlGaAs layers has progressed even further leaving only thin unoxidized AlGaAs layers surrounded by thicker oxide layers. In Figure 3-33(d), the cross-sectional image at an area closest to the sample edge shows a completely oxidized structure.

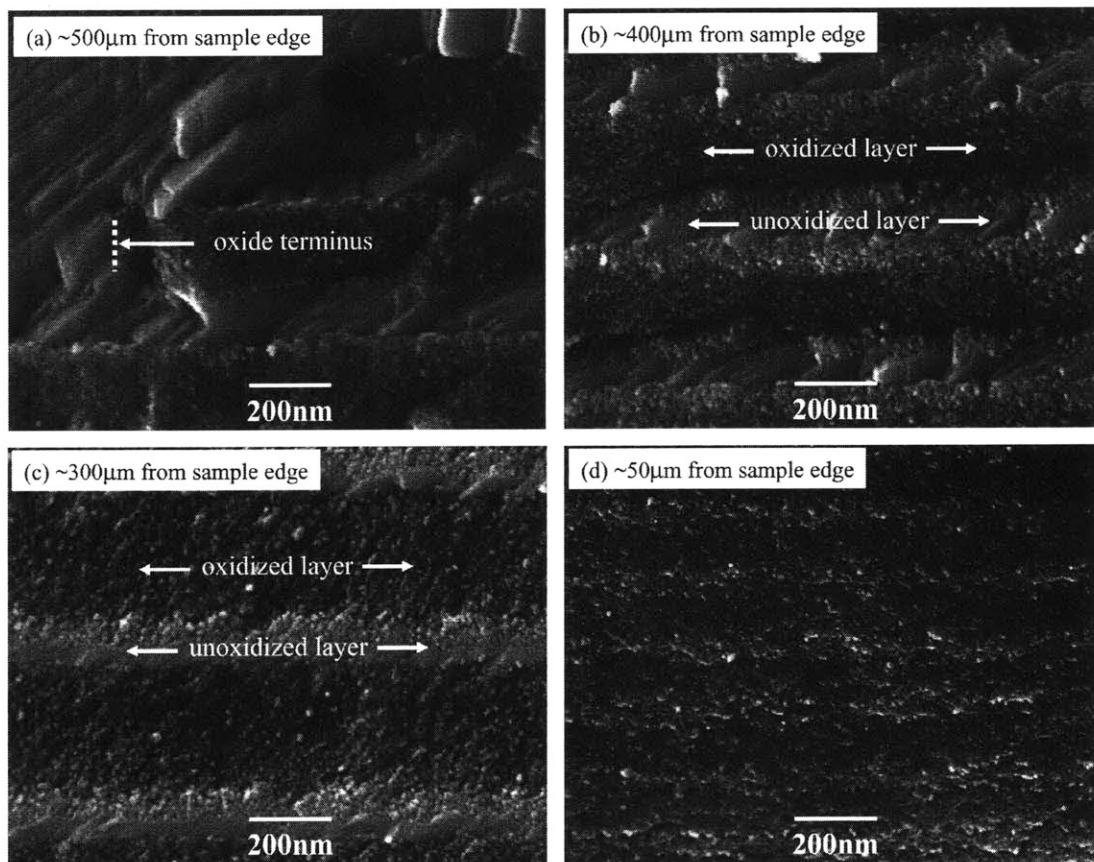


Figure 3-33 Scanning electron micrographs at different locations from the sample edge showing lateral oxidation of AIAs layers with subsequent vertical oxidation of the AlGaAs layers. (Schematic of the structure is shown in Figure 3-32.)

Though the lateral oxidation rate of AlGaAs is slow, the AIAs layers, which oxidize more quickly, allow for subsequent vertical oxidation of the adjacent AlGaAs layers. Thus, the effective rate of oxidation of the AlGaAs layers is increased. In addition, since the AlGaAs layers experience less volume contraction than the AIAs layers, the overall lattice

contraction in this structure has decreased relative to the pure AIAs case resulting in a stable, thick, buried oxide layer.

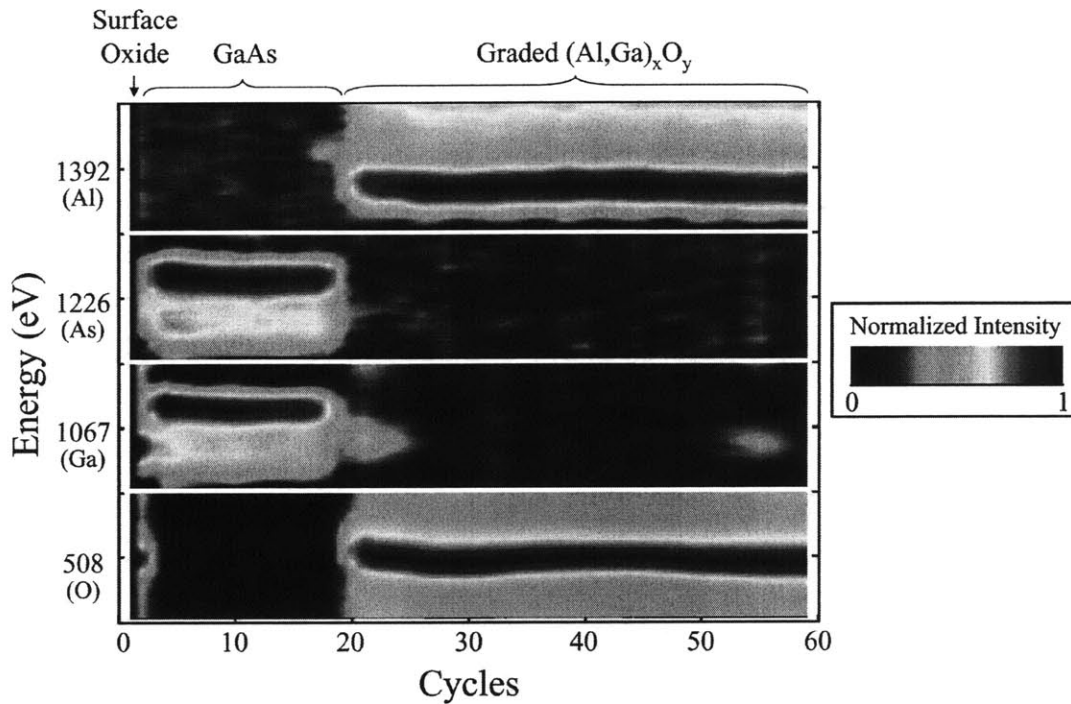


Figure 3-34 Auger electron spectroscopy profile verifying complete oxidation of the layered structure. The presence of each element is detected through the peaks in detected intensity at the characteristic Auger electron energies.

Auger Electron Spectroscopy (AES) analysis verified complete oxidation of the structure as shown in Figure 3-34. Since Auger electron energies are unique to the element from which they were emitted, compositional analysis was performed to detect the presence of aluminum, arsenic, gallium and oxygen at different depths in the layered structure. Cycles of ion sputtering followed by analysis steps with a 3 keV electron beam were used to obtain compositional information versus depth. Figure 3-34 shows the normalized Auger electron intensity versus energy after each sputtering cycle. The native gallium oxide is detected through the presence of oxygen and gallium in the first two analysis cycles. The GaAs layer was sputtered through during cycles 3 to 19 as indicated by the presence of the Ga and As Auger signals. After analysis cycle 19, the arsenic Auger electron intensity rapidly decreases and the aluminum and oxygen intensities increase. The grading of the gallium content in the oxidized AlGaAs layer is also visible at cycles 19 and 54 through the slight increase in the gallium Auger electron intensities. The oxygen content remains approximately flat until the completion of the AES scan after cycle 60 verifying the complete oxidation of the uppermost AIAs/AlGaAs layers in the structure.

This experiment shows that thick buried Al_xO_y layers can be created without delamination by oxidizing a stacked AlAs/AlGaAs structure. However, even after 11 hours of oxidation at 420°C , the greatest extent of oxidation was $500\ \mu\text{m}$. This $500\ \mu\text{m}$ of oxidation was achieved for the AlAs layers as demonstrated by Figure 3-33. Complete oxidation of the AlGaAs layers occurred at lengths of less than $300\ \mu\text{m}$ from the sample edge.

In order to attain the millimeter length scales of oxidation necessary for the superprism, faster oxidation rates are required. The above oxidation at 420°C for 11 hours was performed on a sample with a cleaved facet and resulted in an oxidation rate of about $0.8\ \mu\text{m}/\text{min}$ for the AlAs layers. Oxidations performed on large area square shaped mesas defined with photolithography and wet etchants resulted in similar oxidation rates.

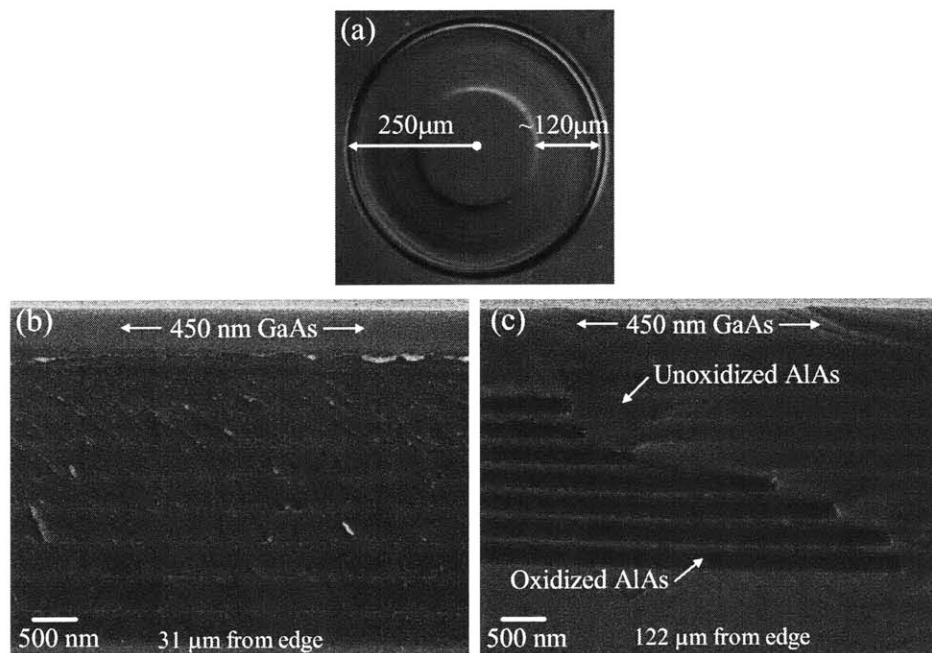


Figure 3-35 (a) Differential interference contrast (DIC) image of partially oxidized $500\ \mu\text{m}$ mesa. (b) SEM image showing complete oxidation of the layered structure $31\ \mu\text{m}$ from the mesa edge. (c) SEM image at a location $122\ \mu\text{m}$ from the mesa edge showing the edge of the AlAs oxidation front. (R935, 450°C , 1hr, 10/29/02)

Faster oxidation rates were observed for circularly shaped mesas. For example, the oxidation front progressed approximately $160\ \mu\text{m}$ from the edge of a $500\ \mu\text{m}$ circular mesa after a 2 hour oxidation at 420°C . This result implies an oxidation rate of $1.3\ \mu\text{m}/\text{min}$. Using higher temperatures, the oxidation rate can be increased. As shown in Figure 3-35(a), the oxidation front advanced $120\ \mu\text{m}$ after 1 hour at 450°C implying a rate of $2.0\ \mu\text{m}/\text{min}$. The SEM image, shown in Figure 3-35(c), shows that at the oxidation front,

complete oxidation of the AlAs layers has occurred but without complete oxidation of the AlGaAs layers. Figure 3-35(b) shows that near the mesa edge, oxidation of all Al-containing layers is complete. As shown in Figure 3-36, the oxidation front advanced $145\mu\text{m}$ after 1 hour at 460°C implying a rate of $2.4\ \mu\text{m}/\text{min}$. SEM images again show that the AlAs is oxidized at the oxidation front but with incomplete AlGaAs oxidation. At a higher temperature of 475°C , the oxidation front advanced $150\mu\text{m}$ after 1 hour implying a rate of $2.5\ \mu\text{m}/\text{min}$ (see Figure 3-37). However, discoloration of the mesa surface was observed. SEM images presented in Figure 3-37(b) and (c) show that this discoloration is most likely due to oxidation of the top $450\ \text{nm}$ layer of GaAs. An AES scan verified that significant oxidation of the top GaAs surface had occurred. The oxidation of GaAs proceeds in the vertical direction from the exposed surface downward. As apparent from Figure 3-37(c) and in the AES scan, a layer of unoxidized GaAs remains underneath a layer of oxidized GaAs. Therefore, while increasing the oxidation temperature does help to increase oxidation rates, the oxidation of GaAs layers must also be considered.

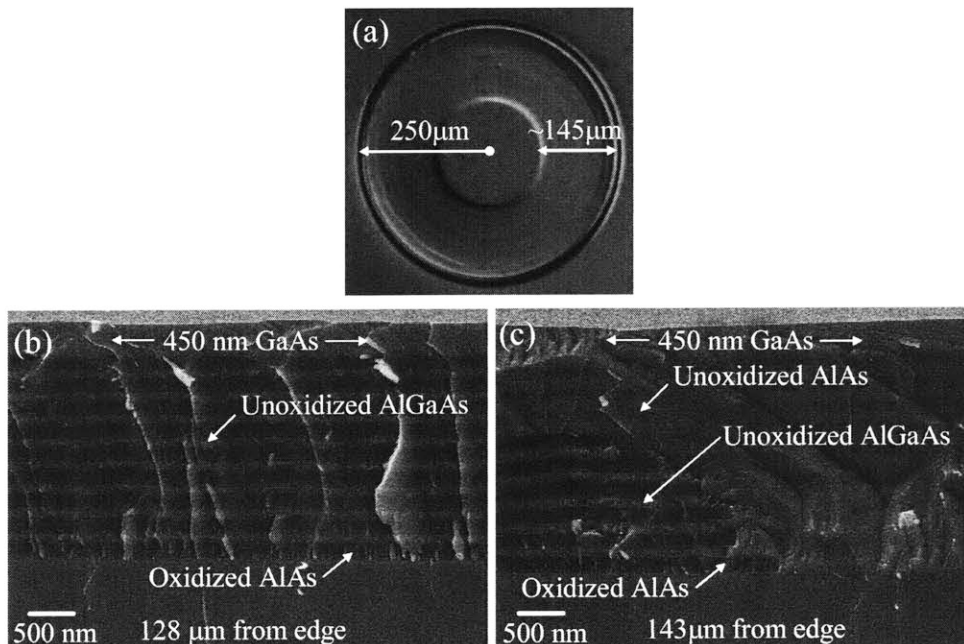


Figure 3-36 (a) DIC image of partially oxidized $500\mu\text{m}$ mesa. (b) SEM image showing complete oxidation of AlAs but unoxidized AlGaAs $128\mu\text{m}$ from the mesa edge. (c) SEM image at a location $143\mu\text{m}$ from the mesa edge showing the edge of the AlAs oxidation front. (R935, 460°C , 1hr, 10/30/02)

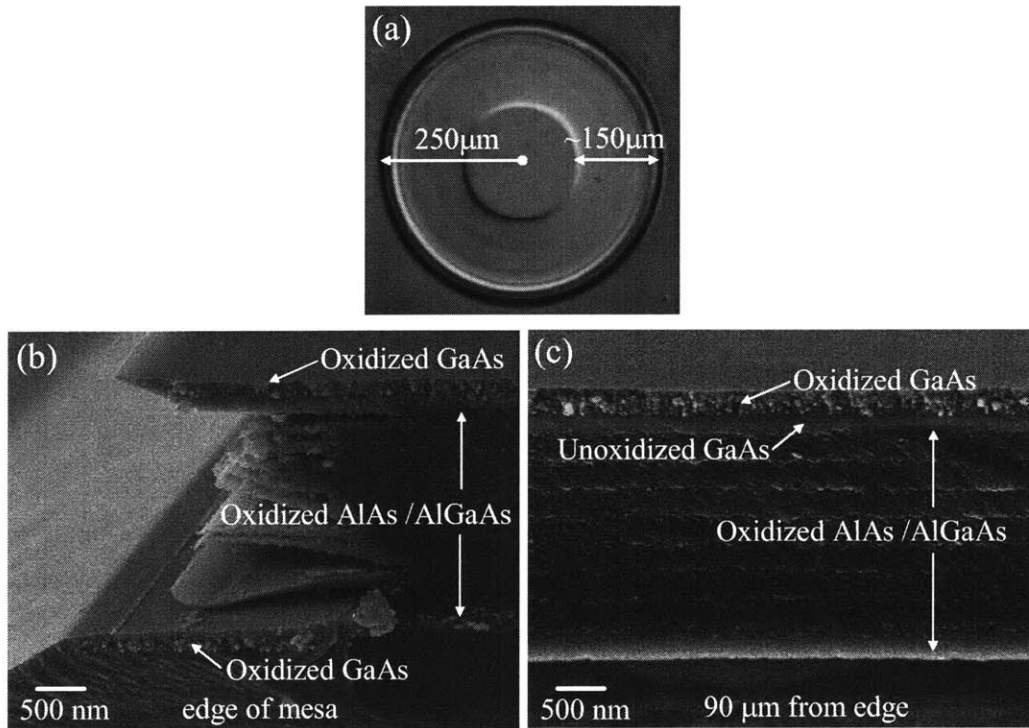


Figure 3-37 (a) DIC image of partially oxidized 500 μm mesa. (b) SEM image at the mesa edge showing complete oxidation of AlAs and AlGaAs layers but also partial oxidation of GaAs. (c) SEM image at a location 90 μm from the mesa edge showing the edge of the AlAs oxidation front. (R935, 475°C, 1hr, 10/29/02)

Utilizing a cap layer has been shown to protect the GaAs layer during oxidation. A 5mm x 5mm square mesa with a 250 nm cap layer of HSQ was oxidized for 12 hours at 460°C as shown in Figure 3-38. The top view in Figure 3-38(a) shows how the oxidation front progressed approximately 350 μm from the flat edge of the square mesa while progressing ~600 μm from the square's corner, demonstrating the geometrical dependence of the oxidation rate. A discoloration of the mesa surface was observed at the edges of the mesa. SEM analysis in Figure 3-38(b) indicated that although the HSQ successfully protected the GaAs layer from vertical oxidation, lateral oxidation of the GaAs layer progressed from the mesa edges. After 12 hours of oxidation, the lateral oxidation of GaAs proceeded ~40 μm from the edge of the mesa—therefore with an oxidation rate much slower than that of AlAs or AlGaAs. Lateral oxidation of the substrate is also apparent. An SEM image [Figure 3-38(c)] at the oxidation front of the AlAs layers indicates that vertical oxidation of the GaAs layers is not significant. Again, the AlGaAs layers remain unoxidized at this location.

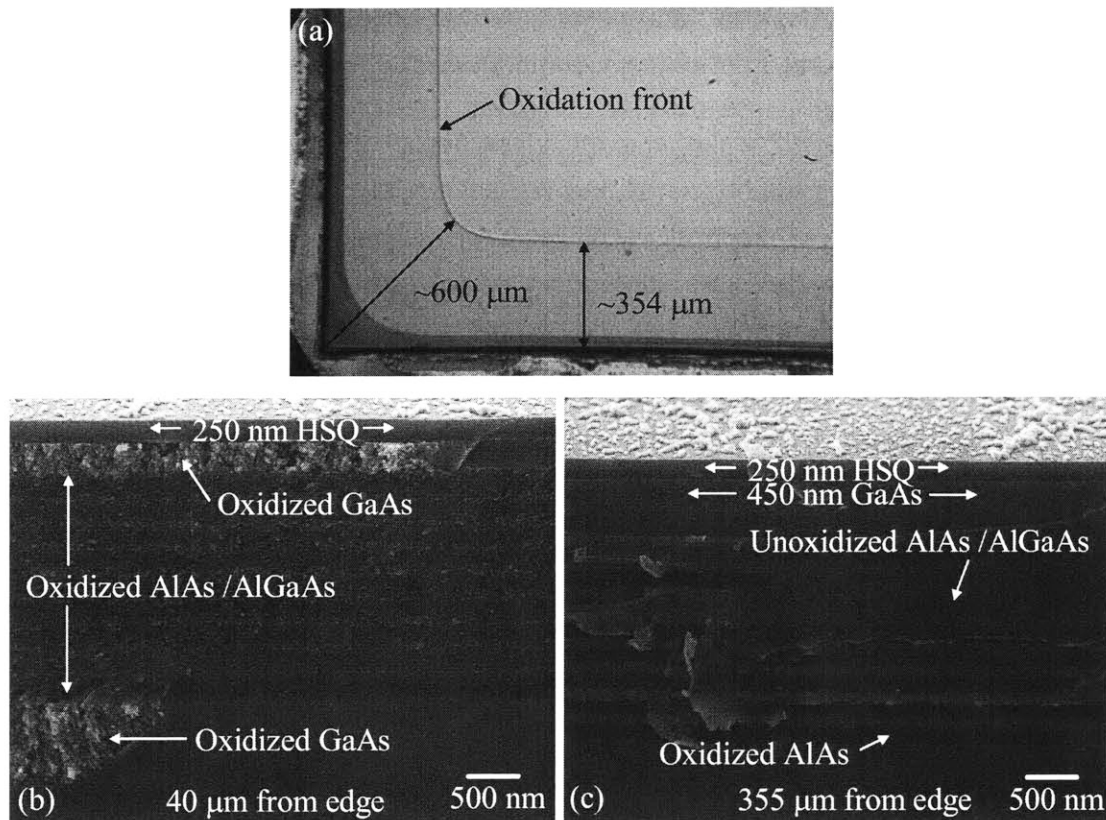


Figure 3-38 (a) DIC image of the corner of a partially-oxidized 5mm square mesa. (b) SEM image at 40 μm from mesa edge showing complete oxidation of AlAs and AlGaAs layers. A 250 nm HSQ cap layer protects the 450nm GaAs layer but lateral oxidation of GaAs is apparent. (c) SEM image at a location 355 μm from the mesa edge showing the edge of the AlAs oxidation front. (R935, 12 hr, 460°C, 4/7/2003)

Though a strategy for creating thick buried oxides has been developed using a layered AlGaAs/AlAs structure of high aluminum content, implementing this strategy for millimeter-scale oxidation lengths is challenging. With the oxidation rates of AlAs demonstrated at approximately 1-2 $\mu\text{m}/\text{min}$ depending on geometry and temperature, oxidizing 1 millimeter requires over 16 hours of oxidation making lateral oxidations with greater length scales impractical. Other techniques have been considered to reduce this oxidation time. Etching holes through the wafer to allow steam to flow to the underside of the structure is one idea. With large-scale lateral oxidation techniques, even with a protective cap layer, oxidation of GaAs layers must also be considered. However, partial oxidation of GaAs layers may even be desirable for coupling light into the side of the structure due to the low refractive index of the oxide. Another observation which is apparent from the results presented above is the slower oxidation rates associated with the $\text{Al}_{0.7}\text{Ga}_{0.3}\text{As}$ layers. Even with the effects of vertical oxidation from AlAs layers, oxidation of these lower aluminum content layers is

appreciably slower. Perhaps in future work, higher aluminum content layers can be explored such that structural stability is not compromised.

Though the oxidation length scales and thickness described above represent the largest scales of oxidation in both the horizontal and vertical directions in the literature reported to date, lateral oxidation is not practically achievable for millimeter length scales. As a result, fabricating the full centimeter-scale superprism device in the GaAs materials system was not pursued further. For superprism device designs where lateral oxidation lengths are on the order of 100's of μm , the strategy described above could be readily implemented.

3.2.8 Device fabrication results

All of the design and processing steps necessary for fabricating the large area superprism have been described in the previous sections. These steps were integrated to realize a superprism device in the silicon materials system. The device consists of a two-dimensional photonic crystal slab with a square lattice of air holes etched in silicon. As shown in Figure 3-39(a), the photonic crystal slab occupies a 1 cm x 1 cm square area and rests on a low index SiO_2 layer. SOI (silicon on insulator) wafers purchased from Soitec, Inc. were used for this device. These wafers have a silicon thickness of 700 nm, and a SiO_2 thickness of 3,000 nm. The fabricated structure is designed to operate at a wavelength of 3.1 μm , so that the photonic crystal lattice constant is 750 nm, and the hole radius is 300 nm. The input and output facets of the structure are air-silicon boundaries positioned at specific angles with respect to the photonic crystal to facilitate coupling from air as discussed in Section 3.2.2 and illustrated in Figure 3-25. For this structure, the input angle (θ_1) was 38°, and the output angle (θ_2) was 11° as measured from the input and output Si/PC interfaces respectively. Calculations indicate that for this structure, an angular swing of +/- 2° about the normal at the input results in a +/- 30° swing about the normal at the output.

As described in Section 3.2.4, the high index silicon region with the input and output facets was patterned using photolithography leaving an open square area for the subsequent patterning of the photonic crystal. The large area photonic crystal was patterned using two-beam interference lithography (IL) as discussed in Section 3.1.2. Patterning holes using this technique results in square rather than circularly-shaped holes for large hole diameters. As a result, the size of the holes was adjusted to maintain the same air/silicon ratio as the design. The alignment technique described in Section 3.2.6 was implemented to align the photonic crystal to the open square area. With this technique, alignment of the photonic

crystal to the boundary of the high index region, as illustrated in Figure 3-39(b), was accomplished with an angular precision of approximately $1 \mu\text{radian}$ as measured with a scanning electron microscope (SEM). An additional photolithography step was then used to protect the photonic crystal in order to remove the holes patterned outside of the square photonic crystal region during the IL step. Reactive ion etching as described in Section 3.1.4 was used to transfer the superprism pattern into an HSQ hard mask layer and then into the silicon layer of the SOI layered structure. The cross-sectional profile of the photonic crystal in a silicon monitor sample after reactive ion etching is shown in Figure 3-39(c). Fabricating the device for an operating wavelength of $\lambda=1.55 \mu\text{m}$ would proceed in the same fashion as described above but with smaller feature sizes. A device at this wavelength was not fabricated in this work.

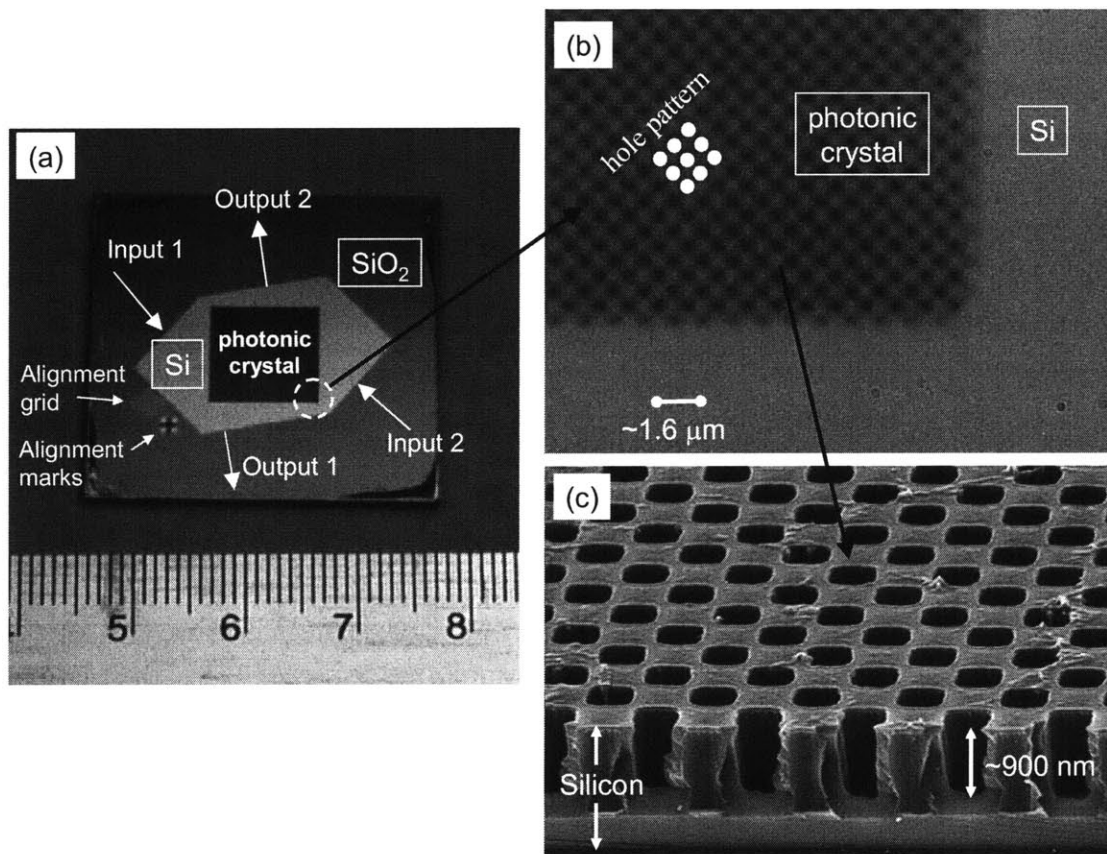


Figure 3-39 Images of a fabricated superprism structure. (a) Digital photograph showing the full sample. (b) Differential interference contrast image showing the magnified corner area of the photonic crystal. (c) SEM micrograph showing cross-sectional image of a Si monitor sample.

3.2.9 Testing Requirements and Challenges

Though a process for fabricating the superprism device was explored and a structure was realized, a number of existing factors created challenges for device testing. In order to successfully observe the superprism effect, the input excitation light must:

- 1) Approximate a "plane wave" ($>100\ \mu\text{m}$ wide),
- 2) Be well collimated,
- 3) Couple uniformly to the silicon guiding layer (100's of nm thick).

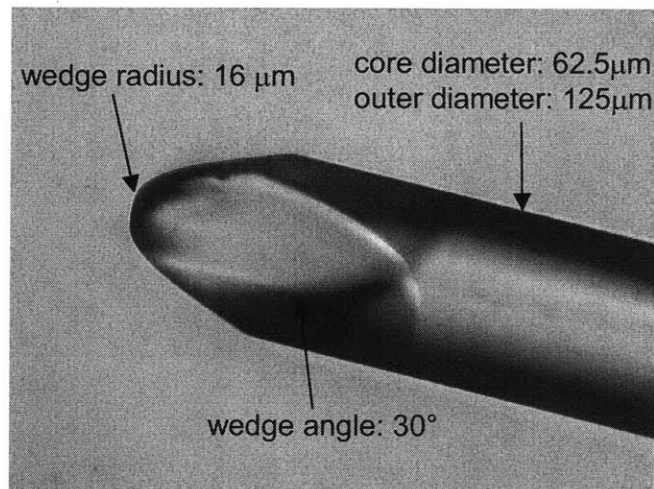
The time domain simulations presented in Figure 3-24 showed how an input excitation of a finite width results in significant divergence of the beam at the output of the device. A diverging or focused input beam is a beam composed of a range of k -vectors. Because the propagation of light through the superprism is inherently highly sensitive to the orientation of the k -vector, observing angular magnification with an input beam composed of multiple k -vectors will obscure superprism operation. In order to clearly observe the superprism effect, the beam at the output should be as close to a plane wave as possible. A plane wave at the output requires a plane wave at the input. Because a plane wave is difficult to create in a lab environment, a realistic approximation would be wide excitation beam with little divergence (*i.e.* well collimated). Simulations suggest that the width of the excitation would need to be greater than $100\mu\text{m}$ in order to decrease the divergence of the output beam to acceptable levels.

Three ideas have been proposed to create a wide collimated beam:

- 1) Cylindrical lenses
- 2) Tapered fiber
- 3) Excitation of a plane wave using an integrated active device

A free space cylindrical lens can be used to focus a stripe of light onto the edge of the superprism slab. However, such lenses are susceptible to aberrations which may compromise the beam's profile. A specially tapered lensed fiber like the one illustrated in Figure 3-40 can create a beam profile resembling a thin, stripe. The fiber tip is specially polished into a wedge shape as shown. The wedge angle and radius are designed so that the output beam focuses to a stripe which is parallel to the tip of the wedge. With a

multimode fiber, a wide stripe can be created. For coupling to the superprism, only the fundamental mode would be desired. If III-V materials are used, excitation of a wide stripe could be accomplished with a light emitting diode (LED) integrated on the same chip as the superprism. If a long electrode is used to pump current into a wide active region, a wide stripe could be created at the input facet of the superprism. To steer the stripe's angle, the index of refraction of a slab region between the LED and the superprism input could be electrically tuned to bend the beam. Implementing this solution would require a new superprism design which would be fabricated in III-V materials.



manufacturer: O/E Land Inc.

Figure 3-40 Microscope image of lensed fiber proposed for creating a wide stripe excitation as the input to the superprism. Image courtesy of Marcus Dahlem.

While creating a wide and well-collimated input excitation is not trivial, another challenge is in aligning and coupling this light into the guiding layer of the superprism. For a guiding layer with a thickness on the order of 100's of nanometers (depending on the wavelength of operation), and an excitation beam with a width greater than 100 μm, ensuring that the full beam width couples to the thin guiding layer with a uniform intensity, while remaining collimated, is difficult. Electronically-controlled alignment stages can be used where x-y-z movement on the nanometer scale can be achieved. A small angular tilt in the plane of the superprism slab must also be controlled if angular magnification is to be realized. With a free-space cylindrical lens, performing this function with accuracy would be difficult. In addition, being able to monitor the input angle, while monitoring the other x-y-z and rotational positioning required for coupling the wide excitation stripe, is not trivial. With a tapered fiber, the orientation of the fiber relative to the input facet can be easily monitored with an overhead camera. Ensuring that the input excitation maximally couples to the input

slab would require rotation of the fiber so that the stripe formed by the taper is parallel to the input facet.

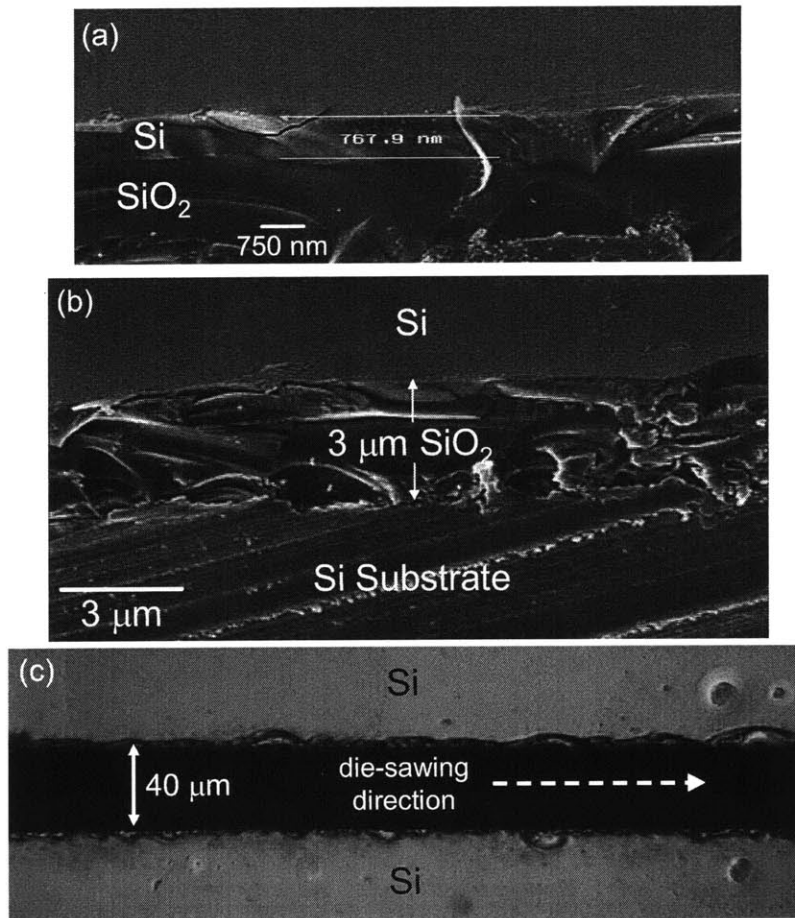


Figure 3-41 (a) and (b) SEM images showing cross-section of a die-sawed SOI sample. (c) DIC image showing top view of die-saw cut with 40 μm blade and die-saw speed=0. Resist is protecting the top silicon layer in this top-view image.

However, another problem exists which makes testing of the superprism difficult. In order to successfully couple light into and out of the superprism, the input and output facets of the silicon guiding layer must coincide with the edge of the device sample. For the fabricated device illustrated in Figure 3-39, notice that the input and output facets shown in Figure 3-39(a) are not at the edge of the square sample but are set in from the edge of the sample, leaving exposed SiO₂ surrounding the device area. Since the input and output facets of the superprism are not at right angles to each other, cleaving the sample to form both facets is not practical. (The current SOI wafer has a (100) orientation.) Die sawing the sample is another option for defining a facet. A number of die saw experiments were performed to assess the viability of this option. The first experiment involved using a die

saw with a thin blade and slow sawing speed to try to define the edge facet of the superprism. The top surface of the sample was protected with a thick layer of photoresist. The result is shown in Figure 3-41 with SEM images taken after photoresist removal. As expected, the facet defined with a die saw is extremely rough even with the slow sawing speed. As evident from Figure 3-41(b), the substrate material appears much smoother than the top silicon or buried SiO₂ layers possibly indicating that smoothness is material dependent or dependent on the location relative to the saw. Polishing could produce a smoother facet. Figure 3-41(c) indicates that at least 10 μm of material would have to be polished in order to create a smooth facet. Polishing could offer an acceptably smooth facet for coupling light into the superprism. However, maintaining a flat facet over a length scale of 100's of μm during the polishing process may be troublesome. Polishing experiments were not performed in this work.

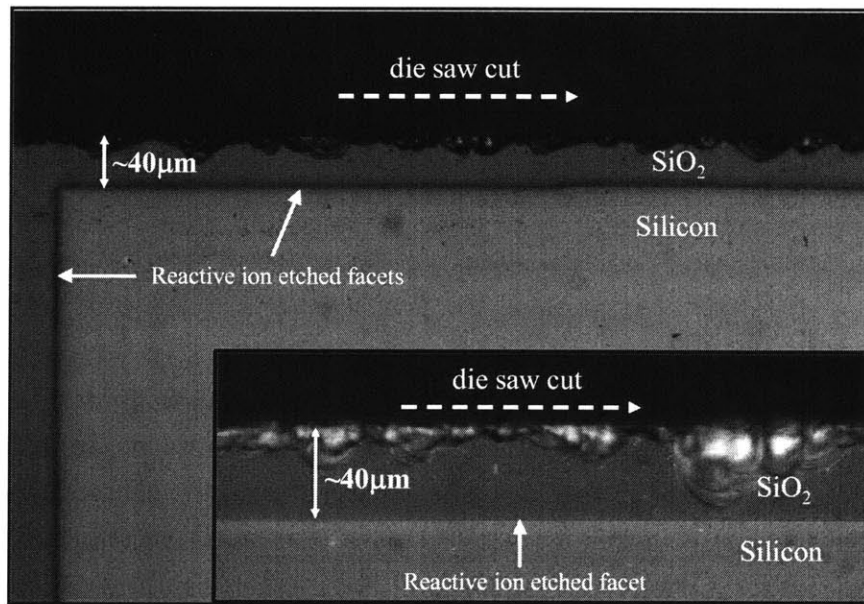


Figure 3-42 DIC images showing top-view of die-sawed SOI sample with a silicon slab defined by reactive ion etched facets.

Another experiment involved defining an edge facet in the upper silicon layer using reactive ion etching and then performing a die-saw cut parallel to the etched facet to remove the oxide and substrate material. In order to couple light into or out of the superprism, the silicon slab ideally should not be recessed from the edge of the sample. A recess of a few microns (1-10 μm) may be tolerable. However, as shown in the die saw results in Figure 3-42, because the die saw removes large pieces of material as it cuts, cutting at a distance of 40 μm from the etched facet did not damage the upper silicon layer. Moving the blade

closer to the facet would likely result in damage. As shown in the inset, even at a distance of 40 μm , material was removed a short distance from the silicon facet.

Coupling evanescently through the surface of the silicon slab could offer an approach to input coupling that would avoid the need for a smoothly defined facet. Defining a grating in the silicon surface, or using a technique known as "prism coupling" may offer a solution. However, the requirement of a wide, planar beam profile remains a challenge for all of these techniques.

In its current design, observing the superprism effect is difficult. Future work would involve modifying the design such that conventional free-space or fiber optics can be used to excite a planar input excitation for the superprism device. Perhaps integration of the superprism with on-chip planar optical elements which convert a focused beam to a plane wave would be more practical to implement. Such an element would need to allow for an angular tilt of the focused input beam to cause a tilt of the resulting plane wave.

With the expertise developed to realize this superprism device, future generations of the large area superprism can be developed. In addition, with this expertise, other devices may be developed where a large area photonic crystal is required.

3.2.10 Conclusions

In this work, a new device to realize the superprism effect in a uniform dielectric material has been presented. The structure relies on sensitivity of the phase velocity in a 2D photonic crystal slab to observe angular magnification outside the photonic crystal medium. Using three-dimensional equi-frequency calculations, the phase velocity superprism effect has been predicted for a photonic crystal slab of finite thickness. The calculations indicate that a dispersion surface with a flat shape is ideal for introducing large changes in the phase velocity for small changes in the input direction. Though the superprism effect can be observed in uniform dielectric materials, free space applications using a modified structure are also explored. Further analysis with finite-difference time-domain simulations indicate that for the clear observation of the superprism effect, a large area photonic crystal and a wide excitation beam are required. A fabrication technique was demonstrated to achieve the required nanometer-sized features of the device over centimeter-sized areas using a combination of interference lithography, photolithography, and reactive ion etching with silicon-on-insulator substrates. A technique was also explored to realize the structure in the GaAs material system using a thick layer of buried aluminum oxide. Buried oxides with a

3 μm thickness were created over 100's-of- μm length scales. Future work will involve modifying the technique such that millimeter-scale buried oxides can be produced for the centimeter-scale superprism design. A number of challenges were identified which make observing the superprism effect difficult. Coupling and alignment of a plane wave excitation, in combination with the challenge associated with defining anti-parallel or non-orthogonal input and output facets preclude successful testing of the device in its current design. Future work will involve redesigning the superprism such that device operation does not necessitate highly specialized testing apparatus allowing for more robust device operation.

3.3 The Super-Collimator

3.3.1 Motivations

Photonic crystals offer unique opportunities for the control and manipulation of light in materials. Like the "superprism" effect, "self-collimation" is another distinctive effect made possible by designing unique dispersion properties of the photonic crystal. The guidance of light for transmission between two points is typically accomplished using a fiber optic cable or a waveguide defined on a planar substrate. Photonic crystals have also been studied for waveguiding applications using defects within the photonic crystal lattice [69-71]. However, for all of the above light-guiding methods, the path of the light is outlined by the material, whether it is the glass of the fiber, the ridge waveguide on a planar substrate, or the line of defects in a photonic crystal. By using the "self-collimation" effect of photonic crystals, a light can be guided within the plane of the PC without physical boundaries which define its path. Material boundaries enable light to be confined to a particular space, and without confinement, light will naturally diverge. However, in a uniform photonic crystal slab, for a particular wavelength, specifically designed *dispersion properties* of the photonic crystal prevents the divergence of light so that the beam is self-collimated--it is collimated on its own. At the wavelength of self-collimation, light experiences propagation with little or no change in the beam width. However, with a change in wavelength, divergence will be observed and the beam width expands. Self-collimation can be explained by the dispersion surfaces of the photonic crystal which describe the spatial dependence of the k -vector. Being able to demonstrate such a phenomenon would be very useful for guiding light in

photonic integrated circuits. In addition, tuning the wavelength between the divergence and collimation case in the photonic crystal offers another possibility for light switching.

A number of groups have presented theoretical discussions [72-75] of self-collimation in photonic crystals, but in the literature reported to date, only three groups have experimentally demonstrated the self-collimation effect of photonic crystals [59, 76, 77]. For all three of these groups, the length scales of collimation have been limited to 100's of microns due to the size of the fabricated devices. Kosaka, *et al.*, demonstrated collimation within a three dimensional photonic crystal consisting of a hexagonal lattice of Si/SiO₂ [59]. With a camera viewing the top surface of the structure, Kosaka, *et al.* observed that by changing the angle of incidence, the beam's path would switch from divergent behavior to collimated behavior over a length of 500 μ m. Wu, *et al.* showed that a "flat" photonic crystal dispersion surface, a surface with little curvature, can be used to observe collimation in a two dimensional (2D) planar configuration [77]. With a semicircular structure with a radius of 19 μ m (similar to their structure that was used to demonstrate the superprism effect [61]), Wu, *et al.* presented evidence that the collimation effect is wavelength dependent. With multiple waveguides used to collect light exiting the photonic crystal, and camera images of the end facet showing either the presence or absence of light in each waveguide, the beam profile associated with the collimation effect was not clearly observed. Prather, *et al.* also fabricated a photonic crystal structure to demonstrate the self-collimation effect in a 2D photonic crystal of air holes in silicon [78, 79]. With camera images of the top surface of the planar device, Prather, *et al.* demonstrated collimation over a length scale of 50 μ m, and showed that reflection and beam-crossing are also possible with self-collimated beams. Prather, *et al.* also explored the losses associated with beam propagation using the self-collimation effect, claiming losses of 1.1dB/mm [79].

This thesis research explores the possibility of realizing the self-collimation effect in photonic crystal slabs over millimeter length scales—an order of magnitude larger than any demonstration reported to date. Thus, the self-collimation effect, is termed "*super-collimation*" because of its greatly magnified length scale. The same expertise developed to realize the large area superprism structure discussed in Section 3.2, is used to realize a large area "super-collimator" using a 2D-periodic photonic crystal slab. As was the case for the superprism, super-collimation can be explained by the uniquely shaped dispersion surfaces which are characteristic of photonic crystals. Frequency domain simulations show that a "flat" dispersion surface allows for super-collimation within a photonic crystal. With a flat dispersion surface, the group velocity, and therefore the direction of energy

propagation, is constant for a tightly focused input beam. Time domain simulations show that the super-collimation effect is frequency dependent and can be sustained for hundreds of lattice constants within the photonic crystal. Interference lithography enables the fabrication of large area photonic crystals in order to create the super-collimator device. Imaging of the photonic crystal with near-field and confocal imaging techniques reveals that super-collimation is indeed frequency-dependent and can be sustained for millimeter length scales. This length scale corresponds to over 14,000 lattice constants of the photonic crystal--the longest length scales ever observed for self-collimation.

3.3.2 Design theory and simulations

The super-collimator device is designed such that collimation is observed within a photonic crystal for a focused input beam. A focused input beam is composed of a large range of k -vectors that enter the photonic crystal from air. Therefore, the photonic crystal was designed such that a large range of input k -vectors in air, translates to k -vectors that have nearly identical group velocities within the photonic crystal. K -vectors with equal group velocities have the same direction of energy propagation even if their phase velocities are different. A dispersion surface of low curvature implies a large range of k -vectors with little variation in the group velocity. Figure 3-43 presents the calculated dispersion surfaces associated with a number of frequencies for the structure shown assuming TE-polarized light. Theoretical calculations were performed in collaboration with Dr. Marin Soljacic and Mihai Ibanescu in the Surfaces and Interfaces Group at MIT.

The structure consists of a square lattice of air holes in silicon resting on a layer of SiO_2 . The device characteristics are scalable with the wavelength of operation and the calculation that is shown in Figure 3-43, is presented on a normalized basis with respect to the photonic crystal period a . The thickness of the silicon layer (t_{Si}), the oxide thickness (t_{ox}) and the hole width (d) are $41a/70$, $60a/7$ and $0.7a$ respectively, assuming square shaped holes. As discussed in Section 3.2.2, the interference lithography step that is used to pattern the photonic crystal, results in square shaped holes for large hole sizes. The dispersion surfaces associated with a number of normalized frequencies ranging from $fa/c=0.23$ to 0.26 are presented. The dispersion surface occurring for a frequency of $fa/c=0.24$ is ideal for demonstrating super-collimation because it is the "flattest" dispersion surface. In other words, the $fa/c=0.24$ dispersion surface has low curvature for the widest range of input k -vectors.

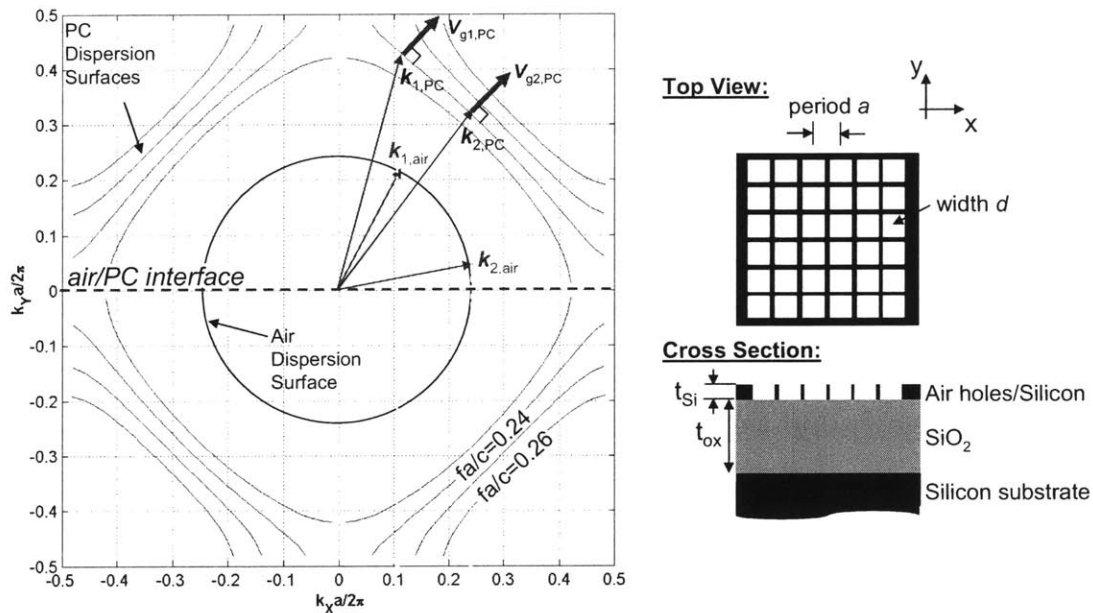


Figure 3-43 Three-dimensional dispersion surface calculation for normalized frequencies showing how two k -vectors in air couple into the photonic crystal. The photonic crystal structure is shown at the right. The flatness of the dispersion surfaces allows two k -vectors of different orientation to propagate with the same group velocity, v_g within the photonic crystal. Simulation by Dr. Marin Soljacic.

Figure 3-43 also demonstrates how a focused beam would couple from air to the photonic crystal across an air/PC interface as defined by the horizontal dotted line. The dispersion surface for air is a circle with a smaller radius than the PC dispersion surfaces. Two k -vectors $k_{1,air}$ and $k_{2,air}$ represent two k -vectors that would comprise a tightly focused beam which is incident upon the interface at an angle of approximately 45°. By conservation of the tangential component of the k -vector at the boundary between air and the PC, the x component of the k -vector remains constant, exciting k -vectors $k_{1,PC}$ and $k_{2,PC}$ within the photonic crystal. The group velocity corresponding to these k -vectors is in the direction perpendicular to the dispersion surface and is indicated by $v_{g1,PC}$ and $v_{g2,PC}$. Though the two k -vectors within the photonic crystal have very different orientations with respect to each other, their group velocities have the same orientation. Moreover, all k -vectors with orientations between $k_{1,PC}$ and $k_{2,PC}$ also have group velocities of the same orientation. Therefore, a wide range of k -vectors in air results in k -vectors with the same group velocity within the photonic crystal, implying a collimated beam of light. For frequencies other than $fa/c= 0.24$, the dispersion surfaces have greater curvature which introduces variations in the group velocity. As a result, at frequencies greater than and less than $fa/c= 0.24$, light will experience divergence within the photonic crystal. It is important to note that the

dispersion surface calculations were performed assuming TE-polarized excitation. Thus the dispersion surface is "flat" for TE-polarized light at a frequency of $fa/c=0.24$. For TM-polarized light, the dispersion surfaces at the same frequency have higher curvature, more akin to an isotropic medium. Therefore TM-polarized light will diverge within the photonic crystal slab and will not be collimated. In addition, note that the direction of the collimated beam (perpendicular to the "flattest" part of the dispersion surface) is along a line which is 45° with respect to the defined interface. This direction on the dispersion surface, corresponds to the diagonal direction for the square lattice photonic crystal structure shown [Figure 3-43].

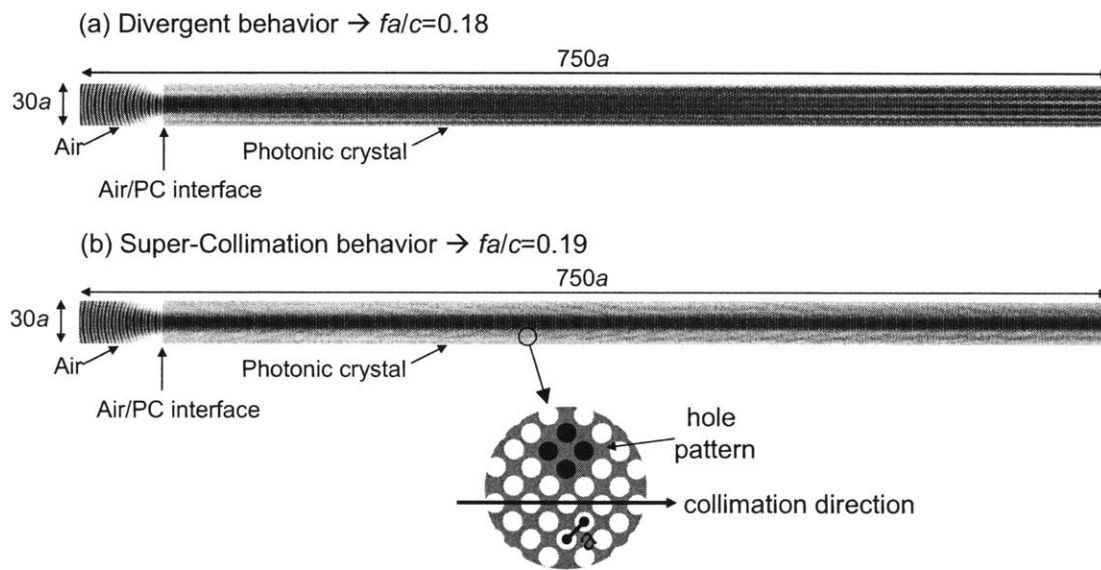


Figure 3-44 Time-domain simulations showing the shift from divergent behavior to super-collimation behavior in a photonic crystal for a shift in frequency. Simulation by Dr. Marin Soljacic.

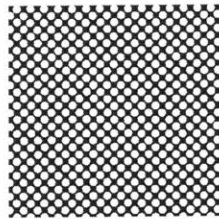
Time-domain simulations presented in Figure 3-44 also demonstrate the frequency dependence of the collimation effect. The simulation was performed on a simplified, more numerically tractable, two-dimensional model. The simplified system has a square lattice photonic crystal of lattice constant a , circular air holes with radius $r=0.4a$, in silicon ($\epsilon=12$), and is purely 2D, assuming infinite structure thickness. The dispersion curves of the 2D system with circular holes are similar to curves for the 3D case with square-shaped holes that were presented in Figure 3-43, but with small quantitative differences which result in an optimal operating frequency of $fa/c=0.19$. In the simulation presented in Figure 3-44, a dipole excitation at the air/PC interface, radiates light both into the photonic crystal and into the surrounding air. The total simulation area is $30a \times 750a$. At a frequency of $fa/c=0.18$ [Figure 3-44(a)], which is not the optimal operating frequency for super-collimation, light

diverges within the photonic crystal. After propagating the length of the simulation, the beam's width has expanded beyond the simulation width of $30a$. However, at the optimal frequency of $fa/c=0.19$, the divergence is significantly reduced as light enters the PC [Figure 3-44(b)]. For the full length of the simulation area, the beam's energy remains collimated, traversing the photonic crystal with a finite beam width of approximately $14a$. The direction of collimation is along the diagonal of the square photonic crystal lattice as shown in Figure 3-44(b). This direction is in agreement with the results of the frequency-domain simulation that was presented in Figure 3-43.

3.3.3 Objective

The goal of this thesis research is to demonstrate super-collimation at millimeter length scales using a two-dimensional photonic crystal. The device will allow a focused input beam of light from air, to result in a collimated light beam within the photonic crystal. Super-collimator fabrication is investigated in the silicon-based material system using silicon on insulator (SOI) wafers, where the silicon layer is 205nm thick and the buried SiO_2 layer is 3000nm thick [Figure 3-45].

Top View:



Wavelength $\lambda = 1.5 \mu\text{m}$
 Period $a = 350 \text{ nm}$
 Hole radius $r = 105 \text{ nm}$

Silicon device layer thickness = 205 nm
 Buried SiO_2 thickness = 3 μm

Cross-section:

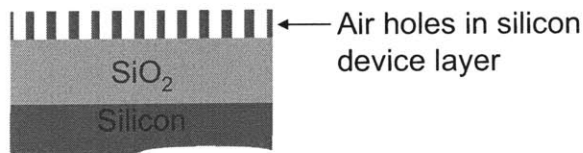


Figure 3-45 Super-collimator device design showing top-view and cross-section.

The device consists of a square lattice of air holes in the 205nm high index silicon layer. Optical isolation of the collimated beam within the silicon layer is achieved using the 3000nm thick buried oxide below the photonic crystal and air above the PC. The feature sizes of the photonic crystal scale with the wavelength of operation. A photonic crystal period of $a=350\text{nm}$ and a circular hole radius of $r=0.3a$ implies an operating wavelength of $1.5\mu\text{m}$. Small variations in hole size, hole shape, or period resulting from fabrication

processes will shift the super-collimation wavelength. The input and output facets consist of cleaved edges of the SOI sample. Samples of varying size were studied.

3.3.4 Device fabrication

The following steps are necessary for fabrication of the super-collimator device:

1. Silicon on insulator (SOI) wafers are obtained from an outside vendor.
2. A 40nm SiO₂ hard mask layer is evaporated onto the SOI samples.
3. The samples are prepared with a trilayer resist stack [200nm OKHA PS4 resist, 20nm SiO₂, 150nm XHRi anti-reflection coating (ARC)].
4. Interference lithography is used to pattern the photonic crystal. The interference lithography step is performed such that the square lattice of the photonic crystal is rotated by 45° from the sample's cleavage plane.
5. Reactive ion etching is used to transfer the hole pattern into the SiO₂ hard mask layer and into the silicon device layer. The SiO₂ hard mask layer is not removed.
6. Device samples are cleaved with parallel input and output facets.

The Lloyd's mirror interferometer discussed in Section 3.1.2 was used to pattern the square lattice photonic crystal. The Lloyd's mirror interferometer was chosen over the two-beam system because it is a more convenient system to use as discussed in Section 3.1.2. In addition, the super-collimator device does not have strict requirements related to the period and hole size, allowing for more relaxed tolerances to be met by the interference lithography step. Small deviations between the designed and fabricated devices with respect to the period, hole size, or hole shape, will shift the wavelength at which super-collimation is achieved. Therefore, by tuning the input laser source during optical characterization, observation of super-collimation will be possible at an alternate wavelength. During the interference lithography step, the photonic crystal was aligned such that the exposed square grid of holes is rotated 45° from the cleavage plane of the SOI sample. Alignment was achieved by positioning the edge of the sample on the exposure chuck at a 45° angle with respect to the edge of the mirror in the Lloyd's mirror setup. With this orientation, the input excitation can be directed in the direction normal to the input facet. However, even without such an alignment step, the input excitation propagates

in the direction of super-collimation for a wide range of input angles as will be discussed in Section 3.3.5. Thus, the alignment is not critical.

After the photonic crystal was exposed using the Lloyd's mirror interferometer, the photonic crystal pattern was transferred through the trilayer resist stack, SiO_2 hard mask layer, and into the device layers using reactive ion etching as discussed in Section 3.1.4. The sample was then cleaved in order to expose smooth facets for input and output coupling. Two parallel cleaves define the input and output facets of the super-collimator. Samples ranging from 3mm to 1cm in length were defined by the distance between the parallel cleaves.

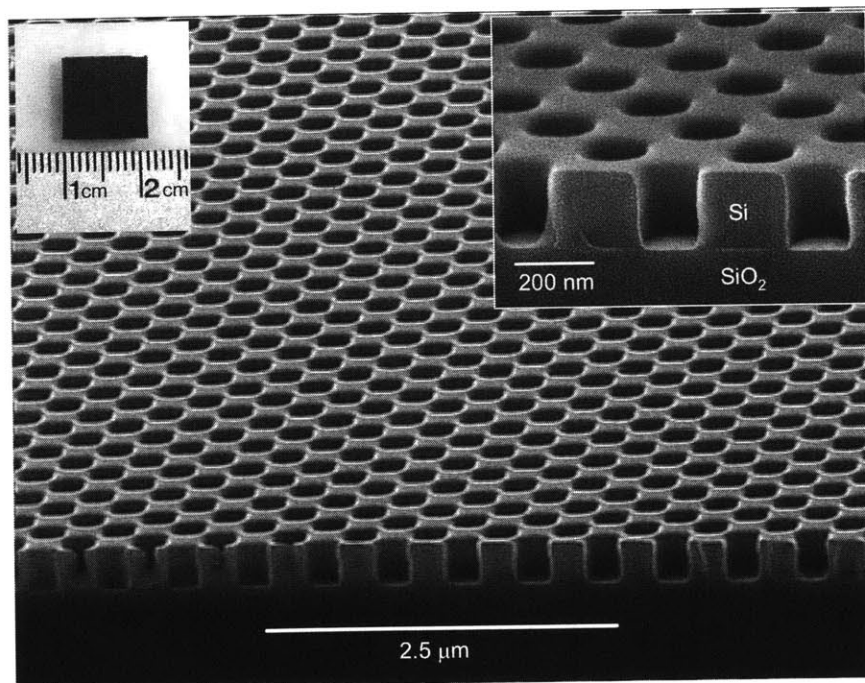


Figure 3-46 Images of fabricated super-collimator device. Center: SEM image showing large area photonic crystal. Inset left: Digital photograph of the 1 cm x 1 cm device. Inset right: SEM image showing detailed cross-section of air holes in silicon on SiO_2 .

Images of fabricated super-collimator devices are presented in Figure 3-46. The left inset shows a digital photograph of the device with cleaved facets on all four sides. Great care was taken to ensure that after cleaving, at least two opposing facets of the sample were never touched by any processing or testing apparatus, keeping the facets as smooth as possible. The center image in Figure 3-46 is a scanning electron micrograph (SEM) of the cross-section of a similar super-collimator sample which highlights the large-area uniformly-periodic photonic crystal. No significant change in the hole size or period was observed over a 1 cm x 1 cm sample area using SEM. Notice that the cleaved edge of the sample is roughly aligned to the diagonal of the photonic crystal's square lattice. The right inset is an SEM

image showing the detail of the super-collimator's cross-section. The air holes of the photonic crystal are etched through the top silicon layer, and terminate on a buried SiO₂ layer.

3.3.5 Optical characterization

A number of optical characterization techniques were used to observe and study super-collimation within the fabricated devices. Characterization was performed in collaboration with Marcus Dahlem and Peter Rakich in the Ultra-fast Optics Group at MIT. Figure 3-47 illustrates three different testing configurations that were used to study super-collimation. In all three cases, two tunable lasers with wavelength ranges from 1430-1515nm and 1510-1610nm excite the photonic crystal through a lensed fiber which produces a sub-micron beam waist at the input of the photonic crystal. The output of the laser was polarized to produce TE polarized light which is the desired polarization for super-collimation. TM-polarized light will diverge within the photonic crystal. Images of the scattered light from the top surface of the photonic crystal were obtained using the setup shown in Figure 3-47(a). An infrared camera (courtesy of Sensors Unlimited, Inc.) collects light which scatters from the surface of the photonic crystal and conveniently provides images of millimeter-scale areas. The scattered light which is imaged, implies propagation losses within the device and may be produced by the roughness of the photonic crystal holes or possibly roughness at the Si/SiO₂ interface. If an image of higher accuracy is required, near-field scanning optical microscopy (NSOM) was implemented as illustrated in Figure 3-47(b). An uncoated fiber probe was brought into contact with the top surface of the sample to detect the evanescent fields associated with propagation of light through the photonic crystal. The fiber probe was scanned along the surface of the photonic crystal with a 10nm resolution scanning stage, to yield images over small PC areas (20 μ m x 20 μ m). By positioning the fiber probe at the output facet of the PC as shown in Figure 3-47(c), the light emitted from the output facet of the device can be imaged with high resolution. In this testing configuration, the fiber probe does not come into contact with the output facet and can be scanned over an area of 18 μ m x 18 μ m with 10nm resolution. The quality of the cleaved facet greatly affects the quality of the output signal detected by the fiber probe. High quality facets at both the input and output facets are essential. However, obtaining a high quality cleave over millimeter length scales for an SOI sample is not trivial since the SOI structure is not single crystal. Therefore, for the tests performed, the positions of the input and output fiber probes were adjusted until a strong output signal with minimal light

scattering was obtained, implying that the input and output facets were of sufficient quality for device testing.

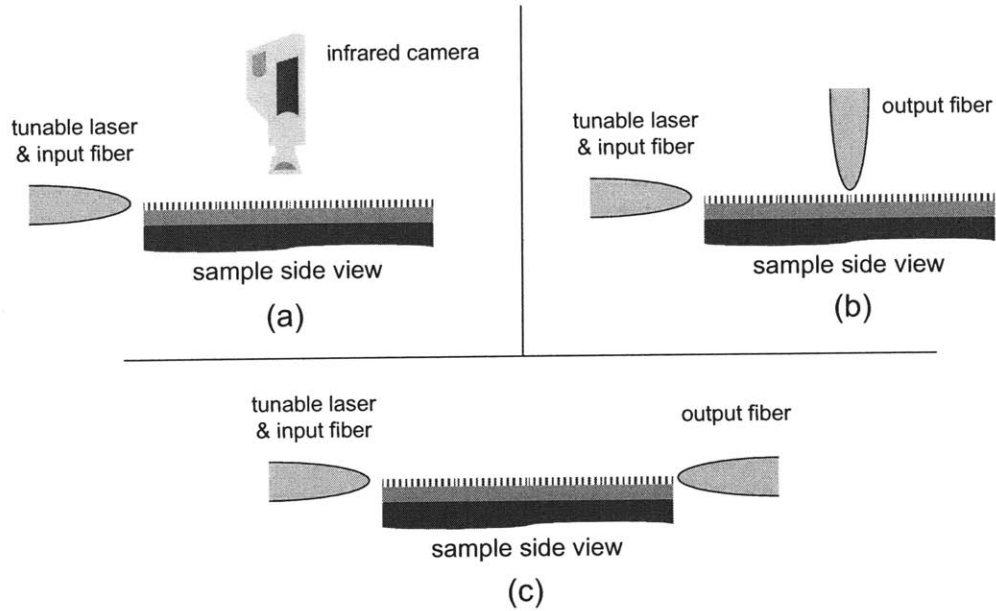


Figure 3-47 Schematic illustrating the three different testing configurations used for studying super-collimation in the photonic crystal slab.

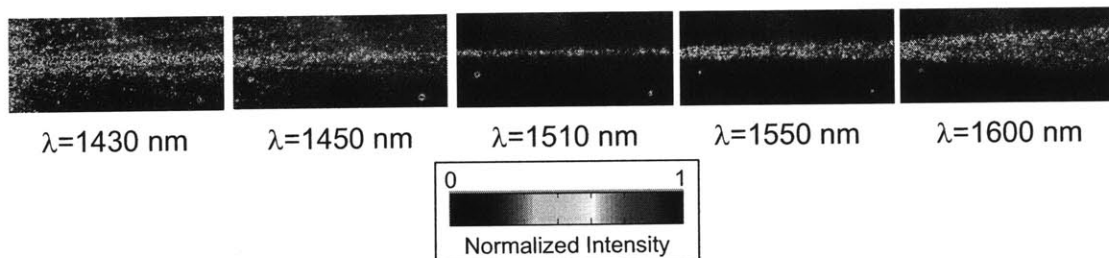


Figure 3-48 Infrared camera images showing the wavelength dependence of super-collimation at the top surface of the photonic crystal. Measurements by M. Dahlem and P. Rakich.

Using the infrared camera, images of light propagation through the photonic crystal for a number of wavelengths could be observed from above the sample as shown in Figure 3-48. Each image represents a $250\mu\text{m} \times 400\mu\text{m}$ area of the photonic crystal approximately $400\mu\text{m}$ from the input facet of the device. Figure 3-48 shows that at a wavelength of 1510nm , light propagation through the photonic crystal was indeed collimated. At this wavelength, the light path resembles a stripe of light which propagates from the left to the right side of the imaging area. By tuning the wavelength of the input laser away from 1510nm , the beam no

longer exhibits collimated behavior and begins to diverge, with the beam width expanding as it propagates the length of the imaging area.

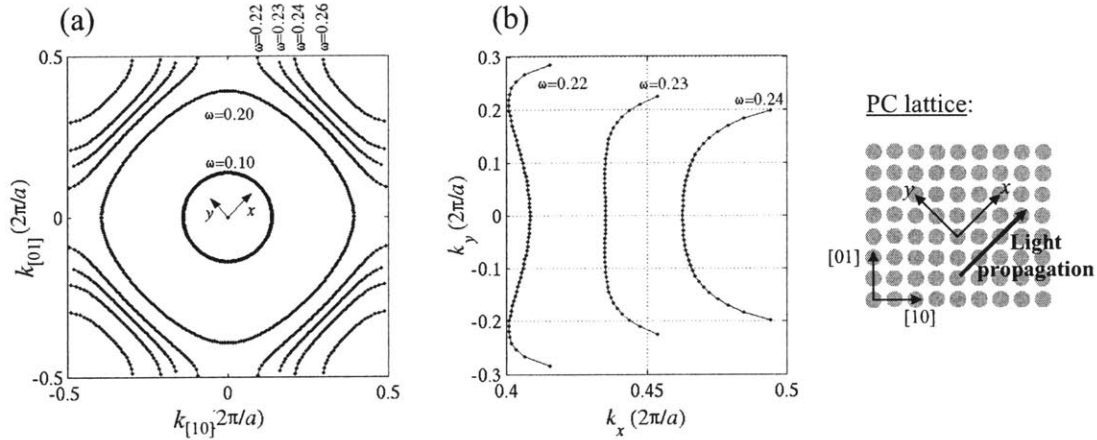


Figure 3-49 (a) Dispersion surfaces for the fabricated photonic crystal. Super-collimation is possible for a normalized frequency of $\omega=0.23$. (b) A detailed view of the of the dispersion surfaces for $\omega=0.22$, 0.23 , and 0.24 . The plot is rotated 45° so that k_x is the k -vector along the propagation direction and k_y is the transverse k -vector. Simulation by M. Ibanescu.

The observed divergence can be explained by examining the dispersion surfaces which were re-calculated based on the characteristics of the fabricated structure. Figure 3-49 presents the 3D dispersion surface calculations for the fabricated structure with $a=350\text{nm}$, $r=0.3a$, and a silicon device layer with a thickness of 205nm . The flattest dispersion surface occurs for a normalized frequency of $\omega=0.23$ ($\omega=fa/c$) as highlighted by the detailed view of the dispersion surfaces in the right plot of Figure 3-49. The results that were shown in Figure 3-48 at operating wavelengths of 1430nm , 1450nm , 1510nm , 1550nm , and 1600nm , correspond to normalized frequencies of $\omega=0.245$, $\omega=0.241$, $\omega=0.232$, $\omega=0.226$, and $\omega=0.219$, respectively, where $\omega=a/\lambda$. At the frequencies of $\omega=0.22$ and $\omega=0.24$, the curvature exhibited by each dispersion surface results in the divergent behavior observed at wavelengths other than 1510nm .

Another interesting observation that is apparent from the results in Figure 3-48 is the "beam-splitting" effect which is present at wavelengths below 1510nm . Though the beam is diverging within the photonic crystal, the divergence angles seem to be discrete rather than continuous. No observation of this kind has been reported in the literature to date. The dispersion surface for $\omega=0.24$ in Figure 3-49, corresponding to $\lambda=1450\text{nm}$, does not suggest that the angles of propagation should be discrete. Future explorations will investigate the origin of this observed splitting effect.

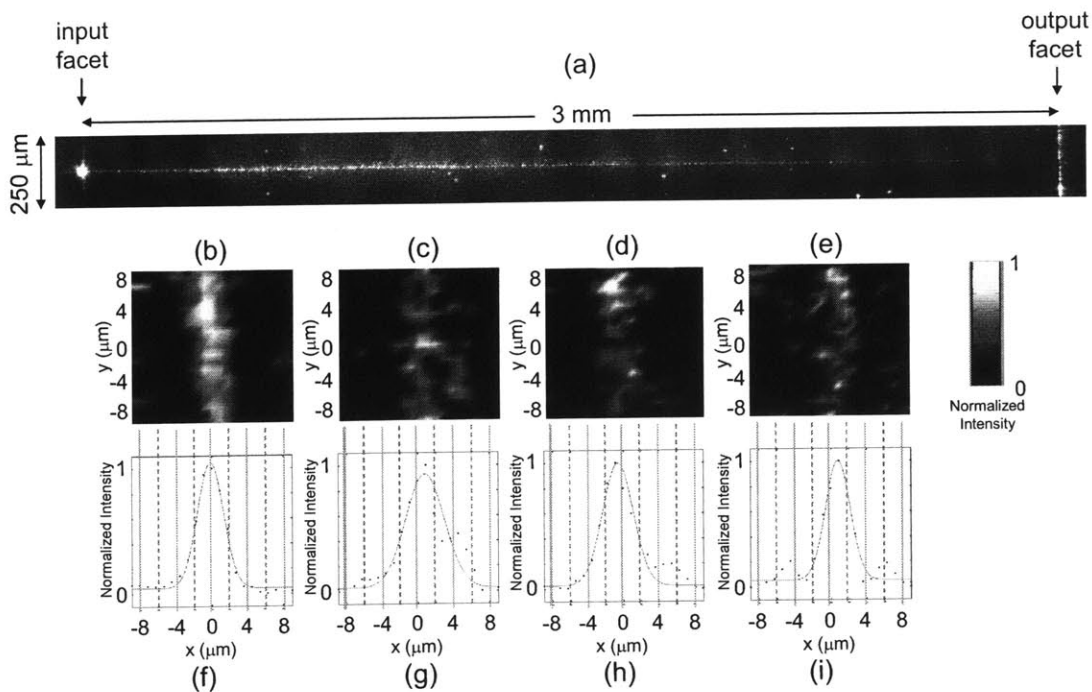


Figure 3-50 Demonstration of the spatial dependence of super-collimation. The operating wavelength is 1510nm. (a) Infrared camera image of light propagation from the input to the output facets of a 3mm sample. (b)-(d) Near-field scanning optical microscope (NSOM) images taken at four different locations along the length of the 3mm sample. No significant beam divergence is measured. Measurements by M. Dahlem and P. Rakich.

With a large area photonic crystal with millimeter length scales, the spatial dependence of the super-collimation could be studied. An infrared camera image viewing the top surface of the photonic crystal [Figure 3-50(a)] demonstrates that super-collimation can be sustained for a length scale of 3 mm without any noticeable divergence, at a wavelength of 1510nm. The image in Figure 3-50(a) represents the first demonstration of super-collimation at millimeter length scales. A more detailed analysis was performed using the NSOM technique applied at various positions along the length of the 3mm collimated beam. Figure 3-50(b)-(e) presents NSOM measurements at the input facet, 1mm from the input, 2mm from the input, and at the output facet. Each plot presents a MATLAB plot of the intensity of the optical signal over an $18\mu\text{m} \times 18\mu\text{m}$ area with piecewise bilinear interpolation. Figure 3-50(f)-(i) plots the average y intensity at each x position in Figure 3-50(b)-(e). The overall intensity was then normalized and fitted to a Gaussian as shown. The plots [Figure 3-50(f)-(i)] demonstrate that no significant broadening of the beam width is observed over the full 3mm length of the sample.

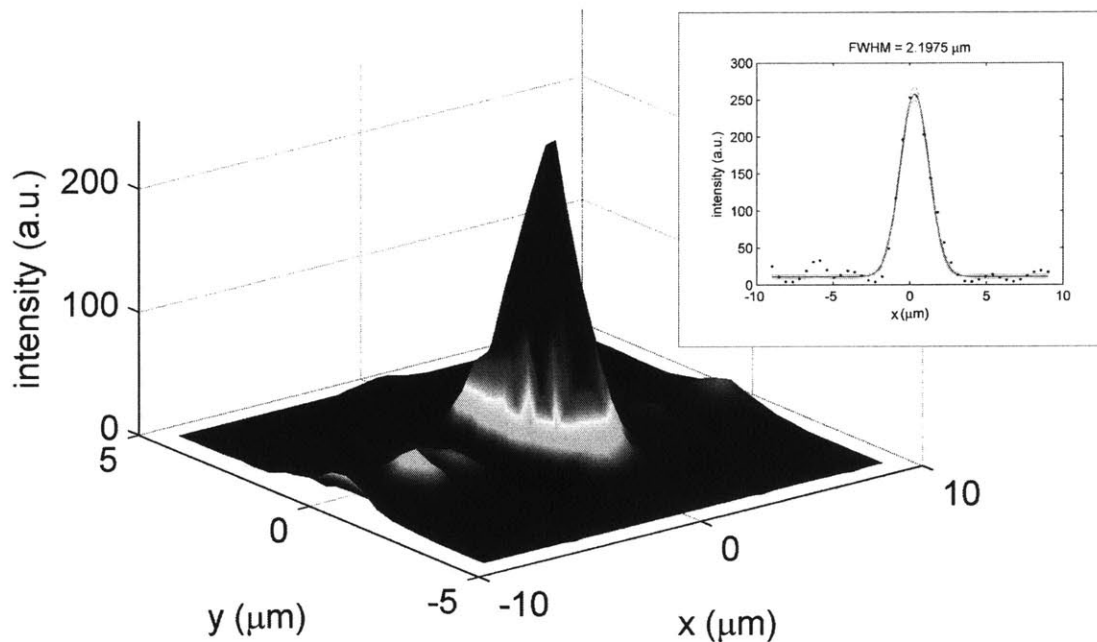


Figure 3-51 Demonstration of super-collimation as measured at the output facet of a 5mm device with a fiber probe. The inset is a plot of the average x intensity at each y position of the 2D intensity plot with a Gaussian fit of the data. Measurements by M. Dahlem and P. Rakich.

For device lengths greater than 3mm, scattering losses within the photonic crystal resulted in significant attenuation of the collimated beam making NSOM measurements difficult. However, measurements of the optical signal could be obtained by scanning the fiber probe at the output facet of the device. Figure 3-51 shows the result of a fiber scan at the output facet of a 5 mm long photonic crystal device. The figure presents a MATLAB plot of the intensity of the optical signal over an $18\mu\text{m} \times 18\mu\text{m}$ area with piecewise bilinear interpolation. The inset is a plot of the average x intensity at each y position with a Gaussian fit of the data, suggesting a full-width-half-maximum (FWHM) beam width of approximately $2\mu\text{m}$. The result indicates that super-collimation is sustained after 5 mm of propagation. Similar observations of an unbroadened beam width were made for an 8 mm long photonic crystal device.

The influence of the input coupling angle on super-collimation was also explored. As described in Section 3.3.2, the direction of super-collimation is in the direction that corresponds to the diagonal of the square lattice of holes that comprise the photonic crystal. In the diagonal direction, the dispersion surface is "flat" for a wide range of k -vectors. As an experiment, the angle of the input fiber was tilted to an angle of approximately 20° with respect to the input facet normal as shown in Figure 3-52. Tilting the angle of the input

beam by 20° did not affect the direction in which the collimated beam propagates. The direction of collimation remained the direction normal to the input interface as was observed for normal input incidence in Figure 3-50. Since the collimation of light within the photonic crystal is a result of the flatness of the dispersion surface, Figure 3-52 experimentally demonstrates that the dispersion surface is "flat" for a wide range of k -vectors--the k -vectors which compose the focused beam incident at a 20° angle.

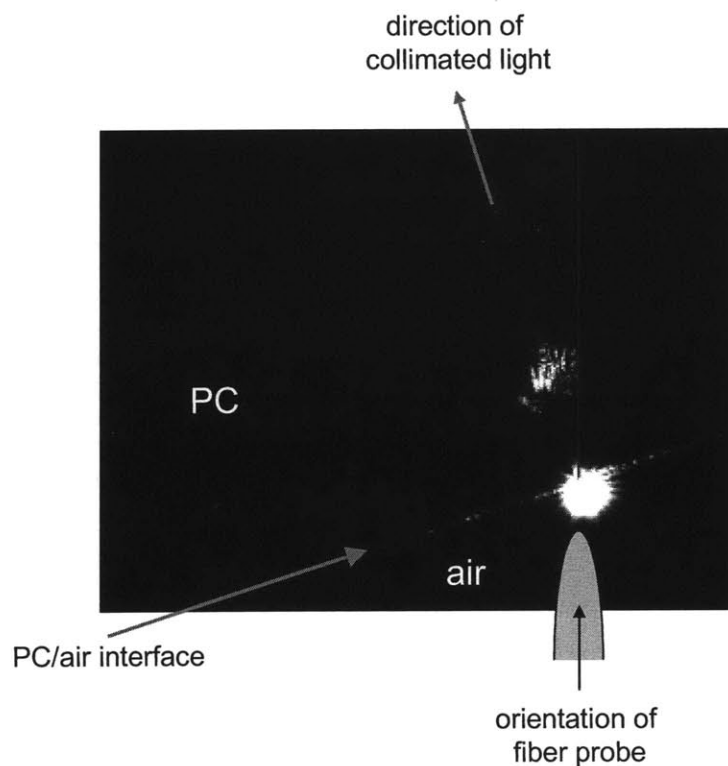


Figure 3-52 Infrared camera image of input coupling at an 20° angle with respect to the normal to the PC/air interface. The operating wavelength is 1500 nm. The collimated beam still propagates normal to the PC/air interface. Original image by M. Dahlem.

3.3.6 Future work

The initial work presented on super-collimation in large area photonic crystals has paved the way for a wide range of future explorations. The "beam splitting effect" observed at wavelengths below the super-collimation wavelength is noteworthy and will require future investigations to determine its origins. Further optical characterization is necessary to measure the precise beam widths over the length of the collimated beam as well as the propagation losses. Future work could explore designs aimed at reducing these losses using other photonic crystal structures. Future work can also explore the effects on super-

collimation when a symmetric layered structure is used. The current super-collimator is a vertically asymmetric structure with the photonic crystal clad by air at its top surface and SiO₂ at its bottom surface. With an asymmetric design, the polarizations of the allowed modes of the photonic crystal are neither purely TE, nor purely TM and are referred to as "TE-like" and "TM-like" respectively. Though the input fiber excites the PC with TE-polarized light at the input facet, "TE-like" light is excited within the photonic crystal and consists of a mix of TE and TM polarizations. Since the super-collimation effect is only observed for TE light propagation, the TM component of the excitation diverges within the photonic crystal and is not useful for device operation. Creating a symmetric structure may reduce the excitation of TM light allowing pure TE excitation within the PC. In the future, explorations can be made where the super-collimator is interfaced with optical components integrated on the same planar chip. To integrate active elements with the super-collimator, devices that are fabricated in III-V materials are necessary. A III-V super-collimator could be implemented with a GaAs guiding layer and a buried low-index Al_xO_y layer for optical isolation. This buried oxide can be created using the wet oxidation process described in Section 3.2.7. The integration of the super-collimator with passive components such as beam splitters, phase shifters, and planar mirrors can also be investigated for use in planar lightwave circuits.

3.3.7 Conclusion

In conclusion, a super-collimator has been designed, fabricated, and characterized such that the collimation effect of photonic crystals is observed and measured at millimeter length scales. Three-dimensional dispersion surface calculations indicate that a "flat" dispersion surface is essential for demonstrating super-collimation. Any curvature in the dispersion surface results in divergence which causes beam spreading within the photonic crystal. Divergence was demonstrated both by two-dimensional time-domain simulations, and optical characterization measurements of fabricated structures. Interference lithography enables the fabrication of large area two-dimensional photonic crystals for millimeter-scale super-collimation. The results of the optical characterization demonstrate that super-collimation is sustained for up to 8 mm without noticeable broadening of the beam's width suggesting that the fabricated photonic crystal remains uniform over millimeter length scales.

3.4 References

- [1] M. E. Walsh, "On the Design of Lithographic Interferometers and their Application." Cambridge, MA: PhD Thesis in Electrical Engineering and Computer Science, MIT, 2004.
- [2] J. T. Hastings, "Nanometer-Precision Electron-Beam Lithography with Applications in Integrated Optics." Cambridge, MA: PhD Thesis in Electrical Engineering and Computer Science, MIT, 2003.
- [3] H. Kosaka, T. Kawashima, A. Tomita, M. Notomi, T. Tamamura, T. Sato, and S. Kawakami, "Superprism phenomena in photonic crystals: Toward microscale lightwave circuits," *Journal of Lightwave Technology*, vol. 17, pp. 2032-2038, 1999.
- [4] H. Kosaka, T. Kawashima, A. Tomita, M. Notomi, T. Tamamura, T. Sato, and S. Kawakami, "Self-collimating phenomena in photonic crystals," *Applied Physics Letters*, vol. 74, pp. 1212-1214, 1999.
- [5] B. E. Nelson, M. Gerken, D. A. B. Miller, R. Piestun, C. C. Lin, and J. S. Harris, "Use of a dielectric stack as a one-dimensional photonic crystal for wavelength demultiplexing by beam shifting," *Optics Letters*, vol. 25, pp. 1502-1504, 2000.
- [6] L. J. Wu, M. Mazilu, T. Karle, and T. F. Krauss, "Superprism phenomena in planar photonic crystals," *Ieee Journal of Quantum Electronics*, vol. 38, pp. 915-918, 2002.
- [7] A. Lupu, E. Cassan, S. Laval, L. El Melhaoui, P. Lyan, and J. M. Fedeli, "Experimental evidence for superprism phenomena in SOI photonic crystals," *Optics Express*, vol. 12, pp. 5690-5696, 2004.
- [8] H. Kosaka, T. Kawashima, A. Tomita, M. Notomi, T. Tamamura, T. Sato, and S. Kawakami, "Photonic crystals for micro lightwave circuits using wavelength-dependent angular beam steering," *Applied Physics Letters*, vol. 74, pp. 1370-1372, 1999.
- [9] S. G. Johnson and J. D. Joannopoulos, "Block-iterative frequency-domain methods for Maxwell's equations in a planewave basis," *Optics Express*, vol. 8, pp. 173-190, 2001.
- [10] A. Tavlove, *Computational Electrodynamics: The Finite-Difference Time-Domain Method*, 2 ed. Boston: Artech House, 2000.
- [11] C. Y. Luo, M. Soljacic, and J. D. Joannopoulos, "Superprism effect based on phase velocities," *Optics Letters*, vol. 29, pp. 745-747, 2004.
- [12] T. Baba, T. Matsumoto, and M. Echizen, "Finite difference time domain study of high efficiency photonic crystal superprisms," *Optics Express*, vol. 12, pp. 4608-4613, 2004.
- [13] S. N. Tandon, Soljacic, M., Petrich, G. S., Joannopoulos, J. D., Kolodziejski, L. A., "The Superprism Effect using Large Area 2D-Periodic Photonic Crystal Slabs," *Photonics and Nanostructures*, 2005.
- [14] S. Assefa, "The Development of Novel Passive and Active Photonic-Crystal Devices." Cambridge, MA: PhD Thesis in Electrical Engineering and Computer Science, MIT, 2004.
- [15] S. N. Tandon, J. T. Gopinath, A. A. Erchak, G. S. Petrich, L. A. Kolodziejski, and E. P. Ippen, "Large-area oxidation of AIAs layers for dielectric stacks and thick buried oxides," *Journal of Electronic Materials*, vol. 33, pp. 774-9, 2004.
- [16] M. H. MacDougall and P. D. Dapkus, "Wavelength shift of selectively oxidized Al(x)O(y)AlGaAs-GaAs distributed Bragg reflectors," *IEEE Photonics Technology Letters*, vol. 9, pp. 884-6, 1997.
- [17] S. Assefa, G. S. Petrich, L. A. Kolodziejski, M. K. Mondol, and H. I. Smith, "Fabrication of photonic crystal waveguides composed of a square lattice of dielectric rods," *Journal of Vacuum Science & Technology B*, vol. 22, pp. 3363-3365, 2004.

- [18] S. J. McNab, N. Moll, and Y. A. Vlasov, "Ultra-low loss photonic integrated circuit with membrane-type photonic crystal waveguides," *Optics Express*, vol. 11, pp. 2927-2939, 2003.
- [19] X. F. Yu and S. H. Fan, "Bends and splitters for self-collimated beams in photonic crystals," *Applied Physics Letters*, vol. 83, pp. 3251-3253, 2003.
- [20] J. Witzens and A. Scherer, "Efficient excitation of self-collimated beams and single Bloch modes in planar photonic crystals," *Journal of the Optical Society of America a-Optics Image Science and Vision*, vol. 20, pp. 935-940, 2003.
- [21] J. Witzens, M. Loncar, and A. Scherer, "Self-collimation in planar photonic crystals," *Ieee Journal of Selected Topics in Quantum Electronics*, vol. 8, pp. 1246-1257, 2002.
- [22] D. N. Chigrin, S. Enoch, C. M. S. Torres, and G. Tayeb, "Self-guiding in two-dimensional photonic crystals," *Optics Express*, vol. 11, pp. 1203-1211, 2003.
- [23] D. M. Pustai, S. Y. Shi, C. H. Chen, A. Sharkawy, and D. W. Prather, "Analysis of splitters for self-collimated beams in planar photonic crystals," *Optics Express*, vol. 12, pp. 1823-1831, 2004.
- [24] L. Wu, M. Mazilu, J.-F. Gallet, and T. F. Krauss, "Square Lattice photonic-crystal collimator," *Photonics and Nanostructures*, vol. 1, pp. 31-36, 2003.
- [25] D. W. Prather, S. Y. Shi, D. M. Pustai, C. H. Chen, S. Venkataraman, A. Sharkawy, G. J. Schneider, and J. Murakowski, "Dispersion-based optical routing in photonic crystals," *Optics Letters*, vol. 29, pp. 50-52, 2004.
- [26] D. W. Prather, C. Chen, S. Shi, B. Miao, D. Pustai, S. Venkataraman, A. S. Sharkawy, G. J. Schneider, and J. A. Murakowski, "Ultra low loss photonic crystal waveguides based on the self-collimation effect," presented at Photonic Crystal Materials and Devices II, Jan 26-29 2004, San Jose, CA, United States, 2004.

Chapter 4

List of Contributions

4.1 Journal Publications

M. Dahlem, P. Rakich, **S. N. Tandon**, M. Ibanescu, M. Soljačić, G. S. Petrich, L. A. Kolodziejski, J. D. Joannopoulos, and E. P. Ippen. "Centimetre-scale super collimation effect in a 2D photonic crystal." To be submitted to *Nature*.

S. N. Tandon, M. Soljačić, G. S. Petrich, J. D. Joannopoulos and L. A. Kolodziejski. "The Superprism Effect using Large Area 2D-Periodic Photonic Crystal Slabs." *Photonics and Nanostructures*. Accepted for publication February 2005.

S. N. Tandon, J.T. Gopinath, H.M. Shen, G.S. Petrich, L.A. Kolodziejski, F.X. Kärtner, and E.P. Ippen. "Large-area broadband saturable Bragg reflectors by use of oxidized AIAs." *Optics Letters*. **29** (2004) 2551.

S. N. Tandon, J. T. Gopinath, A. A. Erchak, G. S. Petrich, L. A. Kolodziejski, and E. P. Ippen. "Large Area Oxidation of AIAs Layers for Dielectric Stacks and Thick Buried Oxides." *Journal of Electronic Materials*. **33** (2004) 774.

T. R. Schibli, J. Kim, O. Kuzuca, J. T. Gopinath, **S. N. Tandon**, G. S. Petrich, L. A. Kolodziejski, J. G. Fujimoto, E. P. Ippen, and F. X. Kärtner. "Attosecond active synchronization of passively mode-locked lasers by balanced cross correlation." *Optics Letters*. **28** (2003) 947.

4.2 Conference Presentations

S. N. Tandon, J.T. Gopinath, H.M. Shen, G.S. Petrich, L.A. Kolodziejski, F.X. Kärtner, and E.P. Ippen. "Broadband Saturable Bragg Reflectors from the Infrared to Visible using Oxidized AIAs." *Conference on Lasers and Electro-Optics (CLEO)*, 2004. Oral presentation by **Sheila N. Tandon**.

J.W. Sickler, J.T. Gopinath, **S. N. Tandon**, H. Sotobayashi, G.S. Petrich, E.P. Ippen, and L.A. Kolodziejski. "Femtosecond laser using broadband erbium-doped bismuth oxide gain fiber." *Conference on Lasers and Electro-Optics (CLEO)*, 2004.

S. N. Tandon, J. T. Gopinath, T. R. Schibli, G. S. Petrich, L. A. Kolodziejski, F. X. Kärtner, and E. P. Ippen. "Saturable Absorbers with Large Area Broadband Bragg Reflectors for Femtosecond Pulse Generation." *Conference on Lasers and Electro-Optics (CLEO)*, 2003. Oral presentation by **Sheila N. Tandon**.

T. R. Schibli, J.-W. Kim, L. Matos, A. W. Killi, J. Gopinath, G. Petrich, **S. Tandon**, L. A. Kolodziejski, E. P. Ippen, and F. X. Kärtner. "Sub-femtosecond active synchronization of passively mode-locked lasers using balanced cross-correlation." *Conference on Lasers and Electro-Optics (CLEO)* 2003. Oral presentation by Thomas R. Schibli.

4.3 Seminar Talks

S. N. Tandon. "Broadband Saturable Bragg Reflectors for Femtosecond Pulse Generation." MIT Center for Integrated Photonic Systems (CIPS), Cambridge, MA. October 28, 2004.

S. N. Tandon. "Broadband Saturable Bragg Reflectors for Femtosecond Pulse Generation." Applied Micro- and Optoelectronics (AMO), GmbH, Aachen, Germany. August 5, 2004.

Chapter 5

Appendix

5.1 Oxidation Log

The following is a tabulation of the oxidations performed in this thesis. All growth numbers refer to the structures described in Appendix 5.2.

Date	Growth	Temp (C)	Time (hrs)	Oxidized Distance (um)	Sample location on wafer	ramp up	ramp down	Oxidation Result
9/26/2002	R934	435	2.5	250				no delamination; looked underoxidized under microscope; edge of wafer sample
9/26/2002	R933	435	2.5	250				striped delamination at edges
9/27/2002	R934	435	3.5	250				no delamination
9/27/2002	R933	420	3	200				delamination at edges
9/30/2002	R933	405	5	150				no delamination
10/1/2002	R933	405	8	250				no delamination
10/1/2002	R934	405	8	250				no delamination
10/29/2002	R946	435	3	250	center			stripes of delamination and edge delamination
10/30/2002	R946	420	3	230	not center			delamination at edges
11/4/2002	R946	415	2.5	150	not center			outer wafer sample; no delamination
11/4/2002	R946	415	2.5	180				center wafer sample; delamination some delamination at edges
11/13/2002	R946	415	5	250				no delamination but some discoloration possibly due to overoxidation
11/14/2002	R946	420	3	190				no delamination
11/18/2002	R946	420	4.25	250	center			no delamination
12/6/2002	R957	420	4	250	center			delamination at edges with some discoloration possibly due to overoxidation
12/9/2002	R957	405	8	250	center			some delamination at edges; noticeable discoloration and cracking of absorber layer possibly due to overoxidation

Date	Growth	Temp (C)	Time (hrs)	Oxidized Distance (um)	Sample location on wafer	ramp up	ramp down	Oxidation Result
12/12/2002	R957	405	5	230	not center			no delamination
12/16/2002	R957	405	6	250	center			delamination at edges
12/17/2002	R958	420	3.5	250	center			stripes of delamination
12/17/2002	R958	420	2	160	not center			no delamination
12/18/2002	R957	410	4.5	250	center			delamination at edges
12/18/2002	R957	410	2	112	not center			no delamination
12/18/2002	R957	415	2	150	not center			slight delamination at edges
12/18/2002	R958	410	4.5	250	center			stripes of delamination with some edge delamination
12/18/2002	R958	410	2	133	not center			no delamination
12/18/2002	R958	415	2	140	not center			slight delamination at edges
2/14/2003	R957	410	4.5	250	edge			no delamination
2/14/2003	R957	410	4.5	250	center			delamination
2/14/2003	R958	410	4.5	250	long strip			delamination on mesas from center of wafer; no delamination on mesas from outer parts of wafer
2/21/2003	R959	410	4.5	250	long strip			delamination on many mesas from center of wafer; mesas at the very center had no delamination; no delamination on mesas from outer parts of wafer
3/31/2003	r958	435	3	250	strip			stripe delamination at center parts & less delamination at edges; SEM shows delamination is between 1st AlGaAs and 1st oxide layer
3/31/2003	r946	435	3	250	strip			one stripe of delamination at center mesa & much less edge delamination at edge mesa
3/31/2003	r957	435	3	250	strip			no stripe delamination. Edge delamination which becomes more severe at center mesas.
4/8/2003	r946	420	4.25	250	center			edge delamination
4/8/2003	r968	410	4.5	250	center			no delamination
4/10/2003	r946	410	5.5	250	center			no delamination
4/10/2003	r968	410	5.5	250	center			delamination on opposing sides of mesas
4/11/2003	r946	410	4.5	250				
4/11/2003	r968	410	4.5	250				
4/24/2003	r946	410	4.5	227	center			
4/24/2003	r968	410	4.5	232	center			
4/24/2003	r970	410	4.5	221	center			
4/25/2003	r946	410	5	200				
4/25/2003	r968	410	5	250				
4/25/2003	r970	410	5	234				
4/25/2003	r946	410	6	240				
4/25/2003	r968	410	6	250				
4/25/2003	r970	410	6	250				
4/28/2003	r970	410	5.5	250				
5/9/2003	r968	410	4.75	250				edge delamination
5/9/2003	r971	410	4.75					severely delaminated
5/12/2003	r971	410	4.83					uneven oxidation; probably due to improper resist removal
5/19/2003	r970	410	5.5	250				
5/21/2003	r970	410	5.5	250				
5/23/2003	r970	410	4.66	250				
7/17/2003	r981	410	5.5	100				cleaved sample
7/21/2003	r981	400	6.5					cleaved sample; ran out of N2 during oxidation
7/22/2003	r958	410	2.5					sample w/ 10um holes
8/11/2003	r981	410	4	130	center	100-410, 50min	100-410, 50min	cleaved sample
8/13/2003	r981	410	3	180	edge	100-410, 31min	100-410, 31min	
8/13/2003	r958	410	3	170	edge	100-410, 31min	100-410, 31min	
8/13/2003	r971	410	3	140	edge	100-410, 31min	100-410, 31min	
8/13/2003	r979	410	3	180	edge	100-410, 31min	100-410, 31min	
8/14/2003	r958	410	4.5	250	center	100-410, 50min	100-410, 50min	
8/14/2003	r979	410	4.5	250	center	100-410, 50min	100-410, 50min	
8/14/2003	r981	410	4.5	250	center	100-410, 50min	100-410, 50min	
8/15/2003	r971	410	5.5	220		100-410, 50min	100-410, 50min	
8/21/2003	r971	410	6	250	center	100-410, 50min	100-410, 50min	
8/25/2003	r979	435	2	250	edge	100-435, 55min	100-435, 55min	

Date	Growth	Temp (C)	Time (hrs)	Oxidized Distance (um)	Sample location on		ramp up	ramp down	Oxidation Result
					wafer				
8/27/2003	r979	435	1	165	edge		100-400, 50min; 400-435, 60min	100-400, 50min; 400-435, 60min	
8/27/2003	r981	435	1	165	edge		100-400, 50min; 400-435, 60min	100-400, 50min; 400-435, 60min	
9/2/2003	r979	435	2		center		100-400, 50min; 400-435, 60min	100-435, 50min	delamination towards mesa middles
9/4/2003	r981	435	2		center		100-400, 50min; 400-435, 60min	100-435, 60min	delamination towards mesa middles
9/10/2003	r981	410	4.75	250	center		100-410, 50min	100-410, 50min	
9/16/2003	r979	435	2	250	edge		100-400, 50min; 400-435, 60min	100-435, 60min	
9/16/2003	r981	435	2	250	edge		100-400, 50min; 400-435, 60min	100-435, 60min	
9/24/2003	r958	410	4.5	250	center		100-410, 50min	100-410, 50min	
9/24/2003	r1000	410	4.5		center		100-410, 50min	100-410, 50min	cleaved sample
9/30/2003	r1000	410	3.5	200	edge #7		100-410, 50min	100-410, 50min	
10/2/2003	r1000	410	4.5		#1		100-410, 50min	100-410, 50min	
10/10/2003	r1000	410	4.5	250	#3		100-410, 50min	100-410, 50min	water overflowed into furnace drowning sample
10/16/2003	r1000	410	4.5	250	#3 & 11		100-410, 50min	100-410, 50min	
10/17/2003	r1000	410	4.5		#12		100-410, 50min	100-410, 50min	nitrogen flow turned off
10/20/2003	r1000	410	4.5		#12		100-410, 50min	100-410, 50min	
10/20/2003	r958	410	4.5	228	strip sample		100-410, 50min	100-410, 50min	strip sample etched 9/16/03
10/23/2003	r1000	410	4.5	250	#13, 14, 15, 16		100-410, 50min	100-410, 50min	
10/27/2003	r958	410	0.66				100-410, 50min	100-410, 50min	reoxidation of part of strip sample oxid 10/20/03
11/10/2003	r1000	410	4.5	250	18, 19		100-410, 50min	100-410, 50min	
11/12/2003	r1000	435	2	227	20		100-435, 50min	100-435, 50min	
11/12/2003	r1000	435	2.5	250	21		100-435, 50min	100-435, 50min	
12/17/2003	r1014	410	4.83	250	1		100-410, 50min	100-410, 50min	nitrogen ran out
12/17/2003	r1015	410	4.83	220	1		100-410, 50min	100-410, 50min	nitrogen ran out
1/7/2004	r1014	410	4.5	250	2		100-410, 50min	100-410, 50min	
1/8/2004	r1015	410	5	250	2		100-410, 50min	100-410, 50min	
1/23/2004	r1015	410	4.75	230	3		100-410, 50min	100-410, 50min	
1/26/2004	r1015	410	5	250	9		100-410, 50min	100-410, 50min	good sample
1/27/2004	r1015	410	0.42		3		100-410, 50min	100-410, 50min	reoxidation
1/30/2004	r1015	410	5	250	4,5,6,7,8		100-410, 50min	100-410, 50min	good samples
3/1/2004	r1000	435	2.5	250	22		100-435, 50min	100-435, 50min	
3/9/2004	r979	435	2				100-400, 50min; 400-435, 60min	100-435, 60min	not an oxidation, no steam present, samples: unprocessed #1 & unoxidized center sample
3/10/2004	r958	410	4.83	250	1		100-410, 50min	100-410, 50min	cleaved 3/10/04, etched 9/16/03; ramp up w/ no steam, ramp down w/ steam
3/11/2004	r958	410	4.83	250	2		100-410, 50min	100-410, 50min	cleaved 3/10/04, etched 9/16/03; ramp up w/ steam, ramp down w/o steam
3/16/2004	r958	410	4.83	250	3		100-410, 50min	100-410, 50min	cleaved 3/10/04, etched 9/16/03; both ramps w/ steam
3/17/2003	r979	410	4.5	170	center		100-410, 50min	100-410, 50min	same sample as 3/9/04 temp ramp
4/14/2004	r1020	435	2		1		100-435, 50min	100-435, 50min	etched 4/13/04; sample lost
4/15/2004	r1000	435	6		sq1		100-435, 50min	100-435, 50min	1mm squares etched 4/13/04; delamination all over sample
4/20/2004	r979	410	5	250	1		100-410, 50min	100-410, 50min	etched 4/13/04
4/20/2004	r1021	410	5	250	1		100-410, 50min	100-410, 50min	etched 4/13/04; edge delamination
4/21/2004	r1023	410	6		1		100-410, 50min	100-410, 50min	severe cracking; etched 4/13/04
4/22/2004	r1020	435	2.5	250	2		100-410, 50min	100-410, 50min	spotted delamination across sample; etched 4/13/04; noticed a temperature overshoot of ~15deg on ramp up
4/23/2004	r1021	410	4.25		2		100-395, 50min; 395-410, 15min	410-100, 50min	severe cracking; etched 4/13/04
4/26/2004	r1021	410	4.25		2.5		100-395, 50min; 395-410, 15min	410-100, 50min	severe cracking; noticed problems w/ water leaking back into furnace & cooling temp w/ subseq. overshoot

Date	Growth	Temp (C)	Time (hrs)	Oxidized Distance (um)	Sample location on wafer	ramp up	ramp down	Oxidation Result
4/27/2004	r1021	410	4.25	250	3	100-395, 50min; 395-410, 15min	410-100, 50min	
4/29/2004	r1020	435	2.25	200	3	100-410, 50min; 410-435, 25min	435-100, 50min	etched 4/13/04; underoxidized
4/30/2004	r1020	435	2.75	250	4	100-410, 50min; 410-435, 25min	435-100, 50min	sample looked great
5/3/2004	r1020	435	2.75		5	100-410, 50min; 410-435, 25min	435-100, 50min	power went out after ~1.25 hrs; then restarted oxidation cycle
5/6/2004	r1020	435	2.75	250	6	100-410, 50min; 410-435, 25min	435-100, 50min	
5/10/2004	r1020	435	2.75	250	7	100-410, 50min; 410-435, 25min	435-100, 50min	
5/11/2004	r1021	410	4.5	250	4	100-385, 50min; 385-410, 25min	410-100, 50min	
5/12/2004	r1000	435	5	300	sq2	100-410, 50min; 410-435, 25min	435-100, 50min	1mm squares; had 400-430um diameter => 200-215um radius left to oxidize
5/14/2004	r1000	435	7	365	sq3	100-410, 50min; 410-435, 25min	435-100, 50min	
6/3/2004	r971	410	5.5	250	center	100-410, 50min	100-410, 50min	sample was etched 8/13/03; edges of mesa cracked due to room temp oxidation
6/7/2004	r1015	410	5	250	10	100-410, 50min	100-410, 50min	edge delamination
6/7/2004	r1021	410	5	250	5	100-410, 50min	100-410, 50min	edge delamination but also some striped delamination
6/7/2004	r981	410	5	250	1; etched 6/4/04	100-410, 50min	100-410, 50min	edge delamination but also some striped delamination
6/7/2004	r968	410	5	250	1; etched 6/4/04	100-410, 50min	100-410, 50min	slight edge delamination
6/7/2004	r1027	410	5	250	1; etched 6/4/04	100-410, 50min	100-410, 50min	extreme delamination over the full mesa
6/8/2004	r971	410	6	250	1; etched 6/4/04	100-410, 50min	100-410, 50min	slight edge delamination
6/9/2004	r968	410	4.5	250	2; etched 6/4/04	100-385, 50min, 385-410, 30min	100-410, 50min	no delamination
6/9/2004	r981	410	4.5	250	2; etched 6/4/04	100-385, 50min, 385-410, 30min	100-410, 50min	some delamination across the areas of some mesas
6/9/2004	r1015	410	4.5	250	11; etched 1/26/04	100-385, 50min, 385-410, 30min	100-410, 50min	no delamination
6/9/2004	r1021	410	4.5	250	6; etched 4/13/04	100-385, 50min, 385-410, 30min	100-410, 50min	no delamination
6/9/2004	r1027	410	4.5	250	2; etched 6/4/04	100-385, 50min, 385-410, 30min	100-410, 50min	some delamination on some mesas
6/10/2004	r1027	410	4.5	250	3 (long strip); etched 6/4/04	100-385, 50min, 385-410, 30min	100-410, 50min	some delamination on a few mesas
6/11/2004	r968	410	4.5	250	3; etched 6/4/04	100-385, 50min, 385-410, 30min	100-410, 50min	no delamination
6/14/2004	r1015	410	4.5	250	17; etched 1/26/04	100-385, 50min, 385-410, 30min	100-410, 50min	no delamination; mesa edges cracked due to atmospheric oxidation
6/15/2004	r981	410	4.5	250	3; etched 6/4/04	100-385, 50min, 385-410, 30min	100-410, 50min	no delamination
6/16/2004	r971	410	6	250	2; etched 6/4/04	100-410, 50min	100-410, 50min	slight edge delamination

Date	Growth	Temp (C)	Time (hrs)	Oxidized Distance (um)	Sample location on wafer	ramp up	ramp down	Oxidation Result
6/24/2004	r1000	435	9.5	375	sq4; etched 4/13/04	100-410, 50min; 410-435, 25min	435-100, 50min	spotted delamination across sample
6/24/2004	r1026	435	2.75	250	1; etched 6/4/04	100-410, 50min; 410-435, 25min	435-100, 50min	spotted delamination across mesas

5.2 SBR growth log

The following is a tabulation of the SBR structures referred to in this thesis. All thicknesses numbers refer to the design thicknesses of the as grown structure and are do not reflect thickness measurements or non-uniformity over the wafer area.

<u>R933 (Cr:YAG):</u> 111nm InP 10nm InGaAs 111nm InP 7 pairs: 110nm AlGaAs 213nm AlAs GaAs substrate	<u>R934 (Cr:Fo):</u> 88nm InGaP 2 pairs: 10nm GaAs 4nm InGaAs 4ML InAs 82nm GaAs 7 pairs: 92nm AlGaAs 182nm AlAs GaAs substrate	<u>R946 (Cr:Fo):</u> 67nm GaAs 40nm InGaAs 67nm GaAs 7 pairs: 92nm AlGaAs 200nm AlAs 92nm AlGaAs GaAs substrate	<u>R957 (Cr:YAG):</u> 102nm GaAs 10nm InGaAs 102nm GaAs 7 pairs: 111nm AlGaAs 240nm AlAs 111nm AlGaAs GaAs substrate
<u>R958 (Cr:Fo):</u> 52nm GaAs 80nm InGaAs 52nm GaAs 7 pairs: 100nm AlGaAs 216nm AlAs 100nm AlGaAs GaAs substrate	<u>R959 (Cr:YAG):</u> 109nm InP 10nm InGaAs 109nm InP 7 pairs: 111nm AlGaAs 240nm AlAs 111nm AlGaAs GaAs substrate	<u>R968 (Cr:YAG):</u> 102nm GaAs 10nm InGaAs 102nm GaAs 7 pairs: 111nm AlGaAs 240nm AlAs 111nm AlGaAs GaAs substrate	<u>R970 (Cr:Fo):</u> 52nm GaAs 80nm InGaAs 52nm GaAs 7 pairs: 100nm AlGaAs 216nm AlAs 100nm AlGaAs GaAs substrate
<u>R971 (Cr:YAG):</u> 109nm InP 10nm InGaAs 109nm InP 7 pairs: 111nm AlGaAs 240nm AlAs 111nm AlGaAs GaAs substrate	<u>R979 (Er:Bi₂O₃):</u> 68.4nm InP 6 pairs: 10nm InGaAs 7nm InP 68.4nm InP 7 pairs: 119nm AlGaAs 259nm AlAs 119nm AlGaAs GaAs substrate	<u>R981 (Er:Bi₂O₃):</u> 68.4nm InP 6 pairs: 10nm InGaAs 7nm InP 68.4nm InP 7 pairs: 119nm AlGaAs 259nm AlAs 119nm AlGaAs GaAs substrate	<u>R1000 (Ti:Sapph):</u> 60nm InGaAlP 10nm GaAs 60nm InGaAlP 7 pairs: 65nm InGaAlP 150nm AlAs 65nm InGaAlP GaAs substrate

<u>R1014 (Er:Bi₂O₃):</u> 68.4nm InP 6 pairs: 10nm InGaAs 7nm InP 68.4nm InP 7 pairs: 119nm AlGaAs 259nm AlAs 119nm AlGaAs GaAs substrate	<u>R1015 (Cr:Fo):</u> 22nm GaAs 80nm InGaAs 82nm GaAs 7 pairs: 100nm AlGaAs 216nm AlAs 100nm AlGaAs GaAs substrate	<u>R1020 (Ti:Sapph):</u> 38nm InGaAlP 20nm GaAs 68nm InGaAlP 7 pairs: 140nm AlAs 65nm InGaAlP GaAs substrate	<u>R1021 (Er:Bi₂O₃):</u> 50nm GaAs 6 pairs: 12nm InGaAs 9nm GaAs 50nm GaAs 7 pairs: 119nm AlGaAs 259nm AlAs 119nm AlGaAs GaAs substrate
<u>R1023 (Cr:YAG):</u> 109nm InP 10nm InGaAs 109nm InP 7 pairs: 111nm AlGaAs 240nm AlAs 111nm AlGaAs GaAs substrate	<u>R1026 (Ti:Sapph):</u> 44nm InGaAlP 10nm GaAs 74nm InGaAlP 7 pairs: 140nm AlAs 65nm InGaAlP GaAs substrate	<u>R1027:</u> 67nm InP 100nm InGaAs 67nm InP 7 pairs: 119nm AlGaAs 259nm AlAs 119nm AlGaAs GaAs substrate	

5.3 Table of Relevant Refractive Indices for SBR Designs

The following is a tabulation of the refractive indices for the center wavelengths of the laser systems considered in this work. SBR software simulations performed by H. M. Shen in the Ultrafast Optics Group at MIT, considered the wavelength dependence of the refractive index over the full wavelength range of interest using the Sellmeier formula.

	$\lambda=800\text{nm}$	$\lambda=1300\text{nm}$	$\lambda=1550\text{nm}$
Al _x O _y	1.6	1.61	1.66
In _{0.15} Ga _{0.15} Al _{0.35} P	3.1	not available	not available
GaAs [1]	3.67-0.08i	3.41	3.38
AlAs [1]	3.01	2.91	2.89
Al _{0.3} Ga _{0.7} As [1]	3.45	3.25	3.23
InP [1]	3.55-0.16i	3.22	3.17
In _{0.5} Ga _{0.5} As [1]	4.03-0.29i	3.60-0.05i	3.53

5.4 Table of Optical Constants for Tri-Layer Processing

The following is a table of optical constants for the materials considered in this thesis at a wavelength of $\lambda=325\text{nm}$. This listing was based on a more comprehensive listing compiled by Dr. M. E. Walsh [2].

Material	Complex index of Refraction $\lambda=325\text{nm}$
Aluminum	0.33-3.95i
Chromium	1.12-2.95i
Silicon	4.68-2.03i
SiO ₂	1.48
Al ₂ O ₃	1.80
Si ₃ N ₄	2.06
GaAs	3.50-1.90i
XHRi (ARC)	1.52-0.20i
BARLi (ARC)	1.55-0.14i
FOX HSQ	1.436
Shipley 1813 (positive resist)	1.75-0.02i
PFI 88 (positive resist)	1.79-0.02i
OKHA PS4 (negative resist)	1.681-0.016i

5.5 References

- [1] E. D. Palik, *Handbook of Optical Constants*: Academic Press, 1985.
- [2] M. E. Walsh, "On the Design of Lithographic Interferometers and their Application." Cambridge, MA: PhD Thesis in Electrical Engineering and Computer Science, MIT, 2004.